UNIVERSITAT DE BARCELONA

FACULTAT DE FÍSICA I QUÍMICA

Departament de Ciència dels Materials i Enginyeria Metal.lúrgica

Tecnologia de Materials 2004-2006

STUDY OF THE STRUCTURE-PROPERTIES RELATIONSHIP OF Fe-Al, Nb-Al AND Ni-Ti INTERMETALLIC COATINGS OBTAINED BY THERMAL SPRAY TECHNOLOGIES

Memòria per optar al Grau de Doctor per la Universitat de Barcelona, presentada per Núria Cinca i Luis sota la direcció del Prof. Josep M. Guilemany i Casadamon

Barcelona, Octubre 2008

Josep Maria Guilemany i Casadamon, Professor Catedràtic del Departament de Ciència dels Materials i Enginyeria Metal·lúrgica de la Universitat de Barcelona certifica que:

El present treball titulat "Study of the structure-properties relationship of Fe-Al, Nb-Al and Ni-Ti intermetallic coatings obtained by Thermal Spray Technologies" ha estat realitzat en el Departament de Ciència dels Materials i Enginyeria Metal.lúrgica de la Universitat de Barcelona per la Srta. Núria Cinca i Luis i constitueix la seva Memòria de Tesi Doctoral.

"Education is an admirable thing, but it is well to remember

from time to time that nothing that is worth knowing can be taught."

Oscar Wilde

Per dir-me que amb esforç tot era possible,
per confiar sempre en mí,
per la teva reserva d'amor inexhaurible,
per donar-me ànims a seguir.

GRÀCIES

Dedico aquesta tesi a la meva mare i els meus avis
sense els quals no seria la persona que sóc ara i
no hauria arribat fins on he arribat.

AGRAÏMENTS / ACKNOWLEDGEMENTS

M'agradaria deixar constància de que aquests quatre anys m'han ajudat a créixer no només com a investigadora sinó també com a persona; vaig entrar amb una base de coneixements adquirida al llarg de la meva formació que havia despertat en mi una inquietud científica, i en surto amb l'afany de superar nous reptes i fer front al meu futur professional.

L'elaboració d'aquest treball no hauria estat possible sense una bona direcció al darrere; vull agrair doncs, al Prof. Guilemany, la confiança que ha dipositat en mi en tot moment des del primer dia. A la resta de l'equip directiu en general, per ser uns grans professionals i fer que aquest grup es superi cada dia: al Dr. Joan Ramon per aconseguir apropar més les relacions universitat-empresa; el Prof. Javier Fernández i la Dra. Irene García Cano amb els quals m'he assegut en tantes ocasions per raonar el perquè de les coses i, al meu company, el Dr. Sergi Dosta que és un exemple d'esforç i superació i, al qual li estic agraïda per molts consells que m'ha donat.

Voldria agrair a la Generalitat de Catalunya i al Ministeri d'Educació i Ciència la concessió de les beques pre-doctorals FI i FPU respectivament i, als projectes 2005 SGR 00310 (Generalitat de Catalunya) i MAT2006-06025 (Ministeri d'Educació i Ciència), així com al projecte europeu NAMAMET (NAnostructured MAterials through MEtastable Transformations).

També donar les gràcies a aquells que un dia van ser companys meus al CPT i ara ja són doctors, en especial a la Sílvia, per poder compartir tantes converses de temes tant de treball com personals i, al Marc, per donar tanta vida al CPT i estar sempre disposat a donar un cop de mà.

Fer extensió d'aquest agraïment als actuals doctorants i aprofitar per donar-los ànims en la feina que comencen: a la Sandra per ser la primera en apuntar-se a organitzar trobades fora de la feina, a la Maria per mostrar-se sempre tan assenyada i al Pablo pels cafès a última hora. A les tècniques

actuals: la Jèssica i la Verònica, i a tots els tècnics/ques i alumnes interns que han passat per aquí ... ha estat un plaer compartir tantes vivències amb tots vosaltres.

Un especial agraïment amb gran afecte a tots aquells altres col·laboradors externs, començant pel Prof. C R C Lima que ens va visitar durant el meu primer any i, al qual li tinc un apreci especial i, seguint pel Prof. A. V. Benedetti i els seus valuosos coneixements en corrosió electroquímica. També al Prof. A. Isalgué, al qual li estic molt agraïda pel gran interès mostrat en tots els aspectes relacionats amb la memòria de forma del NiTi, al Prof. C. Muller del Dept. d'Electroquímica i, al Prof. E. Molins i en Lluis Casas, de la Universitat Autònoma de Bellaterra, per ajudar-me en la obtenció i discussió dels resultats d'Espectroscopia Mossbauer.

A special thank to Prof. E. Lavernia and Prof. S. Sampath to accept me to work in their respective research groups from University of Davis (Califòrnia) and University of Stony Brook (Nova York). Also, to Nuno and Janet who are still good friends from my stay in Davis and helped me a lot; I hope we continue in touch.

No vull acabar sense fer menció de l'ajuda prestada pel personal dels Serveis Cientifico-tècnics, a la secció de DRX, en especial al Dr X. Alcobé pels seus coneixements de Rietveld i, a la secció de Microscopia Electrònica de Transmissió.

Finalment, cal dir que no tot han estat moments alegres sinó que també hi hagut cabuda per moments de desànim quan no sabia com tirar endavant; per tant, reiterar el meu agraïment al suport sempre prestat per la meva mare i els meus avis, així com els meus tiets i tots aquells que heu sabut escoltar-me i, per tant, heu compartit amb mi part d'aquesta experiència: a tots els meus amics tant la colla de química com d'enginyeria, i altres externs al món universitari, molts d'ells companys d'aula, però més important, companys en el camí de l'amistat.

.... a tots GRÀCIES

CONTENTS

APPENDIX I: Families of compounds and Miscellaneous applications

APPENDIX II: Refinement of X-ray data

APPENDIX III: Fundamentals of Mossbauer spectroscopy

APPENDIX IV: Principles of High Velocity Oxy-Fuel and Plasma Spraying

APPENDIX V: Paper 2: J. M. Guilemany, N. Cinca, C. R. C. Lima, J. R. Miguel. Studies of Fe40Al coatings obtained by High Velocity Oxy-Fuel. *Surface and Coatings Technology*, 201 (2006) 2072-2079.

APPENDIX VI: Paper 5: J. M. Guilemany, N. Cinca, S. Dosta, C. R. C. Lima, Oxidation behaviour of HVOF-sprayed ODS-Fe40Al Coatings at 900ºC. International Thermal Spray Conference (2007) Beiging (China).

APPENDIX VII: Paper 7: I.G. Cano, N. Cinca, S. Dosta and J.M. Guilemany. Study of NiTi Metastable Powders and Coatings Obtained by Plasma Spraying. *Revista de Metalúrgia,* 44, 3 (2008) 197-205.

Prefrace

The idea of a thesis focused on intermetallics arose after carrying out an exhaustive research within the literature which made realize the worldwide activity around these compounds. Therefore, following CPT's philosophy in answering industrial challenges and developing new technologies to meet the need for competitive products with improvement service life by cost effective methods, we bet for this new line of research.

Due to the difficulties on their manufacture as bulk materials, this work evaluates the use of intermetallics as coatings by using Thermal Spray technologies, which provide improved surface component properties.

After this first attempt, where the coatings have been obtained and tested in laboratory conditions, the next step will be to test them into real industrial environments in order to prove their application feasibility.

As long as the results are presented through the different chapters, a comparison with other thermal sprayed materials is reviewed as well in order to provide background information on this field.

CHAPTER 1: Introduction

1.1   General considerations

1.1.1   Brief historical remarks

Intermetallic-based materials have been used all over the world for thousands of years in a number of applications exploiting not only their mechanical properties but also their chemical, magnetic, optical and semiconducting. According to the elements combination, the appropriate stoichiometry can lead to unique properties which will make them appropriate for many purposes.

The use of intermetallic compounds (IMCs) can be early found in the history. In prehistoric times, humans used the ordered alloys Nature provided (e.g., meteoritic Fe-Ni for tools, and native Au-Cu for jewellery and fish hooks). Afterwards, from ancient to modern-times, alloy compositions and processing techniques were optimised for particular applications without the realization that IMCs were responsible of such successes. Some examples may be cited: SbSn to harden tin and other low-melting alloys for tableware, printing type, and bearings; δ-CuSn for mirrors; Ag_2Hg_3 and Sn_8Hg for dental fillings; and (Cu, Fe) Zn for ship sheathing and hardware. In the modern period, with a good understanding of the relations between composition, structure, properties and processing, simple systems could be selected having IMCs with desirable properties. Examples include $Ni_3(Al,Ti)$-strengthened superalloys, $Fe_{14}NdB$-based permanent magnets, $(Nb,Ti)_3Sn$ multifilament, high-field superconducting solenoids, and shape memory devices from NiTi [1].

Then, it is seen that practical metallurgical application of such materials occurred before they were recognized as distinct entities in alloys. The initial references in the literature date of the beginning of last century but the inflexion point was marked by the experiments carried out by Aoki and Izumi (1980) [2] who discovered that small additions of boron to Ni_3Al improved significantly its poor ductility; as it will be discussed, due to their crystalline

structure and bonding, fragility is considered one of the main limitations for their use as structural components.

We are just now entering a period of true alloy design where, using the available fundamental data (phase diagrams, crystal structures, thermodynamic quantities and atomic parameters) and having in mind the combination of properties desired for an application, we should be able to define the particular IMC system and structure that will achieve the goal sought.

According to the studies, there are estimated about 11000 distinct binary IMCs, most of which are known only through phase diagrams and crystallographic studies but there is no knowledge on the properties they can offer. Even more amazing, 500 000 true ternary intermetallics are calculated, only 3% of which are known to exist, and for only an infinitesimally tiny fraction of these do we have any knowledge of their properties. For the likely 10×10^6 quaternary IMCs, less than 0,01% are even known.

1.1.2   Structure and properties

An IMC is a true compound (with its chemical formula) of two or more metals that has a distinctive structure, in which the metallic constituents are in relatively fixed abundance ratios and are usually ordered on two or more sublattices, each with its own distinct population of atoms.

It is worth notice that several types of substances may be included in a preliminary broad definition of an intermetallic phase: both stoichiometric compounds and variable-composition phases and, as for their structures, both fully ordered or (more or less) disordered phases. In the strict sense of the definition given at the former paragraph, a stoichiometric compound would be seen such as that line phase in the phase diagram of figure 1.1a; however, intermediate solid solutions (fig. 1.1b) are many times included.

a   b
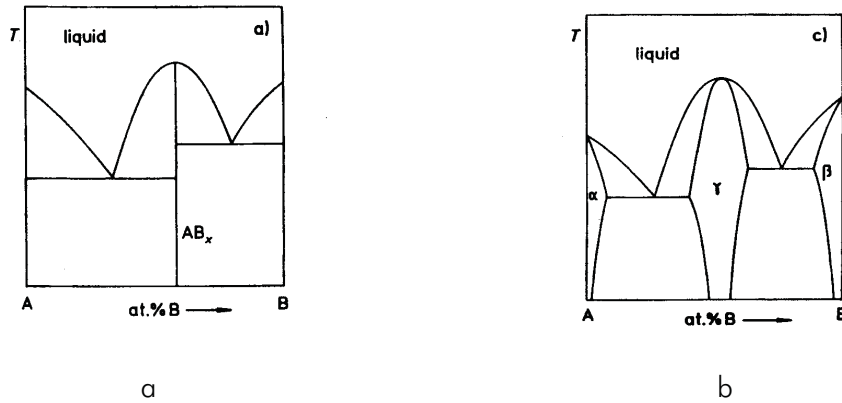
Figure 1.1. Examples of simple binary diagrams: (a) a stoichiometric compound is formed at the composition of AB_x formula, (b) an intermediate phase is formed in a certain composition range.

Figure 1.2 shows some of the typical structures for the intermetallic compounds. Several authors have attempted to define the best way to describe intermetallic phase structures such as Schubert (1964) and Frevel (1985); however, the most recommended by the IUPAC is the so-called Pearson notation (1972), which consists of a sequence of two letters plus a number. The first (small) letter corresponds to the crystal system of the structure type involved; the second (capital) letter represents the lattice type. The symbol is completed by the number of atoms in the unit cell. In addition, Strukturbericht notation[1] is still reported in the literature. According to this, the
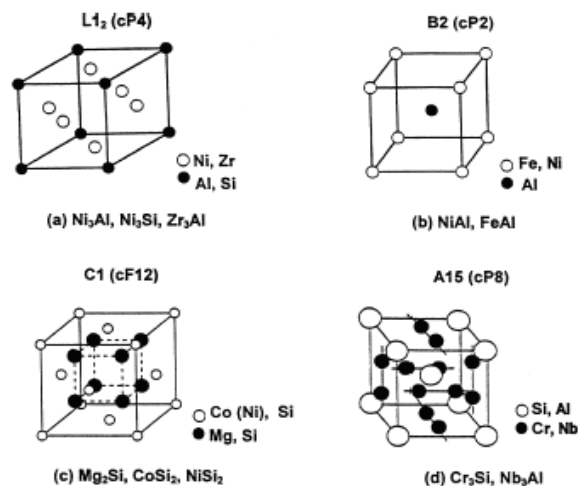
Figure 1.2. Generic cubic lattices of some aluminides and silicides.

---

[1] Designation adopted earlier than Pearson notation, in which each structure type is represented by a symbol composed of a letter related to the stoichiometry (A- unary phases, B- binary compounds having 1:1 stoichiometry, C- binary 1:2 compounds, D- binary m:n compounds, E…K types: more complex compounds; L: alloys, O: organic compounds and S: silicates) and a number.

examples in figure 1.2 [3] are presented with the Strukturbericht designation and accompanied by the Pearson symbol in parentheses.

Under these statements, differences from conventional alloys can be clearly stated in a number of important ways [4-8]:

1.   Conventional alloys consist of a disordered solid solution of two or more metallic elements. In opposite to IMCs, they do not have any particular chemical formula, and are best described as consisting of a base material to which certain percentages of other elements have been added. Therefore, their crystal structure is the same of the predominant element with some changes on the lattice parameter due to the addition of the alloying atom; IMCs however, might have structures completely different from that of original pure elements.

2.   The atoms in conventional alloys are linked with weak metallic bonds; intermetallics however, have partly ionic or covalent bonds, and therefore stronger. Alternatively, the bonding may be entirely metallic, but the atoms of the individual elements take up preferred positions within the crystal lattice. This condition, which is referred to as "ordering" leads to an abrupt change in the mechanical properties of the material. It must be pointed out that perfect ordered crystallographic structure of an intermetallic compound exists only at the exact stoichiometry of its formula and below certain critical temperature, generally known as the critical ordering temperature. For many materials, this T_c is close to the melting temperature. Whenever those premises are not accomplished, the lattice loses its order. Complete disorder may be reached as a result of a low ordering energy or the intervention of some external treatments such as rapid solidification, milling or irradiation. Some IMCs exist over a range of compositions, which implies that deviations from precise stoichiometry in either one side or the other of the nominal atomic ration, needs some disordering and/or the introduction of vacancies.

3.   Because of the ordered structure, intermetallic compounds tend to have much lower self-diffusion coefficient than do disordered alloys. The self-diffusion

coefficients of an ordered alloy can be several orders of magnitude smaller than that of the disordered alloy at a given temperature.

A number of characteristics derive from this arrangement of atoms: high melting points, great strength (particularly at high temperatures) but poor ductilities. In these respects, they resemble ceramic materials. Unlike ceramics however, they have a metallic lustre and, conduct heat and electricity well.

Figure 1.3. Hardness at room temperature of metals and intermetallic compounds. Pre-existing data are shown as circles, and recent data are shown as squares.

With emphasis on mechanical properties, they are, in many ways, intermediate between those of disordered metals, on the one hand, and covalently bonded materials, on the other. They tend to have higher strengths than metals but, at the same time, they also tend to have much lower ductilities. However, they are less brittle than ceramics. Problems associated with low ductility and/or fracture toughness have limited the applications of these alloys for structural uses [7, 9].

Figure 1.4. Shear moduli at room temperature of intermetallic compounds as a function of their melting temperatures. Pre-existing data are shown as circles, and recent data are shown as squares.

Figures 1.3 and 1.4 plots show respectively room-temperature hardness and shear moduli G versus melting temperature for many IMCs. In spite of scattering of values, there is a clear trend: from one hand, modulus increases dramatically with an increase in the melting point of the compound and, from the other hand, hardness of the IMCs is higher and increases much more rapidly with melting temperature than pure metals [10].

7

They also have many properties in addition to strength that make them more appealing than disordered alloys for high-temperature use. First, and perhaps most important, as stated above, intermetallic compounds tend to be intrinsically strong (high yield or fracture stress) and the strength tends to be maintained up to high temperatures. The modulus also tends to be high with a tendency to decrease more slowly with increasing temperature than does that of disordered alloys. In addition, those compounds based on light elements, such as transition metal aluminides, can have extremely low densities. The low density combined with the high strength and modulus give rise to very attractive specific properties, which are especially important for rotating machinery and aerospace applications. This is why these materials have been currently classified as new advanced materials.

The following section describes the materials to be dealt in the present thesis; however, as long as more knowledge is sought for other IMCs systems and their applications, the *Annex I* gives a brief review.

1.2 Transition metal aluminides

Aluminides, as well as silicides, have sufficient amounts of aluminium to form protective alumina scales under hostile conditions. They have relatively low density, high melting points, good thermal conductivity, and superb high-temperature strength; many intermetallics also show a yield strength anomaly, this is, their strength increases rather than decreases with temperature [6]. As a result, these intermetallics are particularly investigated for structural applications at elevated temperatures.

Figure 1.5a and b show two maps which relate fracture toughness and young modulus and, strength and density comparing those of iron, titanium and nickel aluminides with iron-base, titanium-base and nickel-base alloys. A general increase in material stiffness, as well as a slight increase in strength and a lower ductility, is associated to the strong interatomic bond of

intermetallics. Moreover, with the addition of a light element such as aluminium, the overall material density falls.

a   b
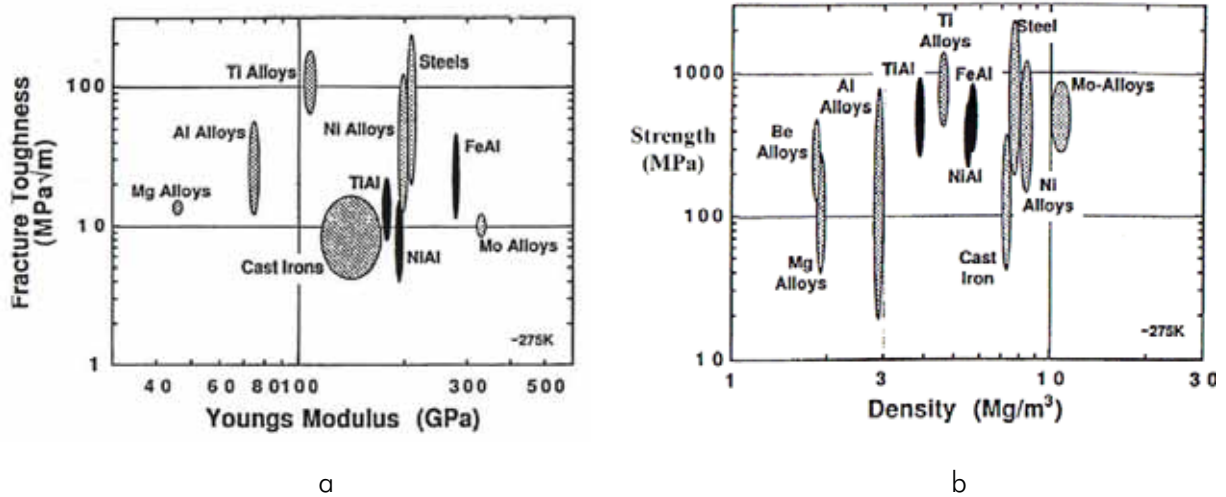
Figure 1.5. Maps comparing (a) ductility versus stiffness, (b) strength versus density of FeAl, NiAl and TiAl with Fe, Ni and Ti alloys.

Table 1.1 is a list of the main iron, nickel and titanium aluminides with their corresponding characteristics. It is worth noting their low relative densities and, for most of them, the coincidence of their critical ordering temperature to the melting temperature.

Table 1.1. General characteristics of selected intermetallic compounds [11]

Intermetallic	Critical ordering temperature (°C)	Melting point (°C)	Density (g/cm3)	Young's modulus (GPa)
Ni_3Al	1390	1390	7.50	179
NiAl	1640	1640	5.86	294
Fe_3Al	540	1540	6.72	141
	760	1540	-	-
FeAl	1250	1250	5.56	261
Ti_3Al	1100	1600	4.2	145
TiAl	1460	1460	3.91	176
$TiAl_3$	1350	1350	3.4	-

1.2.1   Nickel aluminides

The Ni-Al phase diagram (fig. 1.6) shows two stable intermetallic compounds (Ni_3Al and NiAl), formed on the Ni-rich end. The compound Ni_3Al has an $L1_2$ crystal structure, a derivative of the face-centered cubic (FCC) and NiAl has a B2 structure, a modification of the body-centered cubic (BCC). Because of the two different crystal structures, they have quite different physical and mechanical properties [12-15].
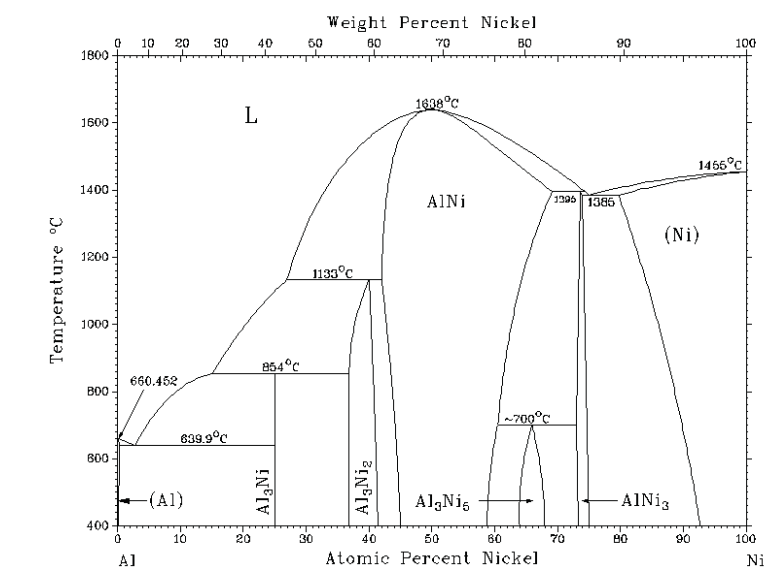
Figure 1.6. Ni-Al phase diagram.

The Ni_3Al is of interest because of its excellent strength and oxidation resistance at elevated temperatures. The discovery that small boron additions not only eliminated its brittle behaviour but converted the material to a highly malleable form arose the interest on IMCs. The major advantages that can be derived from their use include:

- Resistance to oxidation and carburization in both oxidizing and reducing carburizing atmospheres up to 1100°C
- Good tensile and compressive yield strengths for temperatures up to 1100°C. Ni_3Al is one of a number of intermetallic alloys that exhibits a yield strength anomaly, that is, their strength increases rather than

decreases with temperature. This fact confirms its suitability for structural applications at elevated temperatures.

- Fatigue resistance superior to that of nickel-based superalloys.
- Superior creep strength.
- Excellent wear resistance at high temperatures ($\geq$ 600°C). In fact, wear resistance increases with temperature.
- Surface pre-oxidation that provides good chemical compatibility for many environments owing to the formation of an alumina layer.

Nickel aluminide containing more than approximately 41 at% Al (NiAl) offers more potential for high-temperature applications than Ni_3Al. It has excellent oxidation resistance, higher thermal conductivity, higher melting temperature and lower density. Nevertheless, it has poor ductility at ambient temperatures and low strength and creep resistance at elevated temperatures.

1.2.2   Iron aluminides

Iron aluminides of interest are Fe_3Al and FeAl with ordered body-centered cubic structures, corresponding to DO_3 and B2 crystal structures, respectively. Fe_3Al exists over the composition range 23-36 at% Al and from room temperature to 550°C. Above such temperature, it transforms to an imperfectly ordered B2 structure, which ultimately changes to a disordered solid solution. On the other hand, FeAl exists with B2 structure and is stable from about 36-48 at% Al; the transition from B2 to solid solution occurs well above 1100°C.

The DO_3 to B2 transition temperature decreases and the B2 ordered temperature increases with an increase in aluminium concentration above 25%. Figure 1.7 shows the phase diagram of Fe-Al system.
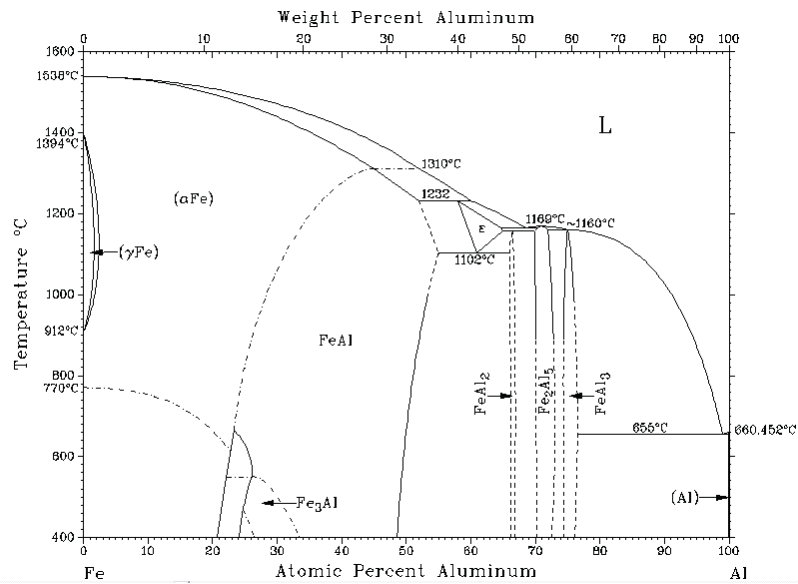
Figure 1.7. Fe-Al phase diagram.

The principal properties of iron aluminides are the following [12-16]:

- A density lower than that of many stainless steels and, therefore, they offer better strength-to-weight ratios.

- Higher resistance to sulfidation and carburizing atmospheres as well as in molten nitrates and carbonate salts, than that of any other iron- or nickel based alloys.

- Excellent oxidation resistance at temperatures up to 1200°C.

- High electrical resistivity that increases with temperature.

- Good corrosion resistance in many aqueous environments.

- Thermal conductivities of iron aluminides are lower than those of nickel-base alloys, and their thermal expansion coefficients are similar to those of stainless steels.

Fe_3Al alloys also show anomalous yield strength temperature dependence. The mechanical behaviour is improved by reduction of Al content, alloying with further elements and thermomechanical treatments, which leads to alloys for eventual applications in conventional power plants or in coal conversion plants. FeAl shows the same crystal structure as NiAl, and its behaviour is

indeed similar. Aluminides based on FeAl exhibit better oxidation and corrosion resistance than Fe_3Al alloys and are also lower in density.

Mechanical properties of intermetallic compounds can be improved by control of microstructure, alloying and adding more ductile second phase particles. For example, toughness and ductility of FeAl and Fe_3Al can be improved by additions of molybdenum, zirconium and boron which make them potential materials for heat exchangers having service temperatures between 700 and 800°C.

1.2.3   Titanium aluminides

Among the intermetallic compound phases identified in Ti-Al alloys, Ti_3Al, TiAl, Al_2Ti and Al_3Ti phases are stable at room temperature (fig. 1.8).
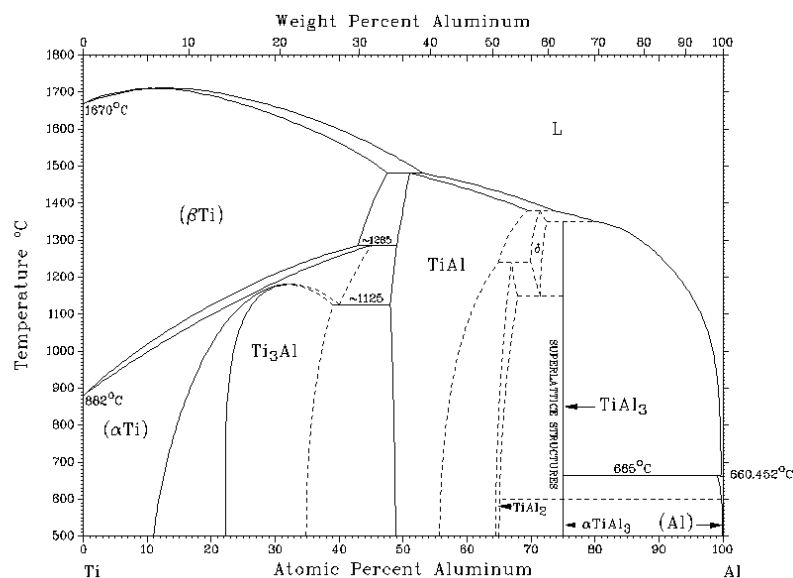
Figure 1.8. Ti-Al phase diagram.

In comparison to conventional titanium alloys, TiAl- based alloys are the most intensively studied because of their low densities, strength and modulus retention at high temperatures, some tensile ductility at room temperature, and reasonably good oxidation resistance. This make them very attractive as a new class of light-weight high-temperature materials for structural applications,

especially in advanced aerospace engine and airframe components [17, 18]. Their oxidation resistance, however, is lower than desirable at elevated temperatures. Titanium aluminides are characterized by a strong tendency to form TiO_2, rather than the protective alumina.

1.2.4 Niobium aluminides

In the binary Nb-Al phase diagram (fig. 1.9) there are three niobium aluminides: Nb_3Al (A15), Nb_2Al ($D8_b$) and $NbAl_3$ ($D0_{22}$). These niobium aluminides have more complex crystal structures than the above aluminides and thereby they are extremely brittle at ambient temperatures. This means that ductility or toughness improvement at ambient temperatures is required to use them as structural materials [19, 20].
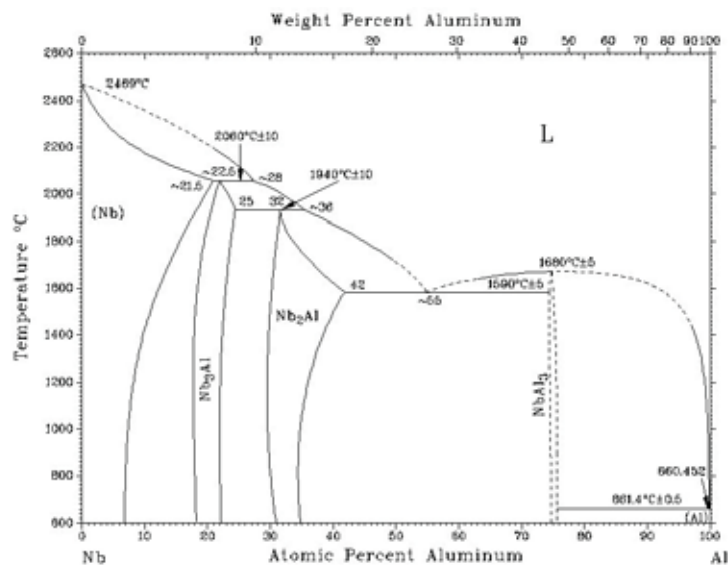
Figure 1.9. Nb-Al phase diagram.

The A15 Nb_3Al has been recently examined for its potential as a high temperature structural material. Its ductilization has been studied through the incorporation of a ductile phase; also, ternary Nb_3AlX (X= Mo, Ta, Cr, Ti, Si, Sn and Ge) have been examined.

Few studies on monolithic Nb_2Al claim that it fails in a brittle manner before plastic strain below 1200°C. Nevertheless, it has yield stresses even higher than those of monolithic Nb_3Al.

The binary $NbAl_3$ intermetallic alloy possesses several properties that make it attractive for use as a high-temperature structural material. These include a relatively low density (4.5 g/cm^3), high melting point (1605°C), and excellent oxidation resistance at 1200°C by Al_2O_3 scale formation when alloyed with chromium, silicon, and yttrium.

Instead of most iron, nickel and titanium aluminides which exist over a composition range, $NbAl_3$ is a line compound. This fact, however, leads to different oxidation behaviour. NiAl, for example, forms above 1000°C a slow-growing protective alumina layer with the intact metal beneath; by contrast, $NbAl_3$ initially leads to alumina, but the Al depletion causes the formation of lower stoichiometric compounds beneath. Cracking of the Al_2O_3 layer promotes a rapid oxidation to Nb_2O_5 and $NbAlO_4$. Such phenomenon is known as "pesting". Several approaches for avoiding this failure are under investigation.

1.3 Structure and properties of nitinol[2] (NiTi alloy)

The Ni-Ti phase diagram (fig. 1.10) shows three different equilibrium intermetallic phases: Ni_3Ti, NiTi and $NiTi_2$. Ni_3Ti is a close-packed superlattice and $NiTi_2$ has a complex face-centered cubic structure.

---

[2] **Ni**ckel **Ti**tanium **N**aval **O**rdenance **L**aboratory
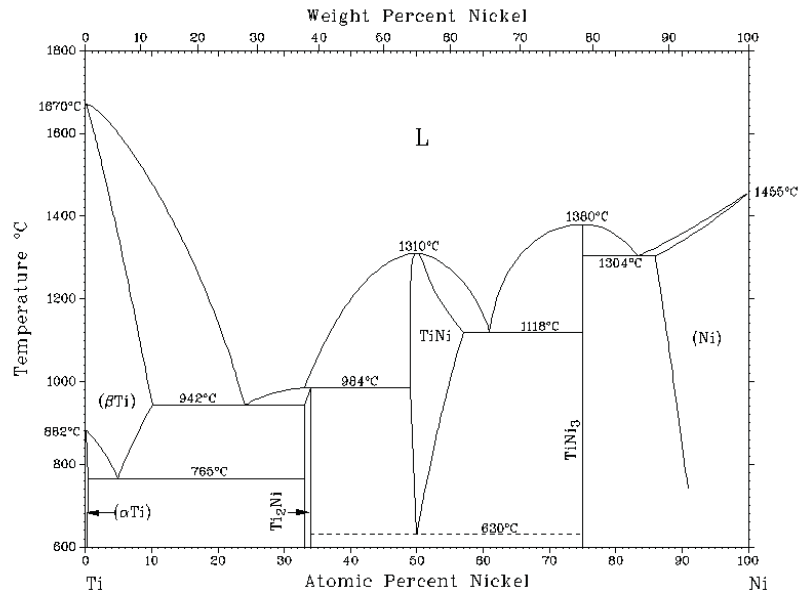
Figure 1.10. Ni-Ti phase diagram.

The structure of the intermetallic NiTi phase has a high technological interest because such alloys provide controlled material and damping properties and to change their shape with temperature and load. This means they can be set at a particular shape, cooled below a critical temperature range (M_s-M_f^3) and then deformed to a different shape. On being re-heated towards the original temperature (A_s-A_f^3), the original shape will be restored (fig. 1.11-a- *shape memory effect*). If this is prevented by a restraining force, the material will exert a force capable of doing a work as an actuator or if partially constrained to prevent a full recovery of its shape, it will develop a force capable of gripping the constraint. If the material is deformed close to, but above the A_f temperature, it will deform in an apparently elastic manner at a low stress and will resume its original shape on removal of the stress (fig. 1.11-b-*superelasticity*); under these conditions it can act as a spring [21, 22, 23].

---

[3] Shape memory effects and pseudoelastic behavior are associated with the reversible martensite (monoclinic B19′ -type structure)-austenite (B2 CsCl- type structure) phase transformation and the reorientation of martensite variants. M_s (martensite start) - M_f (martensite finish) / A_s (austenite start) – A_f (austenite finish); A_s>M_f and A_f >M_s.
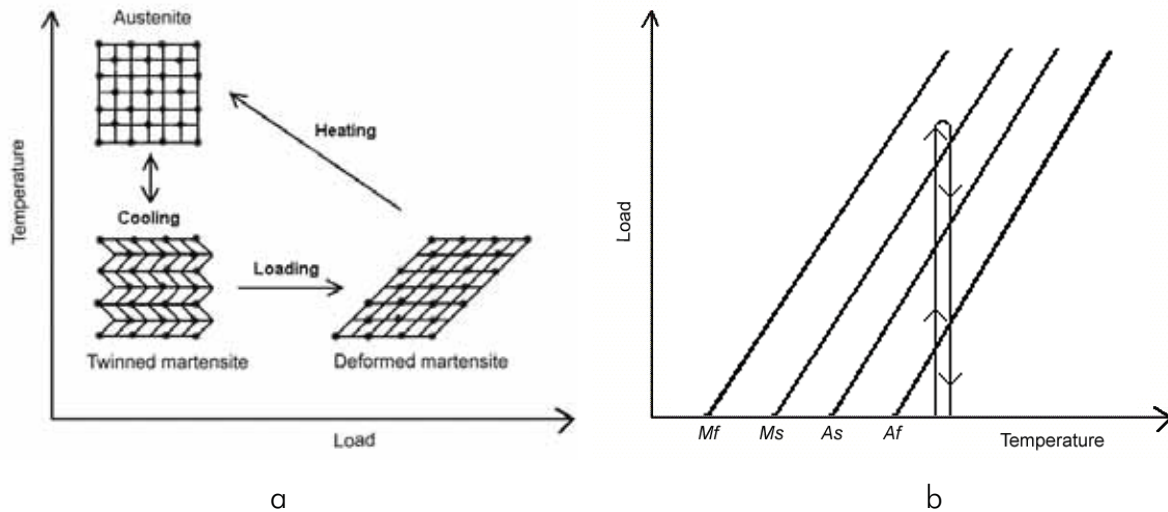
Figure 1.11. (a) Shape memory effect and (b) superelasticity.

The reversible transformation martensite-austenite takes place in the temperature range from 50-100 °C depending on the Ni content. The operating temperatures are really sensitive to chemical composition. They can be lowered considerably either by increasing the nickel content or by the presence of impurities such as oxygen, carbon and nitrogen. The martensitic transformation temperature of NiTi SMAs can be also decreased either with cold work or by decreasing heat treatment temperature.

Some of the basic properties of the stoichiometric NiTi alloys are presented in table 1.2 [24, 25].

Table 1.2. General characteristics of nitinol [26].

Melting point (°C)	1250
Density (g/cm^3)	6.45
Young modulus (GPa)	~95
Ultimate tensile strength, martensite (MPa)	800-1000
Elongation at fracture, martensite (%)	30-50
Transformation temperature range (°C)	-100 - 110

1.4 Processing methods

1.4.1   Transition metal aluminides

Figure 1.12 presents several possible routes for processing intermetallics. Melting is still the primary processing technique to obtain a variety of cast, wrought and powder metallurgical products, and it will determine whether an intermetallic can be obtained economically with good control of the composition and with minimal of defects and porosity in the cast structure. However, the melting process will have to face many considerations [6, 12, 13]:

- Difference between melting points of aluminium and transition metals such as Ni, Fe, Ti and Nb.
- The large amounts of aluminium present in intermetallics.
- The exothermic nature of formation of the intermetallic compound.

The exothermicity can be seen as an advantage in melting and casting of intermetallics since it can save time and energy needed for melting. However, in order to overcome the safety issues due to the uncontrolled nature of the reaction, many efforts have been addressed to a new method called Exo-MeltTm, which consists of a furnace-loading sequence where molten aluminium will react with part of the nickel melt stock in a controlled manner. The target composition of an alloy is reached easily and safely with the Exo-MeltTm process as compared with the conventional process.

Another concern of the melting technique is the use of a wet charge or moisture around the melting crucible, which can result in the generation of large amounts of hydrogen, producing large voids in the solidified aluminide. During air melting, the hydrogen-related porosity can be eliminated by using a dry charge or blowing the molten metal with argon gas. The vacuum-melting processes produce ingots free of gas porosity.

Finally, the conventional method of melting Fe, Ni or Ti and adding aluminium to it causes the rise of molten-bath temperature by several hundred of degrees. Such a rise in temperature causes melt oxidation, longer holding times prior to pouring, and a potential for missing the target chemistry because of alloying element oxidation. The Exo-MeltTm process can take advantage of heat generated from the formation of the compound and allows bringing the melt to the pouring temperature in a gradual manner with minimum oxidation.
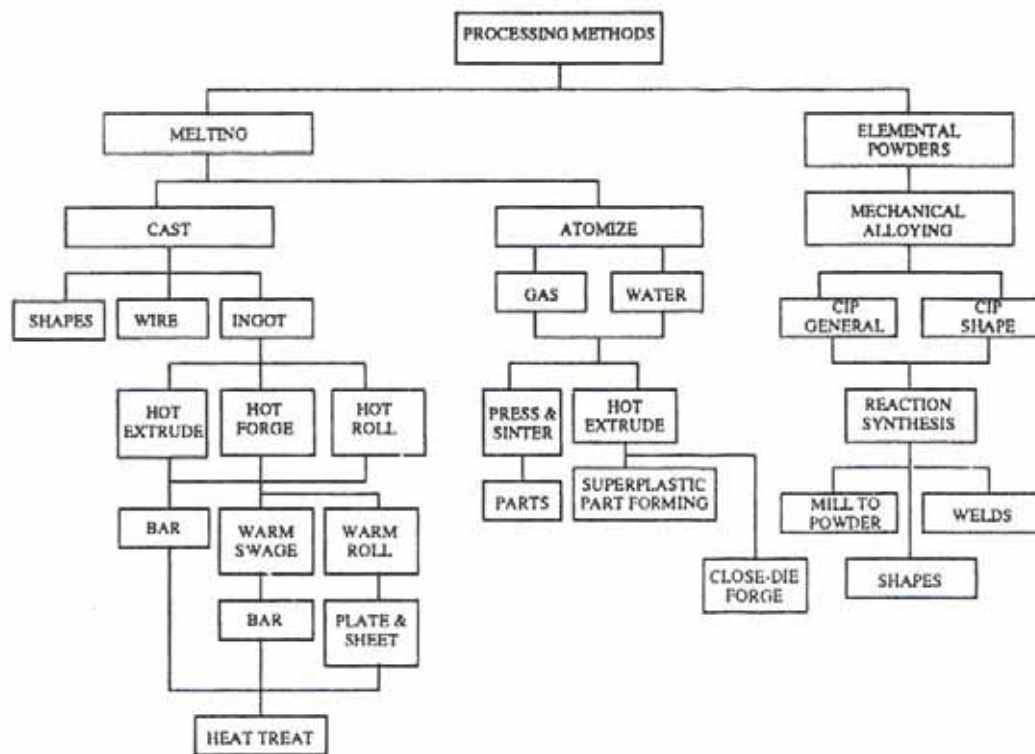
Figure 1.12. Possible methods for the production of iron aluminides.

In view to the difficulties encountered for the fabrication of intermetallics by conventional techniques, another route is considered: mechanical alloying (MA) of elemental powders. Mechanical attrition was first developed to produce oxide dispersion strengthened alloys and is now being considered as a new method for obtaining materials with unique microstructures and properties. Material production can take place at room temperature which can

have advantages over high temperature synthesis, in particular for synthesis of intermetallic compounds. MA can also alleviate the problem of low ductility of IMCs through [27, 28]:

- A reduction in grain size.
- Disordering of the lattice, to improve the dislocation motion.
- Modification of the crystal structure of the phase into a more symmetric, e.g. cubic one.

Mechanical alloying can achieve all the above effects simultaneously and therefore, this processing technique has been extensively employed to synthesize intermetallics and study their mechanical behaviour.

1.4.2   Nitinol

Because of the reactivity of the titanium in these alloys, all melting processes must be done in a vacuum or an inert atmosphere. Conventional routes to produce NiTi for shape memory effect consist first in the synthesis of the alloy starting from pure elemental metals by either vacuum induction melting (VIM) or vacuum arc remelting (VAR), followed by hot-forming such as forging, bar rolling, and extrusion for initial breakdown. Following hot working, nitinol alloys are cold worked and heat-treated to obtain final dimensions with desired physical and mechanical properties [29, 30].

In order to avoid the costly VIM or VAR and associated manufacturing steps, several powder metallurgy routes have been developed. Either prealloyed metal powders or elemental powders can be used, but the latter approach is preferable because of the high cost of manufacturing alloyed powders. Such powders will be then compacted and sintered by one of the following routes:

- Hot isostatic pressing (HIP).
- Reactive sintering.
- Explosive shock synthesis.
- Hot extruding.

- ▪ Metal injection molding.

- ▪ Self-propagation high temperature/combustion synthesis [31].

- ▪ Vacuum plasma spraying / low pressure plasma spraying.

- ▪ Laser plasma spraying.

However, one of the limitations of PM processes is to synthesize single phase NiTi powders. The final products are normally a mixture of several intermetallic phases i.e. NiTi, $NiTi_2$ and Ni_3Ti.

1.5 Attempts at structural applications

1.5.1 Transition metal aluminides

a)   Commercialization of bulk FeAl, NiAl and TiAl-based alloys

   – *Nickel aluminides*

The principal and most known application of Ni_3Al has been as precipitates γ' phase in the Ni-based superalloys, where these are surrounded by a Ni FCC matrix. The intermetallic is the responsible of their high temperature strength. Other applications however, where the components have been manufactured by the Exo-Melt process, include [13]:

-   Transfer rolls to operate at or above 900°C.

-   Heat-treating trays and posts for operation in carburizing furnaces. In this case, Ni_3Al-based alloys perform better because they resist carburization and corresponding embrittlement. It also provides longer life because of its higher tensile and creep strengths and resistance to thermal fatigue resulting from frequent quenching in oil.

-   Rails for walking-beam furnaces, which are used for heating bars of steel prior to their hot forging into shapes.

-   Centrifugally cast tubes and static sand-cast return bends of Ni_3Al for radiant-burner-tube applications in gas-fired heating application.

- Grate bars of IC-221M used for calcinations of ores at high temperatures.

- Die blocks of IC-221M for closed-die for hot forging.

- A paddle for mixing ceramic slurries and a high-temperature guide roller for furnaces. Advantage is taken of superior wear resistance at high temperatures.

- Nuts and bolts of Ni_3Al-based alloys for high-temperature applications.

- Corrosion resistant tool bits for the pulp and paper industry based on Ni_3Al as a binder phase in WC-Ni_3Al composites.

Table 1.3. Target compositions of castable Ni_3Al-based alloys [13].

	IC-50	IC-218LZr	IC-221M
Ni	88.08	83.1	81.146
Cr	-	8.1	7.74
Mo	-	-	1.428
Al	11.3	8.7	7.98
B	0.02	0.02	0.008
Zr	0.6	0.2	1.697

- *Iron aluminides*

Iron aluminides can be an excellent choice instead of 300 and 400 series stainless steels and some nickel-base alloys.

At the moment, the major application of Fe_3Al is for hot gas filters. These filters are manufactured by sintering powders using a proprietary process and are used to remove particulate matter from the gas produced in the coal-gasification process and other processes where the gas contains high sulphur content.

Other potential uses include:

- Heating elements, where the iron-aluminide alloy wire is used in toasters, ovens and dryers. Advantage is taken of the high resistivity, which remains constant up to 1000°C, and the excellent oxidation resistance. Their fabrication has been hampered by limited ductility at room temperature.

- Furnace fixtures: components such as retorts, rollers, beams, etc. The furnace fixtures are expected to be manufactured by various casting processes.

- Catalytic converter substrate. The 0.05mm thick foil for this application is prepared primarily by warm rolling followed by cold rolling in the last few passes.

- Regenerator disks, where the iron aluminide is used as a heat exchanger in a gas turbine engine. The foil requirements for these applications are similar to those for the catalytic converter substrates.

- Components for molten salt applications, where iron aluminides are used as containers, for transference or even rotating components. The components for this application will be manufactured by a combination of the casting process, hot-working ingots, and welding.

- Shielding: for preventing the excessive oxidation of tubes in power plants an incinerators. These shields are typically manufactured by bending the warm-rolled sheet of the desired thickness.

Table 1.4. Composition of Fe_3Al and FeAl-based alloys developed for commercial applications [13].

Element	Alloy (wt%)						
	Fe₃Al-based alloys				FeAl-based alloys		
	FAS	FAL	FA-129	MA-956	FA-385	FA-385M1	FA-386M1
Al	15.9	15.9	15.9	-	21.1	21.2	21.1
Cr	2.20	5.5	5.5	20.0	-	-	-
B	0.01	0.01	-	-	-	0.0025	0.0050
Zr	-	0.15	-	-	0.10	0.10	0.15
Nb	-	-	1.0	-	-	-	-
C	-	-	0.05	-	0.03	0.03	0.10
Mo	-	-	-	-	0.42	0.42	0.42
Ti	-	-	-	-	-	-	0.05
N	-	-	-	-	-	-	0.02
Ni	-	-	-	-	-	-	-
Fe	Bal.	Bal.	Bal.	Bal.	Bal.	Bal.	Bal.

The FeAl-based alloy is currently being used in sheet form for microheaters. Also, in the automobile industry, piston valves based on FeAl have been casted using the Exo-Melt process. However, engine testing will be required to show the total performance improvement over the currently used materials. Apart from the above, intermetallics based on nickel and iron offer potential as piping and tubing in chemical and petrochemical industries, high-temperature strength, exhaust manifolds and catalytic converter substrates.

− *Titanium aluminides*

TiAl has widespread potential for use in both aero and land-based applications because of its refractory nature and very low density. Specially, TiAl alloys for casting have been considered for aero-engineering applications (blades, vanes and compressor cases have been manufactured) [32]. Castable TiAl alloys have potential for use in various automobile engine parts such as the attempt at fabricating automobile turbocharger rotors. The results revealed that the TiAl turbocharger exhibits a better acceleration response and a higher maximum rotational speed than a corresponding Inconel 713C rotor [33]. However, there are still some shortcomings remaining for the use of TiAl turbochargers at large scale: low ductility at room temperature, relatively poor oxidation resistance at high temperatures and excessive cost.

Recently, the intermetallics research group of Toyota Motor Corporation reported that the addition of nitrogen to the two-phase alloys results in dramatic grain refinement and precipitation of numerous fine nitrides. Various automobile engine parts such as valves are said to have been successfully cast using near-equiatomic alloys containing about 0.3wt% N.

− *Niobium aluminides*

Although the metallurgy of niobium alloys began in the earlies 1900's, there never was a commercially viable oxidation resistant niobium alloy. There was an increased development through the early 1970's associated to the

immersion in the missile defense programs; however, all the high strength, high temperature niobium alloys exhibited such difficulties in fabricating into normal mill products (sheet, bar, plate) that their use was significantly limited, if they were available in commercial quantities. Table 1.5 presents some of the surviving attempts on niobium alloys in the mid-1970's [34].

Table 1.5. NbAl-based alloys compositions.

	C103	FS85	Cb129Y	Cb752	Nb1Zr	30-09/15
Nb	Bal.	Bal.	Bal.	Bal.	Bal.	Bal.
Hf	10	-	10	-	-	30
Ti	1	-	-	-	-	-
W	-	10	10	10	-	9-15
Ta	-	28	-	-	-	-
Zr	-	1	-	2.5	1	-
Y	-	-	0.2	-	-	-

b)   High temperature requirements for FeAl, NiAl and TiAl-based coatings

One of the problems encountered when trying to develop new materials for high temperature applications, is the capability to balance oxidation resistance with high-temperature strength. Properties of many of the engineering current materials such as tensile creep and fatigue strength are generally optimized for maximum load-carrying capability, with less emphasis on the environmental resistance. As an example, turbine blades for jet engines are made of precipitation strengthened nickel base superalloys. Although higher aluminium content of the alloys would increase high-temperature oxidation resistance, it is kept at a level below 6% to maximize creep strength. If such bare alloys are exposed to environment of high-pressure modern gas turbine engines, they will degrade fast. Therefore, although an increase in Al levels would be a logical solution, it would reduce, in turn, the load-bearing capability, a "must have" property of turbine blades and other turbine hardware. In addition, Cr is also

a critical element for corrosion resistance but its relatively lower content helps to meet the structural capability requirement to carry load.

Then, one can realize that almost 98% of alloys and superalloys capable of operating above 700°C in oxygen environments contain less than 2%wt Al and invariably contain chromium as high a concentration as 18wt% for oxidation resistance. Alloys containing chromium form Cr_2O_3 on exposure to air or oxygen but the dissociation of Cr_2O_3 to CrO_3 limits their oxidation resistance to 950°C [35, 36]. Therefore, it is difficult to balance environmental resistance toward oxidation and high-temperature corrosion versus high strength, ductility and producibility. All these goals do not normally go hand in hand.

Table 1.6. Temperature limits for iron, nickel and titanium aluminides [12].

Intermetallic	Maximum use temperature (°C)	
	Strength limit	Corrosion limit
Ni_3Al	1100	1150
NiAl	1200	1400
Fe_3Al	700	1200
FeAl	800	1200
Ti_3Al	760	650
TiAl	1000	800

Nickel and iron aluminides provide excellent oxidation resistance in the range 1100°C to 1400°C owing to their high aluminium contents and high melting points. Table 1.6 provides their maximum use temperatures. As it can be seen however, their high-temperature corrosion resistance, more noticeable in iron aluminides, extends to temperatures at which these alloys have limited or poor mechanical strength [35]. Because of this, iron aluminides appear particularly interesting as coatings or claddings on more conventional higher-strength materials which are less corrosion-resistant at high temperatures.

1.5.2 Nitinol

The main application early found for NiTi alloy was in the medical market due to its good corrosion resistance and lower elastic modulus when compared to stainless steel. However, there is some concern around its biocompatibility due to the possibility of Ni ions release and also improvement in the biological response is dependent on the optimization of its surface conditions [37]. As biomedical devices in current use, they find application in the isothermal elastic condition, in orthodontics (brackets and wires) and in surgery (porous NiTi SMA for implants, as guidewires, stents, suture replacement, etc.). Also, as a corrosion resistant alloy, it has reported to possess a high corrosion resistance in marine environments where, similar to other passive metals, a passive oxide film is naturally formed on it [38].

Other applications include sensitive actuators, e.g. in thermostats and fire protection devices (as it changes shape, it can activate a switch or a variable resistor to control the temperature), automotive actuators and safety valves. For more sophisticated applications, they can be even used for microdevices in aerospace industry for miniature latching valves and micromachined pneumatic valves. These alloys can also be used as fixing and gripping devices, e.g. to join tubes in inaccessible locations, as well as erosion resistant materials due to their recovery capability [25].

Nevertheless, the disadvantages of (NiTi) SMAs are (1) the high price of the alloying elements and the high requirements during fabrication and (2) the A_s temperature, which is limited to around 100°C. Primarily due to the first reason, the coating of the components is effective for taking advantage of their good erosion and corrosion properties.

1.6   Thermal Spraying technologies

With regard to the above comments, we can see that coating methods are really promising in order to encompass many of the most challenging industry

requirements. In general, the metallic coatings should present the following properties:

- ▪ For service performance:
- - Oxidation/corrosion resistance.
- - Thermodynamically stable, protective surface scale of uniform thickness.
- - Slow growth rate of protective surface.
- - High concentration of scale former.
- ▪ Stability
- - No undesired phase changes within the coating.
- - Low diffusion rate across interface at use temperature.
- - Minimized brittle phase formation.
- ▪ Adhesion
- - Good adherence of coating to substrate.
- - Matched coating/substrate properties to reduce thermal stress.
- - Minimized growth stresses.
- - Optimized surface condition.
- ▪ Structural properties
- - Can withstand service-related creep, fatigue, and impact loading of surface without failure of function.

The selection of the proper process for coating deposition depends on the component design and the application. One can find:

- *Diffusion coatings*, which consist of a substrate alloy surface layer enriched with the oxide scale formers Al, Cr, Si or their combination to a depth of 10 to 100 microns. These elements combine with the primary constituents of the substrate alloy to form intermetallics with significant levels of the oxide scale formers.

- *Overlay coatings*. The behaviour of diffusion coatings strongly depends on the composition of the substrate alloys because the alloy participates in the formation of the coating. As a result, these coatings do not offer wide flexibility for the incorporation of minor elements. In order to address this

limitation, the new class called "overlay" coatings has been developed with minimal direct contribution of the substrate alloys. The overlay coatings are usually deposited either by electron beam physical vapour deposition (EB_PVD) or by spray processes.

The *Thermal Spray technologies* are those on which the present thesis has focused. Their basic principle is to impart sufficient kinetic and thermal energy to the raw material (in powder, wire or rod form) to create a confined high-energy particle stream, and propel the energetic particles toward the substrate using high-pressure carrier gas. The particles plastically deform on impact with the substrate creating cohesive bonds with each other and adhesive bonds with the substrate (fig. 1.14). This coating technology combines a variety of positive characteristics:

- Numerous combinations of base material and coating material are possible.
- Shortages of raw materials, and resulting high prices, are forcing industry to use high-grade materials specifically for the production of high-quality surfaces which possess properties the base materials do not have.
- The flexibility of thermal spraying means that high-grade worn parts can be repaired in a variety of ways. Low repair costs and relatively short downtimes represent major advantages in relation to other refurbishing methods.

Therefore, thermal spray coatings are really versatile as means of protecting metals from aggressive environments e.g. for corrosion or wear resistance. The coating materials include metals, ceramics, polymers and combinations of those. Depending on to what materials is going to be sprayed, one technique or another will be used and several parameters can be optimised in order to reach the desired microstructure.
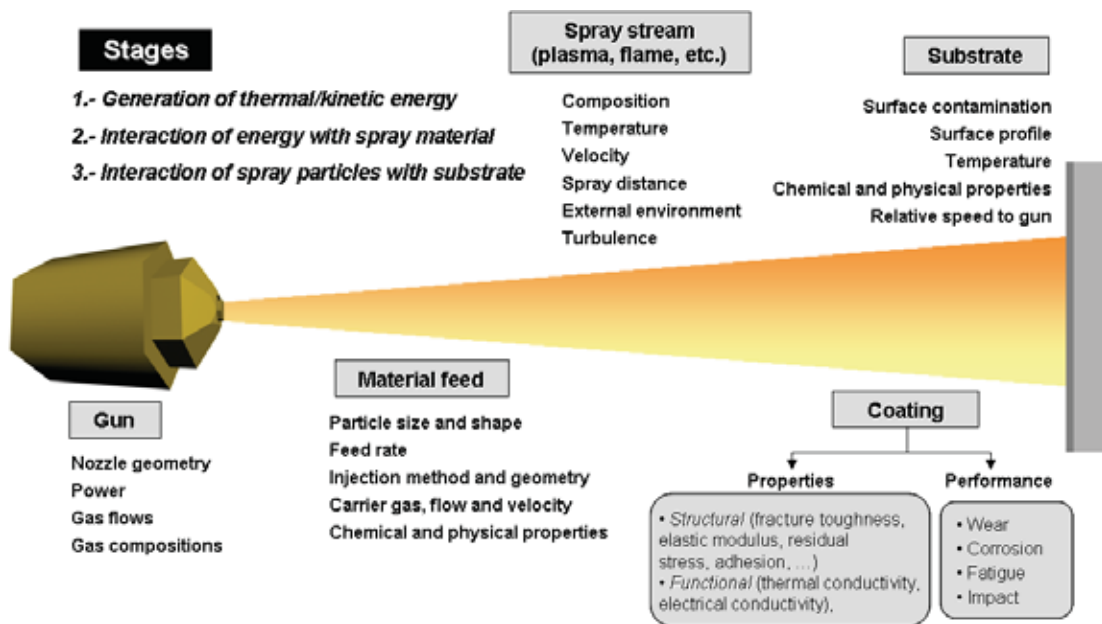
Figure 1.14. Schematic basics of thermal spraying.

The term "thermal spraying" covers a range of spray processes which can be classified according to the type of spray material, type of operation or type of energy source. The most common classification is that which presents the techniques according to the energy source. Therefore, the energy sources currently in use are: *combustion* (detonation of combustion gases -Detonation Gun-, flame created by combustion of gases -Flame Spray and High-velocity Oxygen Fuel HVOF-) and *electric energy* (sustained plasma created by electrical discharge -Plasma Spray- and electric arc -Arc Spray-) [39-44].

Figure 1.15 shows a very schematic plot broadly locating the different thermal spray techniques according to flame / plasma temperature versus particle velocities.
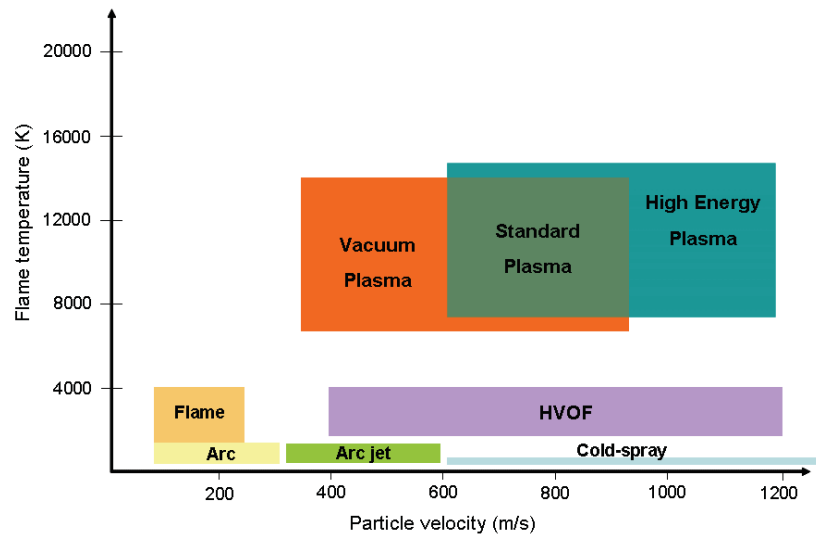
Figure 1.15. Temperature-velocity distribution of thermal spray processes.

It is worth noting that phase diagrams that are so useful in many technologies of materials engineering, prove to be less useful in predicting the final coating composition. The reasons for this are threefold: first, thermal spraying involves rapid solidification leading to new phases or amorphous structures, secondly, it might be accompanied by a change in chemical composition (e.g. selective evaporation of a component of multicomponent powder), and thirdly the spraying atmosphere may lead to oxidation or reduction. The building-up process of a sprayed deposit may also promote, depending on the technique, retention some level of porosity, typically between 0 and 10%, unmelted or partially melted particles, fully melted and deformed *splats*, metastable phases and oxidation from entrained air (fig. 1.16).

There are many process variables that will finally affect the quality of the coating such as particle size and particle velocities, temperature, powder feed rate, spraying distance, and so on. A proper optimisation is critical in order to achieve the optimal structure for the final application. Thus, for example:

- Oxides may increase coating hardness and wear resistance and may provide lubricity. By contrast, excessive and continuous oxide networks

31

can lead to cohesive failure of a coating and contribute to excessive wear debris, as well as reduce corrosion resistance.

▪ Porosity may be also beneficial in tribological applications through retention of lubricating oil films. It is also beneficial in coatings on biomedical implants.

▪ The retention of unmelted and/or resolidified particles can lead to lower deposit cohesive strengths, especially in the case of as-sprayed materials without post-deposition heat treatment or fusion.
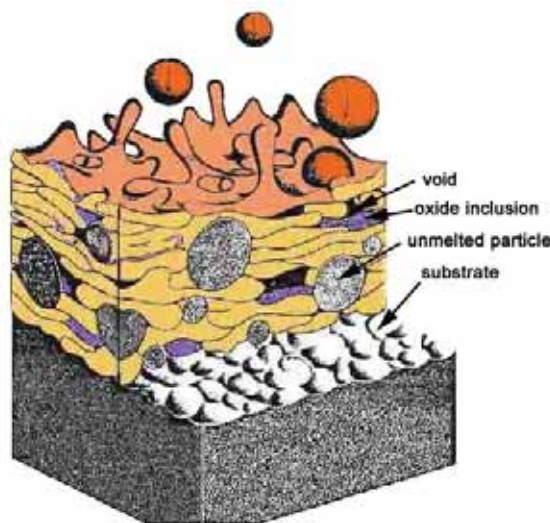
Figure 1.16. Typical features of a thermal sprayed coating

Therefore, selection of the appropriate spraying method will be determined by: coating material characteristics, coating performance requirements, economics and, part size and portability.

1.6.1 Possible applications for intermetallic coatings

This section outlines some industrial problems where the materials studied in the present thesis could provide noticeable improvements.

a)   FeAl coatings

In many industrial high-temperature applications, both high-temperature strength and high-temperature corrosion-resistance are required. However, it

is usually very difficult to develop steels and alloys that can satisfy these requirements. Because alloys based of Fe_3Al and $FeAl$ form Al_2O_3 during exposure to oxidising gases, they typically display relatively low oxidation rates when compared to iron-based and other alloys that do not form alumina or silica in comparable temperature ranges. Their oxidation rates have been studied in air or oxygen at temperatures in excess of ~900°C. However, as the use of aluminides as structural materials at elevated temperatures is very limited because of their inadequate strength properties, several approaches are being tried to apply the Fe aluminides as overlays on more conventional higher-strength materials which are less corrosion-resistant at high temperatures. Efforts at synthesizing iron-aluminide coatings have included weld overlay, electro-spark deposition (ESD), pack cementation, and thermal spray techniques.

Iron aluminide overlays are especially attractive for power generation industry which has been making great efforts to increase the efficiency of coal-fired boilers by increasing the operating temperature and steam pressure. It is known that combustion gases can cause high temperature oxidation and also hot corrosion at many locations in boilers and gas turbines. Therefore, the corrosion requirements will depend on the component parts of the system: in the combustion environment, especially in fluidized-bed and pulverized-coal-fired systems, the environment is generally high in oxygen partial pressure pO_2 and low in sulphur partial pressure pS_2. By contrast, in coal gasification[4], pO_2 is low and pS_2 is moderate-to-high. It will also depend on what is being burned; for boilers burning coal flue gases and syngas[5] may contain chlorine

---

[4] Gasification is a process that converts carbonaceous materials, such as coal, petroleum, or biomass, into carbon monoxide and hydrogen by reacting the raw material at high temperatures with a controlled amount of oxygen.

[5] Syngas (from synthesis gas) is the name given to a gas mixture that contains varying amounts of carbon monoxide and hydrogen generated by the gasification of a carbon containing fuel to a gaseous product with a heating value. Examples include steam reforming of natural gas or liquid hydrocarbons to produce hydrogen, the gasification of coal and in some types of waste-to-energy gasification facilities. The advantage of gasification is that using the syngas is more efficient than direct combustion of the original fuel; more of the energy contained in the fuel is extracted.

and/or hydrogen [35]. In such case, the steam temperature is usually limited to 560°C, whereas in high-chlorine fuels the temperatures must be considerably lower [45]. As a result, the modification of surfaces for corrosion minimization in these systems must focus on a given application [46, 47, 48]. An additional challenge is to decrease the emissions of CO_2, and of SO_x and NO_x. Fluidized-bed combustion is one of the methods to address these challenges, with remarkably low adverse emissions and improved efficiency compared to other existing combustion techniques. However, the also aggressive conditions in fluidized-bed boilers (high temperatures, oxidizing atmospheres and impacts by fluidized sand particles) can cause significant degradation of some components, such as heat exchanger tubes, by a combination of oxidation attack and erosion wear [49, 50]. A first industrial approach for their use in thermal energy advanced systems was carried out in Belgium, where heat exchanger tubes in low carbon steel were coated by thermal spray and then tested in a new industrial plant burning a very poor fuel. After 5000 hours of operation in a rich erosive high temperature environment (850-900°C), no significant wear was observed on coated tubes whereas the uncoated tubes showed appreciable diameter reduction [51].

Furthermore, within the European Project "SUPERCOAT" (Coatings for Supercritical Steam Cycles), work has been concentrated in the development of coatings to withstand 50 000-100 000 hours of operation at 650°C under high pressure steam. Whereas such diffusion FeAl coatings are not expected to reach the maximum desirable life-time, thermal sprayed coatings might present even better steam oxidation resistance [52, 53, 54].

Thermal spray coatings have typically been used for corrosion and erosion protection, but they possess oxide inclusions and porosity, which can cause flaking of the coating. Recently, High-velocity Oxy-fuel (HVOF) processes have been used to create dense, low-oxide coatings for high-temperature corrosion testing [55]. Some current investigations evaluate the performance of iron and

nickel aluminide coatings in complex chemical composition atmospheres [56, 57, 58].

Iron aluminide coatings might also found application in protection of hot sections of gas turbine engines. Coating life of such parts is one of the most critical concerns. Coating technology has evolved from simple diffusion aluminides, to more complex dual layer metallic coatings, all the way to ceramic, thermal barrier coatings. It has been shown that even most advanced coatings have failed in less than one hot gas path inspection interval. The transition from aluminides to MCrAlYs, dual layer metallic coatings and to TBCs with time is self-evident. Stand alone aluminide coatings are not currently used on the airfoil surfaces of turbine blades but do find application on the cooling passages of the blades, and as a top coating on MCrAlY type coatings. In the overaluminised, dual layer coatings, the presence of high Cr and Co concentrations in the MCrAlY coating provides hot corrosion resistance, while the outer aluminide layer, which contains ~25wt%Al, provides high temperature oxidation resistance. The schematic diagram in figure 1.17 shows the effect of composition on the hot corrosion and oxidation resistance of several types of overlay and diffusion aluminide coatings.
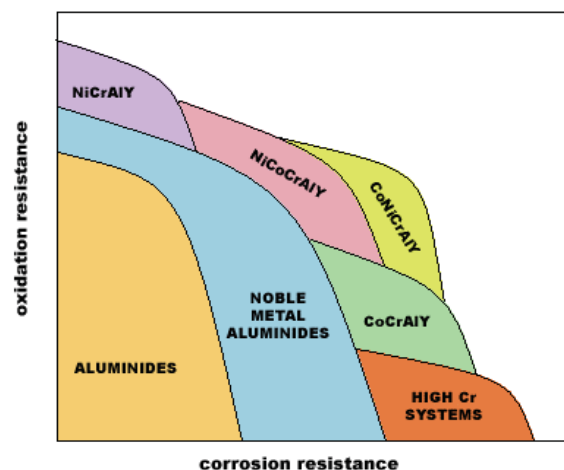
Figure 1.17. Effect of composition on hot corrosion and oxidation resistance of overlay and diffusion aluminide coatings.

Selection of the coating often depends on the fuel, the type of corrosion encountered, the mode of turbine operation and many other factors. For example, when natural gas is used as fuel, oil fuel contaminants such as Na and S are not present to cause any form of hot corrosion, and hence protection is needed for oxidation alone [59].

Also in the petrochemical field, the wear-corrosion resistance is also great concern. The appropriate selection of bulk materials and coatings of valve components is an important factor for the economic success of oil and gas production activities. The wear of high pressure valves of gas system will lead to pollution, safety problems and costs. Consequently, some studies have been addressed on the use of hard cermet coatings using an intermetallic matrix [58].

b)   NiTi coatings

Potential application for NiTi films can be divided into two groups: high and low transition temperatures [60].

High transition temperature nitinol coatings:

- Switches and relays (replacements for solenoids).
- Shape control (airfoils, mirrors and structural members).
- Vibration damping devices.
- Coatings on structural components (aircraft leading edge components and spacecraft structures).
- Mirrors (for aircraft, automobiles, ships and lasers).
- Heater elements.
- Impellers on pumps.
- Seals for low temperature applications.
- Actuators (hydraulic and air valves).

Low transition temperature nitinol coatings:

- Coatings on structural components to prevent corrosion (navy ships, weapons, etc.).

- Coatings to reduce erosion on vehicles (water craft and spacecraft).

- Linings for piping for corrosion resistance (salt water piping and concrete pump lines).

- Coatings for food processing equipment.

- Aerospace applications: coatings for landing gears on aircraft, wind leading edge on helicopters, aircraft, etc.

- Sensors (vibration, displacement and temperature).

The former applications are related to those NiTi alloys with shape memory effect. Their promising wear properties are even related with this; it has been basically investigated its cavitation erosion resistance as impacts can be elastically accommodated by the superleastic properties of the alloy, and damped by the stress-strain hysteresis. But even without this property, they are also good candidates for corrosion protection both in biomedical technology and in marine environments, which is associated to the naturally forming film of TiO_2 oxide surface. Applications where one could take advaantages of both properties would be: in hydraulic pumps, hydroturbines, and other fluid-handling machinery.

REFERENCES

[1]   J. H. Westbrook, Applications of Intermetallic Compounds, MRS Bulletin, Vol. 21, Issue 5 (1996), pp. 26-28.

[2]   K Aoki, O Izumi. Improvement in Room Temperature Ductility of the L 12 Type Intermetallic Compound Ni3Al by boron additions, Journal of the Japan Institute of Metals, 1979.

[3]   R. A. Varin, Intermetallics: Crystal Structures, Encyclopedia of Materials: Science and Technology, K. H. J. Buschow Ed., !st. ed., Elsevier Science Publ. Co. (2001) 9913 p.

[4]   D. A. Porter, K. E. Easterling, Phase Transformations in Metals and Alloys. Ed. Van Nostrand Reinhold (1981).

[5]   C. N. Foster, W. Shockley, Order-disorder transformation in Alloys, Reviews of Modern Physics, Vol. 10, 1 (1938).

[6]   C. T. Liu, J. O. Stiegler. Ordered Intermetallics. Properties and selection: nonferrous alloys and special purpose materials. Metals Handbook. ASM International. Tenth Edition, Vol. 2: Properties and selection: nonferreous alloys and special-purpose materials (1990).

[7]   R. W. Cahn, P. P. Haassen, Physical Metallurgy, Ed. North Holand (1996).

[8]   P. Adeva, Revista de la Asociación Española de Científicos, Vol. 1 (1999), pp. 1-6.

[9]   R. W. Cahn, Intermetallics: new physics, Contemporary Physics, Vol. 42, 6 (2001) pp. 365-75.

[10]   Vinod K. Sikka, Intermetallic-based high temperature materials, Oak Ridge national Laboratory, CORROSION-NATIONAL ASSOCIATION OF CORROSION ENGINEERS (1999).

[11]   C. T. Liu, J. O. Stiegler. Ordered Intermetallics. Properties and selection: nonferrous alloys and special purpose materials. Metals Handbook, Vol 2. ASM International. Tenth Edition, 1990.

[12]   S. C. Deevi, V. K. Sikka, C. T. Liu, Processing, properties and applications of nickel and iron aluminides, Progress in Materials Science, Vol. 42 (1997) pp. 177-192.

[13]   S. C. Deevi, V. K. Sikka, Nickel and iron aluminides: an overview on properties, processing and applications, Intermetallics, Vol. 4 (1996) pp. 357-375.

[14]   C. T. Liu, J. Stringer, J. N. Mundy, L- L. Horton, P. Angelini, Ordered intermetallic alloys: an assessment, Intermetallics, Vo.l 5 (1997) pp. 579-596.

[15]   E. P. George, M. Yamaguichi, K. S. Kumar, C. T. Liu, Ordered intermetallics, Annual Review in Materials Science, Vol. 24 (1994) pp. 409-51.

[16] V. K. Sikka, Processing and applications of iron aluminides, TMS Annual Meeting Proceedings Publication, Oak Ridge National Laboratory (1994).

[17] H. Clemens, H. Kestler, Processing and applications of intermetallic γ-TiAl-based alloys, Advanced engineering materials, Vol. 2, Issue 9 (2000) pp. 551-570.

[18] M. Yamaguchi, High temperature intermetallics - with particular emphasis on TiAl. Materials Science Technology, Vol. 8 N4 (1992) pp. 299-307.

[19] S. Hanada, Niobium Aluminides, Institute for Materials Research, Tohoku University.

[20] C. Colinet, A. pasturel, D. Nguyen, D. G. Pettifor, P. Miodownik, Phase-stability study of the Al-Nb system, Physical review B, Vol. 56, N2 (1997) pp. 552-564.

[21] Hhttp://www.tdcat.cesca.es/TESIS_UPC/AVAILABLE/TDX-0629105-094737//07Sfl07de14.pdfH

[22] I. Itin, V. E. Gyunter, S. A. Shabalovskaya , R. L. C. Sachdeva, Mechanical Properties and Shape Memory of Porous Nitinol, Materials Characterization, Vol. 32 (1994) pp. 179-187.

[23] A. Michiardi , Nuevo tratamiento de oxidación en aleaciones de NiTi para aplicaciones biomédicas. Caracterización superficial y respuesta biológica in Vitro (2005). Memoria de Tesis presentada para optar al grado de Doctor por la Universitat Politècnica de Catalunya

[24] N, A, Waterman and M. F. Ashby, Eds., Elsevier Materials Selector. Vol II, Elsevier (1991).

[25] A. K. Sinha. Physical Metallurgy Handbook. Ed McGraw-Hill

[26] D. E. Hodgson, Shape Memory Alloys, Properties and selection: nonferrous alloys and special purpose materials. Metals Handbook, Vol 2. ASM International. Tenth Edition, 1990.

[27] C: C. Koch, J. D. Whittenberger, Review: Mechanical milling/alloying of intermetallics, Intermetallics, Vol. 4 (1996) pp. 339-355.

[28] C. Suryanarayana, Mechanical alloying and milling, Progress in Materials Science, Vol. 46 (2001) pp. 1-184.

[29] M. H. Wu, fabrication of nitinol materials and components, Proceedings of the International Conference on Shape Memory and Superelastic Technologies, China (2001) pp. 285-292.

[30] E. Gaffet, Ni-Ti: State of the Art, NAMAMET (2004).

[31] B. Y. Li, L. J. Rong, Y. Y. Li. Fabrication of cellular NiTi intermetallic compounds. J. Mater. Res., Vol. 15, No.1 (2000) pp.10-13.

[32] D. J. Duquette, N. S. Stoloff, Aerospace applications of intermetallics, Key Engineering Materials, Vols. 77-78 (1992) pp. 298-300.

[33] T. Noda, Application of cast gamma TiAl for automobiles, Intermetallics, Vol. 6 (1998) pp. 709-713.

[34   ]
    Hwww.cbmm.com.br/portug/sources/techlib/science_techno/table_content/sub_3/images/pdfs/016.pdfH

[35] P. F. Tortorelli, K. Natesan, Critical factors affecting the high-temperature corrosion performance of iron aluminides, Materials Science and Engineering A, Vol. 258 (1998) pp. 115-125.

[36] S. Bose, High Temperature Coatings, Ed. Elsevier (2007).

[37] S. A. Shabalovskaya, Physicochemical and biological aspects of Nitinol as a biomaterial, International Materials Review, Vol. 46, Issue 4 (2001) pp. 1-18.

[38] W. J. Buehler, F. E. Wang, A summary of recent research on the nitinol alloys and their potential application in ocean, Ocean Eng, Vol. 1 (1968) pp. 105-120.

[39] Introduction to Thermal Spray Processing, ASM International, Materials Park, Ohio, USA

[40] C. Berndt, Thermal Spray: A Case History for the Integration of Materials Science and Thermo-Fluid Dynamics. Department of Materials Science and Engineering, State University of New York, Stony Brook, NY. Hhttp://www.swin.edu.au/iris/staff/cberndt/publications/2001%20BERNDT%20Thermal%20ASME%20%20C&R.pdfH

[41] M. L. Berndt, C. Berndt, Thermal Spray coatings,

[42] P. Hanneforth,   The global Thermal Spray Industry- 100 years of success: so what's next?, Advanced materials & processes (2006) pp. 68-70.

[43] L. Pawlowski, The science and engineering of Thermal Spray coatings, Jonh Wiley & Sons, New York, NY (1995).

[44] C. C. Lima, R. Trevisan, Aspersao Térmica. Fundamentos e aplicaçoes, Ed. Artliber (2002).

[45] M. A. Uusitalo, P. M. J. Vuoristo, T. A. Mantyla, Elevated temperature erosion-corrosion of termal sprayed coatings in chlorine containing environments, Wear, Vol. 252 (2002) pp. 586-594.

[46] K. Natesan, Surface modification for corrosion resistance, Workshop on Materials for Coal Gasification Power Plant (1993).

[47] K. Natesan, W. D. Cho, High temperature corrosion of iron aluminides, in: R. R. Judking (Ed.), 8th Annual Conference On Fossil Energy Materials Conf., US Department of Energy (1994).

[48] J. L. Blough, W. W. Seitz, Fireside corrosion testing of candidate superheater tube alloys, coatings and claddings, Hhttp://www.netl.doe.gov/publications/proceedings/02/materials/blough02.pdfH

[49] E. Huttunen-Saarivirta, F. H. Stott, V. Rohr, M. Schütze, Erosion-oxidation behaviour of pack-aluminized 9% chromium steel under fluidized-bed conditions at elevated temperature, Corrosion Science, Vol. 49 (2007) pp- 2844-2865.

[50] V. H. Hidalgo, J. B. Varela, A. C. Menéndez, S. P. Martínez, High temperature erosion wear of flame and plasma-sprayed nickel-chromium coatings under simulated coal-fired boiler atmospheres, Wear, Vol 247 (2001) pp. 214-222.

[51] A. Magnee, E. Offergeld, M. Leroy, A. Lefort, Fe-Al intermetallic coating applications to thermal energy conversion advanced systems, In: Proceedings of the 15th Thermal Spray Conference, vol. 2. Nice (France); 1998. p. 1091e1096

[52] A. Agüero, J. García de Blas, R. Muelas, A. Sánchez, S. Tsipas, Steam oxidation resistant coatings for steam turbine components: A feasibility study, Materials Science Forum, Vols. 369-372 (2001) pp. 939-946.

[53] A. Agüero, R. Muelas, M. Gutierrez, R. Van Vulpen, S. Osgerby, J. P. Banks, Cyclic oxidation and mechanical behaviour of slurry aluminide coatings for steam turbine components, Surface & Coatings Technology, Vol. 201 (2007) pp. 6253-6260.

[54] A. Aguero, R. Muelas, A. Pastor, S. Osgerby, Long exposure steam oxidation testing and mechanical properties of slurry aluminide coatings for steam turbine components, Surface & Coatings Technology, Vol. 200 (2005) pp. 1219-1224.

[55] J.R. Regina, J.N. DuPont, and A.R. Marder, Evaluation of Iron Aluminide Weld Overlays for Erosion-Corrosion Resistant Boiler Tube Coatings in Low NOx Boilers, Research Sponsored by the U.S. Department of Energy, Office of Fossil Energy Advanced Research and Technology Development Materials Program

[56] T. C. Totemeier, R. N. Wright, Coating microstructure-property-performance issues, in: R. R. Judking (Ed.), 19th Annual Conference On Fossil Energy Materials Conf., US Department of Energy (1995).

[57] B. Formanek, J. Cizner, B. Suzucka-Lasota, R. Prezeliorz, The corrosion resistance of HVOF sprayed coatings with intermetallic phases in aggressive environments, Journal of Achievements in Materials and Manufacturing Engineering, Vol. 16, Issue 1-2 (2006) pp. 46-50.

[58] A. Scrivani, S. Ianelli, A. Rossi, R. Groppetti, F. Casadei, G. Rizzi, A contribution to the surface analysis and characterization of HVOF coatings for petrochemical application, Wear, Vol. 250 (2001) pp. 107-113.

[59] N. S. Cheruvu, K. S. Chan, R. Viswanathan, Evaluation, degradation and life assessment of coatings for land based combustion turbines, Energy materials, Vol. 1, Issue 1 (2006) pp. 33-47.

[60] G. J. Julien, A. Sickinger, G. A. Hislop, Plasma spraying of nickel-titanium compound, United States Patent 6043451 (2000).

CHAPTER 2: THESIS SCHEDULE AND OBJECTIVES

This thesis focuses on the research around Thermal Spraying technology of intermetallic compounds from the standpoint of those more relevant issues in the current society. From one side, the increasing industrial interest for high temperature alloys has emphasized the necessity to explore and establish the potential applications IMCs can offer. Materials for high-temperature applications can be broadly divided into two categories: those whose purpose is seeking a replacement for Ni-base superalloys, but with significant reductions in density (it is in this area where Fe-, Ni- and Ti- aluminides might be included) and, the second category which involves materials with high-temperature capabilities beyond those of superalloys (>1100°C). In response to these latter needs, other aluminides, silicides and chromium-containing Laves phases have been investigated. In representation of the first group, the intermetallic FeAl has been studied, whereas, $NbAl_3$ was first thought as a candidate for the second one, although not leading to the expected results.

A fundamental research has been carried out on transition metal aluminide coatings, especially on Fe-, Ni- and Ti- aluminides, aiming at the implementation of these intermetallics in aerospace, automotive and land-based applications, but a long way has to be still prosecuted before their commercialization. Nb-Al system is even rarer and few works deal with it. Hence, it has been a real challenge to deepen in this area.

Almost in parallel, another intermetallic has been studied but not for high temperature characteristics. The so-called NITINOL (NiTi alloy) has arisen during many years good expectatives owing to its shape memory

effects as a bulk material. It has been lately investigated in its coating form by deposition through Vacuum Plasma Spraying (VPS).

FeAl and $NbAl_3$ coatings have been obtained by High Velocity Oxy-Fuel because this is the technique which provides more dense and less oxidized deposits. NiTi however, has been tested after spraying through VPS, APS and HVOF.

The following manuscript has been divided according to the different compositions with their corresponding results on the characterization and properties evaluation. Some of these results have already been published in different journals. These have been referenced and enclosed to the corresponding part of the study along the discussion.

CHAPTER 3: EXPERIMENTAL PROCEDURE

3.1   Raw materials

The feedstock powders correspond to the intermetallic compounds FeAl, NiTi and NbAl$_3$, with nominal compositions as presented in tables 3.1, 3.2 and 3.3 respectively. These were sprayed onto rectangular (100x20x5 mm^3) and cylindrical (∅=25,4mm y h=35mm) low alloyed carbon steel G41350 samples according to the performed tests.

Table 3.1. Nominal composition of iron aluminide powders.

	supplier	manufacturing process	Fe	Al	Zr	B	Y$_2$O$_3$
FeAl	CEA-DTEN Mecachrome	atomising and ball-milling	Bal.	40at.%	0.05at.%	50ppm	1wt.%
	experimental UC-Davis	cryomilling*	75wt.%	25wt.%	-	-	-

with up to 0.3$_7$ wt.% N

The cryomilled powder was processed from a blend of pure Fe and Al (325 mesh, 99,9% purity) powders supplied by Atlantic Equipment Engineers. A modified Union Process attritor (fig. 3.1) was employed at a 180 rpm rate and with a ball-to-powder ratio 32:1. In order to prevent sticking to the milling media, 0.15wt% of stearic acid was added as control agent to the blend before placing the sample inside the vial. The vials were sealed in a glove box under Ar to protect the powders from oxidation during milling.

Figure 3.1. Cryomilling attritor.

Table 3.2. Nominal composition of nickel titanium powders.

	supplier	manufacturing process	Ni	Ti	O$_2$
NiTi	I.M.R	atomising	54.62wt.%	44.54wt.%	7000 ppm

Table 3.3. Nominal composition of niobium aluminide powders.

	supplier	manufacturing process	Nb	Al
NbAl$_3$	ABSCO Ltd.	Mechanical alloying	25wt.%	75wt.%

3.2 Methods of powders characterization

The most important powder parameters are: particle size, chemical and phase composition, density, shape and flowability. All these variables have been evaluated as following:

a) <u>Particle size</u>: using a Laser Diffraction Particle Size Analyser Beckman Coulter LS 13320.

b) <u>Density</u>: apparent density and vibrated density were determined according to the ASTM B-212-89 [1] and ASTM B-527-93 [2] standards respectively. For a more approximated value to the real density, a known mass of powder was introduced into a 25ml flask and was filled with a high wettable liquid with a known density, here ciclohexanone

$$\rho = \frac{m_p}{\left(25 - \dfrac{m_T - m_p}{\rho_{liq}}\right)}$$

where m_p is the mass powder introduced, m_T is the total mass (powder+ciclohexanone) and ρ_{Liq} is the ciclohexanone density at working temperature.

c) <u>Flowability</u>: according to ASTM B-213-30 standard [3].

d) <u>Morphology</u>: in order to get complete information about the powder it is necessary to observe the grains from the outside as well as the inside. For this purpose, Scanning Electron Microscopy has been used. It serves to recognize the manufacturing technique as well as to complete the information of the particle size analysis by the examination of the different scale particles. A JEOL 5510 microscope equipped with secondary electrons, back-scattered electrons and x-ray detector has been employed.

e) <u>Phase composition</u>: phase analysis has been carried out with the well known X-ray diffraction (XRD) technique using a Bragg Brentano $\theta/2\theta$ Siemens D-500 diffractometer with Cu Kα radiation. The specific conditions used are included for each case along the text. A special reference on X-ray profile analysis has been included in *Appendix II*. Although this procedure is more commonly used for phase quantification, it enabled here to discuss the evolution of order-disorder processes through refinement of occupancy factors and lattice parameters. It was also used as an attempt on the assessment of the grain size and microstrain of the experimental FeAl powder.

f) <u>Phase transformations</u>: it has been performed by means of calorimetric measurements through Differential Scanning Calorimeter DSC Perkin-Elmer DSC-7

g) <u>Magnetic ordering</u>: it only concerns iron aluminide powder. Structural order-disorder changes have been further complemented by means of Mössbauer spectroscopy (briefly explained in *Appendix III*), where it can be observed a correlation between lattice and spin ordering. Mössbauer measurements were performed using a conventional transmission Mössbauer spectrometer with a ^{57}Co source diffused into a Rh matrix. Calibration was done using a 25-μm-thick natural iron foil. Spectra were recorded at 300 K and 80 K. The spectra were fitted using Normos program.

3.3 Thermal Spraying techniques

The High Velocity Oxy-Fuel technique was employed to produce dense coatings spraying the different feedstock powder materials, whereas Plasma Spraying just served to obtain NiTi coatings trying to reduce at maximum the oxidation content. In each case, a careful parameter optimisation was

performed both through modification of gas flow rates and spraying distances. Such evaluations involved an examination of the microstructure according to porosity and oxidation levels as well as deposition efficiency.

3.3.1   Equipment

─   *High Velocity Oxygen-Fuel (HVOF)*

A Diamond Jet Hybrid gun model 2600/2700 has been used for powder deposition. The optimization of parameters was performed by modifiying the type of fuel (hydrogen or propylene) and the relative oxygen-fuel ratios. The spraying conditions are presesnted in the next chapter (tables 4.1 and 4.2 for the Fe-Al system and table 4.9 for the Ni-Ti system).

─   *Atmospheric Plasma Spraying (APS)*

For Plasma Spraying in atmospheric conditions, the Sulzer Metco F4 system was used with a nitrogen cooling system but with a nitrogen cooling system [4]. In figure 3.2, it is seen a scheme of the set up. This technique was used for spraying the NiTi powder and the spraying parameters are exposed in the results presentation of this alloy (see table 4.9).
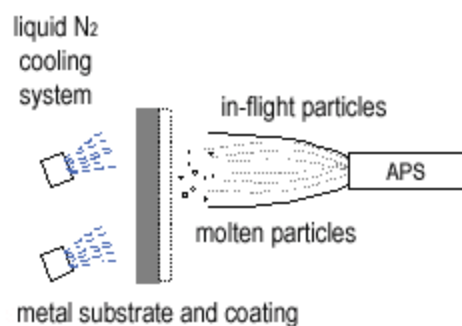
Figure 3.2. Set-up of the APS-quenching (APS+Q).

–   *Vacuum Plasma Spraying (VPS)*

A VPS Plasma System from Sulzer Metco (originally Plasma Technik) with plasma gun F4VB and a std vacuum nozzle was employed for NiTi deposition in order to prevent its high affinity to oxygen. A first attempt was carried out for a splat run with 1 spray pass down at low federate and, once the vacuum conditions reached the optimum, the coating runs were performed with 1 preheat cycle (one down, one up pass) and 4 spray cycles at higher federate. Using Vacuum Plasma Spray, oxide content is normally reduced to ppm levels and, particle velocities are much higher than that of conventional APS, in the range of 240-610 m/s.

3.4   Methods of coatings characterization

There is still a long way before these materials can be incorporated in service conditions; coatings produced in this work are still in a R & D stage which has involved two steps:

- Quality control: visual observation of the sprayed specimens in order to detect adhesion failure, cracks at the edges, etc. and, in more detail microstructure investigations have been carried out with the Scanning Electron Microscope (JEOL 5510 microscope), X-ray diffraction (Bragg Brentano $\theta/2\theta$ Siemens D-500 diffractometer with Cu Kα radiation) and Transmission Electron Microscopy JEM Jeol2100.

- Testing: those coatings sprayed with the optimized spraying conditions were tested according to the ASTM standards and other laboratory tests.

As the specific conditions have already been included in the corresponding articles, just a brief explanation is here presented.

3.4.1   As-sprayed structural and phase evaluation

A first non-destructive evaluation of the as-sprayed coatings included their roughness examination and x-ray analysis of the deposited material. At the same time, these were mounted and polished until a mirror-like surface was achieved in order to observe the cross section: presence of cracks, porosity, intersplat oxidation and so on.

3.4.2   Mechanical properties

The mechanical properties such as microhardness, tensile strength, fracture strength, elastic modulus, toughness or wear resistance are probably the most often checked. The wear resistance however, has been studied separately.

- The _microhardness_ has been evaluated by means of a Matsuzawa MTX-α Vickers equipment according to the ASTM E384-99 standard [5]. The mean values result from at least 20 indentations performed in the polished cross-sections of the coatings. The used loads were between 100 or 200gf depending on the coating thickness.

- _Tensile strength_: coating adhesion has been evaluated following the ASTM C-633 standard [6]. The test consists of gluing a cylindrical coated specimen with a resin to an uncoated sand-blasted specimen (fig. 3.3).

Figure 3.3. Set-up for the adherence test.

- _Elastic modulus_: the material stiffness has been calculated automatically by using a nanoindentation Nano Indenter® XP system (Systems Corporation) equipped with Test Works 4 Professional level software. Elastic modulus of the samples was calculated according to Oliver and Pharr equations [7]:

Equation 1: $E* = \dfrac{\sqrt{\pi}}{2}\dfrac{S}{\sqrt{A}}$; $\dfrac{1}{E^*} = \dfrac{1-v_s^{\;2}}{E_s} + \dfrac{1-v_i^{\;2}}{E_i}$ where A is the

projected area at the selected load, S the elastic constant stiffness calculated from the load/unload curve, E^* is the effective elastic modulus, E_s, E_i are specimen and indenter moduli, and v_s, v_i are Poisson's ratio of specimen and indenter, respectively. The indentations have been performed on the mirror-like sample for comparison.

3.4.3   Corrosion performance against hostile environments

− *High temperature oxidation tests*

Isothermal oxidation tests were performed for iron and niobium aluminide coatings, where the edges were covered with cement so that interface substrate-coating oxidation is minimized. The tests were performed at different temperatures for various times in a Hobersal CR 32 furnace under air atmosphere. Once each test was finished, the sample was air-cooled.

The oxidation behaviour has been also evaluated through termogravimetic measurements in a TA Instruments SDT 2960 DSC-TGA equipment.

− *Hot corrosion in molten salts*

Coated specimens of 2x2 cm^2 were corroded by exposition of an eutectic KCl:ZnCl$_2$ 52:48 %wt. salt mixture (60mg/cm^2) on their top surface and left in a furnace at 450°C for 240h. This test was specifically intended to reproduce an atmosphere of intermediate temperature aggressive conditions such as those found in heat exchange tubes in coal-fired systems. Actually, because of the nature of the chloride salts and, for comparison with previous tests [8], it better reproduced the environment of typical municipal waste incinerators.

− *Corrosion in a marine environment*

The analysis of corrosion resistance by means of a salt fog apparatus is just of interest for NiTi coatings as FeAl deposits were observed not to possess any

long resistance. This was performed following the instructions on the ASTM B-117 standard [9] in a Dycometal SSC-400 equipment. It consists of a 5% NaCl vapoured solution and the samples are removed from the chamber whenever these corrode. The limit for being considered to have a good resistance was chosen in 1500h.

- *Electrochemical tests*

The corrosion resistance of the samples was evaluated by means of electrochemical measurements in 80 mL of an aerated and unstirred 3,4% NaCl solution according to ASTM D-1411 standard [10]. A three electrode cell was used, with a Ag/AgCl as the reference electrode, a Pt-filament as counter electrode and the sample as the working electrode. The coating surface was pressed against a teflon gasket leaving 1cm^2 exposed surface. A PC-programmed EG&G 263A potentiostat/galvanostat (Princeton Applied Research, UK) was employed.

3.4.4   Wear performance

The test conditions are already explained in detail along the different published articles.

- *Friction wear*

The Ball-on disc test (ASTM G99-03 [11], fig. 3.4) has allowed the examination of the friction coefficient of the polished coating materials and the wear rates were calculated from the Δvolume in the wear track by means of White Light Interpherometry. The examination of the damaged surfaces determines the wear mechanism.

Figure 3.4. Set-up for the Ball-on disc test.

− *Abrasive wear*

The abrasive wear was evaluated according to the ASTM G65-00 standard [12] with a rubber-wheel apparatus. Abrasion occurs in contacts when one of the surfaces is considerably harder than the other or when hard particles are introduced between the contact surfaces. In the present work, the abrasion resistance was studied as the second case, often known as third-body abrasion.

− *Erosion wear*

The wear process known as solid particle erosion occurs when discrete solid particle strike a surface. It differs from three-body abrasion, which also involves loose particles, primarily in the origin of the forces between the particles and the wearing surface. In abrasion the particles are pressed against the surface and move along it, usually because they are trapped between two sliding surfaces. In erosion, neighbouring particles may exert contact forces and a flowing fluid, if present, will cause drag. The erosion properties have been evaluated according to ASTM G76-04 standard [13].

3.4.5   Magnetic properties

The hysteresis loops (first *M(H)* curves) were recorded for the different iron aluminide coatings in the attempt to relate the microstructure and composition with the ferro-paramagnetic properties. The measures were carried out at ambient temperature by using a SQUID (*S*urperconducting *QU*antum *I*nterference *D*evice) magnetometer. It consists of two superconductors separated by thin insulating layers to form parallel Josephson junctions [14]. The great sensitivity of SQUID devices is associated with measuring changes in magnetic field associated with one flux quantum.

The coatings were debonded from the substrate and the magnetization was measured when increasing the magnetic field. It allowed us to evaluate the main parameters as shown in figure 3.4.
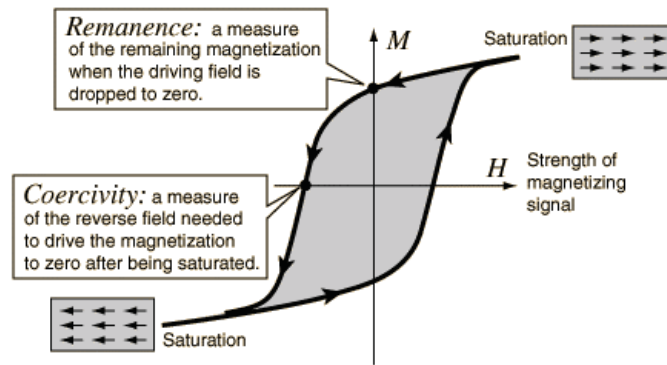
Figure 3.4. Coercivity and remanence in permanent magnets [15].

REFERENCES

[1]   Standard Test Method for Apparent Density of Free-Flowing Metal Powders Using the Hall Flowmeter Funnel, ASTM B212-99, ASTM International, West Conshohocken, PA, Hwww.astm.orgH.

[2]   Standard Test Method for Determination of Tap Density of Metallic Powders and Compounds, ASTM B527-93(2000)e1, ASTM International, West Conshohocken, PA, Hwww.astm.orgH.

[3]   Standard Test Method for Flow Rate of Metal Powders. ASTM B213 – 03, ASTM International, West Conshohocken, PA, Hwww.astm.orgH.

[4]   J.M. Guilemany, J.R. Miguel, J. Fernández, S. Dosta, I.G. Cano, Tntellectual Property Protection of Plasma+quench Process (APS+Q), iPP (AVCRI 040)

[5]   Standard test method for Microindentation Hardness of Materials. ASTM E384-07, Book of Standards 03.01. ASTM International, 2007.

[6]   Standard test method for Adhesion or Cohesion Strength of thermal spray coatings. ASTM C633-01, Book of Standards 03.01. ASTM International, 2001.

[7]   W. Oliver, G. Pharr, HAn improved technique for determining hardness and elastic modulus using load and displacement sensing indentation experimentsH, Journal of Materials Research, Vol. 7 (1992) pp. 1564-1583.

[8]   M. Torrell, TESI: Millora de la resistencia a la degradació de bescanviadors de calor en plantes IRSU mitjançant recobriments de Projecció Térmica HVOF (2008).

[9]   Standard Practice for Operating Salt Spray (Fog) Apparatus. ASTM B-117-07. Book of Standards 03.02. ASTM International, 2007.

[10]   Standard Test Methods for Water-Soluble Chlorides Present as Admixtures in Graded Aggregate Road Mixes. ASTM D-1411-04, Book of Standards 03.01. ASTM International, 2004.

[11]   Test Method for Wear Testing with a Pin-on-Disk Apparatus. ASTM G99-03, ASTM International, West Conshohocken, PA, Hwww.astm.orgH.

[12]   Standard Test Method for Measuring Abrasion Using the Dry Sand/Rubber Wheel Apparatus. ASTM G65-00, ASTM International, West Conshohocken, PA, Hwww.astm.orgH.

[13]   Standard Test Method for Conducting Erosion Tests by Solid Particle Impingement Using Gas Jets. ASTM G-76-04, Book of Standards 03.01. ASTM International, 2004.

[14]   Hhttp://hyperphysics.phy-astr.gsu.edu/Hbase/solids/squid.html#c3H

[15]   Hhttp://hyperphysics.phy-astr.gsu.edu/Hbase/solids/hyst.htmlH

CHAPTER 4: EXPERIMENTAL RESULTS

4.1   Fe-Al system results

4.1.1   Powder characterization

All the structural and morphological characterization of the iron aluminide powder is almost already included in the articles. However, this is summarised in the next few pages before the introduction of the paper "Ordering and disordering processes in MA and MM intermetallic iron aluminide powders", which basically explains the lattice changes upon disordering by milling and ordering by posterior annealing.

As already presented in the previous chapter, two FeAl powders have been used:

- Atomized[6] + ball milled Fe40at.%Al powder (FeAl grade 3): basically, about chemical composition, it's worth to say that boron and zirconium were introduced to improve ductility in the material and, yttria (ODS, Oxide Dispersed Strengthening particles) was added during the milling step so that:
  - Fine grain size is kept after hot consolidation and forming in order to improve both the mechanical strengths (Hall-Petch mechanism) and room temperature ductility (reduction of the environmental embrittlement caused by water vapour at RT thanks to grain size reduction down to 1 micron) [1, 2].
  - The creep life is improved by a factor of 3 (Orowan mechanism) [2].

- Cryomilled Fe25wt.%Al (50%at.Al) powder: the production of the alloy was studied along the milling time. Although the slight rise in temperature during conventional mechanical alloying in dry conditions at RT would have helped to reach the intermetallic composition by the heat input energy provided, milling in a cryogenic media avoids contamination because of the presence

---

[6] In this process molten metal is broken up into small droplets and rapidly frozen (either by high energy jets of gas or liquid) before the drops come into contact with each other or with a solid surface. .

of an atmosphere without oxygen, and reaches smaller average grain size by the formation of nitrides that favour thermal stability, the same role as Y_2O_3 in the other powder [3, 4, 5].

a)   Particle size distribution and flowability

Particle size and flowability are two parameters of great importance when thermal spraying. In figure 4.1a and b, one can see the particle size distribution of the mechanically milled (MM) prealloyed powder -FeAl grade3- and the mechanically alloyed (MA) in a liquid nitrogen atmosphere.
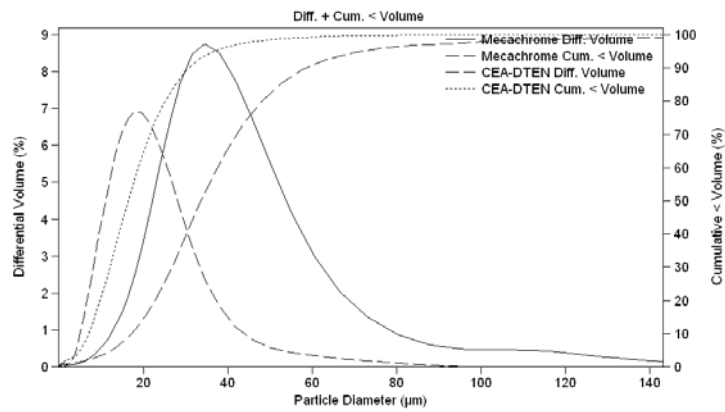
a
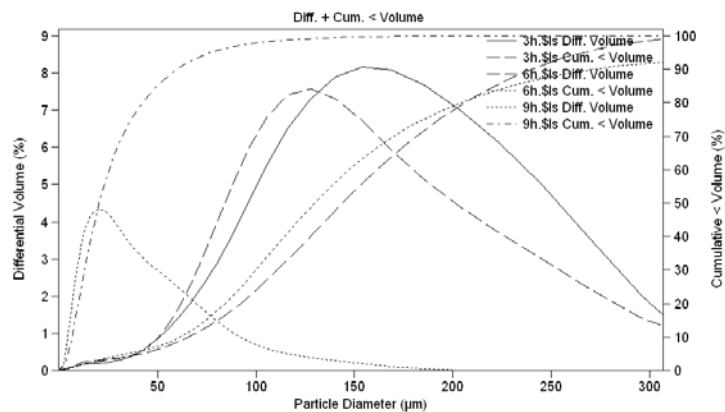
b

Figure 4.1. Particle size distribution for the (a) MM and (b) MA powders.

The distribution indicated by the dashed line in figure 4.1a is representative of the powder provided by CEA-DTEN, while the continuous line corresponds to

that one provided by Mecachrome, both with the same chemical composition. In figure 4.1b, there are the distributions of the samples taken out from the cryomilling run at 3, 6 and 9h. Both curves, differential and accumulative volume % are plotted. By contrast to those presented in figure 4.1a, where differential volume showed near Gaussian peak shapes, in this case, the sample milled for 3h presents a very broad distribution where 90% of particles are below 250 microns. Upon milling, this distribution is reduced and becomes more homogeneous. The powder cryomilled for 9h was chosen for being sprayed because it showed a suitable particle size.

Both powders showed good flowability indicating that no problems might be expected when spraying. If this test had resulted in a negative response, it would not have been so easy the injection of the powder.

b)   Morphology and phase analysis

Figure 4.2 shows the morphology of the as-atomized Fe40Al and ball-milled powder. The as-atomized presents the typical spherical morphology whereas the as-milled shows a more angular shape as result of fracturing+cold-welding.

a   b
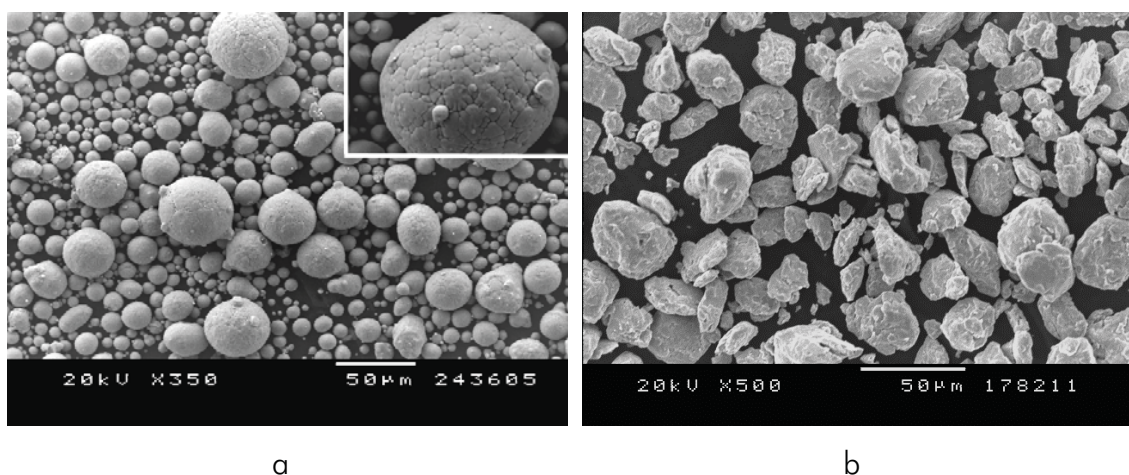
Figure 4.2. Morphologies of the: (a) as-atomized and (b) ball-milled Fe40Al grade3 powder.

By contrast, during the mechanical alloying (cryomilling), the starting ductile phases (Fe+Al) are forced to deform plastically causing flattening; the new surfaces created enable the particles to weld together leading to an increase in particle size (fig. 4.3a); these have a layered structure consisting of various combinations of the starting constituents. Due to further ball collisions, the particles get work hardened and fracture (fig. 4.3b); the structure of the particles is steadily refined. After milling for a certain length of time, an equilibrium state is attained when a balance between welding-fracturing is achieved (fig. 4.3c and d) [6].

a   b

c   d
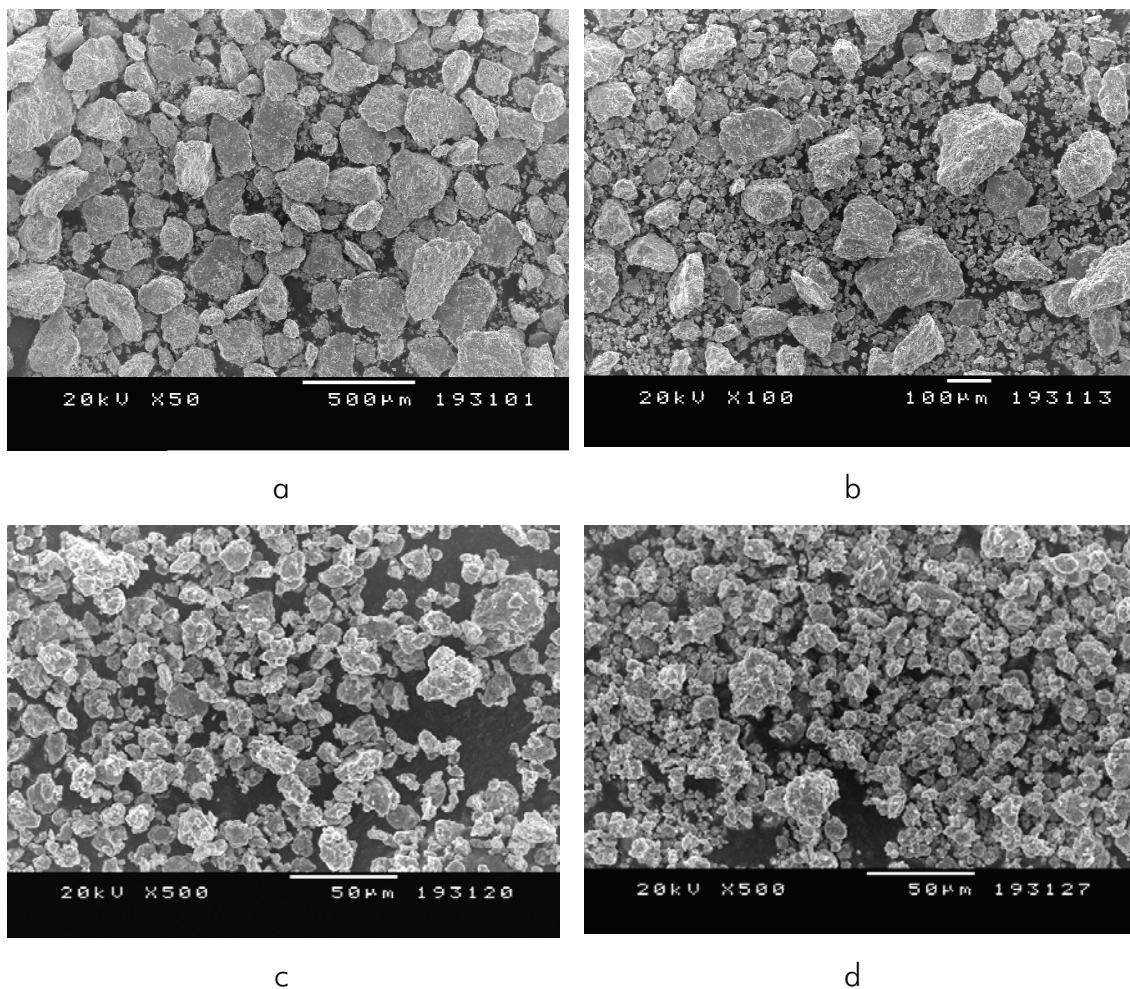
Figure 4.3. Morphologies of the cryomilled powder at different times: (a) 3h, (b) 6h, (c) 9h and (d) 12h.

The cross section and X-ray analysis is already discussed in the next section in the article entitled "Ordering and disordering processes in MA and MM intermetallic iron aluminide powders". Just a brief explanation and a few points to be added: upon milling, the cryomilled (MA) powder shows a decrease of inter-layer spacing and so an increase of the number of layers in a particle; however, the refinement at 9h is not good enough to produce diffusion at the atomic level yielding to a solid solution Fe(Al) instead of the intermetallic FeAl. On the other hand, the ball-milled (MM) Fe40Al powder shows a refinement of grain size, accounted by the broadening of X-ray peaks and TEM studies (fig. 4.4). Transmission Electron Microscopy studies revealed a nanocrystalline disordered structure but did not work to find the Y_2O_3 dispersed particles introduced during milling [7].

a   b
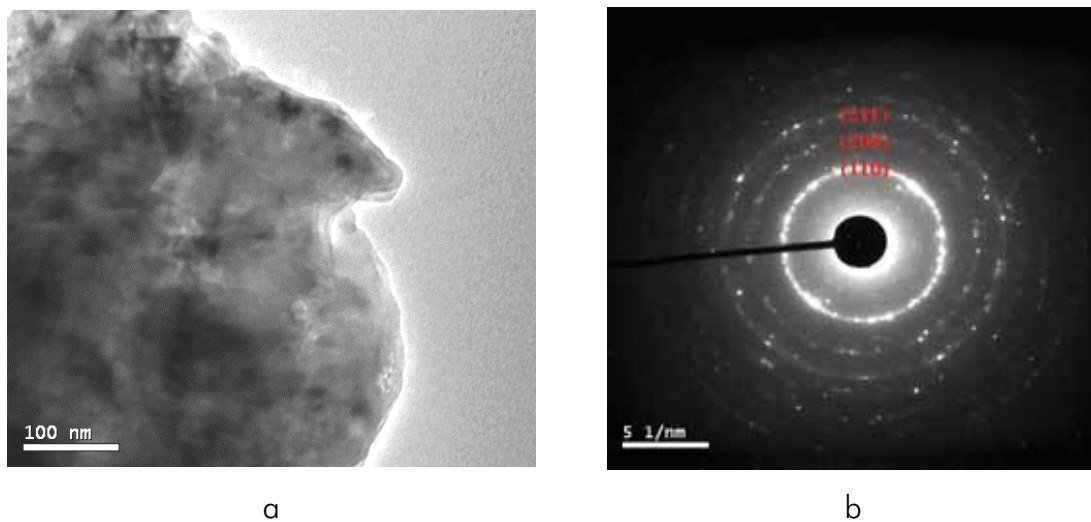
Figure 4.4. (a) TEM bright-field images showing a milled powder particle with nanocrystalline structure and (b) the SAED ring pattern corresponding to the disordered FeAl phase, where just the fundamental reflections (h+k+l=even are shown).

The grain size refinement was evaluated by fitting the X-ray peaks (*Appendix II*) and using the Williamson-Hall plot approach (fig. 4.5). Nevertheless, it was difficult to obtain certain values from the intercept and the slope because the measurements are difficultly fitted as straight lines; approximately, the initial pure Fe was found to have, on average, grain sizes of about 200nm, which

lead to about 15nm after 9h of milling (~7nm for the Fe(Al) phase). Overlapping lines and coincidence of Fe and Al peaks might have difficulted the study; however, a certain tendency is observed by looking at each reflection individually. Krasnowski et al. [8] also used this method and were more successful when fitting, reaching crystalline values of 15nm after 30 hours of milling. However, it is difficult to make comparisons of these results with the ones obtained by other authors as there is a strong dependence on milling parameters. Depending on how energetic the method is, the grain size, microstrain and degree of order will vary at different milling times.
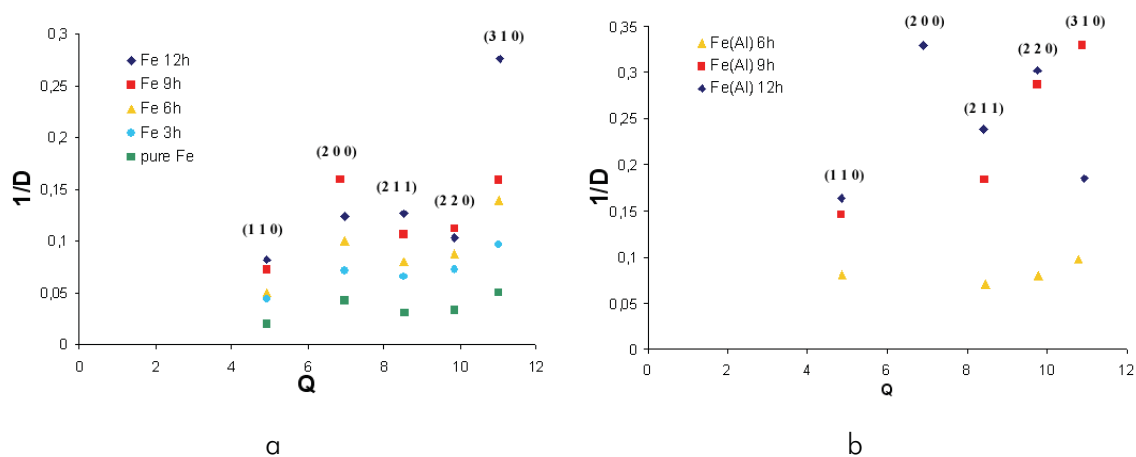
Figure 4.5. (a) Fe and (b) Fe(Al) Williamson-Hall plots.

c)   Advanced studies on thermal stability

This section is focused on the effect of annealing both powders in terms of lattice ordering. The whole discussion is included in the following article:

Paper 1: J. M. Guilemany, N. Cinca, Ll. Casas, E. Molins, Ordering and disordering processes in MA and MM intermetallic iron aluminide powders, *Journal of Materials Science* (submitted).

Fe40Al grade 3 (mechanically milled) and Fe50Al (mechanically alloyed in cryogenic conditions) are studied in terms of their structure evolution by means of the lattice parameter, long-range order and magnetic changes when these are annealed at different temperatures.

Ordering and disordering processes in MA and MM intermetallic iron aluminide powders

J. M. Guilemany[1] , N. Cinca[1], Ll. Casas[2], E. Molins[3]

[1] Thermal Spray Centre (CPT). Dpt. Ciència dels Materials i Enginyeria Metal.lúrgica. Universitat de Barcelona.

[2] Unitat de Cristal·lografia i Mineralogia, Dept. Geologia, Universitat Autònoma de Bellaterra

[3] Institut de Ciència de Materials de Barcelona, ICMAB-CSIC

Abstract

The formation of the FeAl intermetallic compound has been investigated by annealing a mechanically milled powder and a mechanically cryoalloyed powder. First, the morphological transformations that result from both milling processes were analysed, giving special emphasis to the cryoalloyed powder; the evolution of continuous cold welding and fracturing during milling was assessed by means of Scanning Electron Microscopy (SEM). The lattice parameter changes of both powders were then evaluated as a function of milling time using profile fitting and Rietveld analysis of the XRD data. The powder thermal stability was also examined by differential scanning calorimetry (DSC) and the detected transformations were discussed according to the structural changes observed in x-ray temperature-dependent measurements.

Furthermore, Mossbauer data has been used to compare the different atom rearrangements, from that of an ideal B2 structure and a typical bcc-Fe type to a disordered A2-solid solution and their temperature-induced ordering processes.

Keywords: intermetallics (based on FeAl); mechanical alloying; order-disorder effects; diffraction (x-ray); mossbauer spectroscopy

1   Introduction

The idea of disordering intermetallic compounds (IMCs) arose from the challenge of improving their formability. The ordered nature of these compounds leads to attractive high-temperature properties such as high strength, increased stiffness, and excellent corrosion/oxidation resistance. However, their low ductility at room temperature as well as their fracture toughness have been a barrier to develop applications during many decades. Nevertheless, since it was discovered that introducing some disorder in the lattice provides a reliable improvement of these mechanical properties, many attempts have focused on this issue. Intermetallics can be disordered either by heavy plastic deformation like ball milling, by irradiation or by rapid solidification (partially, by a quench from high T in the solid state); among them, the first one has been considered the most effective method. Besides that, milling results in additional benefits, the inherent embrittlement of the alloy is also overcome by reducing the grain size and modifying the crystal structure [1, 2, 3].

Mechanical milling (MM) of ordered intermetallics results in one of the following: a solid solution, an amorphous phase or a different ordered phase with a complex crystal structure. From another standpoint, milling can also be regarded as a synthesis route by which the compound is formed from the mixture of elemental powders; this is usually referred as mechanical alloying (MA).

Structural order of IMCs is related to the arrangement of atoms and its deviation from an ideal structure (i.e. compositionally pure, with no dislocations or even lattice vibrations). This order can be quantified using the LRO parameter (Eq. 1), which is related to the range within a given atom arrangement keeps its periodicity.

(1) $LRO = \dfrac{r_\alpha - X_A}{Y_\beta} = \dfrac{r_\beta - X_B}{Y_\alpha}$

where r_α and r_β are the fraction of A sites and B sites occupied by the "right" atoms (atomic occupation), i.e. A atoms and B atoms respectively and, X_A and X_B are the fraction of A and B atoms in the alloy. Y_α and Y_β correspond to the fractions of α and β-sites [4, 5].

LRO is larger (maximum 1) at low temperatures and for stoichometric compositions. Actually, there is a particular temperature (critical temperature, Tc) above which disordering becomes inevitable. Such transition has been observed to be either sharp or progressive and therefore Tc can coincide with Tm (melting temperature) of the material or these become disordered much earlier. However, besides this, the concept order can refer to electronic and nuclear spin states. Electronic magnetic moments come from the presence of unpaired electrons; atoms behave as tiny magnets and impart magnetism to the lattice when present in a parallely ordered state. Such phenomenon leads to the well-known ferromagnetic order. Here again, there is also a characteristic temperature above which materials become magnetically disordered or paramagnetic [6, 7, 8, 9]. All these aspects are studied here for the Fe-Al system using several techniques such as x-ray diffraction at different temperatures, differential scanning calorimetry and Mössbauer spectroscopy.

Both MM and MA processes were used, the first to disorder a prealloyed compound and the latter to synthesize alloys from pure iron and aluminium powders. The whole detailed study of those powders stated a basis for the order-disorder transition. Both milling methods possess interesting features in the frame of this study: (a) On one hand, ball-milled Fe40Al, hereby referenced as *FeAl-grade 3*, which is a nanocrystalline intermetallic compound (with yttria particles dispersed within it in order keep a fine grain sized microstructure after hot consolidation treatments [10, 11, 12]) that was subjected to mechanical milling (MM) and, (b) on the other hand, the cryomilling of Fe and Al powders, hereby referenced as *FeAl-cryo*, was a kind of mechanical alloying process (MA). Cryomilling results in a better thermal stability because of the formation of nitrides [13]. Thus, by both paths grain growth is reduced; it is worth noting that cryomilling is a new method which is opening new expectations. Once both powders have been produced, these will serve to be sprayed by using cold-spray technologies and thus form coatings without the influence of any oxidation.

2   Experimental procedure

In order to study the disordering process induced by MM, the commercial *FeAl grade 3* powder (nominal composition Fe-40Al-0.05Zr (at%.) + 50 ppm B + 1wt%.Y_2O_3) supplied by CEA, was investigated. It was supplied as-milled but some unmilled powder was provided for their comparison. In contrast, the MA route was studied starting from a blend of pure elements with a composition Fe25wt%.Al (*FeAl-cryo*). This mixture was mechanically alloyed in a modified Union Process attritor with continuous flux of liquid nitrogen. The balls and vial were made of stainless steel and the ball-to-powder ratio used was 32:1 with a rate of 180 rpm. In order to prevent sticking to the milling media, 0.15wt% of stearic acid was added to the blend before placing the sample inside the vial. The milling time was set to 3, 6, 9 and 12 h in order to observe the evolution of particle

morphology and grain size. The vials were sealed in a glove box under an Ar atmosphere to prevent oxidation during milling.

The samples were examined by Scanning Electron Microscopy; using a JEOL 5510 operated at 20 kV and equipped with an Energy Dispersive Spectroscopy (EDS) for microanalysis.

For phase identification and their evaluation, two different types of X-ray diffraction (XRD) analyses were performed:

- Using a Bragg Brentano θ/2θ Siemens D-500 diffractometer with Cu Kα radiation, scans from 20º to 120º were recorded with a step size of 0.03º and a step time of 17 s to fit the profiles and undertake Rietveld analysis. The softwares used were XRFIT and FULLPROF, both included in the WinPLOTR graphical tool software package.
  The refinement of the occupational factors enabled the calculation of the long range order parameter according to equation 1.

- The temperature-dependent X-ray scans were performed on a Bragg Brentano θ/2θ Bruker diffractometer, type D8 Advance, provided with a temperature chamber Anton Paar HTK1200. The recorded θ/2θ scans range from 28-32º and 42.5-47º. This permits to follow the evolution of the most intense superlattice and fundamental lines, (100) and (110) respectively. The temperature range was from 100ºC to 800ºC taking records every 100ºC and every 50ºC around the temperature peaks observed in the DSC analysis.

The ordering processes were induced by heating in a DSC calorimeter Perkin-Elmer DSC-7 under Ar atmosphere with a constant heating rate of 40ºC/min.

Mössbauer measurements were performed using a conventional transmission Mössbauer spectrometer with a ^{57}Co source diffused into a Rh matrix. Calibration was done using a 25-μm-thick natural iron foil. Spectra were recorded at 300 K and 80 K. The spectra were fitted using Normos program [14]. This technique provides information about Fe oxidation state, iron oxide phase and magnetic structure.

3   Results

3.1   Structural changes upon milling

Morphological evolution of the cryomilled powder is not shown here. However, the alloying process is well represented from cross sections of polished particles (figure 1). The higher the milling time, the thinner the iron and aluminium lamellae are. After 3h of milling, these are well distinguished by the different grey contrasts and they become more uniform when fracturing and cold-welding phenomena become balanced. Nevertheless, the homogeneity never reaches the levels exhibited by the *FeAl-grade 3* sample -both as-atomised or after MM- (figure 2).

Figure 3a shows the XRD patterns of *FeAl-grade 3* sample (as-prepared (atomised) and after MM), whereas 3b shows the cryomilled powder (i.e. MA) at different milling times. Comparing the atomised with the subsequently milled powder, it is apparent that the milling process induces a peak shift towards lower angles as well as a noticeable broadening of these peaks. On the other hand, the Fe-Al blend milled under cryogenic conditions (*FeAl-cryo)*, exhibits a progressive disappearance of the Al peaks, while the Fe peaks become asymmetric. The

appearance of the second phase identified as a solid solution only must be only assigned to the spectra milled for more than 3h because at 3h Al and Fe peaks are still visible and non-asymmetric.

The evolution of the interatomic distances with the milling time was studied for the experimental *FeAl-cryo* powder by means of a profile fitting methodology and the Rietveld method, as well as for the as-atomised and ball-milled *FeAl-grade 3* powder. Regarding the cryomilled powder (*FeAl-cryo*), it is observed that the iron lattice parameter undergoes a slight and progressive expansion as the new alloy phase Fe(Al) is formed (figure 4); the same phenomenon is observed in the *FeAl-grade 3* powder, being the starting value of the lattice parameter 2.89_6 Å (for the atomised sample) and 2.92_1 Å (for the as-ball milled)**.**

The Mössbauer spectra of *FeAl-grade 3* and *FeAl-cryo* samples are presented in figure 5. Both spectra are fitted with two components: the minor one consists of a paramagnetic doublet, which is related to Fe atoms introduced in a site surrounded mainly by Al atoms. The other component is a dominant magnetically ordered phase but appears significantly different in both samples. In the *FeAl-grade 3* sample this magnetically ordered phase is not homogeneous and exhibits a very broad distribution of hyperfine fields (see figure 5a-inset on the right), whereas in the *FeAl-cryo* sample the magnetically ordered phase appears to be similar to pure Fe although the hyperfine field has been slightly reduced. *FeAl-cryo* sample comes from a blend of pure powders and thus, before any milling, the Mössbauer spectrum shows already a magnetic component, i.e. the 33 T Fe sextet. *FeAl-grade 3* sample instead, comes from a prealloyed product which is paramagnetic and thus shows a magnetically non-ordered Mössbauer spectrum (see figure 5a-inset on the left); the magnetically heterogeneous but ordered phase that forms after milling is due to strain-induced ferromagnetism [15, 16]. Low-temperature spectra (at 80K) appear to be similar to those recorded at 300K limiting the relevance of dynamic effects such as superparamagnetism. Alloys with even more than 50at%.Al have shown a ferromagnetic behaviour as result of incompleted milling; a rapid grain refinement occurs leading to a metastable Fe-Al solid solution [17, 18].

3.2   Structural changes upon heating

Figure 6 shows the thermal responses of both powders. The ball-milled powder (*FeAl-grade 3*) exhibits an exothermal peak around 200ºC, while cryomilled samples (*FeAl-cryo*) show two different peaks indicating that two exothermic processes are taking place at higher temperatures. Increasing milling time, the energy released by these processes decreases, reaching almost zero at 12h. Table 2 shows the peak temperatures and table 3 presents the energies released. Second heating runs were performed on each sample without removing it from the calorimeter and no peaks were detected proving the irreversibility of the observed transitions.

XRD patterns of both powders upon temperature were recorded in order to discern the structural changes. Figure 7 and 8 correspond to the evolution of (100) and (110) lines for *FeAl-grade 3* and *FeAl-cryo* respectively. It is seen that heating produces the appearance of the superlattice B2 line (100) line in both cases. With regard to the fundamental line (110), the *FeAl-grade 3* sample displays a shift to lower angles, whereas the *FeAl-cryo* sample shows a bit more complicated behaviour: the asymmetric peak observed at room temperature results in two narrower but still overlapped peaks at 350ºC. They become sharper and exchange their relative intensities from 400 to 450ºC, that corresponding to the Fe phase decrease over a Fe(Al) increase. Above 450ºC, the peak assigned to Fe (that at higher angles) disappears and the remaining peak moves slightly to lower angles. Comparing the XRD profile of the atomised powder to that of the ball-milled and subsequently annealed at

700ºC, it is seen that, both show the fundamental and superlattice peaks located at the same positions but the annealed sample exhibits broader peaks.

In figure 9, LRO and lattice parameters are ploted against annealing temperature. The *FeAl-grade 3* samples (as-atomised and after MM) present a decrease of the distance between neighbouring atoms correlated to a rise of the LRO value. For the *FeAl-cryo* powder the same tendency is observed at 500 and 700ºC; at 300ºC the alloys had not been ordered yet, so the calculation is not presented; the values are referred to the 9h-annealed powder because it is the one which has the optimum particle size for posterior spraying.

Thermally induced changes can also be followed by Mössbauer spectroscopy, see figure 10. Upon annealing, milled *FeAl-grade 3* powder loses magnetic ordering and recovers the initial paramagnetic state (figure 10a), this would correlate with the return to the previous structurally ordered alloy. *FeAl-cryo* powder also loses progressively the magnetically ordered phase that transforms into a paramagnetic phase, after annealing at 700ºC the magnetic sextet has apparently completely disappeared. However some magnetism remains since the powder reacts to the presence of a permanent magnet.

Low temperature measurements (see figure 10 insets) reveal that some magnetic ordering is still present, even after annealing at 700ºC, though with different features: *FeAl-grade 3* sample shows a wider peak with respect to the room temperature singlet and *FeAl-cryo* powder reveal the presence of a significant amount of a Fe-rich phase phase (with a hyperfield of around 32 T), which is actually at room temperature.

4   Discussion

A mechanical alloying process consists of a continuous deformation-cold welding-fracturing process. According to the morphological changes, the different stages can be described by the following sequence:
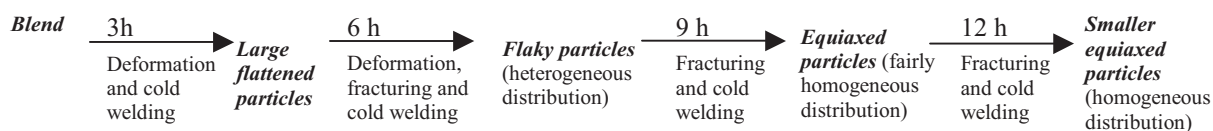
Such evolution was observed for the *FeAl-cryo* sample. The less heterogeneity upon milling indicates the evolution of the alloying mechanism. This is associated to the diffusivity of Al atoms into Fe lattice due to the high temperature reached on milling. The major research carried out on FeAl holds the simple theory that its formation comes from diffusion processes but it can be actually associated to a microscale layers welding. The temperature rise upon milling can be above that of the crystallization point of the quasicrystalline phase produced and therefore an equilibrium intermetallic phase forms under this condition of milling [1]. Few even claim a possible melting of aluminium as a mechanism for FeAl formation [19]. Actually, NiAl has been synthesized through a combustion reaction during milling, but what supports those results is the fact that the ordering energy of NiAl is almost three times higher than that of FeAl [20]. In the present case, it could have been difficult to accomplish the stoichiometry even at longer milling times; cryogenic conditions reduce the additional energy contribution supplied by repeated collisions between particles and balls. X-ray and Mössbauer data assert the previous comments. The appearance of low-intensity broad peaks at slightly lower angles than the Fe lines (actually, to some extend, they overlap) reveal the presence of a solid solution, Fe(Al). This new phase has the same bcc structure as α-Fe but with a slightly larger unit cell parameter, which has already been assessed

by peak fitting profiles and refinement methods such as Rietveld. The lattice is distorsioned by the introduction of the new Al atoms with larger atomic radius. However, some difficulties arise to determine the exact nature of the new phase: on one hand the assumption that Al atoms do not play a significant role (most of them lie in the same position as those of Fe), on the other hand the deconvolution of overlapped Fe and Fe(Al) lines is a difficult task, the broadening of the XRD peaks during MA may hinder a clear identification of the phases. Mössbauer spectra indicate that the interdiffusion (of Al in the Fe lattice, and Fe atoms in the Al structure) is limited. Although, as it will be commented later, this interdiffusion is greatly reached upon annealing,

As far as the atomised + milled powder is concerned (i.e. *FeAl-grade 3* powder) the morphological evolution from the atomised state to the as-milled upon milling time is not reported because the powder was supplied in its milled state. As a small atomised powder was provided, one can see that the larger lattice parameter compared to that of as-atomised, points out the lower degree of order as a result of the heavy plastic deformation. Most works about B2-ball milled intermetallic phases have also yielded a disordered A2 structure, commonly with a nanocrystalline structure [19, 21, 22, 23, 24, 25]. However, some studies report a transition from crystalline to a completely amorphous state [26, 27] or a reduction of the order degree (related to the particle nanosize) but keeping an ordered nanostructure [2, 28, 29].

Mossbauer spectra reveal the appearance of a strain-induced ferromagnetism [30, 31], not present in the cryomilled sample. It is also worth quoting the role of the grain size and microstrain introduced by such processes [32].

FeAl, as well as Ni_3Al, NiAl and TiAl, is one of those permanently ordered alloys which show LRO right up to the melting point with a critical temperature T>Tm; they can only be disordered by special procedures like irradiation or milling. The two powders studied here possess a disordered structure as a result of milling: one, because the stoichometry is not reached and, the other because, despite having a near stoichiometric composition, a disordering treatment has been carried out. Thus, the evaluation of annealed samples adds extra evidence to the actual production of disordering and is intended to understand both recovering processes until attainment of complete ordering again. On heating both samples, reordering was observed as an exothermic process over a wide range of temperatures. The transition associated to the calorimetric tests of the prealloyed powder (*FeAl- grade 3*) was attributed to the ordering process. Other authors have also reported more complex DSC profiles depending on the milling times. The peak at approximately 200ºC is also common and broad tails are observed at higher temperatures as result of defect recovering and possible grain growth [28, 33, 34, 35, 36]; this is as also seen in the present work as the sharpening of lines.

Previous comments are complemented and confirmed by the results obtained by XRD vs temperature. First, XRD reveals the appearance of superlattice lines and a lattice contraction, returning to those values of the unmilled powder. However, the broadening of the peaks even after annealing indicates that the grain size and microstrain effects are not the same as for the atomised powder.

The disordered arrangement is a metastable state highly strained; thermal energy promotes diffusion, which induces Fe and Al atoms to occupy their most energetically favourable positions. Additionally, the release of strain results in the loss of ferromagnetism because the effect of neighbouring Fe atoms in a B2-structure is not as strong as in a disordered structure. The order parameter approach, which depends directly on the atomic occupation as seen in equation 1, demonstrates a progressive increase of LRO. However, even at 700ºC the maximum order of 0.8 for the composition of 40%at. Al is not reached. The explanation given for such

phenomenon can be discussed as follows: the perfect order of a crystalline structure only exists at very low temperatures; over heating, thermal vibration becomes a competitive process. In addition, the present powder is not the exact 50:50 composition, this is why LRO=1 is not accomplished. Moreover, annealing processes at the same temperatures for longer times (1h) revealed a decrease in LRO, thus highlighting the effect of temperature against the formation of the B2 lattice. Mössbauer spectra show only a singlet indicating a non-magnetically ordered and highly symmetric site. Therefore, the structural order results in a single phase without magnetic ordering.

The ordering process in the cryomilled powder is a bit more complicated because of the starting Fe+Al mixture was that of the 50:50 stoichiometry but this was not reached after milling. This was not accomplished due to the cryogenic media temperatures as commented before. Then, heating involves two processes: an input energy for alloying and then ordering. Other authors [37, 38] also observed two different peaks for calorimetric traces, which move to lower temperatures on increasing the milling time and become negligible for the longest milling times. The major energy released in the first peak for the least milled samples agrees with the assumption that this is related to the alloying formation: after 3h of milling, diffusion processes have not had time to take place; iron and aluminium still exist in their elemental form as a layered structure within the particles. As milling continues, these lamellas become thinner and thinner as seen from cross sections, but it is even difficult to believe that these are thin enough to permit atoms to exchange. Hence, as Mössbauer spectra clearly show, heating is needed to produce the homogenization of the alloy composition. Once the stoichometry is reached, the minimum free energy state corresponds to that of a 3-D periodic arrangement, this is the B2 superlattice. Krasnowski et al [21], who observed three instead of two overlapped peaks, have discussed their transformations according to the suppositions made by Morris-Muñoz [3]. They concluded that up to 450ºC, only alloying and ordering take place, whereas above such temperature, the exothermic processes are attributed to the loss of defects, recrystallization and grain growth. Then, as far as *FeAl-cryo* powder is concerned, apart from the transformation discussed for *FeAl-grade 3*, the alloying process has to be also taken into consideration. This causes that higher temperatures be needed to perform the whole transformation.

From XRD patterns, such transition is clearly illustrated: the iron-rich phase coexists for a certain temperature range with Fe(Al) and, after its disappearance, the later one transforms progressively into FeAl. The LRO and Δa point out a shift of the solid solution lattice parameters towards those of the ordered lattice. Mossbauer confirms the decrease of the Fe rich phase (seen as the decrease of the area of the magnetic sextet up to practically zero, see fig. 10b) and the interdiffusion of Fe and Al atoms in a highly symmetric environment and therefore similar to the situation encountered for *FeAl-grade 3* powder also after application of thermal treatments.

5   Conclusions

The present work reports the changes on ordering-disordering the lattice of iron aluminide powders obtained through different milling techniques with different purposes as well.

With regard to *FeAl-grade 3* powder:

- When milling the atomised Fe40%at.Al powder, the structure is rearranged in the way that iron and aluminium atoms are no more surrounded by unlike neighbours. Consequently, the B2 framework is partially destroyed. This change is noticed by the shift of the lattice parameter and more evident, by the

evolution of a singlet indicating a paramagnetic structure, into a hyperfine distribution in Mössbauer spectra.

- Milling also produces a decrease of grain size and introduces a high strain according to the broader XRD peaks. Both, ordering and recovering processes are encountered when the samples are annealed.

- After annealing at 700ºC, the lattice parameter decrease is about 0.8%, the same order as the increase after milling the atomised powder. The hyperfine field distribution collapses again into a paramagnetic structure similar to the observed for the atomised powder.

As far as *FeAl-cryo* powder is concerned:

- In the as-mechanically milled powder, a lattice expansion is observed as a result of disordering of the lattice. Here however, there is an expansion of the iron lattice because of the introduction of aluminium atoms when the powder mixture is mechanically milled.

  A complete alloying is not reached for as-cryomilled powder because of the low temperature of the synthesis route, which inhibits the diffusion processes. At such temperatures, any heat released would be readily dissipated. Thus, iron clusters keep its ferromagnetic ordering.

- When annealing, the alloying is produced first and the ordering consecutively. A higher energy release is observed in the samples milled for shorter times because more energy is needed to accomplish the intermetallic.

- When the cryomilled powder is annealed, the lattice parameter returns to that of a typical B2 structure. Ferromagnetic clusters become smaller as they diffuse into Al and they only appear as relicts after annealing at 700ºC.

A further interesting step could be the study of the role that dispersed particles (e.g. yttria and nitrides) play in each case in connection with thermal stability and grain growth. Many works report that this is really a difficult task but it would possibly add on the understanding on the nanocrystallization process and its temperature dependent effect.
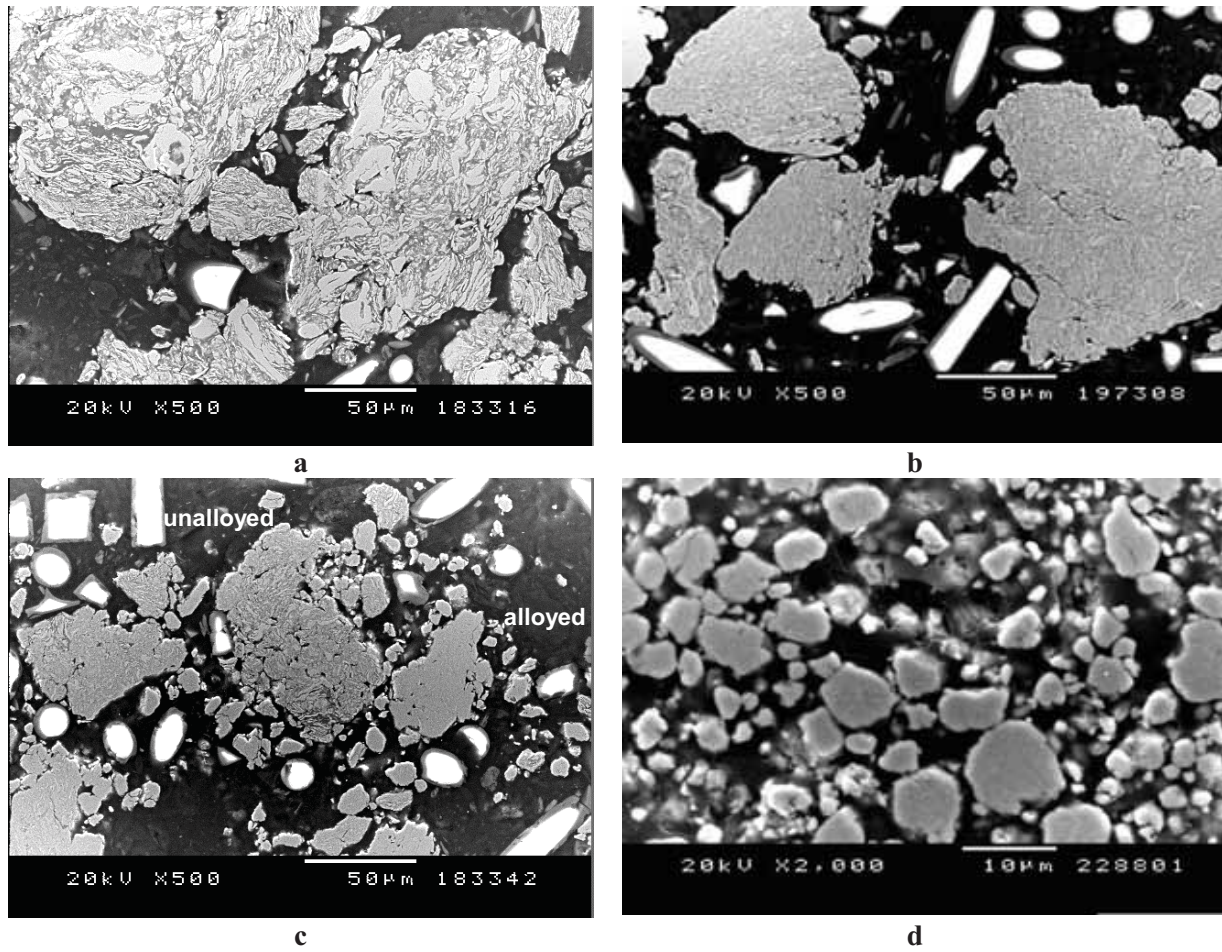
FIGURES

Figure 1. Cross sections of cryomilled powder at different milling times: (a) 3h, (b) 6h, (c) 9h and (d) 12h.
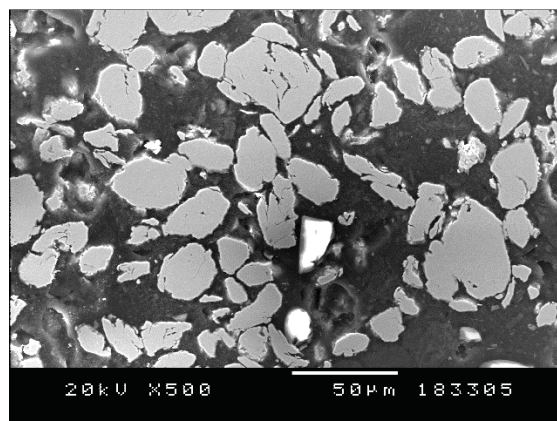
Figure 2. Cross section of ball-milled powder
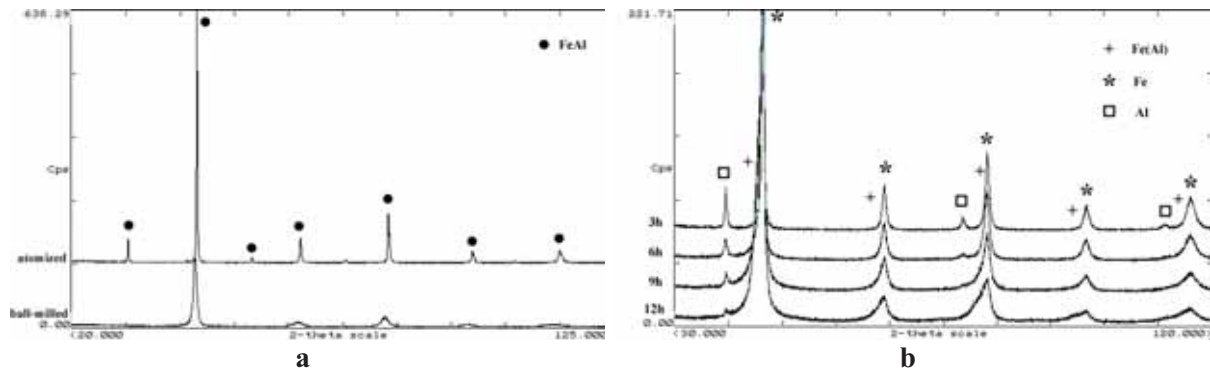
Figure 3. X-ray scans: (a) atomised and ball-milled powder, (b) cryomilled powder at different milling times.
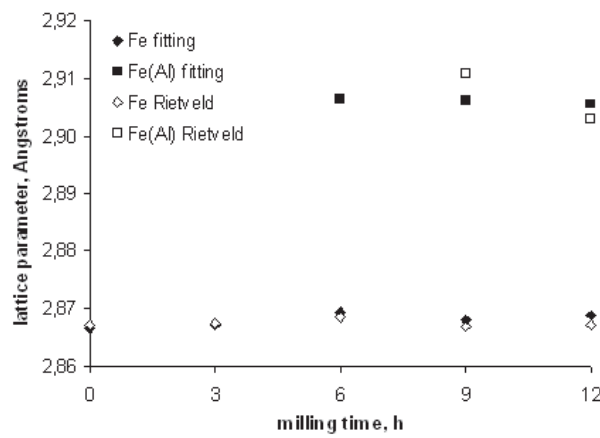
Figure 4. Refined lattice parameters from XRD data of the cryomilled powder versus milling time.
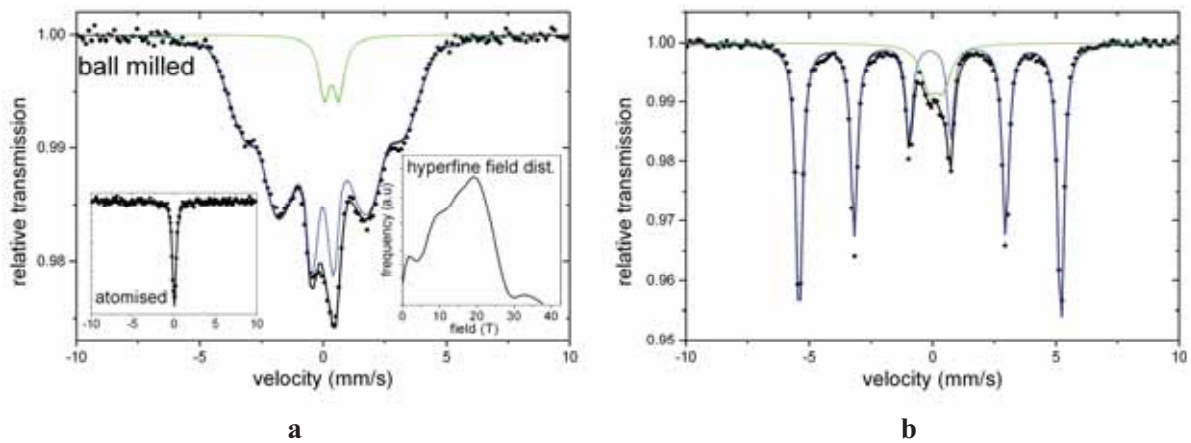
Figure 5. Mössbauer spectra recorded at 300K of the starting products: a) *FeAl-grade 3* (inset as atomised); b) *FeAl-cryo*.

73
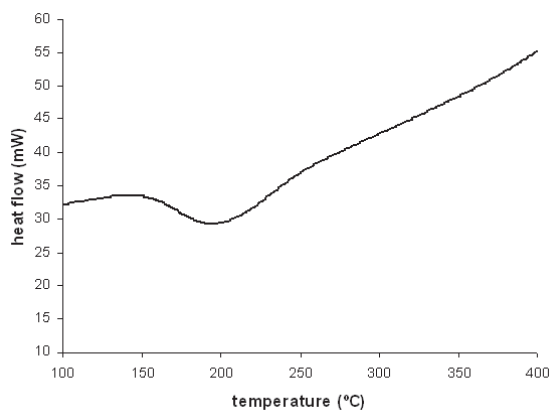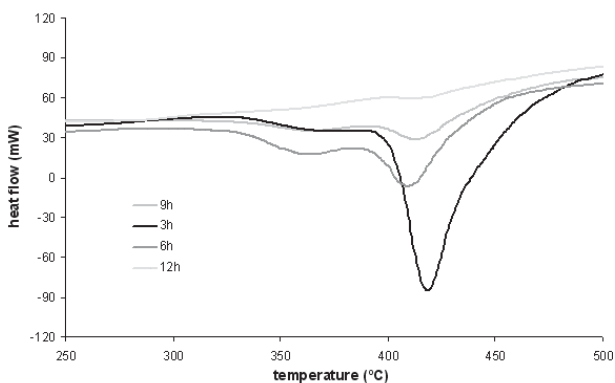
a　　　　　　　　　　　　　　　　　　　**b**

Figure 6. DSC graphics of the (a) ball-milled and (b) cryo-milled samples.
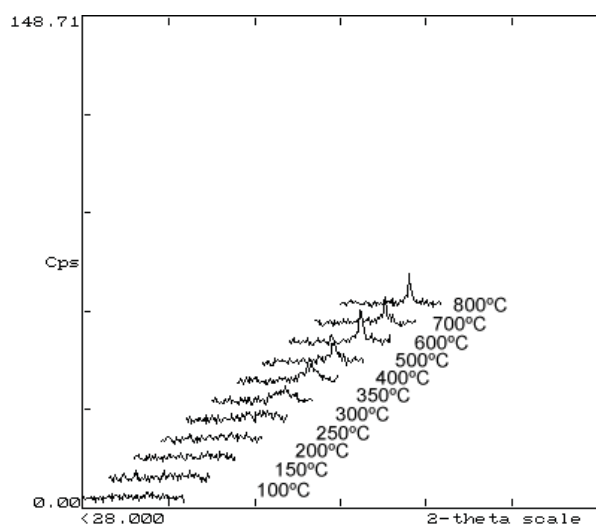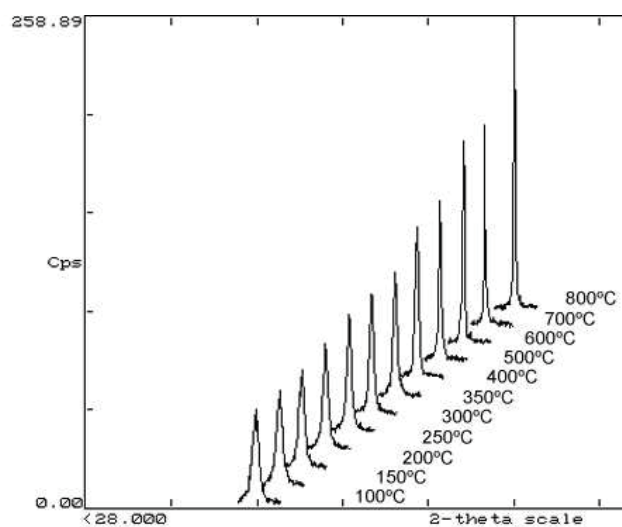
a　　　　　　　　　　　　　　　　　　　**b**

Figure 7. XRD evolution of the ball-milled powder upon temperature: (a) (100) peak; (b) (110) peak.
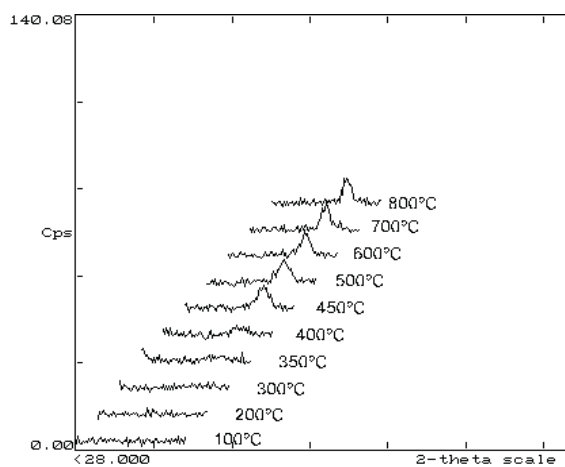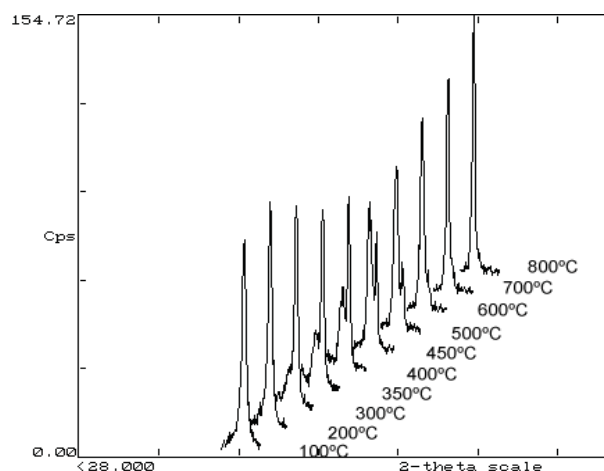
a　　　　　　　　　　　　　　　　　　　**b**

Figure 8. XRD evolution of the cryomilled powder upon temperature: (a) (100) peak; (b) (110) peak.
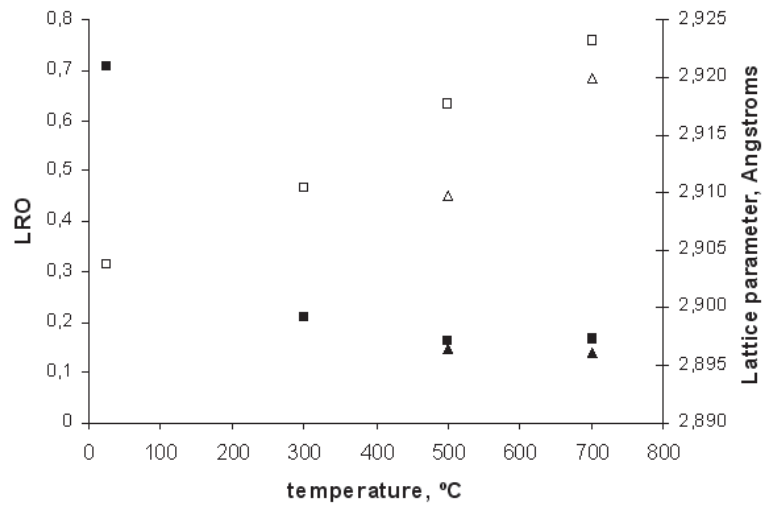
Figure 9. Lattice parameter (full) and LRO (empty) versus temperature: (squares) *FeAl-grade 3* (MM) powder, (triangles) *FeAl-cryo* (MA) powder.
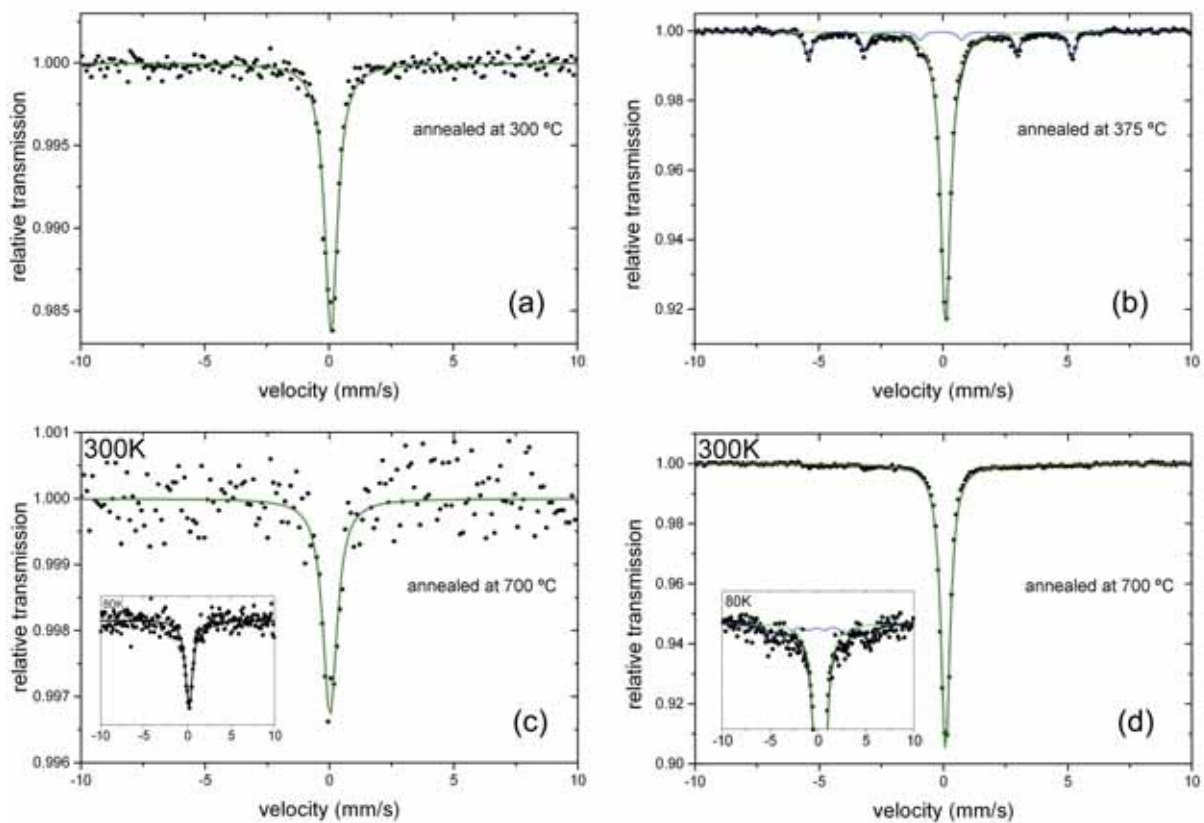
Figure 10. Mössbauer spectra of the annealed samples for 10min: (a) *FeAl-grade 3* annealed at 300ºC and (c) 700ºC; (b) *FeAl-cryo* annealed at 375ºC and (d) 700ºC, recorded at 300K (insets at 80K).

TABLES

Table 1. Mössbauer parameters of ball milled and cryomilled powders: linewidth (Γ), isomer shift (δ), quadrupole splitting (Δ), quadrupole shift (2ε), hyperfine field (B_{hf}) and relative subspectral area, % phase.

	subspectrum	Γ (mm/s)	δ_{Fe} (mm/s)	Δ or 2ε (mm/s)	B_{hf} (T)	%
Ball-milled	sextet	-	0.11(1)	0.04(2)	*	93
	doblet	0.50(8)	0.46(3)	0.59(4)	-	7
Cryomilled	sextet	0.32(1)	0.01(1)	0.00(1)	32.87(1)	86
	doblet	0.76(6)	0.25(2)	0.57(3)	-	14

*wide hypefine field distribution with a maximum at 19.2 T

Table 2. Peak temperatures found in DSC experiments.

	Ball-milled	Cryomilled			
		3h	6h	9h	12h
1r peak, ºC	200,8	373,7	362,6	362,6	-
2n peak, ºC	-	418,8	409,5	415,5	416,7

Table 3. Peak area of the more intense peak in DSC experiments.

	Ball-milled	Cryomilled			
		3h	6h	9h	12h
peak area (J/g)	-29.40	-330.47	-210.12	-114.43	-7.37

Table 4. Mössbauer parameters of annealed ball milled and cryomilled powders: linewidth (Γ), isomer shift (δ), quadrupole splitting (Δ), quadrupole shift (2ε), hyperfine field B_{hf} and relative subspectral area, % phase.

sample	a. t. (ºC)	m.t (K)	sub-spectrum	Γ (mm/s)	δ_{Fe} (mm/s)	Δ / 2ε (mm/s)	B_{hf} (T)	%
FeAl-grade 3	300	300		0.62(3)	0.19(1)	-	-	100
		80		1.04(4)	0.31(1)	-	-	100
	700	300		0.67(13)	0.12(4)	-	-	100
		80		1.01(9)	0.27(4)	-	-	100
FeAl-cryo	375	300	singlet	0.48(1)	0.21(1)	-	-	79
			sextet	0.35(5)	0.00(10)	-0.02(26)	32.85(7)	21
		80	singlet	0.52(1)	0.33(1)	-	-	76
			sextet	0.43(5)	0.11(2)	0.01(3)	33.63(8)	24
	700	300	singlet	0.44(1)	0.19(1)	-	-	92
			sextet	1.01(15)	0.56(9)	-0.47(12)	32.84(40)	8
		80	singlet	0.52(1)	0.31(1)	-	-	86
			sextet	1.25(50)	0.09(10)	0.33(14)	32.17(55)	14

 References

[1] C. Suryanarayana, Mechanical alloying and milling, Progr Mater Sci 46 (2001) 1-184.

[2] D. G. Morris, X. Amils, J. Nogués, S. Suriñach, M. D. Baró, M. A. Muñoz-Morris, Disordering of B2 intermetallics by ball-milling with particular attention to FeAl, International Journal of Non-equilibrium Processing 11 (2002) 379-409.

[3] M. A. Morris-Muñoz, A. Dodge, D. G. Morris, Structure, strength and toughness of nanocrystalline FeAl, NanoStruct Mater 11, 7, (1999) 873-885.

[4] B. D. Cullity, Elements of x-ray diffraction, 2nd ed Addison-Wesley, 1978.

[5] David A. Porter, Phase transformations in metals and alloys, 2nd ed., Van Nostrand Reinhold, New York, 1981.

[6] C.N.R. Rao, K.J. Rao, Phase Transitions in Solids, 1st ed, McGraw-Hill, England, 1977.

[7] W. Pfeiler, B. Sprusil, Atomic ordering in alloys: stable states and kinetics, Mater Sci Eng A 324 (2002) 34-42.

[8] J. Argren, On the classification of phase transformation, Scripta Mater 46 (2002) 893-898.

[9] V. Sima, Order-disorder transformations in materials, J Alloys Comp 378 (2004) 44-51.

[10] G. Ji, T. Grosdidier, N. Bozzolo, S. Launois, The mechanisms of microstructure formation in a nanostructured oxide dispersion strengthened FeAl alloy obtained by spark plasma sintering, Intermetallics 15 (2007) 108- 118

[11] E. Arzt, R. Behr, E. Göhring, P. Grahle, R. P. Mason, Dispersion strengthening of intermetallics, Mater Sci Eng A 234-236 (1997) 22-29.

[12] M. A. Muñoz-Morris, C. Garcia Oca, D. G. Morris, Microstructure and room temperature strength of Fe40Al containing nanocrystalline oxide particles, Acta Mater 51 (2003) 5187-5197.

[13] K. H. Chung, J. He, D. H. Shin, J. M. Schoenung, Mechanisms of microstructure evolution during cryomilling in the presence of hard particles, Mater Sci Eng A 356 (2003) 23-31.

[14] R.A. Brand, Improving the validity of hyperfine field distributions from magnetic alloys. Part II: polarized source and spin texture, Nucl. Instrum. Methods Phys. Res. B 28 (1987), 417-432.

[15] E. Apiñaniz, J. S. Garitaonandia, F. Plazaola, Influence of disorder on the magnetic properties of feAl alloys: theory, J Non-Cryst Solids 287 (2001) 302-307.

[16] Q. Zeng, I. Baker, The effects of local versus bulk disorder on the magnetic behaviour of stoichometric Ni_3Al, Intermetallics 15 (2007) 419-427.

[17] V. Sebastian, N. Lakshmi, K. Venugopalan, Structural and magnetic properties of mechanically alloyed Fe-66 at%Al, Intermetallics 15 (2007) 1006-1012.

[18]   V. Sebastian, N. Lakshmi, K. Venugopalan, Correlation between microstructure and magnetic properties in mechanically alloyed nanogranular $Fe_{100-x}Al_x$, Materials Letters 61 (2007) 4635-4638.

[19] K. Wolski, G. Le Caër, P. Delcroix, R. Fillit, F. Thévenot, J. Le Coze, Influence of milling conditions on the FeAl intermetallic formation by mechanical alloying, Mater Sci Eng A 207 (1996) 97-104.

[20] H. Schröpf, C. Kuhrt, E. Arzt, L. Schultz, Ordering versus disordering tendencies in mechanically alloyed $(Ni_xFe_{1-x})Al$ alloys, Scripta Metall Mater 30, 12 (1994) 1569-1574.

[21] M. Krasnowski, A. Grabias, T. Kulik, Phase transformations during mechanical alloying of Fe50%Al and subsequent heating of the milling product, J Alloys Comp 424, 1-2 (2006) 119-127.

[22] D. Oleszak, P.H. Shingu, Mechanical alloying in the Fe-Al system, Mater Sci Eng A 181–182 (1994) 1217–1221.

[23] D. A. Eelman, J. R. Dahn, G. R. MacKay, R. A. Dunlap, An investigation of mechanically alloyed Fe-Al, J Alloys Comp266 (1998) 234-240.

[24] M. H. Enayati, M. Salehi, Formation mechanism of Fe_3Al and FeAl intermetallic compounds during mechanical alloying, J Mater Sci 40 (2005) 3933-3938.

[25] R. A. Varin, J. Bystrzycki, A. Calka, Characterization of nanocrystalline Fe-45 at% Al intermetallic powders obtained by controlled ball milling and the influence of annealing, Intermetallics 7 (1999) 917-930.

[26] B. Huang, K.N. Ishihara, P.H. Shingu, Metastable phases of Al–Fe system by mechanical alloying, Mater Sci Eng A 231 (1997) 72–79.

[27] Y. D. Dong, W. Wang, H. Liu, L., K. Q. Xiao, Tong S. H., He Y. Z., Structural evolution of mechanically alloyed nanocrystalline FeAl intermetallics, Mater Sci Eng A 134 (1991) 867-871.

[28] H. Shi, G. Debo, O. Yifang, Structural evolution of mechanically alloyed nanocrystalline FeAl intermetallics, J Alloys Comp (2008) 207-209.

[29] S. Gialanella, FeAl alloy disordered by ball-milling, Intermetallics 3 (1995) 73-76.

[30] D. Wu, I. Baker, Strain-induced ferromagnetism in FeAl single crystals, Materials Science and Engineering A 239-331 (2002) 334-338.

[31] L. F. Kiss, D. Kaptas, J. Balogh, L. Bujdoso, J. Gubicza, T. kemeny, I. Vincze, Magnetic properties of ball-milled FeAl nanograins, Phys. Stat. Sol 201, 15 (2004) 333-3337.

[32] A. M. Farghalli, X. Yuwei, Correlations between the minimum grain size produced by milling and material parameters, MaterSci Eng A 354 (2003) 133-139

[33] M. Meyer, L. Mendoza-Zelis, F. H. Sánchez, Mechanical milling of the intermetallic compound AlFe, Phys Rev B 60, 5 (1999) 3206-3212.

[34] S. Gialanella, X. Amils, M. D. Baro, P. Delcroix, G. LeCaër, L. Lutterotti, S. Suriñach, Microstructural and kinetic aspects of the transformations induced in a FeAl alloy by ball.milling and thermal treatments, Acta Mater 46, 9 (1998) 3305-3316.

[35] S. Suriñach, X. Amils, S. Gialanella, L. Lutterotti, M. D. Baro, Kinetics of reordering in a nanograined FeAl alloy, Mater Sci Forum 235-238 (1997) 415-420.

[36] M. Boufenghour, A. Hayoune, D. Hamana, Study of the ordered structures in Fe-Al alloys using dilatometric and calorimetric analysis, J Mater Sci 39 (2004) 1207-1212.

[37] S. Enzo, R. Frattini, R. Gupta, P. P. Macri, G. Principi, L. Schiffini, Scipione G., X-ray powder diffraction and mossbauer study of nanocrystalline Fe-Al prepared by mechanical alloying, Acta Mater 44, 8 (1996) 3105-3113.

[38] X. Amils, J. Nogués, S. Suriñach, J. S. Muñoz, L. Lutterotti, S. Gialanella, M. D. Baró, Structural, mechanical and magnetic properties of nanostructured FeAl alloys during disordering and thermal recovery, Nanostructured Materials 11 (1999) 689-695.

4.1.2   Microstructural coating characterization

a)   Spraying parameters optimization

The optimization of spraying parameters will depend on the final application of the coating; the microstructure determines the properties. A general goal in Thermal Spray technologies is to ensure that all particles impacting the substrate are molten or semi-molten and have a maximum velocity as possible in order to form a dense coating, although in some specific cases certain porosity might be desirable for the application. In the present case, apart from the requirements specified in section 1.6, the first attempts for spraying the ball-milled Fe40Al grade 3 (CEA-DTEN) powder, were carried out bearing in mind the following:

- T_m (FeAl) = 1250°C. Depending on the melting temperature of the material relative to the flame temperature and dwell time, the particle may be molten, semi-molten or solid when it impacts the substrate or pre-coated surface.

- Low porosity and oxidation content is desirable if a good oxidation resistance is pursued, as this is one of the main properties for which these materials are under study.

To accomplish this, the following parameters were tested (tables 4.1 and 4.2). The maximum flame temperature is usually reached off-O_2/fuel stoichiometry, being the propylene and hydrogen flame properties 2896°C (3.7) and 2856°C (0.42) respectively (*Appendix IV*).

Table 4.1. Thermal spraying parameters by using propylene as fuel gas.

	Parameter set 1 (F1)	Parameter set 2 (F2)	Parameter set 3 (F3)
Oxygen flow rate , l min⁻¹	189	189	253
Oxygen pressure, bar		10,3	
Carrier gas (air), l min⁻¹	385	305	305
Air pressure, bar		6,9	
Fuel (propylene), l min⁻¹		87	
Propylene pressure, bar		6,9	
Spraying distance , mm		250	
Oxygen-fuel ratio	3,057	2,874	3,609

Table 4.2. Thermal spraying parameters by using hydrogen as fuel gas.

	Parameter set 4 (F4)	Parameter set 5 (F5)	Parameter set 6 (F6)
Oxygen flow rate , l min^{-1}	147	214	147
Oxygen pressure, bar		11,7	
Carrier gas (air), l min^{-1}	438	344	344
Air pressure, bar		6,9	
Fuel (hydrogen), l min^{-1}	717	635	717
Hydrogen pressure, bar		9,7	
Spraying distance , mm		250	
Oxygen-fuel ratio	0,327	0,445	0,301

b)   Structure morphologies and phase composition analysis

Some initial results were presented in the article entitled "Studies of Fe–40Al coatings obtained by high velocity oxy-fuel" (*Appendix V*), where the optimization of spraying parameters is discussed in terms of microstructure, X-ray and microhardness characterization. However, these have already been included and extended in this section.

-   *Scanning Electron Microscopy and X-ray diffraction*

Figure 4.6 and 4.7 show the coating microstructures of the parameters presented in tables 4.1 and 4.2 respectively. In order to compare the two HVOF coating structures obtained by using H_2 and C_3H_6, the following points must be considered:

- Heat transfer of hydrogen flame is higher than for propylene; thus, powder particles will be more easily melted in the first case. This is actually noticed easily by observing F1 and F2 and, F4, F5 and F6. The ones sprayed employing hydrogen appear further melted than the ones sprayed with propylene.

- Considering that hydrogen pressure is larger than propylene pressure, it is expected that the deposits will be less porous by using hydrogen as there will be a much effective densification. With a higher velocity, the particles might be still molten when impacting the substrate, and will leave fewer voids at the intersplat boundaries.
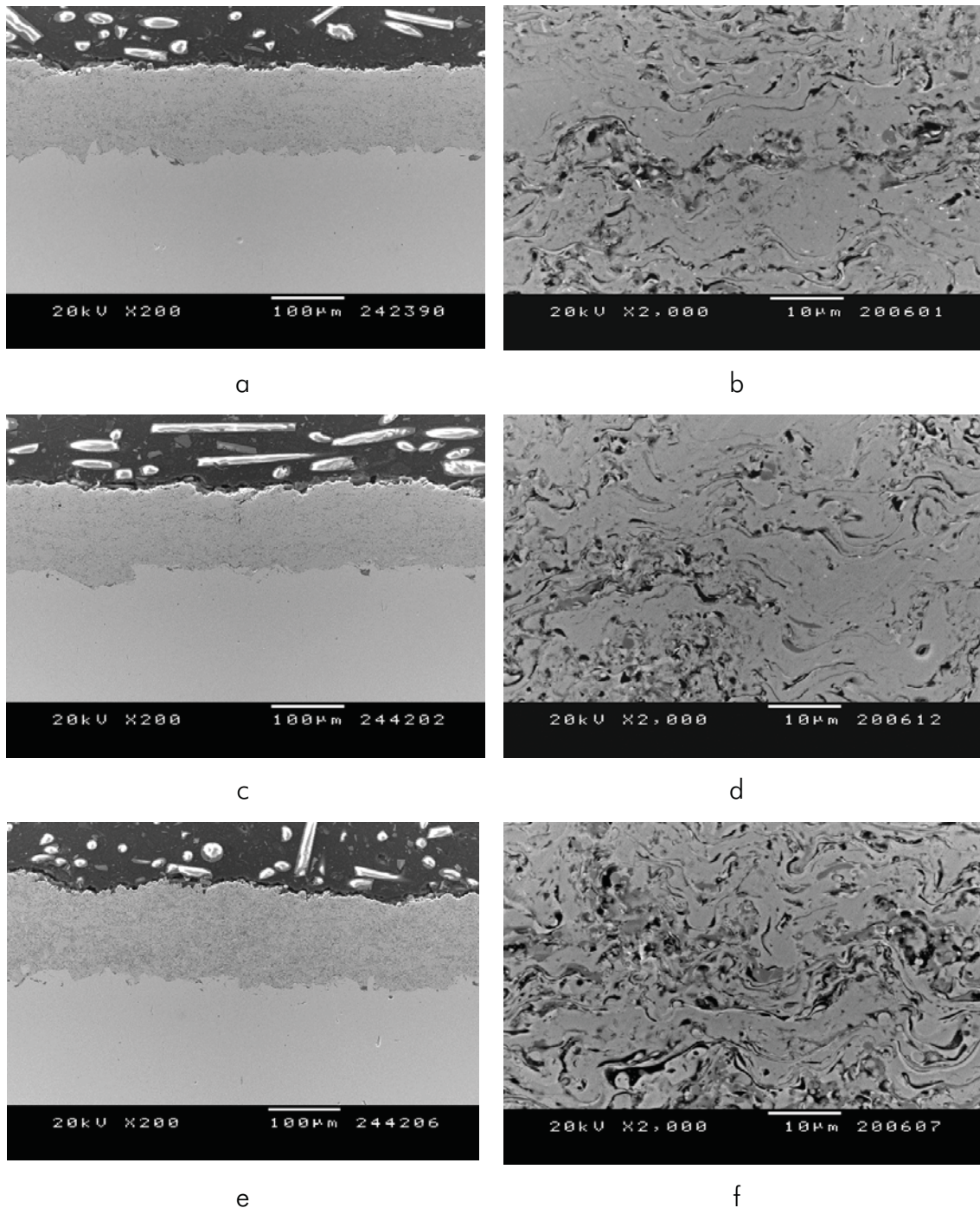
Figure 4.6. SEM cross-section microstructures of: (a)-(b) F1, (c)-(d) F2 and (e)-(f) F3.

The common features found, both in the magnifications of figure 4.6 and 4.7, are the dark and light grey contrasts produced at the intersplat boundaries, being identified as mixed oxides and Al-depleted zones by EDS. Among the microstructures in figure 4.6, F1 and F2 exhibit more partially molten areas than F3, which shows a clear lamellar structure with oxidation at the

intersplats. No differences were actually observed by the examination of F1 and F2, but F3 presents significantly higher oxidation as result of the higher oxygen flow rate. The uniform distribution of the oxidation indicates that it may have occurred in-flight rather than after splat impact, otherwise one could easily make the difference between the several sprayed layers.

<center>a   b</center>

<center>c   d</center>

<center>e   f</center>
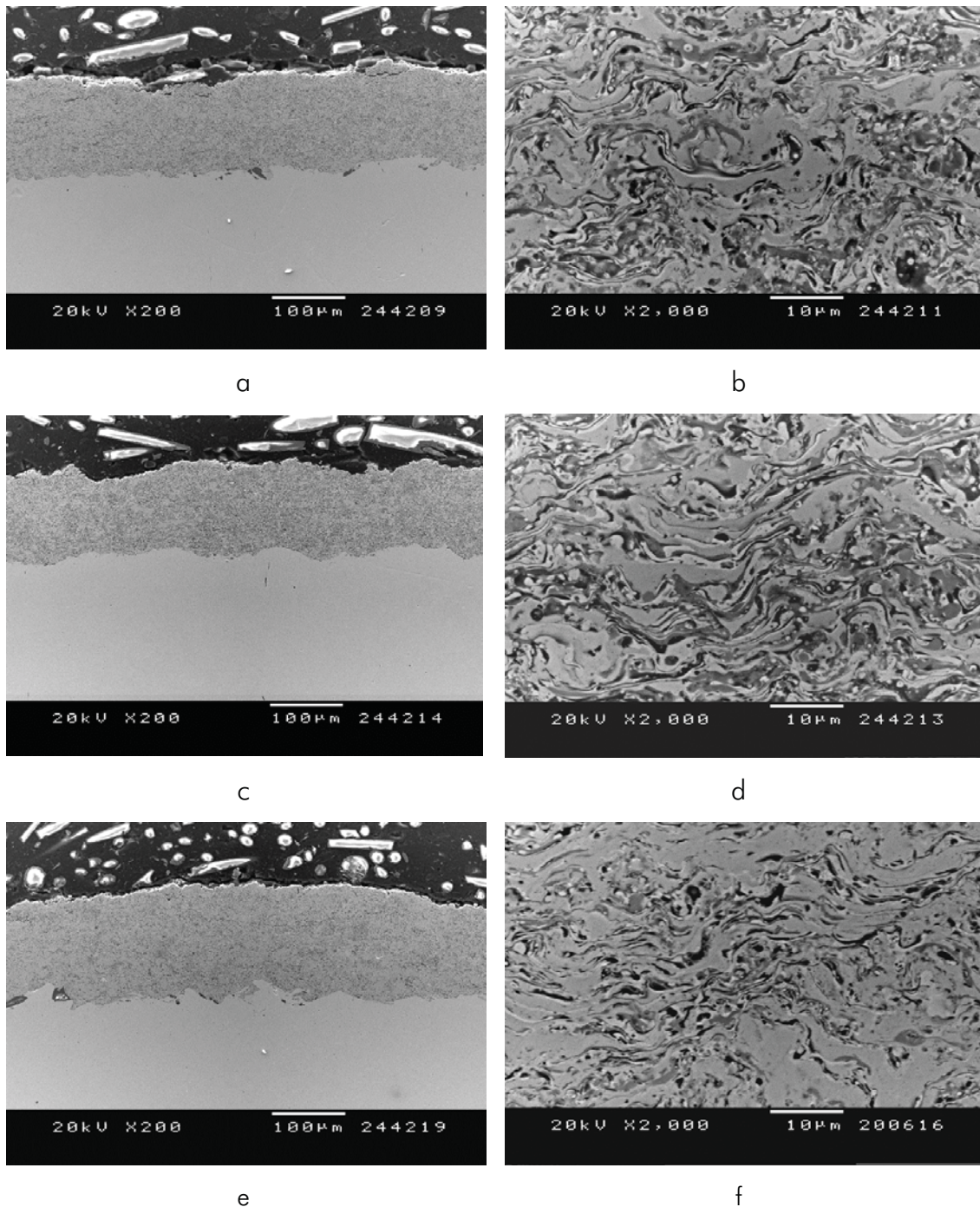
Figure 4.7. SEM cross-section microstructures of: (a)-(b) F4, (c)-(d) F5 and (e)-(f) F6.

From the microstructures observed in figure 4.7, one can see that these appear much more melted and oxidized than F1 and F2 and, resemble more to F3. By their examination, despite the spraying parameter differences, F4 and F5 look like the same and just, regarding F6, it could be said that it seems to have slightly less dark contrasts. In this set of figures, as a consequence of the further oxidation, the Al-depleted zones near splat boundaries are much more noticeable. These appear as light grey contrasts.

X-ray diffraction illustrates the presence of the oxide and Fe-rich phases (fig. 4.8). The mixed oxide identified by EDS corresponds to the spinel structure $FeAl_2O_4$.
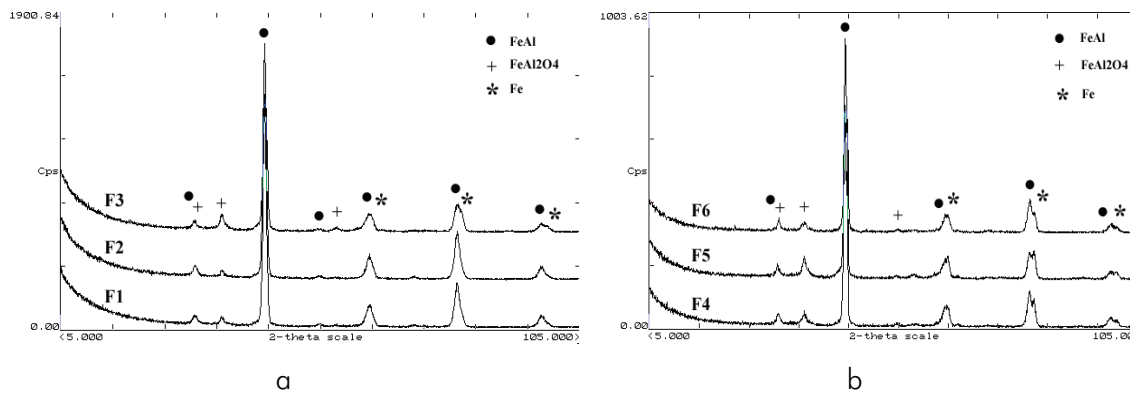
Figure 4.8. X-ray diffraction of: (a) F1-F2-F3 and (b) F4-F5-F6.

Nevertheless, the interesting point to highlight in the previous X-ray results is the presence of some additional and low intense peaks to those observed in the feedstock powder, also identifieds as FeAl phase. These are the superlattice peaks (h+k+l= odd) corresponding to the ordered B2-type phase, indicating that thermal history of the sprayed powder has promoted ordering of the lattice. When these peaks appear and how they are related to the crystallographic nature of the material, is explained by Cullity [9].

From all the previous conditions, those with less oxidation were selected for posterior analysis. Oxidation can significantly influence the properties and therefore performance of sprayed coatings: they might improve wear resistance but be detrimental for oxidizing environments. As the second scope

was pursued, F2 conditions were chosen. From now ahead, this coating will be referred to as CEA, as it was sprayed using the powder supplied by them.

a   b
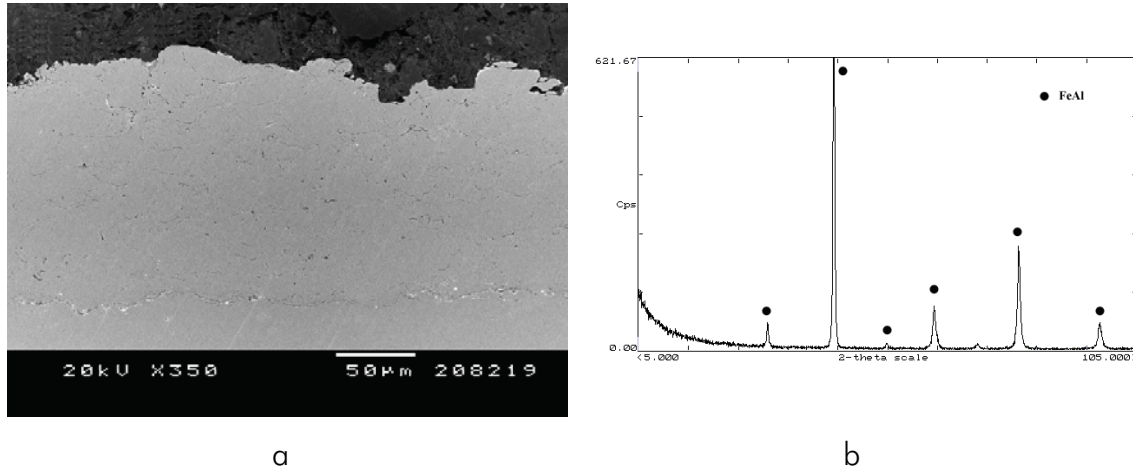
Figure 4.9. (a) SEM cross-section microstructure and (b) X-ray diffraction of MEC40-60.

After working for a while with these coatings and having carried out the oxidation tests presented in section 4.1.3c, it was thought that it would be interesting to produce a coating resembling to a bulk structure. This was achieved by changing the particle size; in that case, the Mechachrome powder was sieved between 40-60 microns. This lead to a decrease in oxidation (fig. 4.9a); smaller particles have oxides distributed over the entire particle whereas with increased particle size, it is found that the particle develops an oxide shell (fig 4.10c). Increasing particle size might also lead to particle rebounding, but the deposits were found to have good adherence. This coating will be referred to as MEC40-60, since it was obtained from the 40-60 fraction size of Mecachrome powder. The oxide shell was not detected by X-ray diffraction (fig. 4.9b).

 A further attempt was proved by annealing the powder (MEC40-60$_{ANN}$ coating); the microstructure and X-ray scan are the same as those presented in figure 4.9 but with the difference that the material properties have changed (grain growth and lattice ordering will be illustrated in TEM analysis).
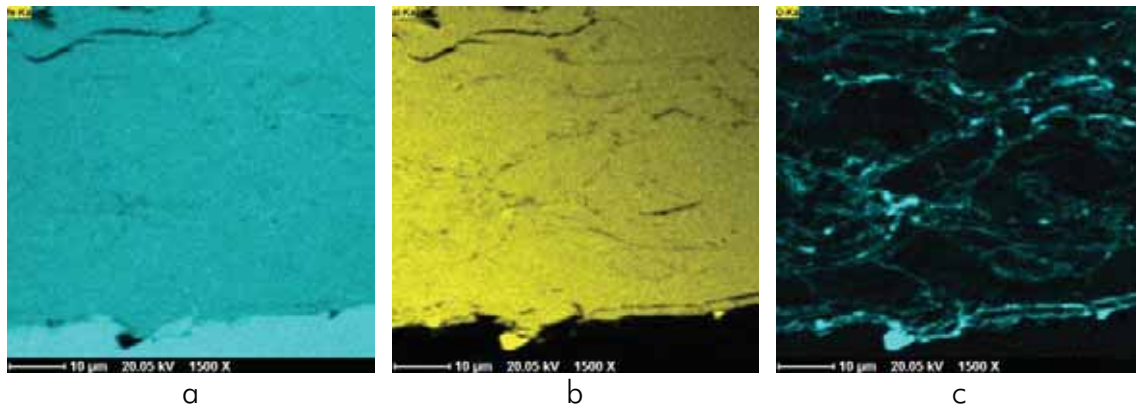
Figure 4.10. Electron microprobe results: (a) Fe, (b) Al and (c) O in MEC40-60.

Finally, there was the attempt to spray the cryomilled powder. The spraying conditions were the same; just the efficiency was proven to be better at a distance of 240mm. The microstructure is very similar to the CEA coating. The amplification in figure 4.11b shows some areas where a heterogeneous contrast can be distinguished. These areas come from those large particles not fully alloyed. The larger amount of oxidation in this coating is attributed to the reaction of higher percentage of partially iron alloyed in the starting material.

a   b

c
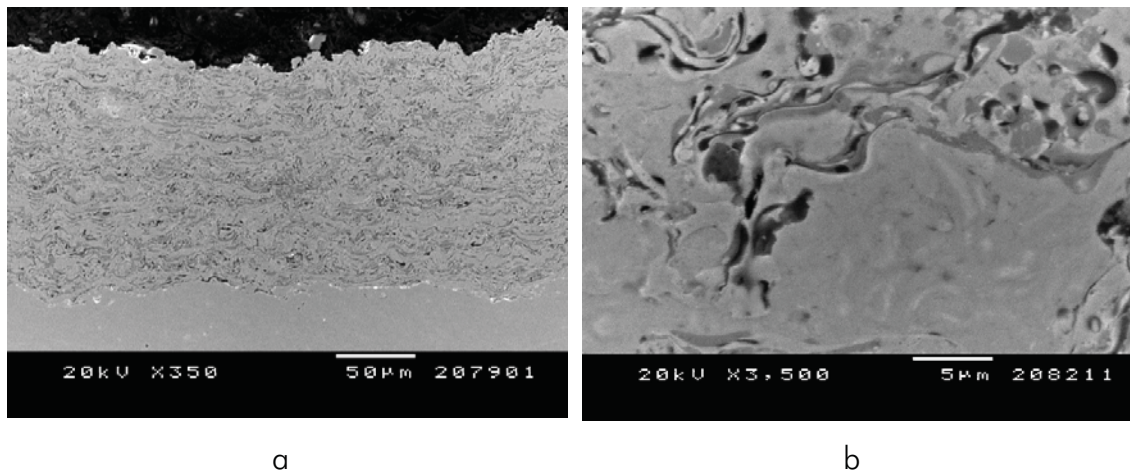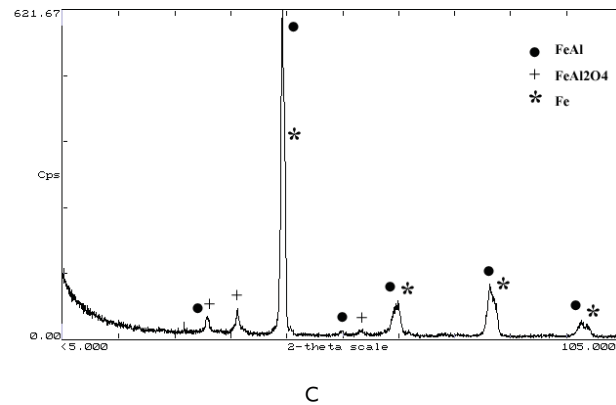
Figure 4.11. (a) SEM cross-section microstructure, (b) detail of the heterogeneous unmelted areas and (c) X-ray diffraction of coating produced with the cryomilling powder.

-        *Transmission Electron Microscopy*

From figure 4.12 to 4.15, the main features of the analyzed coatings are studied by using TEM. Inside a droplet, the CEA coating is characterized by some equiaxed grains below 200nm approximately (fig. 4.12a) and with a mainly disordered structure; some 100 superlattice spots are visible in the SAED (selected area electron diffraction) pattern but no other superlattice reflexions are detected. This indicates that the FeAl phase was retained in a disordered state and that reordering has started in this area [10, 11].

Furthermore, there are some oncoming droplets that arrive onto oxidized zones (resulting from in-flight or post-impact oxidation, fig. 4.12c) or onto slightly oxidized areas, such as in figure 4.12b, where the thin oxide strip indicated by the arrow is formed at the intersplat boundary. Figure 4.12c also exhibits some oxide grains that have grown in a columnar form, while the columnar grains illustrated in figure 4.12d present a SAED diffraction pattern with many spots corresponding to the FeAl and $FeAl_2O_4$ phase. Such columnar grains commonly appear by the rapid cooling rate and the high thermal gradients [12]. Actually, when the solidification of a particle starts after striking the substrate or previously deposited material, it can lead to equiaxed grains throughout the core when low rate of heat is removed away or, in many cases, heat is rather extracted back through the core (centre of splat) at a high

87

rate. This latter case results in the formation of elongated grains in the peripheral areas.

Figure 4.13a-b clearly show a nanocrystalline structure where the grain size is below 10nm; this indicates that in that zone recrystallization is in a early stage; interestingly, although X-ray diffraction did not show any peak from oxide phases, an intense circle makes relevant that oxidation has taken place inside the particle, what would confirm the previous statement that internal oxides are formed. By contrast, there are other areas, as featured in figure 4.13c, where recrystallization seems to be more advanced.

a

b

c

d
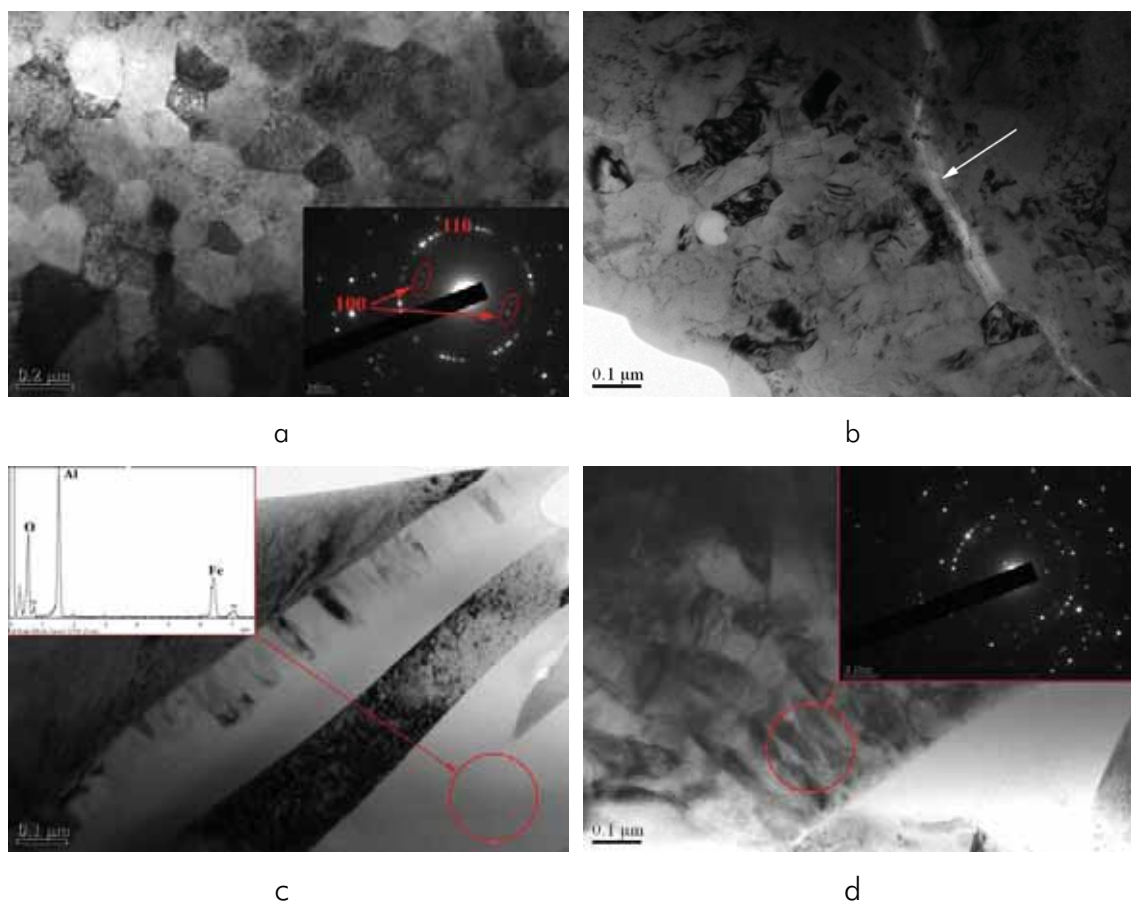
Figure 4.12. TEM images of CEA coating showing: (a) equiaxed grains, (b) thin oxide layer between splats, (c) large oxide areas and (d) columnar grains adjacent to oxide zones.

As already said, no visual differences were noticed by using SEM that could facilitate us the distinction between MEC40-60 and MEC40-60$_{ANN}$, but TEM shows that as result of powder annealing, there has been a grain growth and

atom rearrangement: some of those grains that might have ineffectively annealed are around 100nm size (fig. 4.14a) and still have a disordered structure, whereas those having grown even above 200nm, present an ordered B2 lattice (fig. 4.14b). While the ordering observed in the previous coatings came from the thermal history of particles during the spraying process, the ordering here is much more evidenced by the visible superlattice spots. Figure 4.14a also has some spots corresponding to oxides.

a   b

c
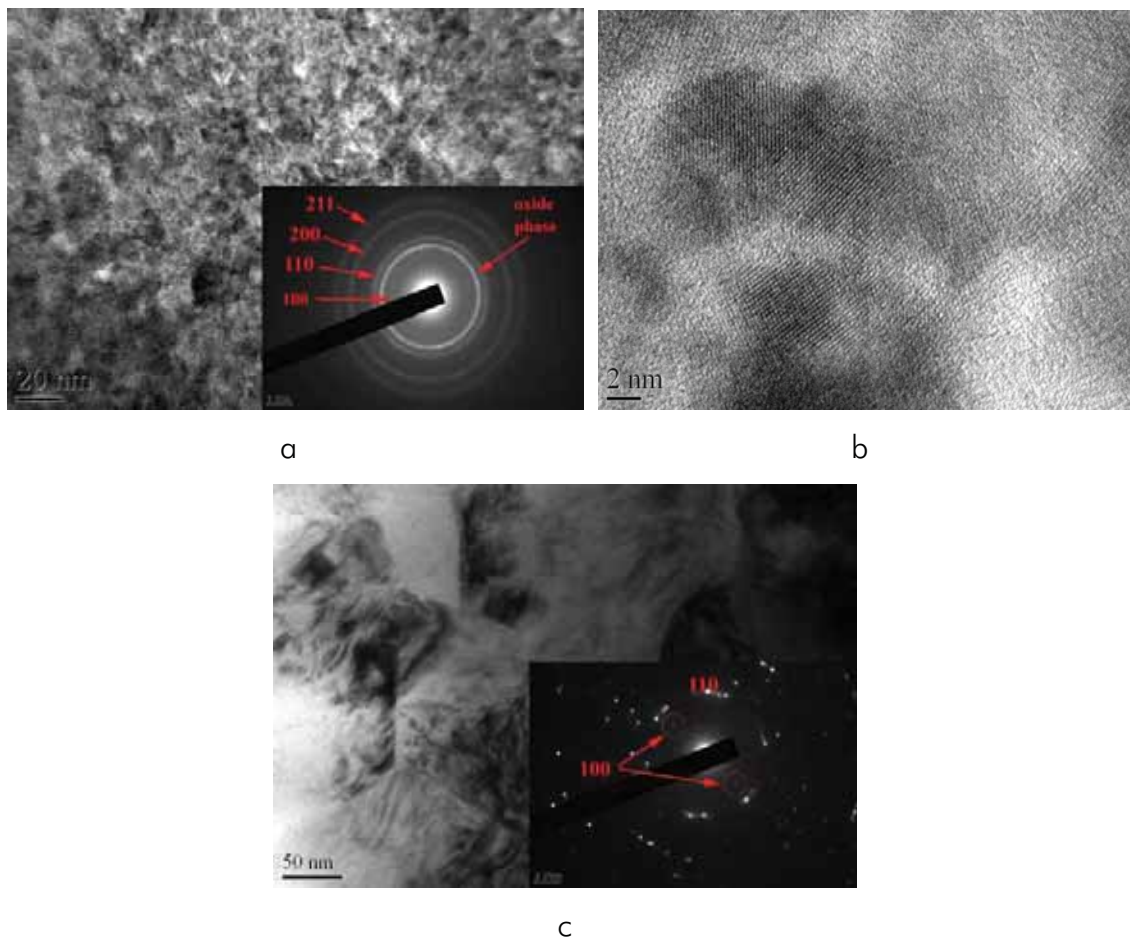
Figure 4.13. TEM images of MEC40-60 coating showing: (a) fine grain structure, (b) orientation of the grains at the nanoscale and (c) growth grains.

a   b
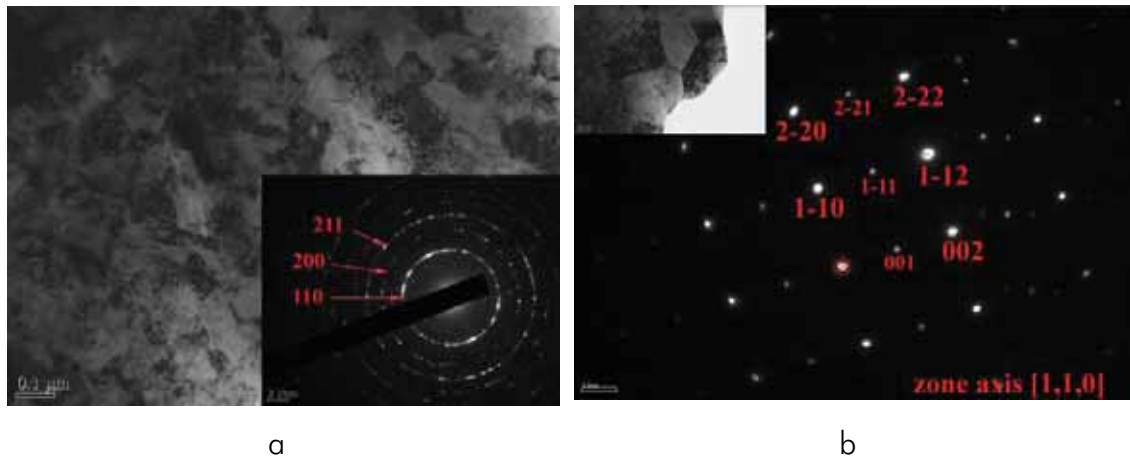
Figure 4.14. TEM images of MEC40-60$_{ANN}$ coating showing: (a) equiaxed fine grains with disordered lattice and (b) enlarged grains with ordered lattice.

Finally, figure 4.15 shows broad oxide strips with iron-rich interlamella sites, as indicated by the absence of any superlattice spot in figure 4.15a. This is consistent with the fact that ordering is much more difficult as the sprayed powder does not attain the suitable stoichiometry.

a   b
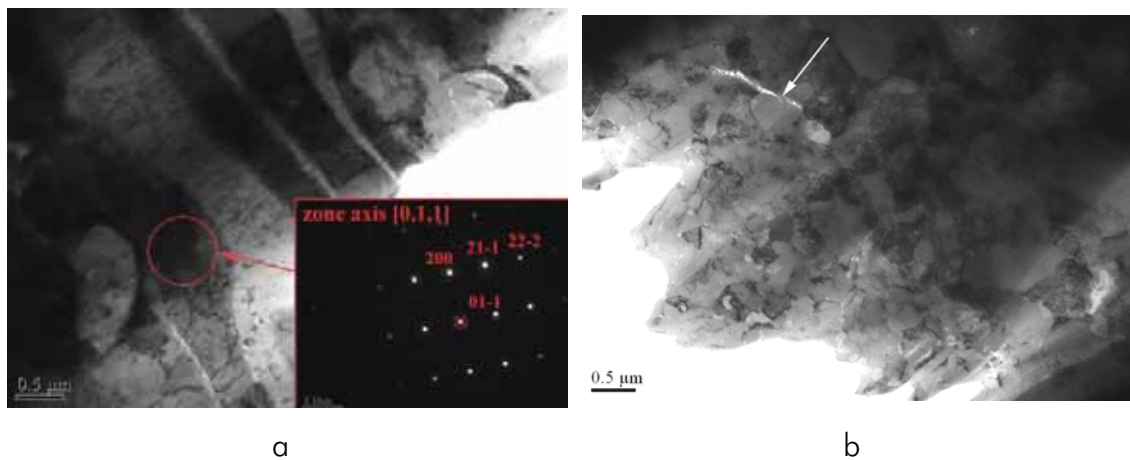
Figure 4.15. TEM images of the coating produced with the cryomilling powder showing: (a) Fe-rich and oxide bands and (b) thin oxide layer between consecutive splats.

4.1.3   Characterization of coating properties

a)   Mechanical properties

–   *Tensile strength*

The tensile bond strengths of the studied iron aluminide coatings are presented in table 4.3. The optimum bond strength for a coating is given

whenever the failure occurs between the glued surfaces (coated and non-coated specimen); none of the iron aluminide coatings showed such kind of failure. CEA and MEC40-60 failed in the coating, concluding that bonding is stronger than coating cohesion, whereas the as-sprayed cryomilled powder (CRYO) exhibited a mixed failure, the rupture was neither entirely within the coating (cohesive failure) nor within the coating-substrate interface (adhesive failure).

The common standards limitations when measuring bond strengths result from the penetration of the resin in the coating and its limited strength (~80MPa) [13].

Table 4.3. Tensile bond strength of iron aluminide-sprayed powders and illustration of a mixed rupture.

	Adherence, MPa	
CEA	$37,2 \pm 4,8$	
MEC40-60	$49,3 \pm 5,1$	
CRYO	$44,4 \pm 9,0$	

    −   *Elastic modulus and microhardness*

The microhardness was first evaluated for the tested spraying conditions, both using propylene and hydrogen (table 4.4). According to the results, on average, the as-sprayed with hydrogen are slightly harder than those sprayed using propylene, which might be due to the higher oxide content.

Table 4.4. Vickers microhardness for the as-sprayed Fe40Al grade 3 powder.

	HV_{200} propylene conditions		HV_{200} hydrogen conditions	
F-1	475 ± 31	F-4	499 ± 22
F-2	**434 ± 48**	F-5	482 ± 37
F-3	468 ± 26	F-6	505 ± 28

Table 4.5 presents the resulting Vickers microhardness and elastic modulus of the final optimized coatings. The hardness values seem to correlate according to the oxidation, porosity and unmelted particles content, with these two final factors lowering coating hardness. The E-values show slightly differences, all below the steel substrate.

Table 4.5. Vickers microhardness and elastic moduli of iron aluminide coatings.

	Vickers microhardness, HV_{200}	Elastic modulus, GPa (50gf)
CEA (F-2)	434 ± 48	160 ± 9
MEC40-60	377 ± 36	154 ± 22
MEC40-60$_{ANN}$	415 ± 21	126 ± 16
CRYO	542 ± 31	152 ± 26

b)   Wear resistance

In this section, mainly three types of wear (abrasive, adhesive and erosive) are examined for the iron aluminide coatings. Some preliminary results for the CEA coating are included in paper 2 (*Appendix V*) but a complete discussion is given in the following article:

<u>Paper 3:</u>   J. M. Guilemany, N. Cinca, J. Fernández, S. Sampath, Erosion, abrasive and friction wear behaviour of iron aluminide coatings sprayed by HVOF, *Journal of Thermal Spray* (accepted).

After a detailed examination of the coating microstructures, the wear performance has been evaluated in terms of spraying parameters and thermal history of powder. It is important to highlight that although hardness has been used in some cases to predict the wear properties, it has been done taking care of other many factors that might influence. It was concluded that CEA possessed the lowest abrasive wear rate, whereas it exhibited the highest wear damage in terms of erosion and friction.

Erosion, abrasive and friction wear behaviour of iron aluminide coatings sprayed by HVOF

J. M. Guilemany[1], N. Cinca[1], J. Fernández[1] and S. Sampath[2]
[1]Thermal Spray Centre, University of Barcelona. Barcelona, SPAIN
[2]Center for Thermal Spray Research. Stony Brook (NY), USA

Abstract

Iron aluminides have been proposed lately as promising materials for wear applications. Many authors have focused their investigations on the friction behaviour of FeAl coatings, emphasizing the role of this intermetallic phase as a new matrix to embed ceramic particles and replace the extensively studied WC-Co cermet system for high temperature. However, few of these studies deal with the evaluation of the different tribological properties and their relationship with the coating microstructure. In the present study, the near stoichometric Fe40Al was successfully sprayed by means of HVOF using different particle size distribution and the tribological behaviour was assessed through solid particle erosion, abrasive and dry sliding tests. The wear mechanisms of the deposited coatings are discussed with regard to the observed results. In addition, oxidized samples were tested to evaluate the role of the oxide top layer; also, the powder was previously annealed to produce a coating with an almost fully ordered FeAl structure.

1   Introduction

One of the current challenges in materials science is to find versatile materials able to withstand a good resistance for different service performance situations. A combination of good mechanical properties, corrosion, oxidation and wear resistance is usually difficult to reach.

Currently, intermetallic compounds (IMCs) are being investigated as a good compromise for the above requirements. They are regarded as advanced materials, attractive due to their unique properties: high melting points, great strength but poor ductilities. In these respects, they resemble ceramic materials. Unlike ceramics however, they have a metallic lustre and, conduct heat and electricity well. Thus, they have been exploited not only for their mechanical properties but their chemical, electrical, magnetic, optical and semiconducting properties as well [1].

Although IMCs have been studied and employed over decades, their interest is relatively new and has been motivated by the demand of finding some sort of materials capable of substituting superalloys, especially for jet engine development [2 ,3]; their particular structure is the reason of their high stability. Whereas conventional alloys are defined by atoms linked with relatively weak metallic bonds, IMCs have either partly ionic/covalent bonds or, having entirely metallic bonds, the atoms take up preferred positions within the crystal lattice. Because of such atom arrangement, intermetallic compounds tend to have a much lower self-diffusion coefficient than do disordered alloys and so their structure can be maintained to high temperatures [4]. Nevertheless, their long-range ordered superlattices reduce dislocation mobility and

diffusion processes leading to their inherent embrittlement. It has been observed that some can even keep such order up to their melting point, otherwise they disorder below a certain critical temperature (T_c) at which an order-disorder transformation might occur.

Contemporary efforts have been addressed to aluminides of transition metals i. e. Fe, Ni, Ti, Co and Nb; these compounds possess relatively low densities, high specific modulus, high melting points, strength and excellent oxidation and corrosion resistance because of the formation of a protective alumina layer [5, 6]. However, since the first investigations about intermetallics carried out by Kumakov et al (1916), their low ductility has hampered their fabrication. To overcome such a handicap, many attempts have been carried out in the last decades to enhance their ductility, such as reduction of grain size [7] or addition of certain alloying elements [8, 9].

Their difficulty to fabricate as structures has stimulated their use as coatings. In a previous study, the oxidation behaviour of HVOF sprayed FeAl coatings was already reported [10]. Such aluminide (B2 ordered structure, CsCl-type) has a density of 5,56 g/cm^3, excellent sulphidation resistance and good strength up to 600ºC [11, 12]. Its applications include, among others, molten salt systems for chemical air separation, automotive exhaust systems, immersion heaters, heat exchangers, catalytic conversion vessels, chemical production systems and coal conversions systems. Since some of the previous applications involve removal of material due to contact damage, few studies have recently evaluated their wear response either in bulk or coating form. Friction has been the most investigated mechanism and delamination was found to be the predominant cause for volume loss in coatings [13, 14, 15]. The wear resistance was further improved by reinforcement with hard particles [14, 16]. The presence of such particles has also been reported to affect the abrasive and erosion properties even for NiAl [16, 17, 18].

The other two wear mechanisms, mainly abrasion and erosion, have been studied for FeAl and NiAl coatings [19, 20]. Almand et al. [15, 17] compared the wear rates of Fe-Al based alloys with those of other metals and ceramics and concluded that their resistance was as much as that encountered in typical austenitic stainless steels. Moreover, the higher the Al content, the further the wear rate decreased relating to bulk hardness of the compound.

Ordering in these compounds is also induced by heat treatments to yield B2 (36-48 at% Al) or D0$_3$ (interpenetrating FCC lattices, composition range 23-36 at% Al and from room temperature to 550ºC) ordered structures [21], which result in lower wear rates compared to these non-long-range ordered iron aluminides [22, 23].

The present study intends to assess all the above wear responses for FeAl intermetallic coatings based on different microstructures. A main comparison is reported concerning two different microstructures obtained by using different particle size distribution; secondly, the effect in lattice ordering is assessed by previously annealing the feedstock powder and, finally, thermal oxidation is intended to evaluate how surface modification would affect to wear properties.

2   Experimental procedure

The FeAl powder alloy namely Grade 3, provided by CEA-DTEN (**C**ommissariat à l'**E**nergie **A**tomique - **D**epartement de **T**echnologie des **E**nergies **N**ouvelles, Grenoble) and Mecachrome (Vibraye, France) [24],

was used to produce the FeAl coatings onto low alloyed carbon steel substrate. The powder with an initial composition of Fe40Al-0.05Zr (at%) + 50 ppm B was prealloyed by gas atomization and subsequently ball-milled. Boron and zirconium were introduced as alloying elements to improve ductility in the material [9,25 , 26, 27] and, yttria (ODS, oxide dispersed strengthening) was added during the milling step in order to keep fine grain size after hot consolidation and forming so that mechanical strength (Hall-Petch mechanism) and room temperature ductility (reduction of the environmental embrittlement caused by water vapour at RT thanks to grain size reduction down to 1 micron) are improved [28, 29, 30].

CEA-DTEN was the first supplier and it was afterwards transferred to Mecachrome. Both suppliers provided the same powder with the same composition but with the respectives powder distributions as observed in figure 1. The whole CEA-DTEN powder distribution was used to produce the coating which will be referenced as CEA, while from the 40-60micron fraction, the one referenced as MEC40-60 was obtained. Furthermore, a third coating was produced by spraying the 40-60 fraction size being annealed at 700ºC for 10 min in order to induce the ordering in the intermetallic structure and then evaluate the properties of the resulting coating compared to that of MEC40-60 (this will be referenced as MEC40-60$_{ANN}$). The annealing treatment was carried out in a controlled atmosphere furnace with a continuous argon flux.

A Diamond Jet Hybrid gun model 2600/2700 was employed for powder deposition and table 1 presents the spraying parameters. Such parameters were previously optimized with the intention to achieve the less oxidation content as possible [31].

The CEA coating was oxidized at 900ºC for 72h (referenced as CEATT). The selection of the temperature for the treatment was based on a previous study where the formation of an adherent oxide scale was shown [10]. The idea came from the work carried out by Xia et al. [32] who claimed that the average wear rate is reduced 16 times when the bulk intermetallic is compared with an untreated specimen. Both the microhardness of the as-sprayed and the oxidized coatings were investigated using a Vickers indentation tester MATSUZAWA MXT-a at 200gf load for 15s in the cross sections. At least 20 indentations were performed for average.

For the microstructural cross sections and top surfaces characterization, a JEOL Scanning Electron Miscroscope was used with EDS (Energy Dispersive Spectroscopy) for microanalysis. XRD (X-ray Diffraction) scans helped to identify the phases present after the spraying process. In addition, the "image analysis" option within the Matrox Inspector 1.71 software was employed for the oxidation and porosity evaluation. This was done by taking a micrograph of the overall coating cross section; at least 10 pictures were analysis like this for each coating.

<u>Abrasive tests</u>

According to ASTM G65-00 , the Rubber Wheel test consists of a rubber wheel rotating at a constant speed of 139 rpm on the specimen while silica particles (particle size in the range of 0,4-0,8 mm) flow by gravity between the two contacting surfaces. The samples were tested in their as-sprayed state.

A normal load of 50 N is applied and the mass loss is measured up to 30 min. The abrasion wear rate W ($mm^3\ N^{-1}\ m^{-1}$) is calculated as:

(1) $W = \dfrac{\Delta m}{t} \dfrac{1}{N} \dfrac{1}{\rho}$

Where Δm is the average mass loss (g), t is the test time (min), N is the normal load and ρ (g cm^{-3}) is the FeAl powder density calculated as follows: a known mass of powder is introduced into a 25ml flask and is filled with a high wettable liquid with a known density, here ciclohexanone.

(2) $\rho = \dfrac{m_p}{\left(25 - \dfrac{m_T - m_p}{\rho_{liq}}\right)}$

where m_p is the mass powder introduced, m_T is the total mass (powder+ciclohexanone) and ρ_{Liq} is the ciclohexanone density at working temperature.

This methodology for calculating the density has been considered a much better approximation to the real value of the material than vibrated and tap densities referenced according to ASTM B-212 and ASTM B-527 respectively. Although it is evident that both coatings do not have the same density, powder density has just been used as approximation.

Erosion tests

The erosion tests have been performed at room temperature using a grit blasting apparatus. The Al_2O_3 abrasive particles whose average size is about 50 microns leave the nozzle at the velocity of 1 g/min controlled by selecting the air pressure at 10 psi (regularly checked by weighting the alumina collected for 1min). The nozzle tube was 1.5 mm inner diameter and 50 mm long.

The sample's dimensions were 20 x 20 x 5 mm and before testing, they were polished down to 1 micron. The distance from the specimens surface to nozzle end was 10 ± 1 mm and the angle between the nozzle axis and the specimens surface was 90º. The mass loss was obtained by weighting on an analytical precision balance every 30 seconds and the test was stopped when the substrate was reached.

The average erosion value of the coatings was calculated by dividing erosion rate (g min^{-1}) by the abrasive flow rate. It is then normally divided by the specimen density (powder density, g cm^{-3}) and the average value is then reported as mm^{3}g^{-1}.

Dry sliding behaviour

Friction tests were carried out with a ball-on-disc system according to ASTM G99-03 , where an 11 mm diameter WC-6Co ball was frictioning the polished coating surface (below 0.8 Ra). A temperature around 25 ºC and the humidity (below 20%) were controlled during the test time into the closed camera where the experiments were performed. A sliding speed of 0,11 m/s, track diameter of 16 mm and sliding distance of 1000 m were constant for all the tests. The variation of friction coefficient with sliding distance was registered at 5 N for the FeAl coatings and a comparison with the wear behaviour of the steel substrate and the thermal treated sample is given. According to the standard, the friction coefficient (FC) is given as the average of the values obtained for the last 200 m.

The volume loss was obtained by means of white light interferometry (SWLI). The interferometric surface analysis microscope (Zygo New View 100) uses SWLI to image and measure tested surfaces and provide surface analysis without contacting it. Depths up to 100 micrometers, with 0.1 nanometer resolution and 0.3 nanometer RMS repetability are imaged independently of the objective magnification; lateral resolution is 500nm. SWLI is a technique based on the constructive or destructive interferences of two light beams, one going to a reference and the other to the sample, which leads to the obtention of a 3D image with the profile of the wear track.

The wear rate K ($mm^3 N^{-1} m^{-1}$) is calculated as:

(3) $K = \dfrac{V}{w \cdot s}$, where V is the worn volume, w (N) is the normal load and s (m) is the total distance.

The as-sprayed coatings were characterized by Scanning Electron Microscopy (SEM) and microhardness indentation. The worn surfaces were also examined using SEM-EDS.

3   Results and discussion

3.1   Coating deposition and characterization

Figure 2a and b shows the XRD and SEM morphology of the powder. X-ray presents the typical fundamental lines of the FeAl pattern (h+k+l=even), being only exhibitted when the structure is disordered as, otherwise, the superlattice lines (h+k+l=odd) would also appear; this was already foreseen as result of the high plastic deformation induced by ball-milling. It is even worth noting that the peak broadening comes from the finer grain size and microstrain introduced during milling. By contrast, when the powder is annealed, the X-ray presents the superlattice peaks conserving a slight broadening, which means that after the annealing treatment, the structure has been partly reordered having some nanocrystalline areas that might result from a recrystallization process or some remaining original zones (Fig. 2b).

Using different particle distributions, a great difference was observed on the resulting microstructures (Fig. 3a and b). Whereas MEC40-60 mainly consists of partially melted particles with some porosity and an oxide layer at the interparticle zones, CEA is well featured by partially and fully melted particles with some light and dark-grey contrasts at the intersplats boundaries. These have been characterized as iron-rich and oxide zones by EDS respectively; the presence of Al-depleted regions suggest that during spraying, oxidation has occurred to the powder to form the Al-rich spinel $FeAl_2O_4$ oxide leaving Fe-rich areas at the lamellar boundaries. XRD also confirms the former results (Fig. 4); the additional peaks also identified as FeAl correspond to the superlattice lines; some authors have attributed their presence to the ordering within the melted areas [33]. The difference in both microstructures can be easily observed also by the examination of the fracture sections, (Fig. 5 and Fig. 6). Figure 5 illustrates the CEA coatings being built up by melted splats aggregation, while figure 6a and b do not exhibit such morphology and one can see two features: one, where a particle has been torn off, and the other where the particle still remains in

that part of the coating. Coating thicknesses, as well as porosity and oxide contents, are presented in table 2; they point out the difference between the two coatings and the features that have been discussed. MEC40-60$_{ANN}$ is not illustrated here as it shows an analogous structure as MEC40-60.

By contrast, oxidized CEA presents a microstructure as shown in figure 7a, where it can be seen that a very thin layer has been formed on the top. Although not being pure alumina as commonly found for bulks, the oxide characteristics are good enough to provide a good corrosion resistance; otherwise an easy oxygen inward diffusion would have produced an increase in oxidation kinetics. Such good performance has been associated to the presence of Al$_2$O$_3$ nuclei among the Fe$_2$O$_3$ nodules that prevent their growth. The X-ray spectrum indicates the presence of the before mentioned phases [10] (Fig. 8b).

Regarding the microhardness values (table 3), it can be seen that despite having different porosity levels, the overall presence of oxidation in CEA produces an increase in hardness as well as an embrittlement compared to MEC40-60. In addition, it might be associated to the higher occurrence of intersplat boundaries; in CEA, the indentation has more probabilities to include representative features of the overall coating structure while in MEC40-60, the indentation might be performed inside an unmelted particle.

The comparison between the hardness values of MEC40-60 and MEC40-60$_{ANN}$ can be discussed as follows: as a consequence of not having the stoichiometric 50:50 FeAl and even more, having a milled strained structure, the lattice must present constitutional defects; according to Jordan and Deevi [34], vacancy hardening can ameliorate hardness and strength of iron aluminides but is detrimental to room temperature ductility. Although the cooling rate during the deposition process might also have a considerable influence on the vacancy concentration [35, 36, 37], the main difference between the two coating structures is the fact that annealing the feedstock powder might have eliminated most of the defects produced by milling and has ordered the lattice; therefore, from this point of view, there has been a strain release and the logical conclusion would be that lowering vacancy defects should lead to a less hard deposit. Nevertheless, the reason why this does not occur must find answer assuming that some oxidation might have occurred during the annealing process even though it was carried out in argon atmosphere as some powder particles seemed to have a different colour tonality.

Furthermore, with regard to CEATT, looking at the standard deviation, HV differences between CEA and CEATT are not really significant.

3.2   Abrasive tests

The present work examines a three-body abrasive wear, where silica particles are introduced and flow by gravity between the two surfaces (rubber rotating wheel and the as-sprayed coating). This kind of wear involves plastic deformation whenever the coating hardness is lower than H$_a$/1.2, where H$_a$ is the hardness of silica particles; otherwise, the abrasive particles would smash [38]. In the case of all studied coatings H$_a$/H$_c$>1.2 (hard abrassion) was observed to cause plastic scratching.

In a previous study, the abrasive behavior was already discussed for the as-called CEA coating [31]. Compared to the others, CEA exhibits the highest abrasive wear resistance, which is assumed to be due to its highest hardness (table 4). Hence, the harder the coating is, the less damage is produced by abrasive silica particles as a harder coating reduces wear by preventing ploughing on both a macro and micro-scale. Abrasive wear has also been found to be dependent on crystal structure and orientation; Alison showed

that cubic metals wear at about twice the rate of hexagonal metals, which was attributed to the lower work-hardening rate of the hexagonal metals. This reasoning serves also to discuss that the ordered FeAl lattice (MEC40-60$_{ANN}$) is less work-hardened than the disordered structure (MEC40-60).

The rapid initial decrease of weight in the oxidized CEA is attributed to removal of the oxide surface layer; figure 8 shows a comparison of both damaged surfaces, that of the as-sprayed CEA and the oxidized one; the as-sprayed coating shows the grooves the hard silica particles have produced during the test (Fig. 8a), whereas the oxidized coating shows the cracks produced on the oxide scale (Fig. 8b). This is not quite enough homogeneous to protect the coating against ploughing. Moreover, the fractured oxide debris can produce a more aggressive three-body abrasive effect.

The additions of hard particles such as TiC or TiB$_2$ in a Fe$_3$Al or FeAl matrix have been shown to reduce the wear rate by an order of magnitude. Such improvement has been also claimed by some authors [39, 40] who focused on the comparison of the use of this intermetallic instead of usual Co as matrix. Interestingly, they stated that WC-40%FeAl exhibits similar wear resistance to that of commercial WC-10%Co. Particularly, FeAl ordered matrix is attractive for wear resistance in high temperature environments.

However, there is not an extensive study on the abrasion resistance of thermally sprayed FeAl coatings and even in the case of their comparison to other deposited materials, the conditions they have been tested with, are not always comparable.

What can be actually compared are the present results with that of other materials tested with the same equipment and following the same standard. NiCr-based coatings exhibit wear rates of the same magnitude as MEC40-60, whereas CEA and CEATT are one order of magnitude lower because of the higher hardness [41]. WC-12Co for instance, showed a wear rate in the order of 10^{-6} mm^3 N^{-1} m^{-1} [42].

3.3   Erosion behaviour

With regard to test variables, in abrasive wear, the amount of material removed depends on the normal load pressing the particles against the surface and on the distance slid. In erosion however, the extent of damage mainly depends on the number and mass of individual particles striking the surface, and on their impact velocity. As in the case of abrasion, mechanisms by which a metallic material is removed, can involve both plastic deformation and brittle fracture; they can either depend on erodent particle sizes, velocities, impact angles or environments. Hence, if plastic deformation dominates, the maximum wear occurs at at low angles ("ductile behaviour"), while at high impact angles erosion by brittle fracture is more rapid ("brittle behaviour"). Striking at low angles with rounded particles normally yields to surface ploughing, whereas using angular particles produces cutting [43]. At 90º, the damage normally occurs by cracking and chipping of surface material; in the case of coatings, this is favoured by low strength of inter-lamella.

Figure 9 shows one of the damaged surfaces, which is clearly associated to the eroding effect of angular shaped particles where the material is displaced forming rims or lips. It is worth noting that such a mechanism, known as *cutting*, is normally encountered in ductile mechanisms (more attributed for metals at low impingement angles). However, the angular dependence of erosion is not a characteristic of the material alone, but depends also on the conditions of erosion. Thus, there can be alloys that erode in a

"brittle behaviour", that is, alloys of high hardness and low ductilities that show their maximum erosion rates at normal incidence. The terms "brittle" and "ductile" in erosion context must be then used with caution [43]. Wang et al. [19, 44] also claimed that; in their results the eroded surfaces also appear to result from a ductile mechanism. Few studies report their results on erosion performance of FeAl coatings; nevertheless, those carried out on NiAl intermetallics also support the former evaluation [45, 19]. The addition of ceria has shown to ameliorate significantly the erosion resistance [44].

Table 5 shows the wear rates having MEC40-60 slightly higher erosion resistance than CEA. This cannot be understood from the reasoning of hardness material as in abrasive wear. There is normally an inverse relationship between wear and hardness. In the most simple way, assuming a single particle striking the surface with mass (m), the work done by the retarding force will be equal to the initial kinetic energy of the particle (v_0), resulting in a final indentation volume (V) [43]:

$$\text{(4)} \qquad V = \frac{mv_0^2}{2H}$$

Even more complex theoretical models predict that erosion rates mainly involving plastic deformation should be inversely proportional to the hardness of the material. However, when using H in the equations, the fact that the material at the worn surface will have been strain-hardened by plastic flow is ignored, and that its hardness will generally be greater than that of the unstrained material; therefore, better correlation would be found between wear resistance and the hardness of the worn surface. It could be found then that as result of the different microstructures, the material is more or less strain hardened [43]. It might be also said that the cohesion between splats in the CEA specimen is not as high as in MEC40-60, maybe because of the presence of much more porosity and oxide embrittlement. It can be compared with difficulty to other investigations because of the different parameters set chosen in each study.

Before choosing the ones established in the present work, there were tested those corresponding to G76-04 ASTM standard but they were discarded for being so aggressive for the coatings.

3.4   Dry sliding behaviour

Figure 10 shows the variation of friction coefficient versus sliding distance at a normal load of 5N for the steel substrate and the different coating systems as well. While the FC of the non-coated sample increases continuously during the entire test, the FC of the CEA coating shows the following trend: in the early minutes, there is a sharp increase and then it rapidly reaches a steady state at about 0.7, which persists during the rest of the test. However, the oxidised sample exhibits a different behaviour slightly increasing during the whole test and showing some fluctuations at the end. MEC40-60 and MEC40-$_{60ANN}$ show, by contrast, surprisingly much lower friction coefficient. A common trace of all these plots is the initial raise, which is associated to the high adhesive contact between the WC-Co counterpart material and the coating material; the slight decrease afterwards may be caused by the hardening effect under the compressive stress the material undergoes.

In the case of similar microstructures but different hardness, lower friction coefficients would have been achieved with the hardest coating. Lower friction indicates that lower shear has taken place and therefore, contact area is much smaller. This can be explained by the examination of the wear tracks.

Figures 11, 12 and 13 show the common features of damaged coatings and table 6 gives the magnitudes of their respective widths as well as the volume loss and the calculated wear rates. SWLI had not enough resolution to detect MEC40-60 track's depth.

The magnification in figure 11 shows the plate-like debris on the worn CEA surface consisting of ploughed portions caused by adhesive mechanism and posterior delamination. EDS analysis indicated that oxidation takes place on the fresh coating when the ball slides over the deposit (Fig. 11b). Such oxidation may be explained by the temperature rise during friction contact. Moreover, the debris observed in the laterals of the wear track could also play some role on constraining laterally and making easier the deformation of the central layer. The debris also entrapped between the two surfaces could have also caused more severe damage in CEA.

Friction coefficients are calculated as an average value of the last 200m. Although there is a fluctuation for CEA TT and steel substrate, according to the standard, these would then result in 0.50_6 and 0.59_1 respectively. In the other cases, that value is more reliable as a uniform stage is reached.

Unlike CEA, which shows delamination as also reported by other authors [46], the as-thermally treated and MEC40-60 exhibit completely different wear mechanisms. Figure 12 corresponds to the wear track of the oxidized sample which is covered by an oxide layer of several microns as shown in the cross section in figure 12b (this is the reason why volume increment is expressed as a positive value, because it is above the surface plane). The thin and brittle layer corresponds to alumina as demonstrated by EDS. It could be thought that it could have a lubricant role as well as the oxidation debris in CEA, but it seems that the continuous break-away of such oxide layer, being alternatively formed and detached from the fresh coating, produces the non-uniformity in the friction coefficient. Xia et al. [47] claimed that a uniform FC value was maintained in their oxidized samples along the whole test. Nevertheless, as they underwent the study in compacted FeAl grade 3 specimens, the wear mechanism was not the same as that of a coating such as CEA. FC graphics are more similar to MEC40-60 because that had a microstructure similar to a bulk sintered material.

Sliding behaviour has also been evaluated by Xu et al. [13, 14] with FeAl HVAF (High Velocity Air Fuel) coatings, which exhibited a microstructure similar to that of CEA with melted particles and oxidation in the interlamellas. After performing pin-on discs at 3, 5 and 7N, they concluded that when load is increased, friction leads to lower FC owing to the presence of a similar oxide film as that encountered in CEA. However, what these authors did not try was to change spraying conditions in order to ameliorate wear response. In the present study, the MEC40-60 coating significantly shows an improvement. MEC40-60 possessed the lowest friction coefficient, no delamination was found but the wear track was identified by some remaining oxidation at both sides (Fig. 13). Splat delamination observed in CEA is commonly associated to the weak bonding between lamellas. Also, porous, oxides-sprayed material interfaces and other imperfections behave as stress concentrators that serve as trigger factors to yield crack initiation. Therefore, it is difficult to predict how a thermal sprayed deposit will behave at friction dynamic contact and often complex simulations are needed; only hypothesis can be made depending on the microstructure obtained. Hence, the absence of these many defects in MEC40-60 is the key for improvement. Here, the annealing treatment of the powder seems not to have a strong influence on the friction behaviour,

indicating that the wear mechanism is more influenced by the microstructure rather than the hardness of the material itself.

As already discussed in terms of erosive and abrasive behaviour, friction has also been compared with other HVOF-coating materials tested under the same conditions. Thus, when volume loss is compared (mm^3 normalized for the whole perimeter) with a cermet WC-metal coating, the damage produced in CEA is as high as two order of magnitudes more [16, 18]. More similar friction coefficients were obtained with NiCr based coatings [17].

4   Conclusions

The results of the present work can be summarised as follows:

- Two very different coatings were obtained from the same powders just modifying the particle size for spraying. This resulted in different microstructures: CEA is dominated by almost fully melted particles surrounded by iron rich and oxide phases, while MEC40-60 is similar to a bulk material where particles have been compacted.

- Different hardness coatings yield to different abrasive wear rates, where CEA showed the higher abrasive resistance.

- The difference between MEC40-60 and MEC40-60$_{ANN}$ hardness has been associated to the internal oxides rather than to the lower vacancy defects produced during annealing the powder. Both, milling conditions from the as-atomized powder and quenching effect produced during the spraying process, have been identical for both powders; thus, knowing that stress release would reduce hardness, oxidation during the annealing treatment must have been enhanced the hardness.

- Erosion tests demonstrated that iron aluminides possess a ductile behaviour even when the impingement angle is 90º, which is normally usual of brittle mechanisms.

- Ball on disc tests were analysed in terms of different microstructures and it was stated that CEA was worn by delamination, whereas MEC40-60 almost does not suffer any damage. The first one exhibits FC more than three times higher than the second one.

- Oxidation of the coating was unfavourable for its wear properties. The formation of the alumina layer when frictioning would have displayed a good role if it would not have been so brittle that its fracture left fresh coating areas ready to be damaged further.

- A good goal of this work has been the idea of previously annealing the powder; MEC40-60$_{ANN}$ shows an analogous microstructure as that of MEC40-60 but higher hardness and abrasion resistance while maintaining the same friction coefficient trend.

FIGURES
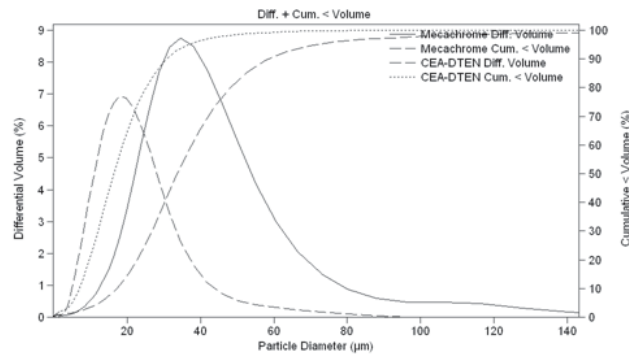
Fig 1. Powder size distribution
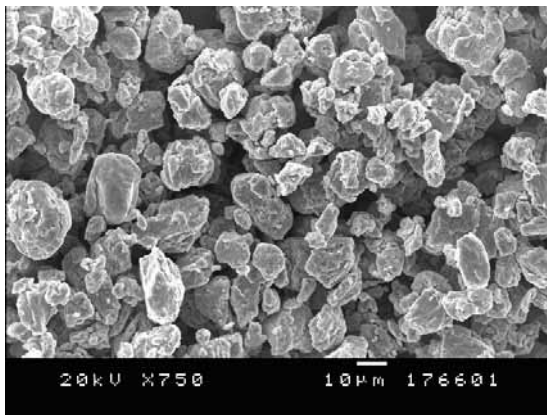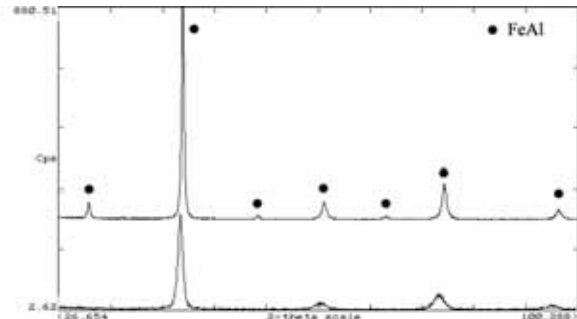
a   b

Fig 2. (a) Morphology and (b) X-ray of the iron aluminide powder grade 3 as-supplied and annealed at 700ºC.
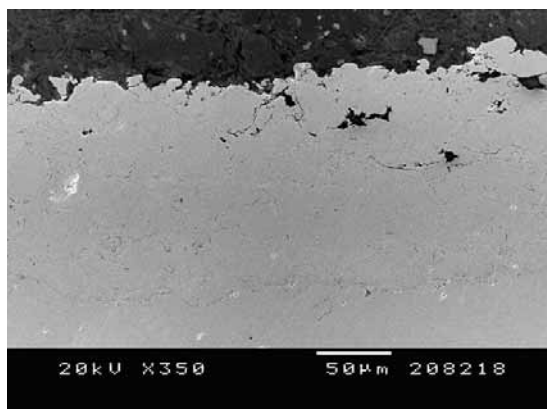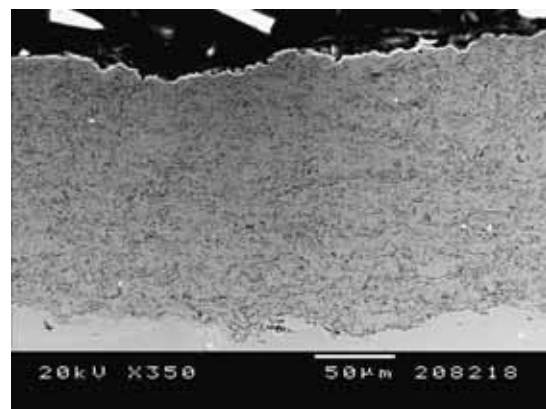
a   b

Fig 3. SEM cross sections of (a) MEC40-60 and (b) CEA.

a   b
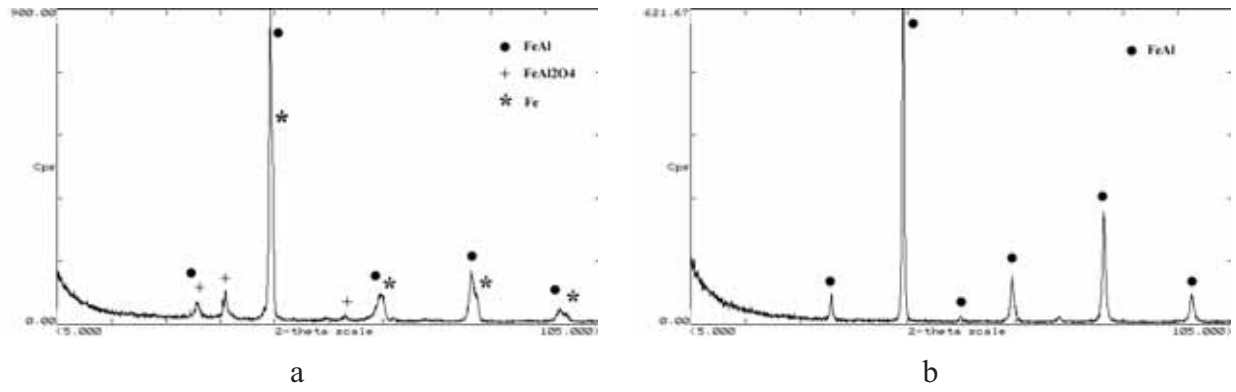
Fig 4. XRD of (a) CEA and (b) MEC40-60 coatings respectively
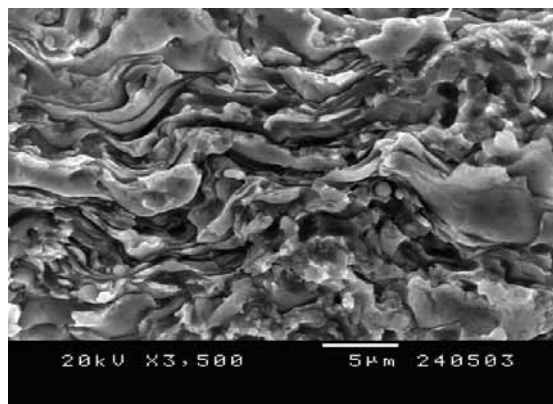
Fig 5. Fracture section of the CEA coating
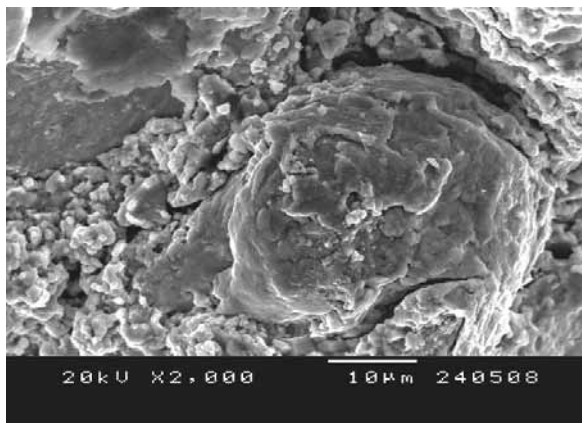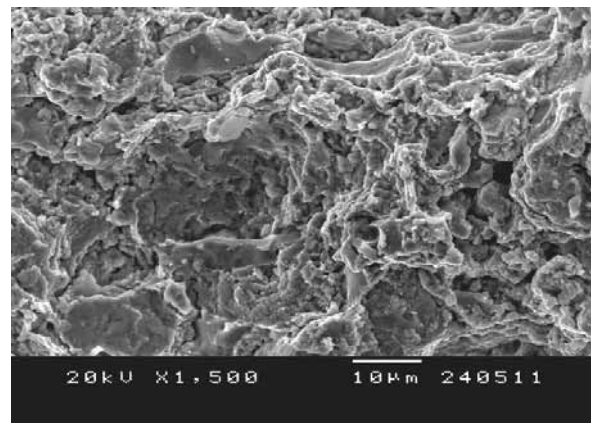
a   b

Fig 6. (a) and (b) Different zones of the fracture section of the MEC40-60 section
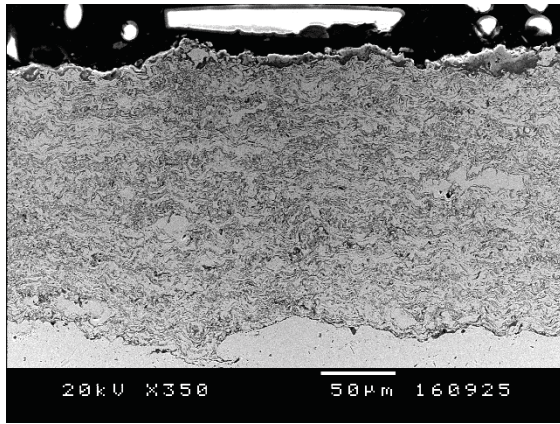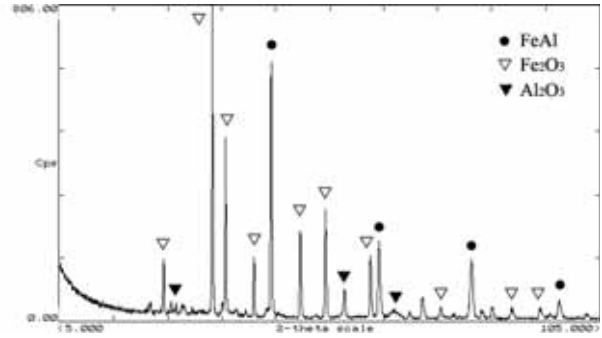
a   b

Fig 7. (a) SEM cross section and (b) X-ray of CEATT.
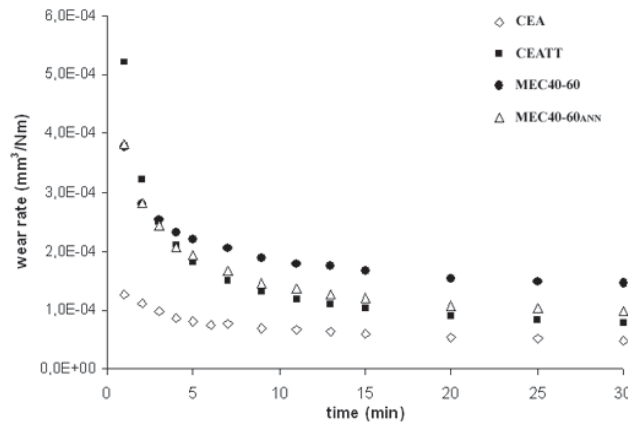
Fig 8. Mass loss (g/min) vs time.
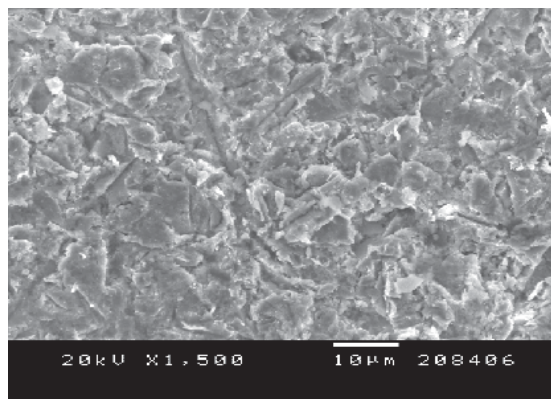
Fig 9. Typical erosion surface morphology
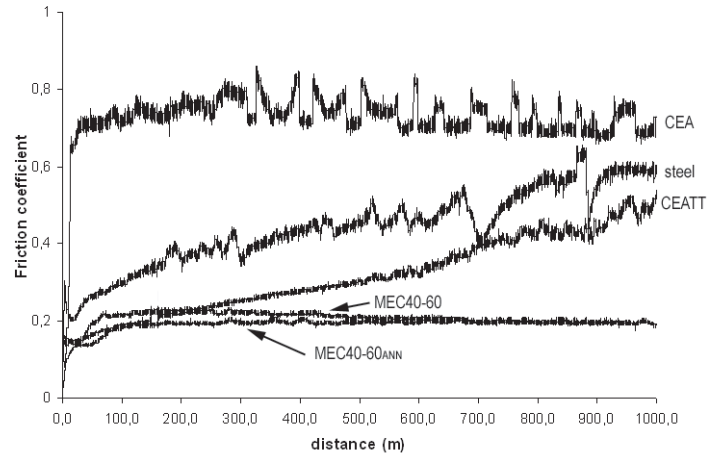
Fig 10. Friction coefficient vs sliding distance.
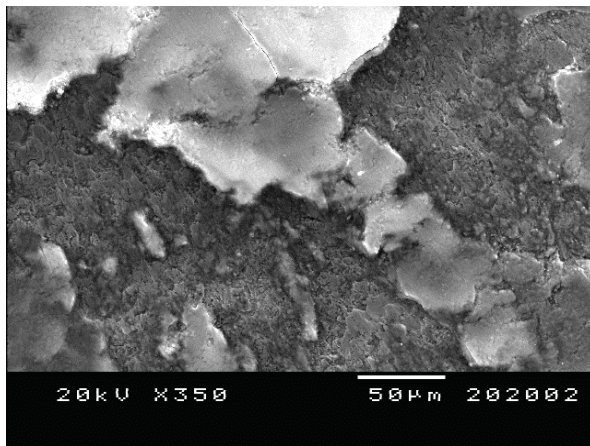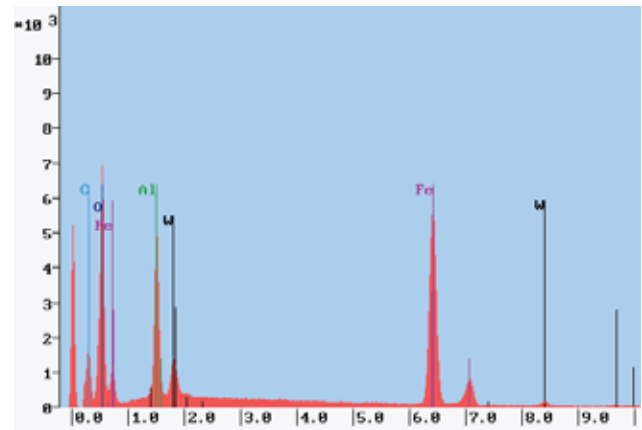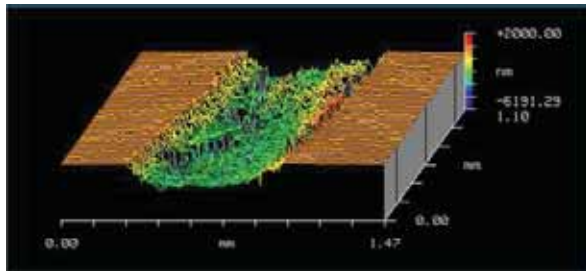
Fig 11. (a) Wear debris after the ball-on-disk test on the CEA sample, (b) EDS analysis on the plate-like debris and (c) wear track profile.

a   b
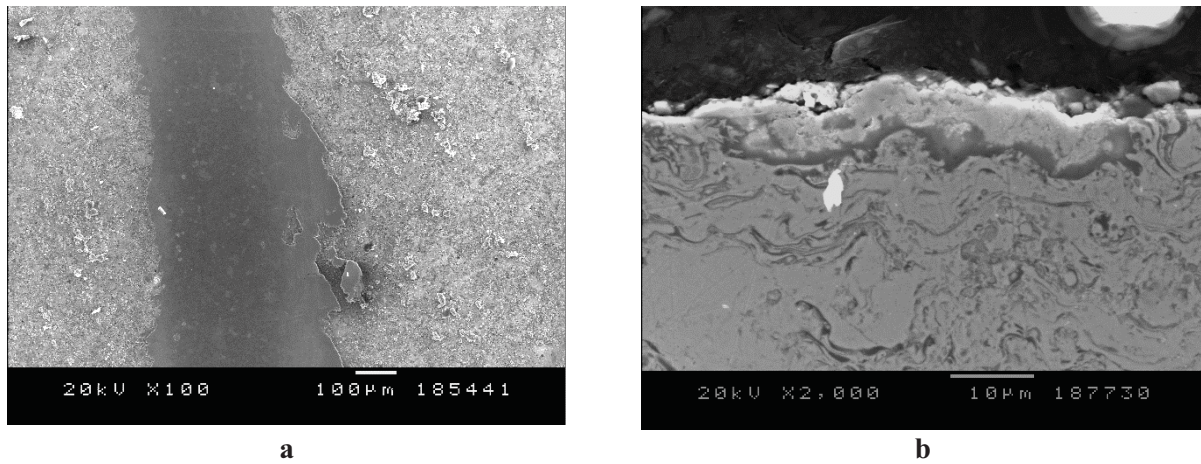
Fig 12. (a) Wear track observed on the oxidized CEA coating, (b) cross section of the oxide layer formed after the sliding test.
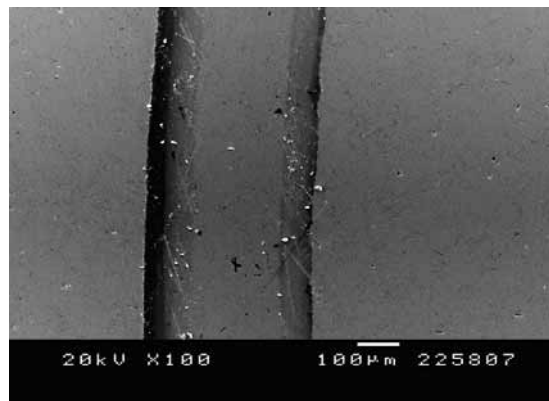
Fig 13. Wear track of the MEC40-60 coating.

TABLES

Table 1. Thermal spraying parameters.

	FeAl
Oxygen flow rate (l/min)	189
Propylene flow rate (l/min)	87
Carrier gas (l/min)	305
Oxygen/fuel ratio	2.874
Feeding rate (g/min)	20
Spraying distance (mm)	250

Table 2. Coating features.

	Thickness	% oxidation	% porosity
CEA	162 ± 6	13.4 ± 2.6	1.8 ± 0.1
MEC40-60	147 ± 9	4.4 ± 0.6	0.3 ± 0.1

Table 3. Microhardness of intermetallic FeAl coatings

	HV_{200}
CEA	434 ± 48
CEATT	426 ± 23
MEC40-60	377 ± 36
MEC40-60$_{ANN}$	415 ± 21

*Thermally treated CEA coating

Table 4. Abrassive wear rates

	Wear rate (mm^3 N^{-1} m^{-1})
CEA	$3.7 \ 10^{-5}$
CEATT	$5.2 \ 10^{-5}$
MEC40-60	$1.2 \ 10^{-4}$
MEC40-60$_{ANN}$	$6.7 \ 10^{-5}$

Table 5. Wear rates of the eroded surfaces

	CEA	MEC40-60
Wear rate mm^3 g^{-1}	$2.42 \ 10^{-4}$	$2.09 \ 10^{-4}$

Table 6. Wear track features.

	CEA	CEATT	MEC40-60	MEC40-60$_{ANN}$
Friction Coefficient	0.706	0.506	0.192	0.190
Track width (μm)	579 ± 8	361 ± 15	377 ± 26	375 ± 20
ΔV (mm^3)	$- 3.3 \ 10^{-2}$	$+ 1.6 \ 10^{-2}$	-	-
Wear rate (mm^3/Nm)	$5.9 \ 10^{-6}$	$3.6 \ 10^{-6}$	-	-

References

[1]   Westbrook J. H., Applications of Intermetallic Compounds, *MRS Bulletin*, 1996, 21 (5), p. 26-28.

[2]   Savolainen K., Mononen J., Ilola R., Hänninen H., Materials selection for high temperature applications, Helsinki University of Technology.

[3]   Tanaka R., Research and development of ultra-high temperature materials in Japan, *Materials at high temperatures*, 2000, 17, p. 457-464.

[4]   Adeva P., Materiales alternativos de las superaleaciones: compuestos intermetálicos. Revista de la Asociación Española de Científicos, 1999, 1, p. 1-6.

[5]   Deevi S. C., Sikka V. K., Nickel and iron aluminides: an overview on properties, processing, and applications, *Intermetallics*, 1996, 4, p. 357-375.

[6]   Liu C. T., Stiegler J. O., Ordered Intermetallics. Properties and selection: nonferrous alloys and special purpose materials. Tenth Edition, Metals Handbook. ASM International., 1990.

[7]   Skoglund H., Knutson M., Karlsson B., Processing of fine-grained mechanically alloyed FeAl, *Intermetallics*, 12, 2004, p. 977-983.

[8]   Deevi S. C., Sikka V. K., Liu C. T., Processing, properties and applications of nickel and iron aluminides, *Progress in Mater Sci*, 1997, 42, p. 177-192.

[9]   Liu C. T., George E. P, Maziasz P. J., Scneibel J. H., Recent advances in B2 iron aluminide alloys: deformation, fracture and alloy design, *Mater Sci Eng A*, 1998, 258, p. 84-98.

[10]   Guilemany J. M., Cinca N., Dosta S., Lima C.R.C, High temperature corrosion of Fe-40Al coatings, *Intermetallics*, 2007, 15, p. 1384-1394.

[11]   Liu C. T., Stiegler J. O.. Ordered Intermetallics. Properties and selection: nonferrous alloys and special purpose materials. Metals Handbook. ASM International. Tenth Edition (1990).

[12]   Sauthoff, State of intermetallics development, *Mater and Corr*, 1996, 47, p. 589-594.

[13]   Xu B., Zhu Z., Zhang W., Ma S., The microstructure and high-temperature sliding wear behavior of Fe-Al coating produced by high Velocity Arc Spraying. *Thermal Spray 2004: Advances in Technology and Application*, ASM International, May 10-12, 2004 (Osaka, Japan), ASM International, 2004, 1129 pp.

[14]   Xu B., Zhu Z., Ma S., Zhang W., Liu W., Sliding wear behavior of Fe-Al and Fe-Al/WC coatings prepared by high velocity arc spraying, *Wear,* 2004, 257, p. 1089-1095.

[15]   Hawk J. A., Alman D. E., Abrasive wear of intermetallic-based alloys and composites, *Mater Sci and Eng A*, 1997, 239-240, p. 899-906.

[16]   Shi-ning M., Jun-zhi H., Xue-rong C., Chang-qing L, Qian L., Hai J., Erosion resistance of arc spray composite coatings at high temperature on boiler tubes of pulverixed coal fired power station, *Thermal Spray 2003: Advancing the Science and Applying the Technology*, B.R. Marple and C. Moreau, Ed., May 5-8, 2003 (Orlando, FL), ASM International, 2003, Vol. 1: 845 pp; Vol. 2, 864 pp.

[17]   Alman D. E., Hawk J. A., Tylczak J. H., Dogan C. P., Wilson R. D., Wear of iron-aluminide intermetallic alloys and composites by hard particles, *Wear,* 2001, 251, p. 875-884.

[18]   Wang B., Lee S. W., Erosion-corrosion behaviour of HVOF NiAl-Al_2O_3 intermetallic-ceramic coating, *Wear* , 2000, 239, p. 83-90.

[19]   Wang Y., Yan M., The effect of CeO_2 on the erosion and abrasive wear of thermal sprayed FeAl intermetallic alloy coatings, *Wear*, 2006, 11-12, p 1201-1207.

[20]   Hearley J. A., Little J. A., Sturgeon A.J., The erosion behaviour of NiAl intermetallic coatings produced by high velocity oxy-fuel thermal spraying, *Wear,* 1999, 233-235, p. 328-333.

[21]   Varin R. A.. "Intermetallics: Crystal Structures". Encyclopedia of Materials: Science and Technology. K.H.J. Buschow Ed., 1st. Ed., Elsevier Science Publ. Co., 2001, 9913 pp.

[22]   Boufenghour M., Hayoune A., Hamana D., Study of the ordered structures in Fe-Al alloys using dilatometric and calorimetric analysis. *Journal of Materials Science*, 2004, 39 p. 1207-1212.

[23]   Suriñach S., Amils X., Gialanella S., Lutterotti L. Baro M. D., Kinetics of reordering in a nanograined FeAl alloy, *Materials science forum,* 1997, 235-238, p 415-420.

[24]   http://www.mecachrome.com/

[25]   Muller D. A., Subramanian S., Batson P. E., Silcox J., Sass S. L., Structure, chemistry and bonding at grain boundaries in Ni_3Al-I. The role of boron in ductilizing grain boundaries, *Acta mater.*, 1996, 44, 4, p. 1637-1645.

[26]   Rico M. M., Greneche J. M., Perez G. A., Effect of boron on structural and magnetic properties of the $Fe_{60}Al_{40}$ system prepared by mechanical alloying, *Journal of Alloys and Compounds,* 2005, 398, p. 26-32.

[27]   Muller D. A., Subramanian S., P. Batson E., Silcox J., Sass S. L., Structure, chemistry and bonding at grain boundaries in Ni_3Al-I. The role of boron in ductilizing grain boundaries, *Acta Mater* 1996, 44 , 4, p. 1637-1645.

[28]   Artz E., Behr R., Göhring E., Grahle P., Mason R. P., Dispersion strengthening of intermetallics, *Mater Sci Eng A* (1997) 234-236, p. 22-29.

[29]   Launois S., Fraczkiewicz A., Environmental effect on mechanical behavior of reinforced FeAl (40at%Al) alloy, *Journal de physique. IV*, 1996, 6 (2) p. C2.223-C2.228.

[30]   Grosdidier T., Ji G., Bernard F., Launois S., Synthesis of FeAl Hetero-Nanostructured Bulk Parts via Spark Plasma Sintering of Milled Powder, *MRS Bulletin* 2007.

[31]   Guilemany J. M., Cinca N., Lima C. R. C., Miguel J. R., Studies of Fe40Al coatings obtained by High Velocity Oxy-Fuel. *Surf & Coat Tech*, 2006, 201, p. 2072-2079.

[32]   Xia J., Li C. X., Dong H., Thermal oxidation treatment of B2 iron aluminide for improved wear resistance, *Wear* , 2005, 258, p. 1804-1812.

[33]   Gang J., Morniroli J., Grosidider T., Nanostructures in thermal spray coatings, *Scripta mater*, 2003, 48, p. 1599-1604.

[34]   Jordan J. L., Deevi S. C., Vacancy formation and effects in FeAl, *Intermetallics,* 2003, 11, p. 507-528.

[35]   Skoglund H., Knutson Wedel M., Karlsson B., Thermal vacancy hardening in Fe(100-x) Alx (28 < x < 40), *Intermetallics,* 2007 15, p. 1127-1131.

[36]   Kupka M., Can vacancies be the main reason of FeAl alloys hardening? *J Alloys Comp,* 2007, 437, p. 373-377.

[37]   Amils X., Nogués J., Suriñach S., Baro M.D., Muñoz-Morris M.A., Morris D.G., Hardening and softening of FeAl during milling and annealing, *Intermetallics,* 2000, 8, p. 805-813.

[38]   Holmberg K., Matthews A., Coatings tribology properties, techniques and applications in surface engineering, 1994, Elsevier Science Pub Co , 442 pp.

[39]   Mosbah A. Y., Wexler D., Calka A., Abrasive wear of WC-FeAl composites, *Wear,* 2005, 258, p. 1337-1341.

[40]   Ahmadian M., Wexler D., Chandra T., Calka A., Abrasive wear of WC-FeAl-B and WC-Ni3AL-B composites, *International Journal of Refractory Metals & Hard Materials,* 2005, 23, p. 155-159.

[41]   Guilemany J.M., Torrell M., Miguel J.R., Study of the HVOF Ni-Based Coatings Corrosion Resistance Applied on Municipal Solid-Waste Incinerators, Journal of Thermal Spray (2007) *online*.

[42]   Guilemany J.M., Dosta S., Miguel J.R. The enhancement of the properties of WC-Co HVOF coatings through the use of nanostructured and microstructured feedstock powders, *Surf & Coat Tech*, 2006, 201, p. 1180-1190.

[43]   Hutchings I. M., Tribology: Friction and Wear of engineering materials, Metallurgy and Materials Science Series, ISBN 0-340-56184-x.

[44]   Wang Y., Chen W., Wang L., Micro-indentation and erosion properties of thermal sprayed NiAl intermetallic-based alloy coatings, *Wear,* 2003, 254, p. 350-355.

[45]   Johnson B. J., Kennedy F. E., Baker I., Dry sliding wear of NiAl, *Wear,* 1996, 192, p. 241-247.

[46]   Prchlik L., Sampath S., Effect of the microstructure of thermally sprayed coatings on friction and wear response under lubricated and dry sliding conditions, *Wear*, 2007, 262, p. 11–23.

[47]   Xia J., Li C. X., Dong H., Thermal oxidation treatment of B2 iron aluminide for improved wear resistance, *Wear*, 2005, 258, p. 1804-1812.

The previous article however, just includes the results for the as-sprayed Fe40Al powder (CEA and MEC40-60) in order to avoid the complication with the addition of the as-sprayed cryomilled powder. Therefore, these are briefly presented in table 4.6. The friction behaviour is very similar to that of CEA, with slightly differences in the friction coefficient and the occurrence of an oxide layer (dark contrast in fig. 4.16a) that forms on the fresh coating (fig. 4.16b). Differently from CEA however, such oxide debris remains stuck instead of being moved to one side; as one can see in figure 4.17, the track profile is not good defined and this is the reason why the wear rate could not be calculated. The abrasion resistance is between those of CEA and MEC40-60 and, the erosion response is much more aggressive than the other two.

Table 4.6. Wear rates comparison for the iron aluminide coatings.

	Abrasion	Erosion	Friction		
	Wear rate $(mm^3\ N^{-1}\ m^{-1})$	Wear rate $(mm^3\ g^{-1})$	Friction Coefficient	Track width (μm)	Wear rate $(mm^3\ N^{-1}\ m^{-1})$
CEA	$3{,}7\ 10^{-5}$	$2{,}42\ 10^{-4}$	$0{,}70_6$	579 ± 8	$5{,}9\ 10^{-6}$
MEC40-60	$1{,}2\ 10^{-4}$	$2{,}09\ 10^{-4}$	$0{,}19_2$	377 ± 26	-
MEC40-60$_{ANN}$	$6.7\ 10^{-5}$	*	0.19_0	375 ± 20	-
Fe50Al (CRYO)	$9{,}9\ 10^{-5}$	$3{,}61\ 10^{-4}$	$0{,}67_5$	526 ± 38	**

*These erosion experiments have not been determined yet.
**It could not be measured
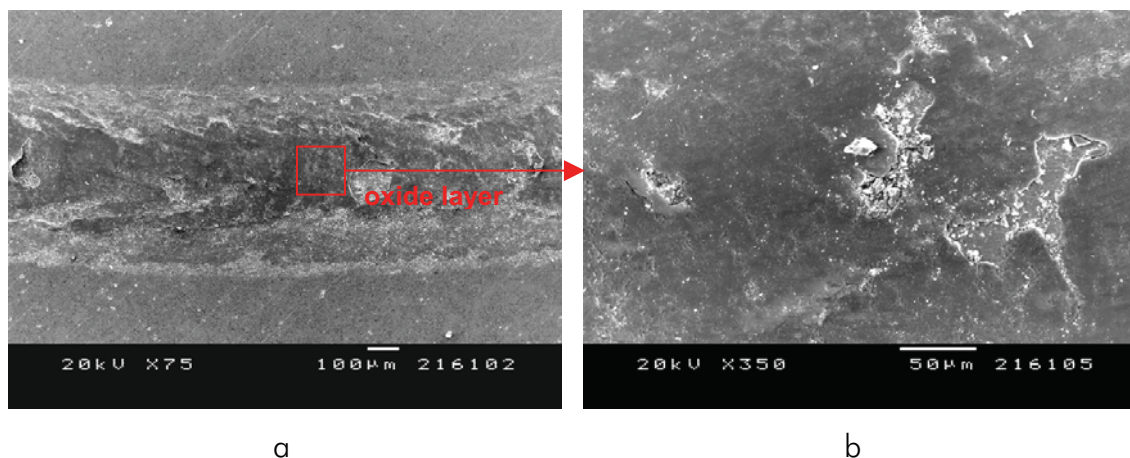
Figure 4.16. (a) General view and (b) details of the wear track of the CRYO coating.
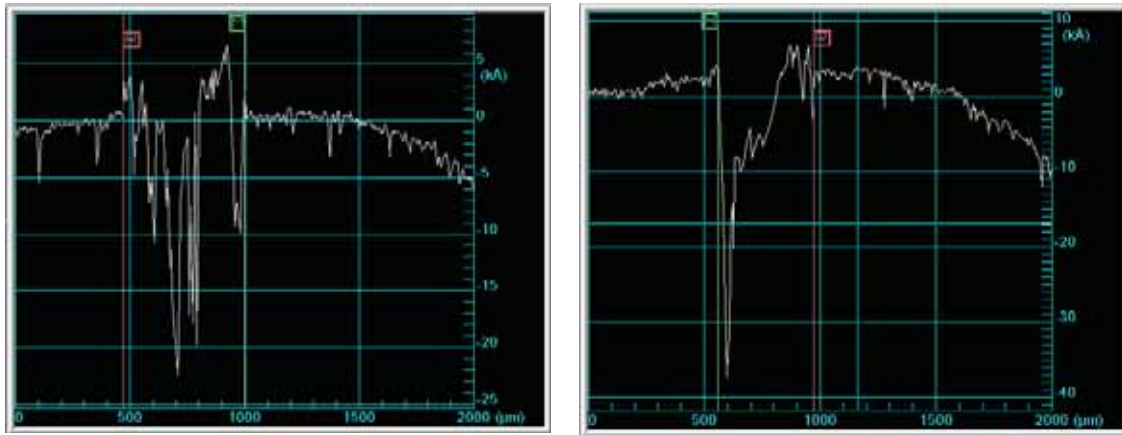
Figure 4.17. (a) and (b) Wear track profiles of the CRYO coating.

c)   Oxidation resistance in high temperature air environments

How iron aluminides perform at high temperatures is a subject of interest nowadays. As already presented in the first chapter, the large Al content in these compounds makes possible to form a protective alumina layer that prevents from further oxidation. Moreover, being used in their coating form allows the use of a more load-carrying capable substrate.

Isothermal high temperature tests were performed on the iron aluminide coatings at 900 and 1100°C for 72h. These two temperatures were chosen as it is in this range where alumina forming alloys change their oxidation behaviour: metastable alumina is usually formed in the earliest stages and progressively, by increasing the time or the temperature, the stable α-alumina forms detrimental to the metastable phase. It is known that bulk iron aluminides tend to oxidize with a parabolic kinetics, but in the present case, at 900°C, rather than a parabolic stage, after a rapid increase of Δm at very short times (about 8h), a saturation occurs (fig. 4.18). During the whole test, the weight gain is superior for the as-sprayed cryomilled powder, which evidences the larger presence of Fe-rich areas being easily oxidized. Moreover, it was found that CEA possessed the lower oxidation rate, whereas the curves of the two MEC40-60 series are close but above. All the curves are, however, below a 10% mass gain.
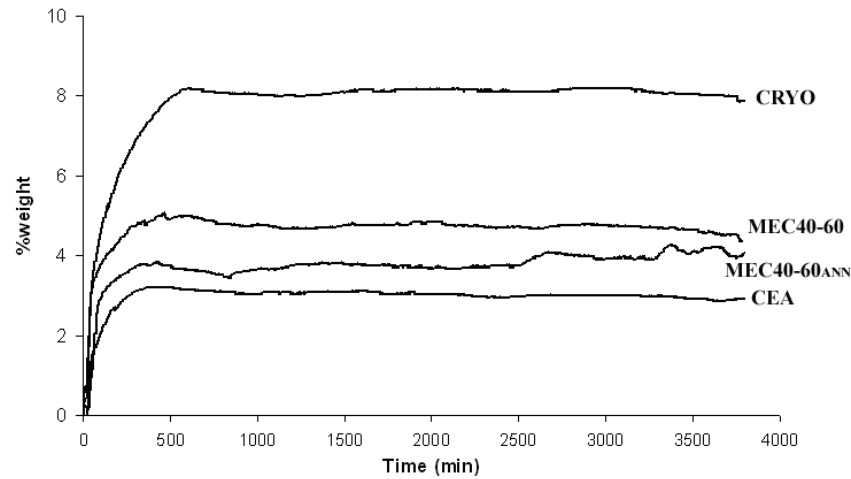
Figure 4.18. Weight gain vs time for the oxidation of the iron aluminide coatings a 900°C.
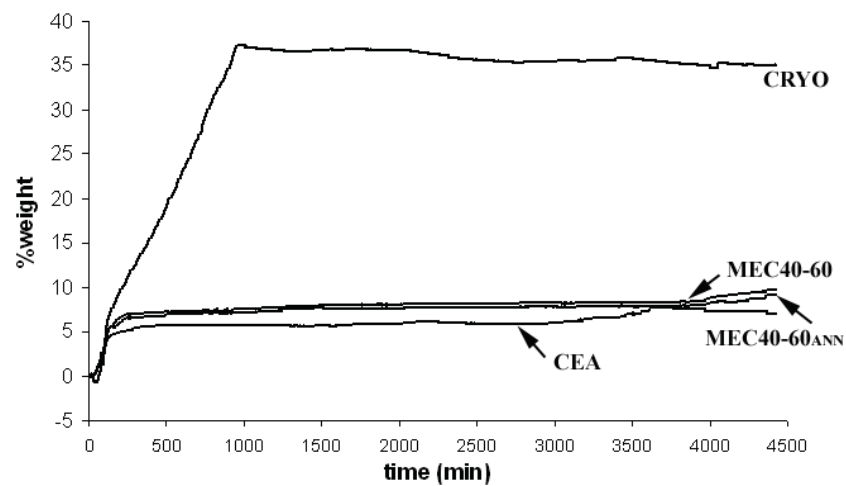
Figure 4.19. Weight gain vs time for the oxidation of the iron aluminide coatings a 1100°C.

At 1100°C (fig. 4.19), there is the same tendency, having the as-sprayed cryomilled powder the largest Δm. Its oxidation can be described in two stages: it is first oxidized linearly until the saturation is reached in a second step. The mass gain for the other three coatings is slightly higher compared to their behaviour at 900°C but still below 10%. Morphological changes during the oxidation of the CEA coating is explained in the following article:

<u>Paper 4:</u> J. M. Guilemany, N. Cinca, S. Dosta, C. R. C. Lima, High temperature corrosion of Fe-40Al coatings, *Intermetallics,* Vol. 15 (2007) pp. 1384-1394.

This paper concludes that a slow growing oxide film is formed during oxidation at 900ºC, thus indicating a reasonable good oxidation resistance; by contrast, at 1100ºC, the inward oxygen penetration takes place easily promoting a rapid degradation of the specimen when the substrate is reached. The better behaviour at 900ºC was presumably attributed to the presence of the high-temperature stable alumina phase formed among the iron oxide nodules and preventing their growth. The accelerated oxidation at 1100ºC is most likely produced by the mismatch of thermal expansion coefficients; a high concentration of thermal stresses promotes spallation and cracking.

High-temperature oxidation of Fe40Al coatings obtained by HVOF thermal spray

J.M. Guilemany [a], N. Cinca [a,*], S. Dosta [a], C.R.C. Lima [b]

[a] *Thermal Spray Centre (CPT), Dpt. Ciència dels Materials i Enginyeria Metal.lúrgica, Universitat de Barcelona, C/Martí i Franqués, 1. 08028 Barcelona, Spain*
[b] *Unimep − Methodist University of Piracicaba, College of Engineering, SP, Brazil*

Abstract

The objective of the present work is to provide insight into the high-temperature performance of iron aluminide intermetallic coatings, sprayed using high velocity oxygen fuel. Isothermal oxidation experiments were completed at 900, 1000 and 1100 °C and the cross sections and free surfaces of the coatings were characterized after 4, 36 and 72 h of exposure. The present results show differences in the oxidation behaviour of the coatings at those temperatures and they are specially remarkable when compared to bulk materials. For example, while at 1000 and 1100 °C where bulk FeAl presents a compact alumina layer, the coatings failed to reveal the presence of the stable α-Al_2O_3 phase, and an accelerated corrosion was observed leading to detachment from the substrate. On the basis of these results, the reasonable good performance exhibited at 900 °C indicates this could be the border line of the oxidation resistance for those coatings.
© 2007 Elsevier Ltd. All rights reserved.

1. Introduction

Intermetallic compounds are of interest to the materials science and engineering community as a result of their unique properties, which are generally ascribed to their long-range ordered crystal structures [1,2]. Such order is exhibited below a critical temperature (T_c), which is characteristic to each particular intermetallic compound. Some of these materials possess a T_c as high as their melting point, which allows them to maintain an ordered arrangement of the atoms and thus hinders diffusion processes at high temperatures; such characteristic has been used to rationalize their reported high thermal stability.

An extended group of intermetallics studied over the past years for structural applications is the aluminides, which primarily involve iron, nickel and titanium aluminides. Interest

in these materials has been stimulated by the possibility of using iron, nickel and titanium aluminides as high-temperature materials for substitution of superalloys since their high aluminium contents render them attractive for use in aggressive environments [3−10]. Unlike the chemical intermediate compounds which exist at fixed compositions, many aluminides are found to extend over a range of compositions, and the higher the deviation from stoichiometry, the lower the degree of order.

Motivated by the above considerations, the present work addresses the behaviour of the iron aluminide Fe40at%Al. The bcc-based B2 ordered phase exists in the range of 36−50 at% Al and has a T_c, which coincides with its melting point at 1250 °C. The properties of this compound include excellent oxidation, corrosion and sulphidation resistance, high electrical resistivity, reasonable strength from room temperature to about 500 °C and acceptable ductility at room temperature, partially dependent on environmental sensitivity. Inspection of the available literature shows that most papers published to date deal with approaches to improve the mechanical properties of

---

* Corresponding author. Tel./fax: +34 934021297.
  E-mail addresses: nuria.cinca@ub.edu, cpt-cmem@ub.edu (N. Cinca).
  URL: http://www.cptub.com/

FeAl, as well as its behaviour in hostile environments. In terms of mechanical properties, two approaches have been proposed to overcome the lack of ductility of polycrystalline intermetallics: one is the addition of alloying elements, such as boron and second, a reduction of grain size. In terms of the second approach, milling techniques have been considered as potential processing routes in order to create nanocrystalline structures [11]. Mechanical alloying is a highly energetic method of fabricating metal powders with a fine microstructure through fracturing and cold-welding mechanisms. In addition, milling allows the introduction of oxide particles as reinforcements. The introduction of dispersed Y_2O_3 particles via this powder metallurgy route is also relevant to the grain refinement objective mentioned above and also assess the iron aluminide performance in oxidising environments [12—14].

Although numerous published studies address the oxidation behaviour of bulk iron aluminides, few investigations have dealt with the use of this alloy in protective coatings [15,16]. Among the literature, the oxidation behaviour of other thermally sprayed Al-based intermediate compounds has been evaluated: NiAl [18] and MCrAlY [19—23]. High velocity oxygen fuel (HVOF) is a well-established thermal-spray technique that provides coatings with minimal porosity and low oxide content [24]. The heat source for particles melting comes from a combustion reaction. Many authors have also used this technique to spray iron aluminide powders based on investigations on the description of the microstructure and its relationship with some of their properties [15—17,25—34].

In view of the above discussion, the objective of the present study is to compare extended results reported by other authors concerning the oxidation behaviour of iron aluminide specimens, with as-deposited powders (Fe—40Al—0.05% Zr (at%) + 50 ppm B + 1 wt% Y_2O_3) by means of HVOF. To accomplish this, several isothermal tests at different times were carried out on the as-obtained deposits at 900, 1000 and 1100 °C. Resulting features in the cross sections and surface morphologies were characterized by scanning electron microscopy—energy dispersive spectroscopy (SEM—EDS) and X-ray diffraction (XRD).

2. Experimental procedure

The powder used in the present study is the FeAl Grade 3, provided by CEA (Grenoble); it is a prealloyed gas atomised powder with a nominal composition of Fe—40Al—0.05Zr (at%) and 50 ppm B. It was subsequently ball milled to introduce fine dispersed yttria particles and reduce the grain size [35]. The equipment used for the spraying process is a Diamond Jet Hybrid (DJH2700) from SULZER METCO. Coatings of 150 μm were obtained and the spraying parameters were modified to provide low temperatures and thus retain the nanostructure from the mechanically milled powder with minimal oxidation in the as-deposited coatings. For this purpose several gas flow rates were assessed for spraying as presented in Table 1. In addition, the samples were cooled with compressed air during the spraying process.

Table 1
Thermal spraying parameters

	Parameter set 1 (F1)	Parameter set 2 (F2)	Parameter set 3 (F3)
Oxygen flow rate, l min^{-1}	189	189	253
Carrier gas (air), l min^{-1}	385	305	305
Fuel (propylene), l min^{-1}	87	87	87
Spraying distance, mm	250		

Isothermal oxidation tests were performed for several as-sprayed powders deposited onto flat low-alloyed steel specimens. The edge was covered with cement so that the preferential interface substrate—coating oxidation is minimized. The tests were performed for 4, 36 and 72 h at 900, 1000 and 1100 °C in air atmosphere. Once each test was finished, the sample was air-cooled. No quantitative results about mass changes were determined due to the difficulty imposed by the presence of the cement; thus, only the results on the features and scales formation process have been reported.

The microstructural characterization of the feedstock powder as well as the initial and oxidised coatings were carried out by SEM using a JEOL 5510 microscope operating at 20 kV. The backscattered images were obtained with a ROBINSON detector. Qualitative microanalysis was performed by EDS with a RÖNTEC detector.

XRD was used to characterize the phases present and assess the degree of order in the feedstock powders and as-sprayed coatings. All X-ray measurements were done on a Bragg—Brentano $\theta/2\theta$ Siemens D-500 diffractometer with Cu Kα radiation.

3. Results

3.1. Microstructure and XRD prior to oxidation

Table 1 presents the detailed spraying conditions. Fig. 1 shows the respective cross section morphologies. The observed features, already characterized in a previous study [36], are the following: the main grey contrast phase was identified by EDS as FeAl, corresponding to the retained phase from the not fully melted particles; the lighter grey zones and dark areas correspond to Fe-rich and spinel phases, respectively. The iron-rich areas found between the splats are claimed to be Fe_3Al by other authors [38,40,41] and confirmed here by EDS; they result from the evaporation of Al during the particle residence in the flame. In the present study, the oxides formed among the splats appear to come from the particle flight rather than the typical oxidation formed after the deposition of each lamella. The porosity of such coatings is found to be about 1—3%.

Although the current investigation has not dealt with a nanoscale study to determine the yttria particles' size and distribution, Grosdidier et al. using the same feedstock powder could not evidence their presence neither in the unmelted nor the fully melted zones [27]. They associated such phenomenon with the fast heat up and the high degree of deformation in
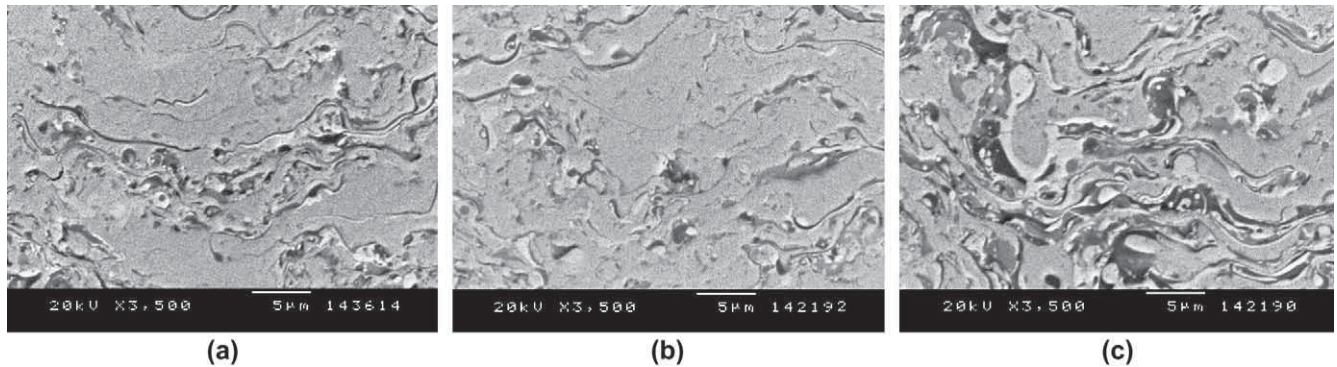
Fig. 1. Backscattered scanning electron micrographs of the coating cross section (a) F1, (b) F2 and (c) F3.

the unmelted areas, and the washing away effect of yttrium from the matrix in the melted areas. In more recent investigations, it still remains uncertain and only hypothesis can be made about it [33].

The microstructural observation indicates the different features present on the coatings depending on the oxygen/fuel ratios. F3, with the highest oxygen/propylene ratio (3.6), presents the highest oxidation content due to the most efficient combustion; thus, the enhanced heat transfer produces an increase of melted particles, which oxidize during flight and flattening. F1 and F2, with a smaller oxygen/propylene ratio compared to F3, imply lower oxygen flow that leads to partially melted particles, which form adherent coating layers less oxidised. The only difference between F1 and F2 is the carrier gas flow. The slightly higher oxygen flow in F1 would increase its oxide content. However, such variation is inappreciable in the microstructure.

Dense iron aluminide coatings were also obtained by Grosdidier et al., using a CDS torch to spray the same starting powders [26,27,30,31,33]. Their investigations focused on the detailed study at nanostructure level and concluded that the disordered FeAl phase remained in those not fully melted particle zones. Actually, they used powder coarser than that normally used for HVOF spraying aiming to retain unmelted particles. In the present study, the particle size distribution comprises the range between 7 and 30 μm [36], greatly different from their 40–63 μm range; that was carried out trying to achieve cool conditions to obtain limited heating and cause minimum oxidation.

Table 2 shows the values of 2θ Bragg angles corresponding to XRD spectra of the powder and of the coating samples. Fig. 2 shows the powder spectrum where those reflections

attributed to planes with $h + k + l$ odd do not appear. These so-called superlattice lines ($h + k + l$ even) with the fundamental lines appear in the XRD of the as-sprayed coatings (Fig. 3).

3.2. Oxidation behaviour

Structural characterization has been systematically carried out through SEM cross sectional and top surface observations and X-ray diffraction studies after 4, 36 and 72 h at 900, 1000 and 1100 °C. It was in this temperature range where the phase change from metastable to α-stable Al_2O_3 was observed in alumina forming alloys.

3.2.1. HVOF Fe40at%Al coating behaviour at 900 °C

Fig. 4 shows the cross section of the oxidised coating obtained with F2 spraying conditions exposed at 900 °C for 72 h. There is no significant difference compared to those at 4 and 36 h. It can be observed the formation of an adherent and fairly homogeneous oxide scale with no cracks, which seems to maintain the same thickness for the three tested periods. Examination of the features in the as-polished samples show that the different grey contrasts observed in the as-sprayed coating cannot be appreciated after the oxidation. The only grey contrasts there show iron-richer zones compared to the initial coating composition. It suggests a diffusion between lighter (Fe-rich) and grey (unmelted particles) zones

Table 2
2θ angles corresponding to FeAl phase for powder and coatings

FeAl theoretical pattern (2θ, °)	Powder (2θ, °)	F1 (2θ, °)	F2 (2θ, °)	F3 (2θ, °)
30.819 (100)		30.750	30.892	30.732
44.187 (110)	43.867 (110)	44.261	44.286	44.341
54.858 (111)		54.949	54.797	54.926
64.318 (200)	63.777 (200)	64.558	64.497	64.459
81.339 (211)	80.607 (211)	81.429	81.435	81.541
97.596 (220)	96.574 (220)	97.733	97.720	97.767
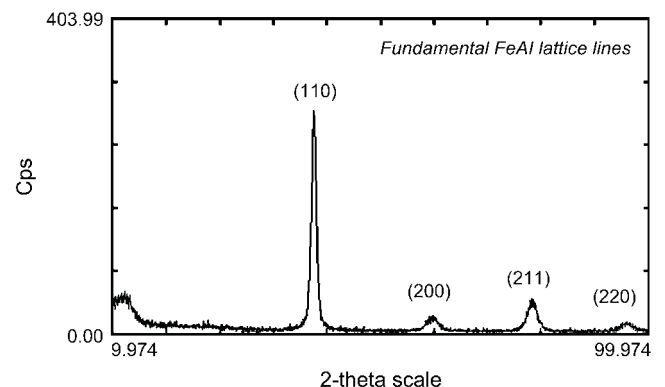
Fig. 2. XRD scans for the powder showing typical lines for the disordered phase.
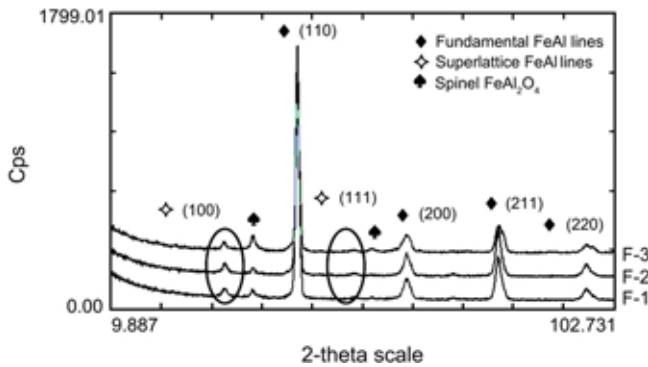
Fig. 3. XRD scans for the coatings showing fundamental and superlattice lines for the FeAl phase.

of the initial coating leading to a homogeneous composition whilst held at 900 °C; such phenomenon was already proposed by Hearley et al. for NiAl [18]. Table 3 shows how the so-designated "grey areas", which correspond to the FeAl alloy in the initial coating, present an increase in wt% of Fe after 72 h. However, the overall compositions studied for areas taken at 1500× magnification do not show significant changes at the studied exposure times. Although no quantitative oxygen content values can be extracted from EDS results, the former information can be assessed qualitatively.

It is worth noting that the interface remains intact without appreciable oxidation indicating a good adhesion resulting from the insulating effect of the cement, which permits to determine only the oxidation, which takes place from the contact of the coating surface with the oxidising atmosphere.

X-ray scans of the top surfaces indicate the presence of Fe_2O_3 as the principal corrosion product with some aluminium oxide (Fig. 5). The presence of FeAl peaks results from the small-scale thickness. Moreover, it should be noted that the superlattice peaks are no more visible. However, the absence of the superlattice peaks does not mean that there is no order but rather the peak intensity is negligible in the background.
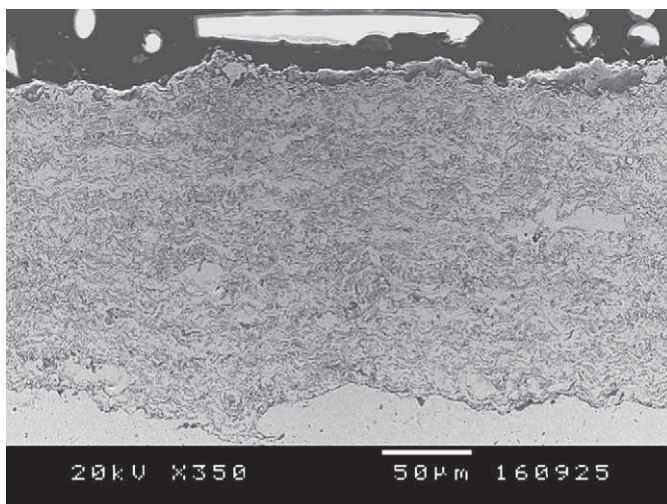
Table 3
EDS results (wt%) of elemental composition at different parts of the coating for the isothermal tests carried out at 900 °C

	Coating part	Fe wt%	Al wt%	O wt%	Y wt%
Before the	Coating area	64.94	20.13	12.68	2.25
isothermal test	Grey contrast	79.88	19.42	–	0.70
4 h	Coating area	64.81	21.91	13.28	–
36 h	Coating area	66.56	21.12	12.32	–
72 h	Coating area	63.04	22.00	12.60	2.36
	Grey contrast	89.55	9.95	–	0.5

Some features can also be characterized from the top surface observation. Fig. 6 shows the topography of the as-sprayed F2 surface coating where no fully melted particles are visible. After 4, 36 and 72 h, iron oxide nodules grew forming a continuous layer. Very fine needles protruded from this coalesced nodular net. At the longest time, some of those needles appear to have developed into whisker morphologies as indicated in Fig. 7a. Alumina is present in the so-called cigar-like morphology (Fig. 7b) at the bottom of the nodules or intersections among the grown nodular nuclei suggesting the presence of some Al-rich oxide beneath.

3.2.2. HVOF Fe40at%Al coating behaviour at 1000 °C

Even though it has presented a fairly reliable behaviour of the iron aluminide coating at 900 °C, the absence of the high-temperature α-Al_2O_3 makes uncertain how long such coatings would be able to withstand. Thus, the experiments carried out at 1000 and 1100 °C intended to clarify whether better oxidation resistance could be reached. However, Fig. 8 evidences that at 1000 °C for 36 h, the coating starts losing its integrity. After 4 h of the isothermal test, the cross section is similar to those encountered at 900 °C; nevertheless, the one after 36 h exhibits porosity at both coating−substrate and gas−scale interfaces leading to some zones separated from the substrate after 72 h.

Similarly as what happened at 900 °C, XRD reveals the formation of Fe_2O_3 and θ-Al_2O_3, but differently from them they also show α-Al_2O_3 (Fig. 9). Whereas at 900 °C the metastable alumina phase was present just in isolated areas while here, it occurs at the overall surface. Fig. 10 shows some α-Al_2O_3

Fig. 4. Cross sections under secondary electron conditions of the as-deposited F2 coatings subjected to oxidation at 900 °C for 72 h.
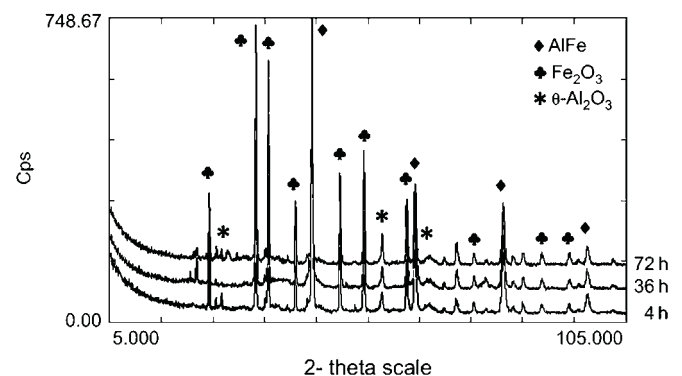
Fig. 5. X-ray diffraction of F2 oxidised coatings at 900 °C: (a) 4 h, (b) 36 h and (c) 72 h.
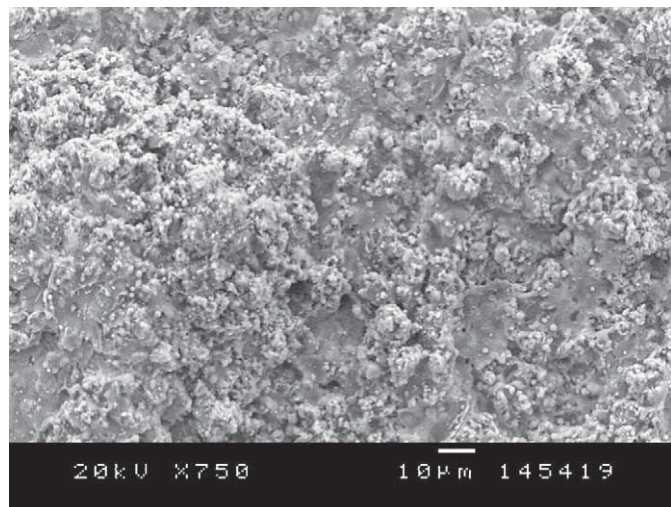
Fig. 6. Free surface of the as-deposited coatings without any thermal treatment.

crystallite difficult to find among the oxide nodular structure. Also interestingly, even after 72 h, no whiskers have developed and iron oxide remain as nodules.

3.2.3. HVOF Fe40at%Al coating behaviour at 1100 °C

After 4 h at 1100 °C, a non-uniform oxide layer has already formed on the tested coating with some characteristic features: a dark film at the coating−scale interface which turns into a lighter grey phase (Fig. 11). Table 4 shows the EDS results of the different contrasts featured in the scale. In order to analyse the elemental evolution from the coating and along the scale, an EDS scan was carried out. Fig. 12 shows the scan and the corresponding picture with an arrow indicating the track of the analysis. The ups and downs within the coating area (A) confirm that dark grey features are Al-rich zones; the wt% of Fe drops at the coating−scale interface (B) indicating the presence of an alumina layer. The similar levels of Fe, Al and O reached in region C indicate the presence of mixed

oxides under the external Fe_2O_3. By contrast, a scan undertaken for the as-sprayed coating did not indicate significant variations. The oxide scale also presents some porosity, which might facilitate the inward oxygen penetration promoting the local attack to the common heterogeneities found in thermal-sprayed coatings. The global diffusion processes lead to an accelerated oxidation and the final debonding of the coating.

Some spalled areas are also observed at the early stage although it was only at higher exposure times when the oxide scale cracked and detached from the samples during the cooling stage. After 72 h a clearly visible spallation made possible the removal of a thick scale with a complex structure. Fig. 13 shows its stratified structure with two well-differentiated zones: the one in the top surface in contact with air exhibiting a more columnar morphology and another rougher part below. The columnar counterpart is suggested to result from the oxidation of the coating, as it is as thick as the initial deposit; however, the rougher part corresponds to the further oxidation of the substrate. Moreover, the columnar counterpart is more equiaxed at the external zone (Fig. 13c). According to the XRD results of the overall milled scale, it is formed by different iron oxides: $FeAl_2O_4$, FeO, Fe_2O_3 and Fe_3O_4 (Fig. 14).

Compared to the tests carried out at 900 °C, significant oxidation at the coating−substrate interface defines a fine layer. However, although no cement appeared to be removed as a result of the cooling stage, it cannot be guaranteed that no oxygen penetration took place through the edges causing an additional via of oxidation.

According to X-ray results, Fe_2O_3 is the only corrosion product detected on the top surface with a whisker-like morphology (Fig. 15). However, at very short exposure times, some alumina cigar-like morphology can be observed among cavities of the iron oxide rich top surface as those exposed at 900 °C. An interesting feature is the sharpening of the XRD peaks indicating a specific growth direction of the grains when oxidised. As shown in Fig. 16, the dominant top surface structure is the whisker-like with a random orientation at 4 h and domains of preferential orientation at 36 h.

Fig. 7. Free surfaces of the as-deposited F2 coatings subjected to oxidation at 900 °C for 72 h showing (a) needles and whiskers and (b) cigar-like morphologies.
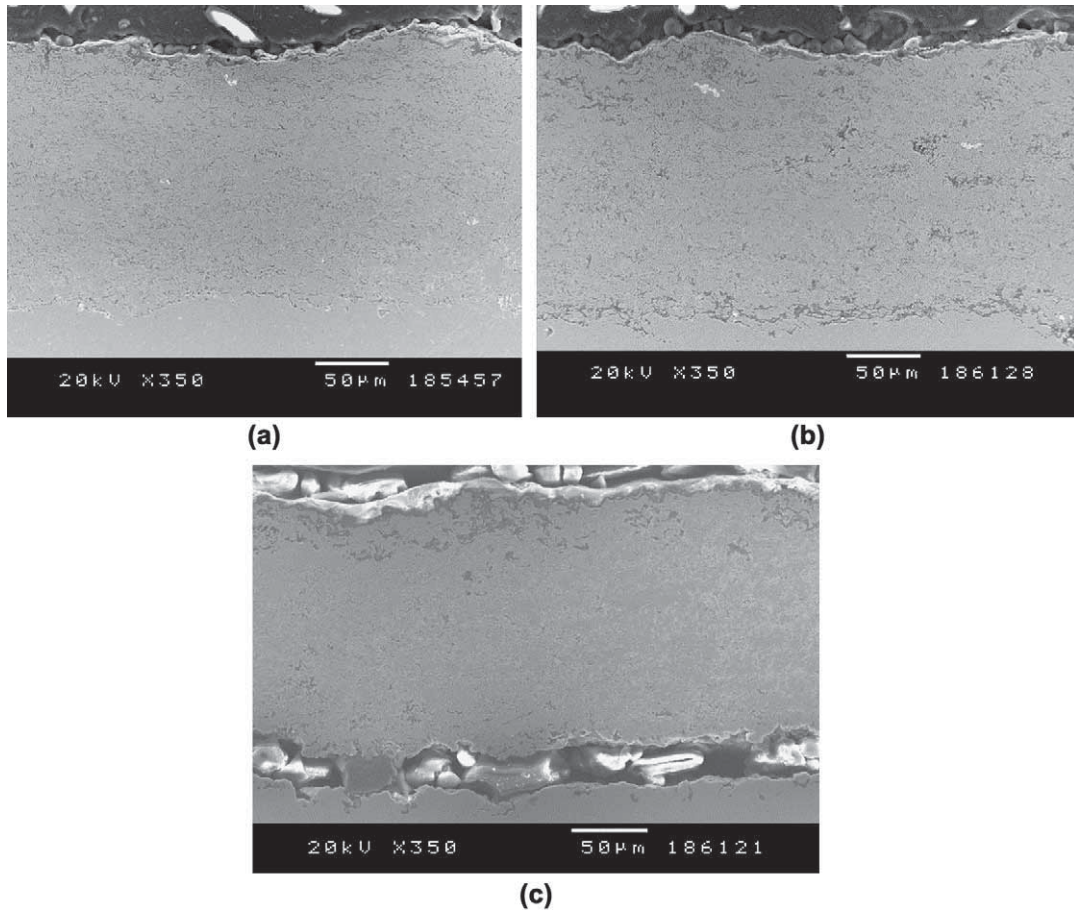
Fig. 8. Cross sections of the as-deposited F2 coatings subjected to oxidation at 1000 °C for (a) 4 h, (b) 36 h and (c) 72 h.

4. Discussion

When it is required that a high-temperature candidate material performs reasonably well at oxidising environments, stable corrosion products must be formed on the surface to prevent continuous oxygen penetration. Basic rules for the scale growth mechanisms and the Pilling−Bedworth criteria are useful for the understanding of pure metals oxidation. Pure iron and aluminium are well known to posses a parabolic oxidation. However, whereas Al forms a protective scale ($P.B_{Al_2O_3} = 1.38$), iron oxide is easily detached from the oxidising substrate ($P.B_{Fe_2O_3} = 2.15$). This is because of the different rate controlling micromechanisms; when Fe is exposed to high temperatures the oxide scale grows at the oxide−gas
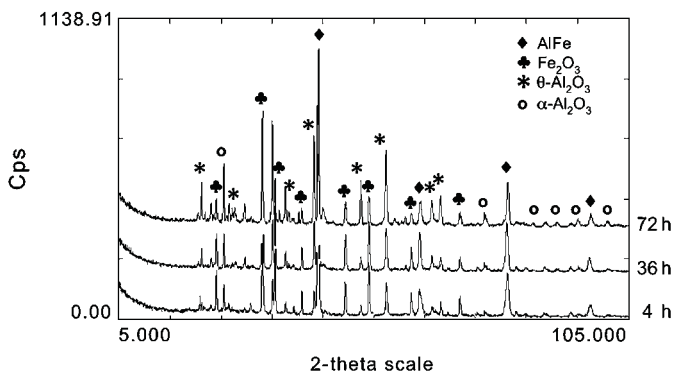
Fig. 9. X-ray diffraction of F2 coatings oxidised at 1000 °C: (a) 4 h, (b) 36 h and (c) 72 h.
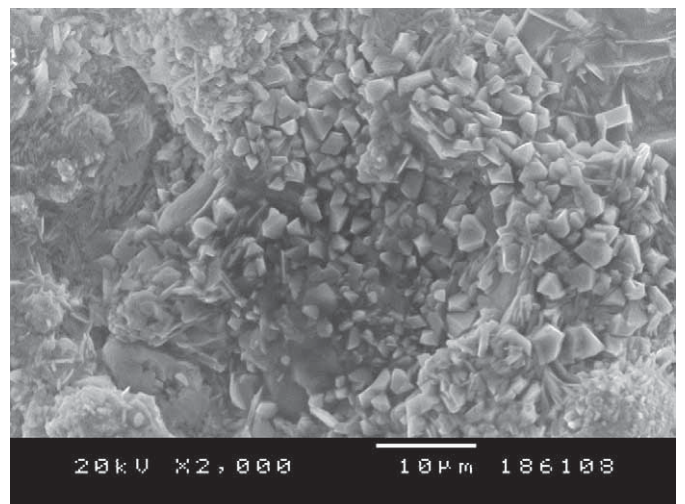
Fig. 10. α-Al$_2$O$_3$ crystallites of the as-deposited F2 coatings subjected to oxidation at 1000 °C for 4 h.
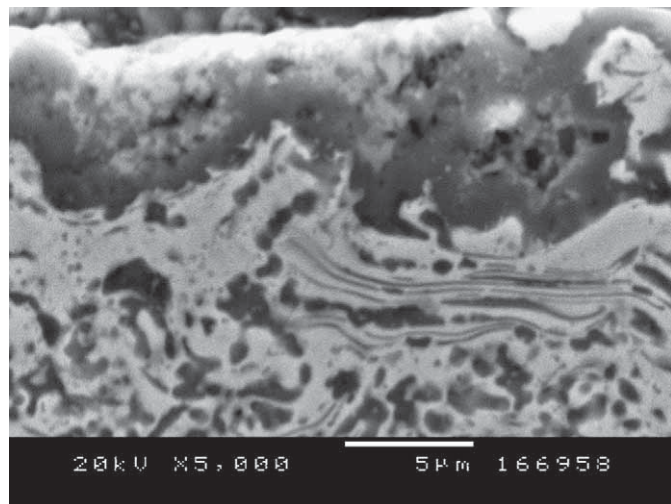
Fig. 11. Cross section of the oxide scale for the oxidised specimen at 1100 °C for 4 h.

Table 4
EDS results (wt%) of elemental composition at different parts of the coating for the isothermal tests carried out at 1100 °C

	Coating part	Fe wt%	Al wt%	O wt%	Y wt%
4 h, 1100 °C	Coating area	69.03	16.15	14.38	0.43
	Grey contrast	90.15	8.48	−	1.38
	Dark contrast in the coating−scale interface	42.91	27.8	23.13	6.17
	Light contrast in the oxide scale	72.16	1.78	26.07	−
72 h, 1100 °C	Oxide scale (middle zone rougher counterpart)	84.98	1.52	13.49	−
	Oxide scale (columnar counterpart)	87.72	−	12.28	−

interface due to the outward cation transport. Fe ions diffuse rapidly originating vacancies within the metal−oxide interface; the voids that form there reduce the adhesion of oxide to metal. By contrast, the alumina scale onto Al substrate grows at the metal−oxide or gas−oxide interface depending on the relative Al^{3+} diffusion to the O^{2-}.

When both elements are alloyed, the relative stability between both oxides has to be considered. In a binary alloy three situations are presented: first, depending on the concentration of the solute element added for the corrosion resistance, it will result in internal or external oxidation [37]; a second situation is when the oxide of the base metal can also form in air and develops until the more stable oxide of the solute prevents the growth of the transient oxide [37]; finally, for intermetallics, some can maintain the growth of the protective scale while for others it fails resulting in the formation of a layer of the next lower compound [38].

In Fe−Al alloys, depending on the Al concentration, the scale morphologies are different. Tomaszewicz et al. reported

the different oxidation products of such alloys exposed from 25 to 100 h in pure and dry oxygen atmospheres at 800 °C [39]. According to their results, those alloys with less than about 2.4 wt% Al exhibited layered scales composed of both iron and aluminium or mixed oxides; between 2.4 and 6.9 wt% Al, they resulted in alumina top surfaces with some iron oxide nodules. With greater amounts of aluminium, only healing Al_2O_3 scales were observed [39]. Such observations agree with the reviewed behaviour reported by Meier et al. [38]. Pint et al. also studied the critical Al content required to form an external protective scale within the composition range of 10−28 at% Al (5−16 wt% Al); they claimed that it increased with temperature between 600 and 1300 °C and only alumina scales were obtained at all the tested compositions [23]. For the Fe_3Al and FeAl bulk intermetallics which show a parabolic rate, the aluminium oxide is expected to form a completely protective scale not only because of its high stability but mainly because in such alloys there is enough Al content [14,40−52].

Nevertheless, massive alloys and thin specimens show different oxidation behaviour. Montealegre et al. already underwent oxidation experiments for non-ODS [53] and ODS [54] intermetallic FeAl foils. The present study concerns the oxidation
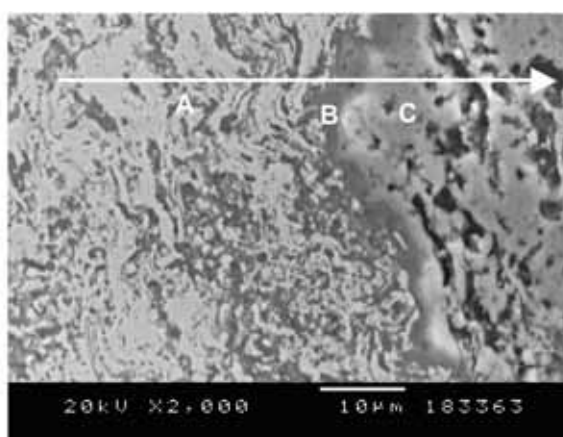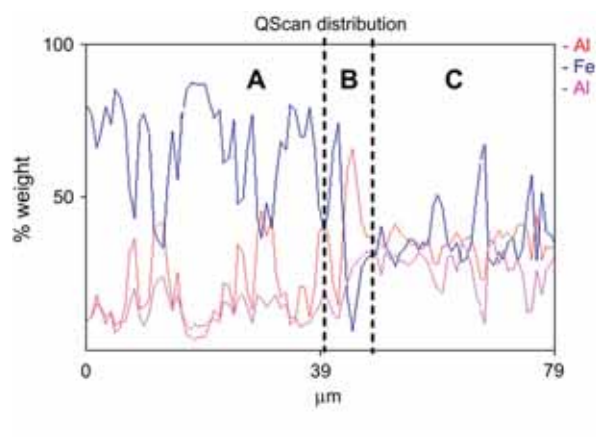
Fig. 12. EDS scan of the oxide scale for the oxidised specimen at 1100 °C for 4 h.
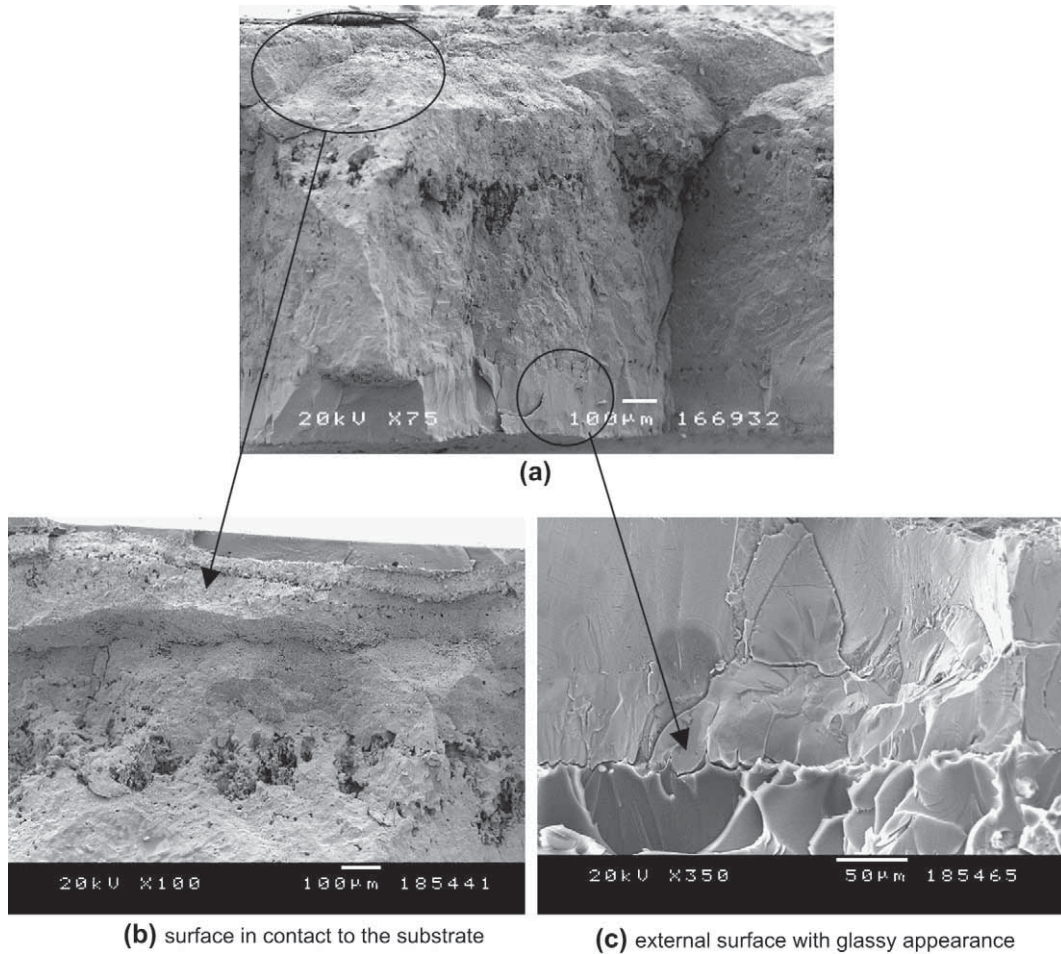
Fig. 13. SEM fractured cross sections of the oxide scale grown after 72 h at 1100 °C.

behaviour of a thermal-sprayed coating; thus, not only elemental composition but also the intrinsic microstructure and further parameters can play an important role in modifying the oxidation kinetics. Pint et al. already claimed the difficulty but also the importance of understanding their oxidation behaviour [14]. They reported that coatings might require a lower critical Al concentration for the formation of a stable alumina layer; however, their heterogeneous structure provides further oxidation paths. In

addition, it is worth noting that apart from the internal coating structure itself, external finishing should also be taken into account. While works performed with bulk materials deal with mirror-like polished surfaces, thermal-sprayed coatings result in their characteristic roughness depending on the powder particle sizes and spraying parameters. Chao and González-Carrasco already modelled the internal stresses developed in thermally grown oxide scales [55]; they claimed that the higher the metal
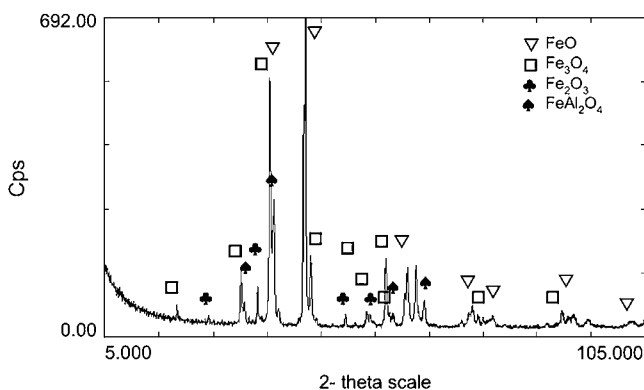
Fig. 14. X-ray diffraction of oxide scale formed after oxidation for 72 h at 1100 °C.
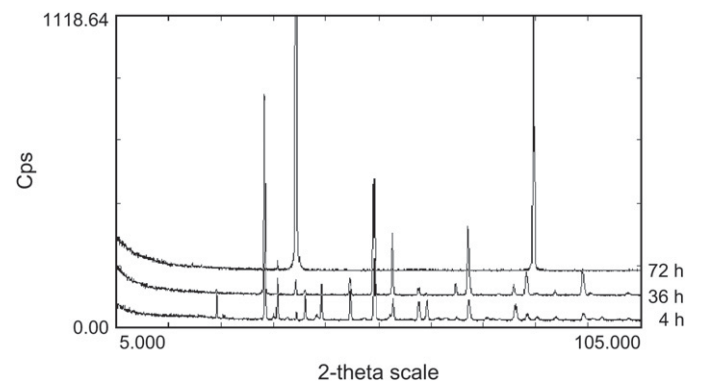
Fig. 15. X-ray diffraction of F2 top surface coatings after oxidation at 1100 °C for (a) 4 h, (b) 36 h and (c) 72 h.
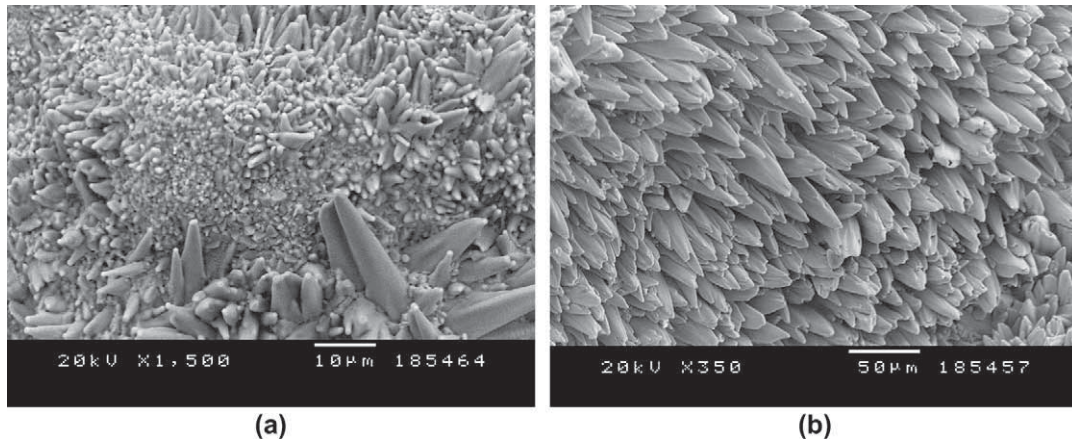
Fig. 16. Different features observed in free surfaces of the as-deposited F2 coatings subjected to oxidation at 1100 °C for (a) 4 h (1500×) and (b) 36 h (350×).

surface roughness, the further spallation occurs. According to this, spallation would impair the establishment of a dense and even alumina scale, favouring the development of Fe-rich oxides that are known to grow faster. Then, several factors may explain the kinetics and why 40 at% Al (25 wt% Al) is not enough to cover the surface of the coating with Al_2O_3.

The observation at 900 °C of iron oxide nodules evidences that there has been outward iron diffusion and the presence alumina cigar-like oxides suggests that the scale growth is also somewhat influenced by outward Al^{3+} diffusion, which is in agreement with the oxidation mechanism of other alumina forming alloys. Furthermore, the fairly reasonable stability of such scale also suggests that the flux of Al atoms to the alloy−scale interface is enough to maintain iron oxides at their nodule stage and prevent their rapid growth. Suzucka et al. also reached this conclusion and proposed a model for that. They also obtained Fe_2O_3 as one of the main corrosion products at 950 °C and, according to their observations, the amount of such iron oxides decreases when aluminium oxides increase [15].

The homogeneous contrast of the oxide scales indicates the formation of a mixed oxide, which would explain the fairly protective effect. The presence of the metastable θ-Al_2O_3 on the surface suggests the possibility of its reaction with iron oxide to form a $FeAl_2O_4$ below the Fe_2O_3 nodules. Several metastable transient oxides are known to exist before their transformation into the high-temperature stable alpha alumina phase at the temperature range of 900−1000 °C [13,41,42]. According to literature the sequence is known to be the following: γ-Al_2O_3 → δ-Al_2O_3 (750 °C); δ-Al_2O_3 → θ-Al_2O_3 (900 °C); θ-Al_2O_3 → α-Al_2O_3 (1000 °C) and the precise temperature transformation from θ to α is influenced by the presence of reactive elements; isothermal tests reported below 1000 °C show some spallation with the presence of θ and α-Al_2O_3 covering the surfaces [41,43,45,50,53]; Pedraza et al. observed the formation of $FeAl_2O_4$ resulting from the reaction of both Fe and Al oxides [45]. Above 1000 °C, the oxidation rates are lower because of the slower diffusivities through the α-Al_2O_3 scale; however, most studies show spallation and failure at the cooling stage due to thermal stresses and differences in thermal expansion coefficients [14,41,42,46,51−57].

The oxidation behaviour in coatings show differences from the bulk materials performance in high temperature environments. No clear explanation can still be given for the small amount of alumina encountered on the top surface of the Fe40Al coating after the isothermal test performed even after 72 h. Surprisingly, our results at 900 and 1000 °C show some kind of analogy with those investigations reported by Tomaszewicz [39]; for the oxidation behaviour of Fe(2.4−6.9)wt% Al, while that of lower Al concentrations is analogue to the Fe40Al sprayed coatings after long time exposed at 1100 °C. Such behaviour is not clearly understood and needs further investigation.

Some α-Al_2O_3 phase is observed for the isothermal tests at 1000 °C. Nevertheless, it is far to be enough to cover the entire surface providing an even non-porous stable scale. Therefore, diffusion processes do not slow down and continue damaging the coating integrity. The cross sections at 36 and 72 h illustrate the mode of failure at the initial stages suggesting that further exposure times might lead to a similar oxidation behaviour as that presented at 1100 °C. Natesan et al. presented two modes of failure of alumina scales: one is iron oxide nodules growing on the surface also observed at 900 °C and second, the formation of voids at the scale−alloy interface [58]. At 1000 °C we observe both nodular structures and voids at the substrate−coating and scale−coating interfaces. The coalescence of voids at the coating−steel interface promotes the separation from the substrate.

While it has been suggested the occurrence of a spinel phase at 900 °C, its formation at 1100 °C is clear and explained by the reaction $Al_2O_3 + FeO → FeAl_2O_4$. At this temperature, a combination of both mechanisms suggested in the review of Stott et al. [13] for the oxide growth could explain the progressive scale development. At an initial stage, the non-uniform thickness and protrusions observed after 4 h can be the result of cation and anion diffusion through short circuit paths (porous networks, grain boundaries, microcracks, intersplats, etc.) [23,39]. At a second stage, the so-called ''stress-assisted diffusional-creep process'' is a good explanation for the columnar morphology exhibited after 72 h. By analogy, the two layered features can be explained by oxygen diffusion along the scale

grain boundaries [12]. The more equiaxed outer surface but columnar inner part has been explained for alumina scales in terms of inward transport of oxygen [12]. In addition, typical columnar morphologies have been reported by the addition of reactive elements at similar temperatures [14]. Thus, the presence of reactive elements such as yttrium in the alloy makes the inward oxygen diffusion to be dominant. Many authors have provided their explanations for their effect on the oxidation behaviour [12,13,59]. Moreover, the Y_2O_3 content has a remarkable influence on the growth rates of the alumina scales; studies on 0.5 and 1 wt% amount of dispersoids concluded that the alloy with the lowest concentration of yttria exhibits improved protective capability [46,50].

Although there is no evidence of the yttria present either dissolved within the grains or in the boundaries, the refinement grain effect of the feedstock powders by ball milling enables to accommodate stresses that could contribute to less spallation at 900 °C. Nevertheless, at 1100 °C nothing prevents a rapid oxidation. The coating is being gradually depleted in Al and further oxidised reaching high oxidation rates. It leads to an unprotective coating, which allows the oxidation of the substrate. Here, the sum of a complex stress system determines the scale failure: initial compressive stresses formed in the HVOF coating, stresses in the layered scale at the oxide–oxide interfaces and, the most important, thermal stresses resulting from air-cooling.

Although no mass gain measurements are presented, two sort of oxidation behaviours are hypothesized at 1100 °C: the first case is a paralinear oxidation where the initial healing $FeAl_2O_4$ layer would gradually change permitting the diffusion through it and resulting in a linear rate; the second is the breakaway oxidation which also starts in a parabolic way until cracks and spallation promote that the below material is continuously exposed to the oxidising atmosphere. Because spallation occurs during the cooling stage rather than oxidation process itself, it might better fit a paralinear kinetics.

The bulky layered scale is composed of $FeAl_2O_4$, FeO, Fe_3O_4 and Fe_2O_3. Although only hematites is detected on the top surface, Al_2O_3 ("thermodynamic" stable oxide) and FeO ("kinetically" fast growing oxide) nuclei grow beneath. As those are miscible oxides, they react to form $FeAl_2O_4$. The outer surface of FeO undergoes further oxidation resulting in higher oxides, which grow more rapidly and finally cover the whole surface. Heterogeneities in the spinel layer facilitate the continuous oxidation.

The sequence of such oxides in the scale growing can be predicted with the most oxygen-deficient oxide contacting the inner part and the most oxygen-rich oxide next to the gas phase. In the Fe–O system, the iron oxide phase sequence above the spinel oxide would be FeO (near substrate)–Fe_3O_4–Fe_2O_3 (contacting atmosphere).

5. Conclusions

After microstructural and compositional studies of the isothermal oxidation tests undergone for as-sprayed coatings, the conclusions of the study can be summarized as follows:

1. Fe40Al intermetallic coatings were successfully deposited by HVOF spraying of FeAl Grade 3 powder. The coating microstructure primarily consists of partially melted powder particles conserving a disordered FeAl structure, with a spinel oxide phase and iron-rich zones at the intersplats.
2. The oxide layer ensures reasonable oxidation resistance at 900 °C. Hematite and metastable alumina phases were seen on the top surface of the coating, which preserves its initial thickness providing protection to the underlying substrate.
3. At 1000 °C also α-Al_2O_3 is present on the top surface but as presented at 900 °C, the outward iron diffusion promotes the formation of Fe oxide nodules, which cover the whole surface. Such phenomenon also with the occurrence of coalesced voids at the coating–substrate interface makes the coating separate from the substrate.
4. The oxide scale developed after 72 h at 1100 °C shows a different layered structure consisting of Fe_2O_3 + FeO + Fe_3O_4 + $FeAl_2O_4$. The high concentration of defects leads to the formation of a less-protective scale, which loses its integrity at short exposure time. The scale failure occurs when the thermal stresses promote spallation and cracking during air-cooling.
5. The addition of yttria to the initial powder can influence the oxidation mechanisms of the coatings. However, as there is no information on whether it remains in the unmelted particles or at the intersplat boundaries as a result of the spraying process, its role is uncertain.

References

[1] Liu CT, Stiegler JO. Ordered intermetallics. Properties and selection: nonferrous alloys and special purpose materials. In: Metals handbook. 10th ed. ASM International; 1990.
[2] Cahn RW, Haafen P, editors. Physical metallurgy. North Holand; 1996.
[3] Sauthoff G. State of intermetallics development. Mater Corros 1996;47: 589–94.
[4] Deevi SC, Sikka VK. Nickel and iron aluminides: an overview on properties, processing, and applications. Intermetallics 1996;4:357–75.
[5] Deevi SC, Sikka VK, Liu CT. Processing, properties and applications of nickel and iron aluminides. Prog Mater Sci 1997;42:177–92.
[6] Sikka Vinod K. Intermetallic-based high temperature materials. Metals and Ceramics Division, Oak Ridge National Laboratory, 1999.
[7] Adeva P. Materiales intermetálicos para aplicaciones estructurales a altas temperaturas. Ibérica Actualidad Tecnológica 1999;425:573–8. Available from: <www.aecientificos.es/empresas/aecientificos/revistashtml/MaterialesAlternativos.html>.
[8] Yamaguchi M, Inui H, Ito K. High temperature structural intermetallics. Acta Mater 2000;48:307–22.

[9] Tanaka R. Research and development of ultra-high temperature materials in Japan. Mater High Temp 2000;17(4):457–64.

[10] Savolainen K, Mononen J, Ilola R, Hänninen H. Materials selection for high temperature applications, Helsinki University of Technology, Department of Mechanical Engineering, 2005.

[11] Suryanarayana C. Mechanical alloying and milling. Prog Mater Sci 2001;46(1–2):1–184.

[12] Hindamtw H, Whittle DP. Microstructure, adhesion and growth kinetics of protective scales on metals and alloys. Oxid Met 1982;18:245–84.

[13] Stott FH, Wood GC, Stringert J. The influence of alloying elements on the development and maintenance of protective scales. Oxid Met 1995;44:113–45.

[14] Pint BA, Leibowitz J, Devan JH. The effect of an oxide dispersion on the critical Al content in Fe–Al alloys. Oxid Met 1999;51(1–2):181–97.

[15] Szczucka-Lasota B, Formanek B, Hernas A. Growth of corrosion products on thermally sprayed coatings with intermetallic phases in aggressive environments. J Mater Process Technol 2005;164–165:930–4.

[16] Magnee A, Offergeld E, Leroy M, Lefort A. Fe–Al intermetallic coating applications to thermal energy conversion advanced systems. In: Proceedings of the 15th Thermal Spray Conference, vol. 2. Nice (France); 1998. p. 1091–1096.

[17] Formanek B, Szymanski K, Szczucka-Lasota B, Wlodarczyk A. New generation of protective coatings intended for the power industry. J Mater Process Technol 2005;164–165:850–5.

[18] Hearley JA, Little JA, Sturgeon AJ. Oxidation properties of NiAl intermetallic coatings prepared by high velocity oxy-fuel thermal spraying. In: Proceedings of the 15th Thermal Spray Conference, vol. 1. Nice (France); 1998. p. 89–94.

[19] Brand W, Grabke HJ, Toma D, Kriiger J. The oxidation behaviour of sprayed MCrAlY coatings. Surf Coat Technol 1996;86–87:41–7.

[20] Brand W, Grabke HJ, Toma D, Kriiger J. The oxidation behaviour of HVOF thermal-sprayed MCrAlY coatings. Surf Coat Technol 1997;93–95:21–6.

[21] Brandl W, Toma D, Grabke HJ. The characteristics of alumina scales formed on HVOF-sprayed MCrAlY coatings. Surf Coat Technol 1998;108–109(1–3):10–5.

[22] Toma D, Brandl W, Köster U. Studies on the transient stage of oxidation of VPS and HVOF sprayed MCrAlY coatings. Surf Coat Technol 1999;120–121:8–15.

[23] Ajdelsztajn L, Picas JA, Kim GE, Bastian FL, Schoenung J, Provenzano V. Oxidation behavior of HVOF sprayed nanocrystalline NiCrAlY powder. Mater Sci Eng A 2002;338(1–2):33–43.

[24] Sobolev VV, Guilemany J, Nutting J. High velocity oxy-fuel spraying. Maney Publishing; 2004. ISBN-1-902653-72-6.

[25] Blackford JR, Buckley RA, Jones H, Sellars CM, McCartney DG, Horlock AJ. Spray deposition of an iron aluminide. J Mater Sci 1998;33:4417–21.

[26] Grosdidier T, Tidu A, Liao H. Nanocrystalline Fe-40Al coating processed by thermal spraying of milled powder. Scripta Mater 2001;44:387–93.

[27] Ji G, Morniroli J, Grosdider T. Nanostructures in thermal spray coatings. Scripta Mater 2003;48:1599–604.

[28] Totemeier TC, Wright RN, Swank WD. Microstructure and stresses in HVOF sprayed iron aluminide coatings. J Therm Spray Technol 2002; 11(3):400–8.

[29] Totemeier T, Wright R, Swank WD. FeAl and Mo–Si–B intermetallic coatings prepared by thermal spraying. Intermetallics 2004;12:1335–44.

[30] Ji G, Grosdidier T, Liao HL, Morniroli J, Coddet C. Spray forming thick nanostructured and microstructured FeAl deposits. Intermetallics 2005; 13:596–607.

[31] Ji G, Elkedim O, Grosdidier T. Deposition and corrosion resistance of HVOF sprayed nanocrystalline iron aluminide coatings. Surf Coat Technol 2005;190:406–16.

[32] Totemeier TC, Wright JK. Residual stress determination in thermally sprayed coatings—a comparison of curvature models and X-ray techniques. Surf. Coat. Technol 2006;200:3955–62.

[33] Grosdidier Thierry, Ji Gang, Bozzolo Nathalie. Hardness, thermal stability and yttrium distribution in nanostructured deposits obtained by thermal spraying from milled—Y_2O_3 reinforced—or atomized FeAl powders. Intermetallics 2006;14:715–21.

[34] Xiao C, Chen W. Sulfidation resistance of CeO_2-modified HVOF sprayed FeAl coatings at 700 °C. Surf Coat Technol 2001;6:3625–32.

[35] Moret F, Baccino R, Martel P, Guetaz L. Propriétés et applications des alliatges intermetalliques B2-FeAl. J Phys IV 1996;6:281–9.

[36] Guilemany JM, Lima CRC, Cinca N, Miguel JR. Studies of Fe-40Al coatings obtained by high velocity-oxy fuel. Surf Coat Technol 2006; 201(5):2072–9.

[37] Gesmundo F, Gleesont B. Oxidation of multicomponent two-phase alloys. Oxid Met 1995;44:211–37.

[38] Meier GH, Petit FS. High temperature oxidation and corrosion of intermetallic compounds. Mater Sci Technol 1992;8:331–8.

[39] Tomaszewicz P, Wailwork GR. Observations of nodule growth during the oxidation of pure binary iron–aluminum alloys. Oxid Met 1983; 19:165–85.

[40] Martínez M, Viguier B, Maugis P, Lacaze J. Relation between composition, microstructure and oxidation in iron aluminides. Intermetallics 2006;14:1214–20.

[41] Mignone A, Frangini S, La Barbera A, Tassa O. High temperature corrosion of B2 iron aluminides. Corros Sci 1998;40(8):1331–47.

[42] Tortorelli PF, Natesan K. Critical factors affecting the high-temperature corrosion performance of iron aluminides. Mater Sci Eng A 1998;258: 115–25.

[43] Dang Ngoc Chan C, Huvier C, Dinhut JF. High temperature corrosion of some B2 iron aluminides. Intermetallics 2001;9:817–26.

[44] Xu C-H, Hyland M, Gong H. Characterisation of high temperature corrosion products on FeAl intermetallics by XPS. Corros Sci 2001; 43:1891–903.

[45] Pedraza F, Grosseau-Poussard JL, Dinhut JF. Evolution of oxide scales on an ODS FeAl intermetallic alloy during high temperature exposure in air. Intermetallics 2005;13:23–33.

[46] Montealegre MA, González-Carrasco JL, Morris-Muñoz MA, Chao J, Morris DG. The high temperature oxidation behaviour of an ODS FeAl alloy. Intermetallics 2000;8:439–46.

[47] Kupka M. High temperature strengthening of the FeAl intermetallic phase-based alloy. Intermetallics 2006;14:149–55.

[48] Xu C-H, Gao W, Li S. , Oxidation behaviour of FeAl intermetallics: the effect of Y on the scale spallation resistance. Corros Sci 2001;43:671–88.

[49] Montealegre MA, Strehl G, González-Carrasco JL, Borchardt G. Oxidation behavior of novel ODS FeAlCr intermetallic alloys. Intermetallics 2005;13:896–906.

[50] Montealegre MA, González-Carrasco JL. Influence of the yttria content on the oxidation behaviour of the intermetallic Fe40Al alloy. Intermetallics 2003;11:169–75.

[51] Lang F, Yu Z, Gedevanishvili S, Deevi SC, Narita T. Isothermal oxidation behavior of a sheet alloy of Fe–40at.%Al at temperatures between 1073 and 1473 K. Intermetallics 2003;11:697–705.

[52] Xu C-H, Gao W, He Y-D. High temperature oxidation behaviour of FeAl intermetallics—oxide scales formed in ambient atmosphere. Scripta Mater 2000;42:975–80.

[53] Montealegre MA, González-Carrasco JL, Muñoz-Morris MA. Oxidation behaviour of Fe40AL alloy strip. Intermetallics 2001;9(6):487–92.

[54] Berlanga, González-Carrasco JL, Montealegre MA, Muñoz-Morris MA. Oxidation behaviour of yttria dispersion strengthened Fe40Al alloy foils. Intermetallics 2004;12:205–12.

[55] Chao J, González-Carrasco JL. The role of the surface roughness on the integrity of thermally generated oxide scales. Application to the Al_2O_3/MA956 system. Mater Sci Eng A 1997;230:39–48.

[56] Xu CH, Gao W, Gong H. Oxidation behaviour of FeAl intermetallics. The effects of Y and/or Zr on isothermal oxidation kinetics. Intermetallics 2000;8:769–79.

[57] Grabke HJ. Oxidation of NiAl and FeAl. Intermetallics 1999;7:1153–8.

[58] Natesan K. Corrosion performance of iron aluminides in mixed-oxidant environments. Mater Sci Eng A 1998;258:126–34.

[59] Corrosion: fundamentals, testing and protection. In: Metals handbook. 10th ed., vol. 13A. ASM International; 1990.

As part of the optimization of the spraying parameters, as high-temperature performance was one of the main subjects of study, it was decided to submit to the same oxidizing conditions the less oxidized coating obtained by spraying with hydrogen, the one with F-6 reference.

Its behaviour at 900°C is explained in paper 5 entitled "Oxidation behaviour of HVOF-sprayed ODS-Fe40Al Coatings at 900°C" (*Appendix VI*) presented for the Thermal Spray Conference 2007. Basically, it was observed that the kinetics of the oxide scale was faster when compared to the propylene conditions; in this case, no alumina was identified in the X-ray spectra.
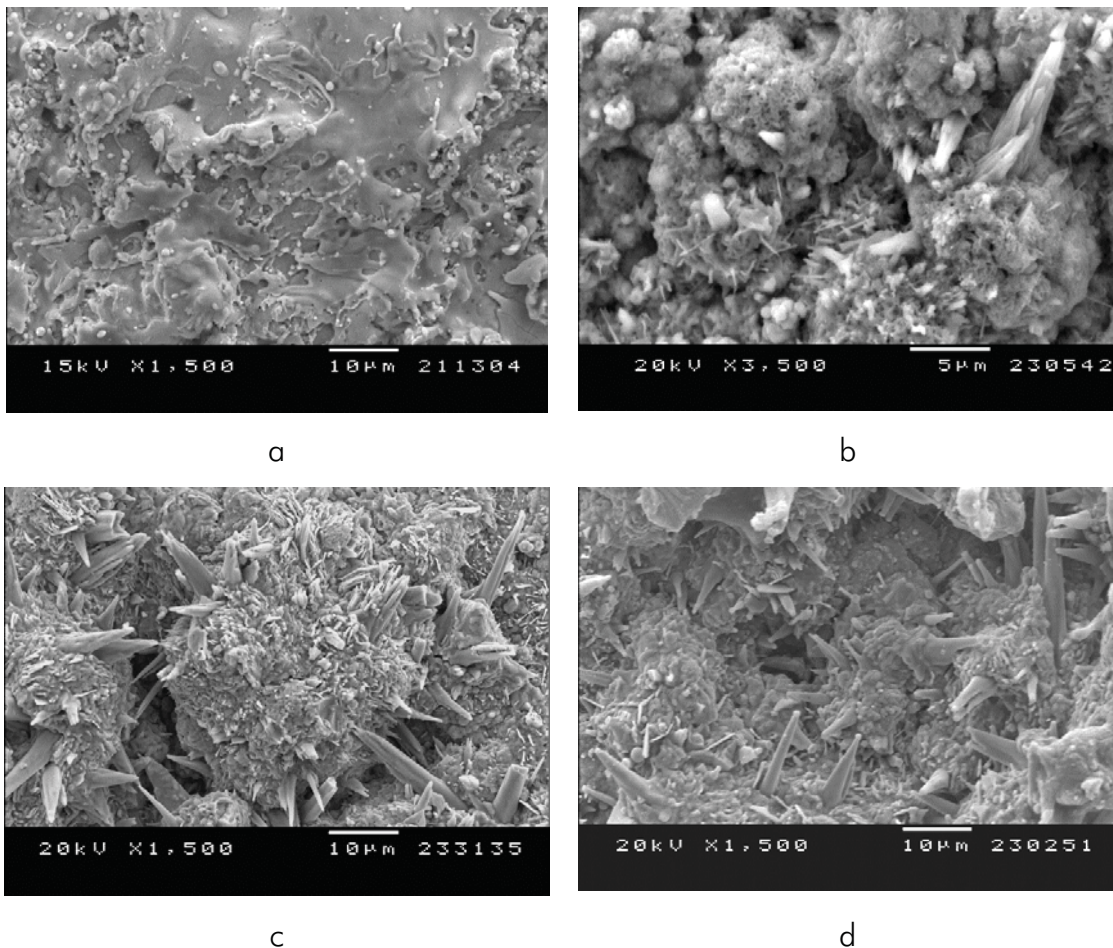
Figure 4.20. (a) As-sprayed and, surface morphologies of the F-6 coating oxidized at 900°C for (b) 4h, (c) 36h and (d) 72h.

a   b

c
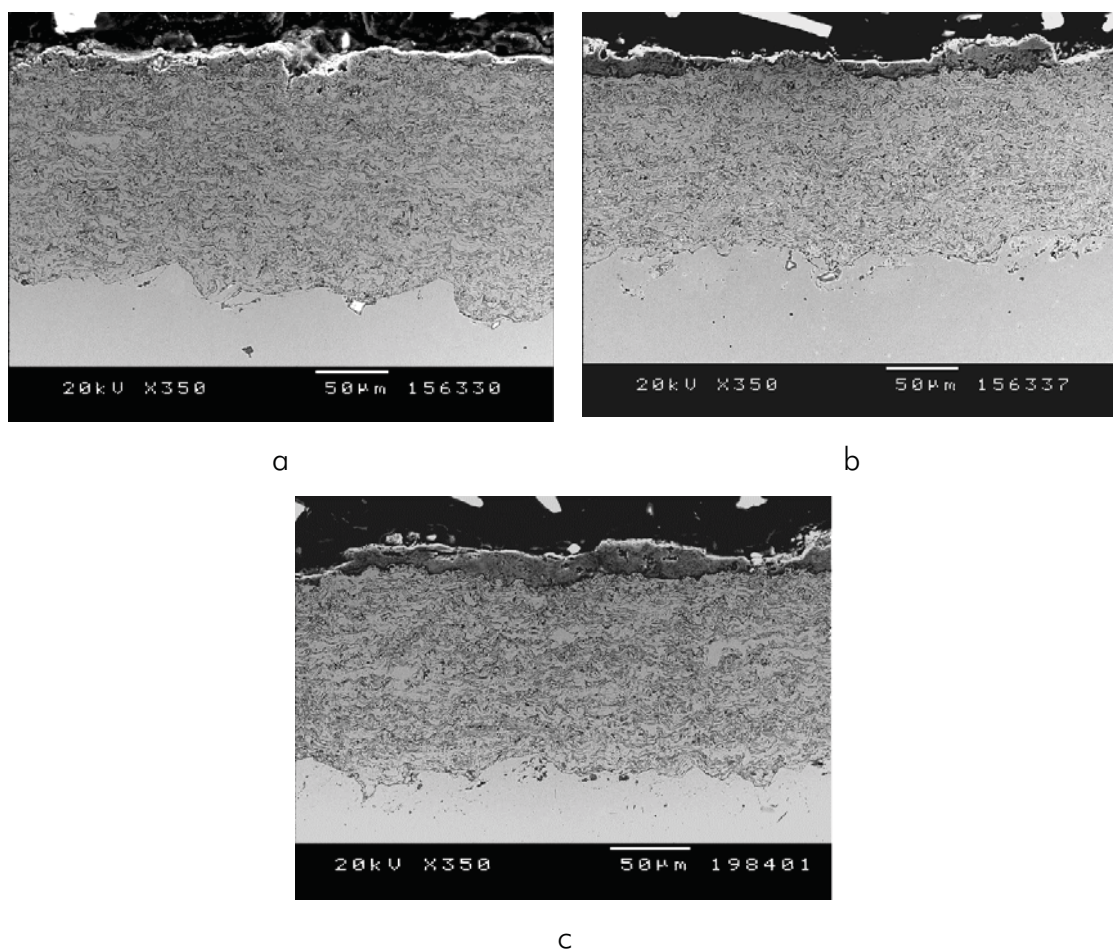
Figure 4.21. (a) Cross sections of the F-6 coating oxidized at 900°C for (a) 4h, (b) 36h and (c) 72h.

Figure 4.20 shows the surface of the coating as-sprayed and after the isothermal oxidation at 900°C for 4, 36 and 72h. By observing figure 4.20a, one can see the more melting produced with these spraying conditions; after 72h at 900°C, the iron oxide has grown in a whisker-like morphology (fig. 4.20b) and the oxide scale (fig. 4.20c) is about 25 microns. Figure 4.21 shows how the oxide scale increases along the time test. The scale at 72h is thicker than that of the F-2 (CEA) after the same time.

At 1100°C, the oxidation is already visible at early stages. After 4h of treatment, there is a thick oxide scale with a thin Al-rich line in the coating-scale interface (fig. 4.22a). The formation of microcavities within the scale might be a consequence of the outward diffusion of Al which is not entirely

counterbalanced by the opposite migration of oxygen atoms. Here, the alumina is non-protective and allows the fast growing of the iron oxide [14]. The top surface is full of whiskers (fig. 4.23a) that grow in a preferential direction (as observed for the F-2 (CEA) coating) leading to a grain morphology as presented in figure 4.23b. According to the diffraction spectra after 36 and 72 h at 1100 °C, the few highly intense lines correspond to Fe_2O_3 growing in the direction (0 0 l).

a   b
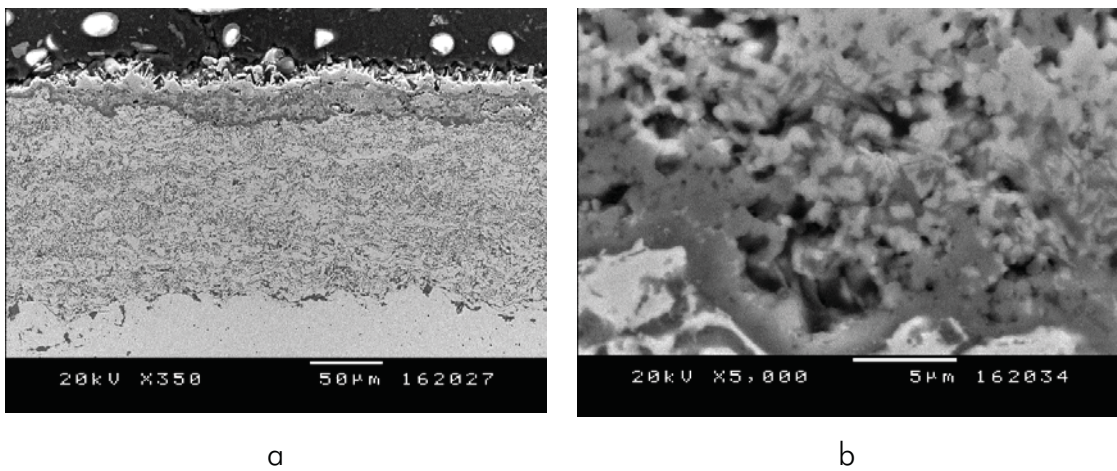
Figure 4.22. (a) Cross section and (b) detail of the microvoids formed within the oxide scale of the F-6 coating oxidized at 1100°C for 4h.

a   b
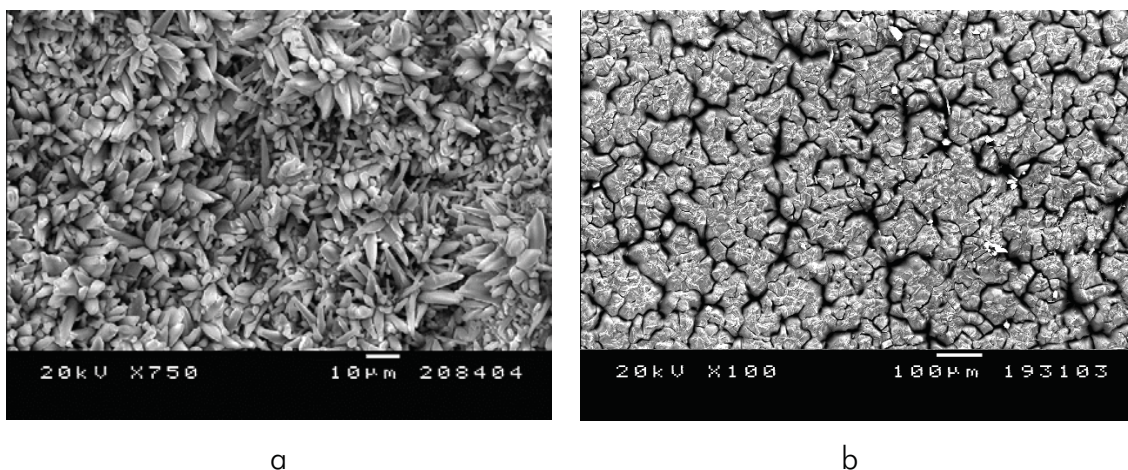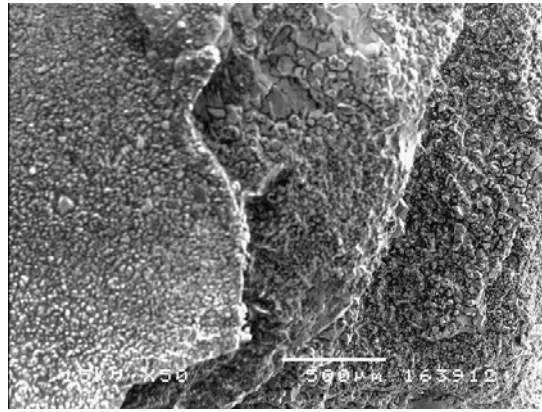
c

Figure 4.23. Surface morphologies of the F-6 coating oxidized at 1100°C for (a) 4h, (b) 72h and (c) spallation observed on the top surface.

The rapid oxidation that took place within the F-2 coating is here even more emphasized. The whole coating was also oxidized after 72h being the oxide scale thicker (fig. 4.24a). By contrast, a columnar zone was observed here below the outer glassy scale (fig. 4.24b).
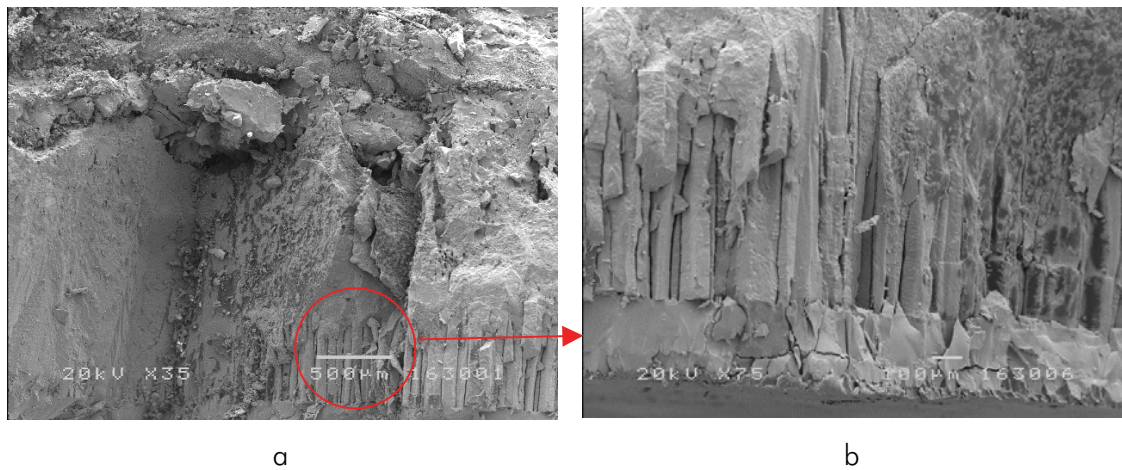
a   b

Figure 4.24. (a) SEM fractured cross sections of the oxide scale grown after 72h at 1100°C and (b) detail of the external surface with glassy appearance.

In the case of the MEC40-60, it was expected an amelioration of the coating resistance as result of suppression of interlamellar oxidation which facilitated

the oxygen penetration. As observed in figure 4.25a, the amount of aluminium oxide has considerably increased and the whole surface is almost full of cigar-like morphologies (fig. 4.25a and b) [15]; whether these are some metastable alumina or an early stage of alpha-alumina phases seems to be a controversy [15, 16, 17], but the featured polygonal-shape oxides are without any doubt associated to α-Al_2O_3 (fig. 4.25c) [18, 19]. Moreover, while CEA showed intense Fe_2O_3 X-ray peaks, these are here not quite noticeable (fig. 4.26).

a   b

c   d
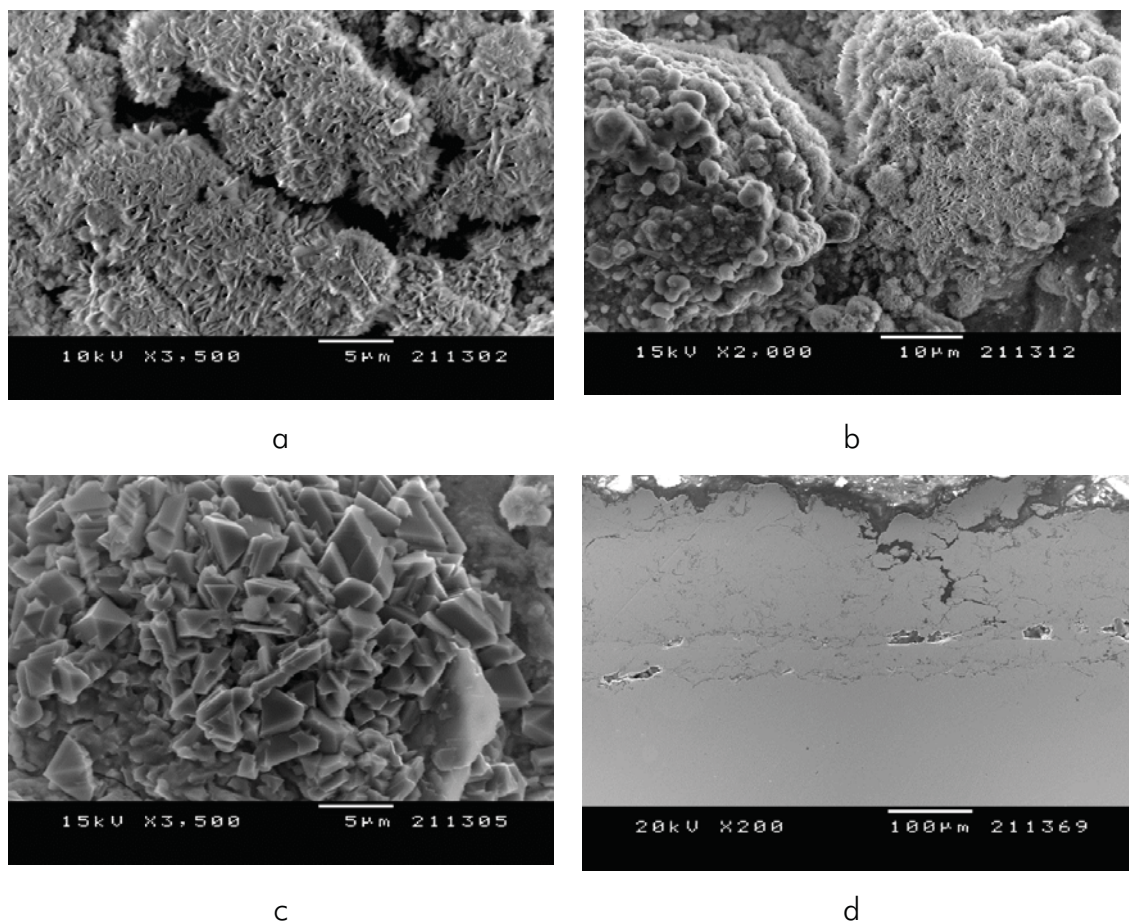
Figure 4.25. (a), (b) and (c) Surface morphologies and (d) cross section of the MEC40-60 oxidized coating at 900°C for 72h.

In this sense, the alumina scale would enable a good protection but, as seen in figure 4.25d, some cracks appear during the oxidation test. These might be attributed to the initial coating stresses that during oxidation have released

promoting such cracking. In the CEA, coating, the splats structure, rather than coarse non-fully melted particles proved to accommodate better this effect.
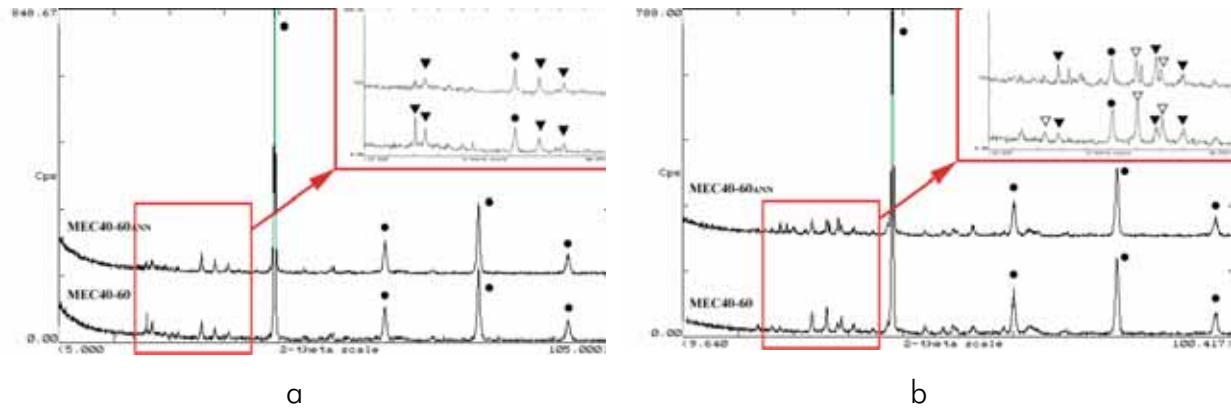
Figure 4.26. X-ray spectra of the MEC40-60 and Mec40-60$_{ANN}$ coatings oxidized at 900°C for (a) 4h and (b) 72h (● FeAl, ▼ α-Al$_2$O$_3$, ▽Fe$_2$O$_3$).

With MEC40-60$_{ANN}$, the intention was to achieve better oxidation performance by ordering the structure of the intermetallic but, as in MEC40-60, despite having a better material (bulk-resembling with minimal oxidation), the coating quality is worst. Above 900°C, the oxidation results in accelerated high-temperature corrosion. Some approaches are thought to be addressed on cold-spraying, where a good sealing is achieved [20, 21, 22].

The as-sprayed cryomilled powder, with a coating structure similar to that of F-6, presents a surface covered by iron oxide nodules and needles with a thick oxide layer (fig. 4.27). This shows however, even worst performance than F-6 after the same period.

a

b

c

d

e
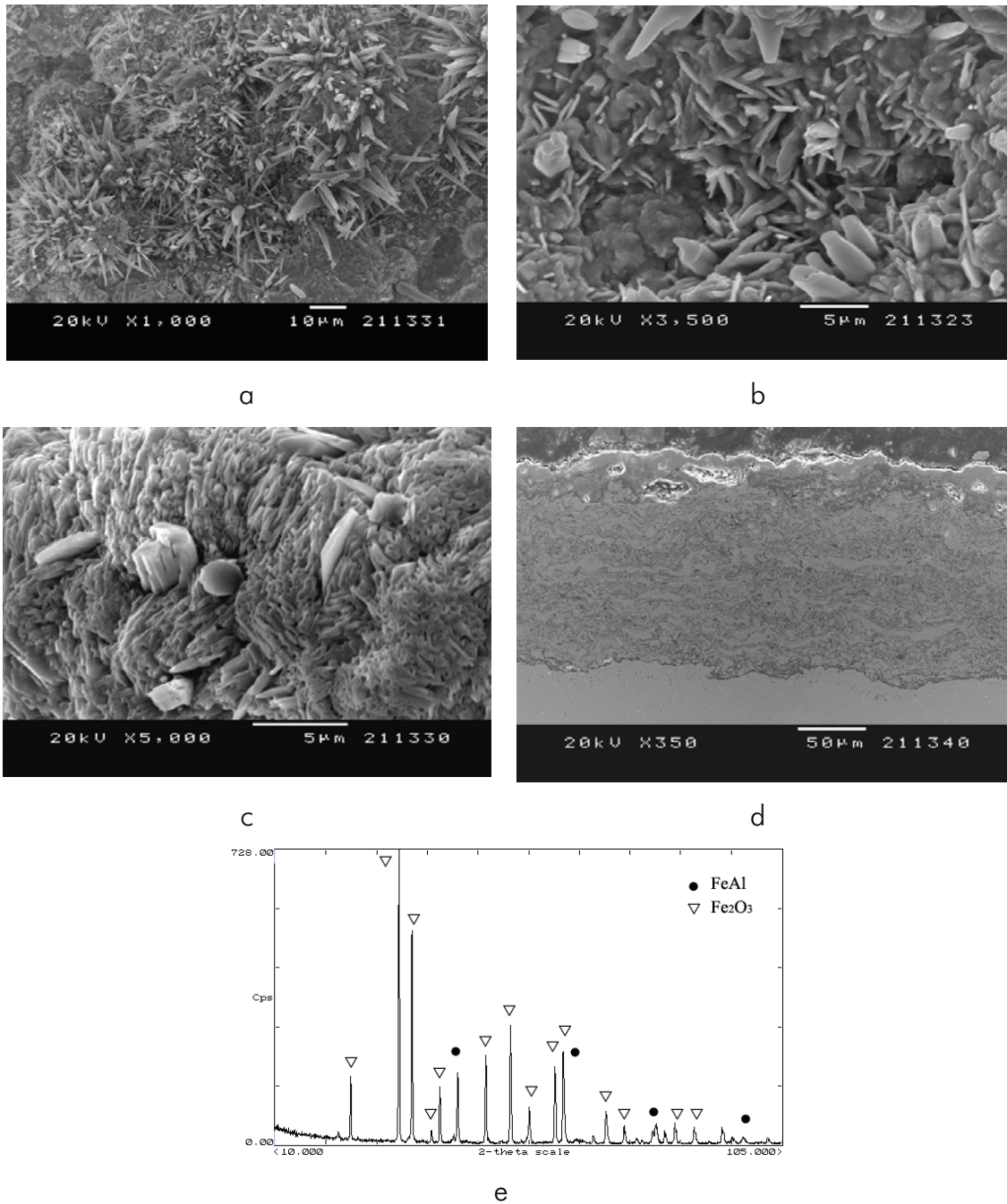
Figure 4.27. (a), (b) and (c) Surface morphologies, (d) cross section and (e) X-ray spectrum of the oxidized CRYO coating at 900°C for 72h.

As in figure 4.23, the CRYO coating exhibits a similar scale morphology after being oxidized at 1100°C for 72h (fig. 4.28). The top surface shows cracking as result of thermal stresses after air cooling from high temperatures.
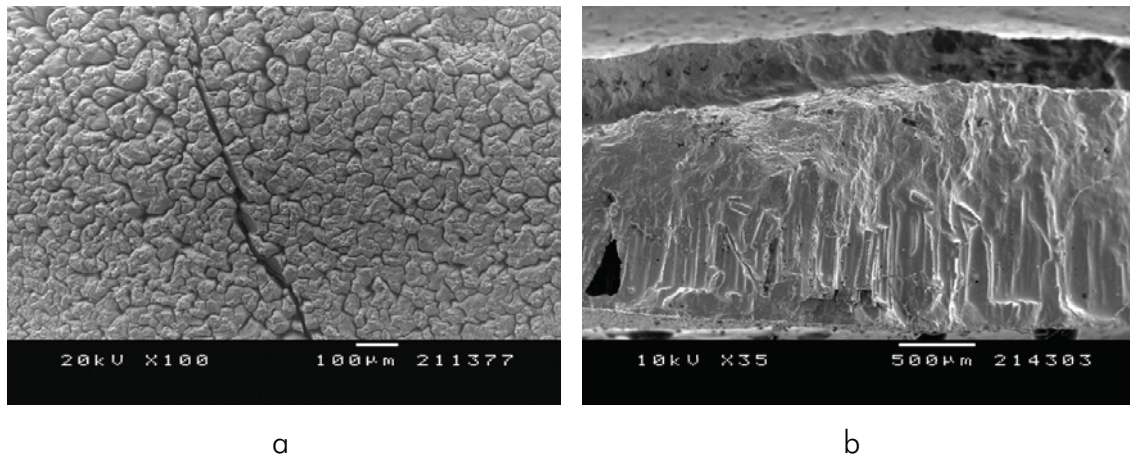
Figure 4.28. (a) Surface morphology and (b) SEM fractured cross section of the CRYO oxide scale grown after 72h at 1100°C

d)   Corrosion resistance in molten salts

The eutectic $ZnCl_2$: KCl is a low melting salt (T_m= 230°C) that in the liquid phase behaves as electrolyte with increased potential for hot corrosion. These chlorides prevent the formation of protective oxides [23, 24, 25, 26].

Figure 4.29 shows some of the surface morphologies formed on the CEA coating by the salts after exposure at 450°C for 240h, and the oxides produced as result of the corrosion process; some of these morphologies are presented below, such as: zinc oxide crystals (fig. 4.29a), Fe_2O_3 nodules (fig. 4.29b) and deposits of salts in figure 4.29c.
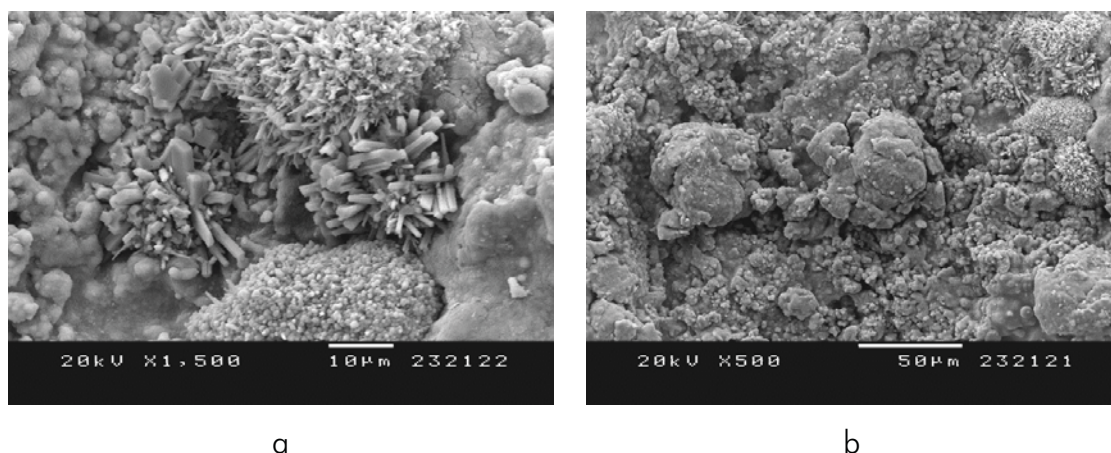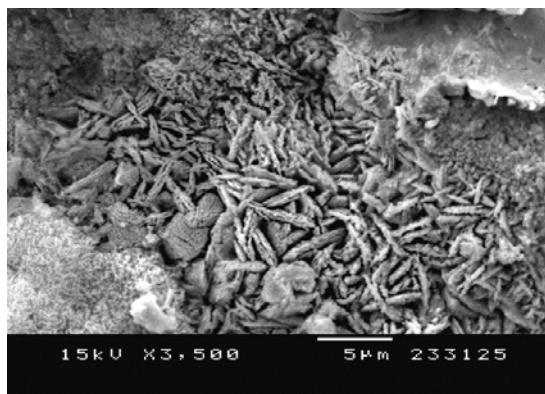
c

Figure 4.29. Surface morphologies of the corroded CEA coating at 450°C for 240h.

Li and Spiegel suggested [27] that, in alumina-forming alloys, Al tends to be displaced in the initial stages of the corrosion process (1), leaving an Fe-enriched subsurface that can be easily attacked by the molten slat; the higher iron activity makes it also susceptible to react with the chlorine liberated in (2) leading to $FeCl_2$ (3); iron chloride decomposes to form a porous oxide (4) that allows further penetration of chlorine [28]:

(1) $2\ Al + 3\ ZnCl_2 \rightarrow 3\ Zn + 2\ AlCl_3$

(2) $2\ AlCl_3 + 3/2\ O_2 \rightarrow Al_2O_3 + 3\ Cl_2$

(3) $Fe + Cl_2 \rightarrow FeCl_2$

(4) $2\ FeCl_2 + 3/2\ O_2 \rightarrow Fe_2O_3 + 2\ Cl_2$
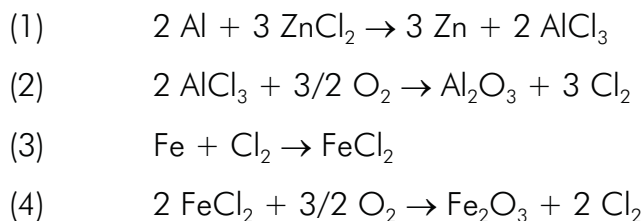
The zinc oxide morphologies might result from the following reaction $ZnCl_2 + 1/2\ O_2 \rightarrow ZnO + Cl_2$, and the metallic iron identified in the XRD (fig. 4.33a) is attributed to the supply of aluminium, which reacts with chlorine as the main oxidant: $2\ Al + 3Cl_2 \rightarrow 2\ AlCl_3$.

Figure 4.30a shows the CEA coating with an enlargement to show the chloride dissolution (K and Zn EDX maps did not show good resolution). In this case, after the test, the coating had a thickness of 161±7 microns (as-sprayed, 162±6 microns). There might be an expansion as result of coating oxidation. From figure 4.30b, it is seen that Al-rich oxides are formed beneath the external layer with the remaining corrosion products.

a   b
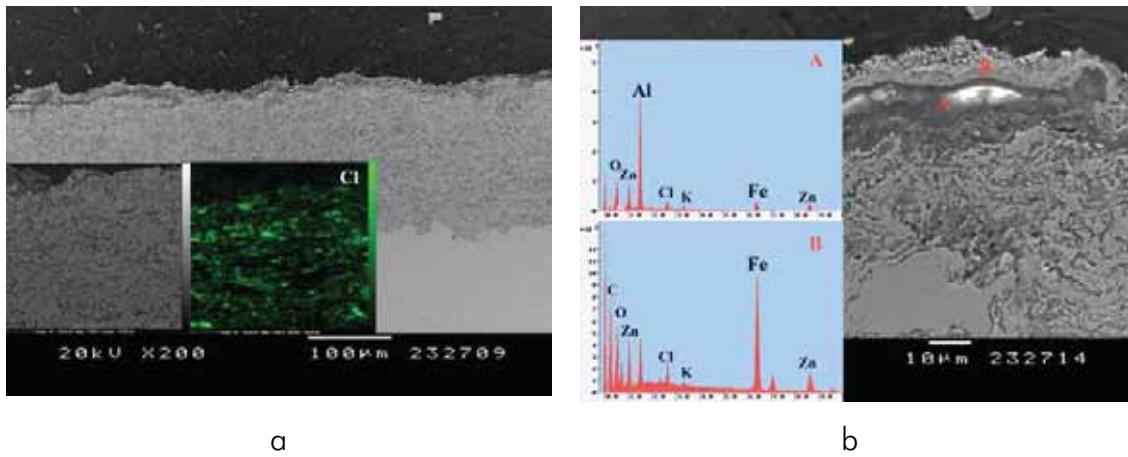
Figure 4.30. Cross section (a) general view and (b) magnification of the corroded CEA coating at 450°C for 240h.

As far as MEC40-60 is concerned, different surface morphologies are also observed (fig 4.31). The features observed in figure 4.31 are not so obvious here because the spallation in this case was more important; at the end of the test, 124±14 microns were left from the initial 147±9 microns. This can be easily understood imagining that when the whole particle boundary is attacked, this is debonded producing a thickness decrease much more noticeable than that of individual well fused spats. It can be said then, that due to the coating microstructure, the corrosion results in a more rapid spallation. Figure 4.32a shows the coating with a thin dark line in the coating-substrate interface suggesting the oxygen penetration.

a   b
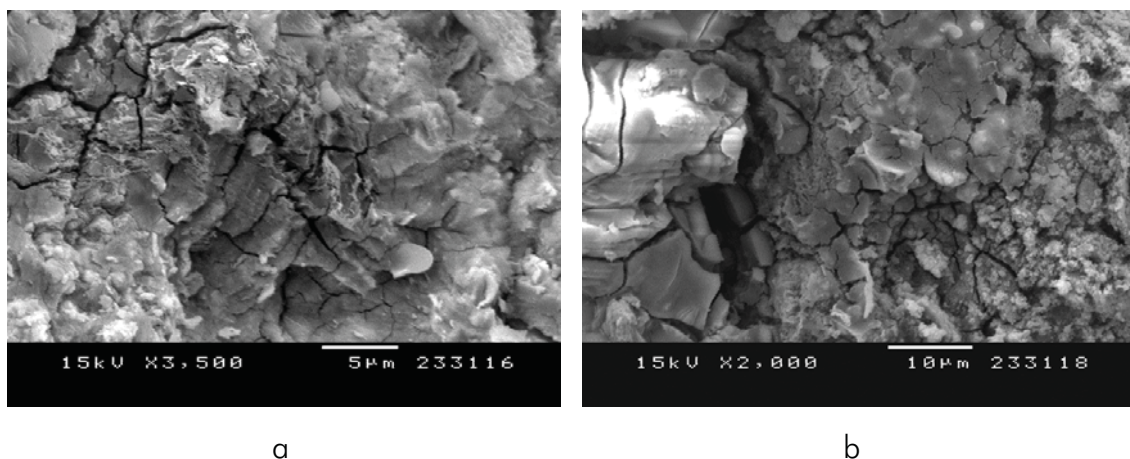
Figure 4.31. Surface morphologies of the corroded MEC40-60 coating at 450°C for 240h.

a   b
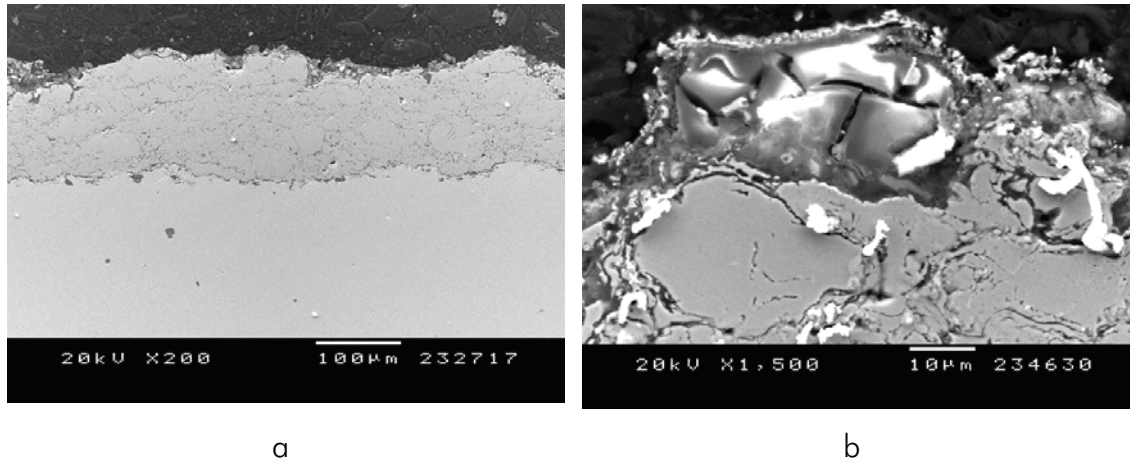
Figure 4.32. Cross section (a) general view and (b) magnification of the corroded MEC40-60 coating at 450°C for 240h.

a   b
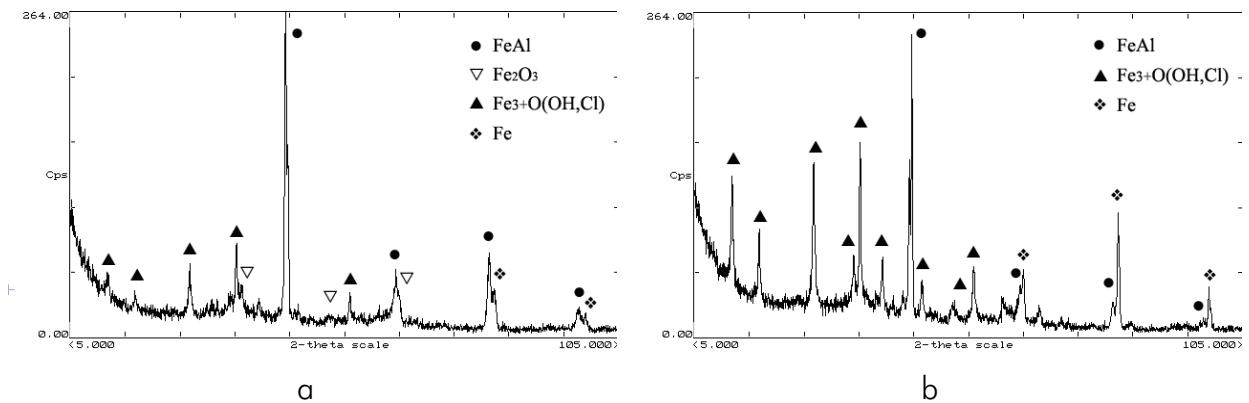
Figure 4.33. X-ray spectra of the (a) CEA and (b) MEC40-60 coatings corroded at 450°C for 240h.

This test was not conducted for the as-referenced CRYO coating since, with larger Al-depleted areas, its corrosion performance was not expected to improve that exhibited by CEA.

e)   Magnetic properties

Figure 4.34 shows the M versus H curves for the studied coatings. All the specimens showed obvious ferromagnetic behaviour and both, CRYO and CEA presented the highest magnetic susceptibility and magnetization. This can be associated to the larger Fe-rich areas compared to the as-sprayed 40-60 particle size range where no Al-depleted zones were encountered; actually,

saturation magnetization is known to decrease with addition of Al as if Al simply diluted the magnetic ions of Fe [29]. In the CRYO sample, the higher Fe content might be also given by the contamination from the stainless steel vessel and balls when cryomilling. These two samples also exhibited higher remanence. According to Harrison and Putnis [30], the Curie temperature (T_C) and the saturation magnetization (M_S) are determined mainly by the fundamental crystal chemical state, whereas coercivity (H_C) and remanence (M_{rs}) are determined by the microstructure of the specimen.
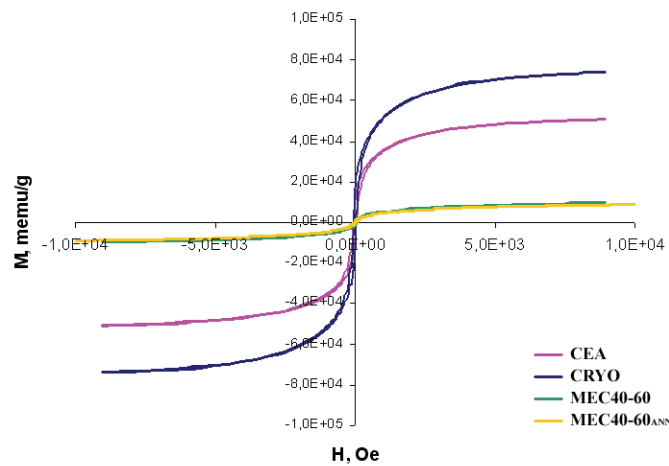
Figure 4.34. M versus H curves for the as-sprayed samples.

They all showed a small hysteretic component and even MEC40-60 type specimens, which showed mainly paramagnetic behaviour, still have non-zero value for coercivity (fig. 4.35).

When comparing MEC40-60 and MEC40-60$_{ANN}$, the first one has slightly higher magnetization (fig. 4.36), which would agree with the fact that in the as-sprayed non-annealed powder, there is a predominant disordered structure with more Fe-Fe nearest neighbours [31, 32, 33]. In the present case, no differences were observed in the coercivity levels among the different specimens; other authors have however, observed for other alloys that coercivity increases with the amount of non-magnetic element addition, and

decreases with the presence of the mixture amorphous and nanostructured phases [34, 35], as well as with decrease of the grains size [36].
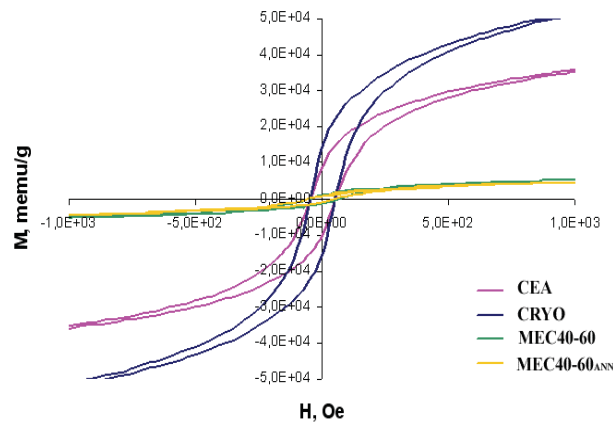
Figure 4.35. M versus *H* curve enlargements for the as-sprayed samples.
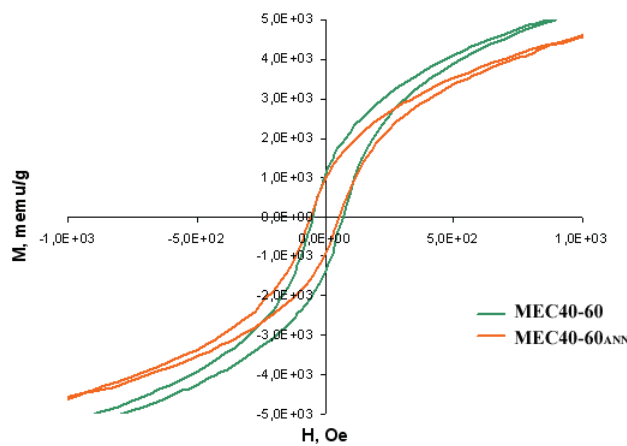
Figure 4.36. M versus *H* curve enlargement for the MEC40-60 type specimens.

4.2 Nb-Al system results

The research around this system was introduced in the last period of this thesis. It has resulted in the submission of the article entitled "FeAl and NbAl$_3$ intermetallic–HVOF coatings: Structure and Properties", where a comparison with FeAl is done. Many reports mention about NbAl$_3$ its good high-temperature strength, high melting point and low density that would make it

attractive for high-temperature applications. However, the main problem is its unstable oxidation resistance at medium-high temperatures. Other authors have already stated the failure this intermetallic suffers in oxidizing atmospheres [37]. Since there have not been previous attempts within the literature to form thermal spray coatings of this alloy, this has been our first goal and some temptatives to improve their oxidation performance might be done afterwards by e.g. ternary alloying.

Paper 6:   J.M.Guilemany, N. Cinca, S. Dosta, I.G. Cano, FeAl and NbAl$_3$ intermetallic–HVOF coatings: Structure and Properties, *Journal of Thermal Spray.*

Considering the higher melting point of NbAl$_3$ (1680°C) compared with that of FeAl (1250°C), it was necessary a hotter flame, so the oxygen flow rate was increased achieving an oxygen/propylene ratio (4.2). The main problem was however, obtaining a homogeneous deposit as during many attempts, the injector was easily blocked by the fine powder producing the oxidation and cracking of the last layers in the coating.

With regard to the mechanical properties, NbAl$_3$ resulted to be harder but less abrasive and friction resistant than the iron aluminide, which was attributed to embrittlement produced by the high oxidation content in the interlamella boundaries; this may then favour the third-body abrasive wear and facilitate the delamination by friction damage. Furthermore, their oxidation kinetics were associated to a logarithmic scale, with an increased rate for NbAl$_3$, where the so-called pesting phenomena leads to the formation of porous and non-protective oxides such as Nb$_2$O$_5$ and NbAlO$_4$.

FeAl and NbAl₃ intermetallic–HVOF coatings: structure and properties

J.M. Guilemany, N. Cinca, S. Dosta, I.G. Cano

Centre de Projecció Tèrmica (CPT). Universitat de Barcelona

Martí i Franquès 1, E-08028, Barcelona, Spain

Abstract

Today transition metal aluminides are being explored in their coating form by means of weld overlays, electro-spark deposition (ESD), pack cementation and thermal spray technologies. Their properties, such as oxidation resistance and mechanical behavior, are being examined. Basically, this current metallurgical interest in transition metal aluminides is due to their high Al content, which makes them attractive for high-temperature applications. This is also an incentive to studying their wear resistance, since this would allow them to be used in wear applications in aggressive environments instead of currently established coating materials.

This study evaluates the microstructure, microhardness, wear and oxidation performance of FeAl and NbAl₃ coatings produced by High Velocity Oxy-Fuel spraying. The main purposes are two: (i) to compare these two systems –a commonly studied aluminide (FeAl) and an exotic combination (NbAl₃) whose deposition by thermal spraying has not been attempted to date–, and (ii) to analyze the microstructure-properties relationship and so clarify their wear and oxidation mechanisms. Finally, although pesting phenomena (accelerated disintegration in oxidizing environments) were already known in bulk niobium aluminides, here we examined their performance in the coating form.

1   Introduction

In recent decades, many approaches have addressed the challenge of using transition metal aluminides for structural applications. These are called advanced materials due to their possible use for high-temperature applications with light-weight benefits and reasonably good strengths [1]. Hence, important advantages such as high melting points, high strength-to-weight ratios and excellent resistance to hostile environments have focused attention on nickel, iron and titanium-based aluminides [2, 3, 4]. The main shortcoming of these materials, however, is their poor ductility, which is improved by changing the processing routes or by addition of ternary elements. This lack of ductility is one of the reasons why they are good candidates for use as coating. Moreover, it allows the addition of enough aluminum content to satisfy oxidation requirements. Otherwise, if the aluminum levels were too high, it would not be possible to manufacture structural components with good load-carrying capabilities.

Current research on these compounds in bulk form focuses mainly on their brittleness and high-temperature behavior. Few wear-related studies have been undertaken, and creep and fatigue resistance must be investigated further. In terms of their use as overlays, as the new material was supplied for steel substrate protection in the early 1970's, a variety of aluminides and silicides were applied as oxidation protective coatings. Aluminides were the earliest choices for lower temperature environments or shorter

thermal cycles. The literature, however, just reports structural properties and gives few characterization results on the hardness and wear performance of thermal-sprayed coatings.

The present study reviews the results obtained for iron aluminide coating (microstructure, hardness, wear and oxidation resistance) and compares this with a niobium aluminide coating. The Fe-Al system is fairly well understood: basically, the stoichiometric compositions Fe_3Al and FeAl are proposed for commercial use. With nearly 50%Al, the Fe40Al composition was selected for our purposes, as Grade 3 powder is commercially available with a nanocrystalline structure. Within the Nb-Al system, there are much more complex crystal structures than that of the CsCl-type for FeAl: this leads to higher melting points and, thus, more affordable temperature efficiencies [5]. Nevertheless, the compound with the highest Al content, i.e. $NbAl_3$, suffers from catastrophic oxidation behavior as a result of the phenomenon known as "pesting". This has been of great concern since the early studies on niobium alloys appeared as a result of developments in the aircraft engine industry. Specifically, much of the development was within the context of the growing space program. In the later 1960's and mid-1970's, there was an increase in research into high-strength niobium alloys. The main survivors were those with alloying elements such as Hf, W, Ta or W [6]. However, Hebda already reported in that historical review [7] that there is little optimism as to the practical use of niobium alloys for long-life turbojet engines because of the unrealiablity of their coating and the inaccessibility of internal components for frequent inspection of coating disintegration. Some authors have attempted to decrease this effect and some recent studies on nanocrystallization, despite being still at the preliminary stage, appear to report some success [8]. This is why there is still interest in a coating with improved life and higher temperature resistance, but no strong demand for higher-temperature niobium alloys.

This paper emphasizes the different properties encountered for both as-sprayed FeAl and $NbAl_3$ by High Velocity Oxy-Fuel (HVOF) technology, in the attempt to balance their mechanical and oxidation properties. Among the group of thermal spray methods, HVOF was employed as a way of reducing the oxidation of the powder particles during their time residence within the flame and of producing dense coatings with the highest amount of intermetallic phase possible.

2   Experimental Procedure

FeAl and $NbAl_3$ feedstock powders were supplied by CEA-DTEN (Grenoble) and ABSCO Ltd manufacturing, respectively. The former is Grade 3 (atomised and ball-milled) with a nominal composition of Fe–40Al–0.05 Zr (at.%) with 50 ppm B and 1 wt.% Y_2O_3, while the latter is the alloy obtained by mechanical alloying. Their particle size distribution was studied by means of a laser diffraction particle size analyzer BECKMAN COULTER LS and their flowability was measured according to the ASTM B-213-30 standard. These powders were sprayed onto low-alloy carbon steel specimens.

A Diamond Jet Hybrid (DJH2700) from SULZER METCO was used to produce the coatings, with the thermal spray parameters reported in Table 1. $NbAl_3$ powder was pre-heated before spraying to improve its flowability through the nozzle. The powders and the as-sprayed coatings were examined by Scanning Electron Microscopy (JEOL 5510) operated at 20 kV with a coupled EDS system. The XRD analyses

were performed in a Bragg-Brentano θ/2θ Siemens D-500 diffractometer with a graphite monochromator using Cu Kα radiation.

For the Vickers micro-indentation tests, Matsuzawa MXT-α equipment with a normal load of 200gf was used. At least 10 measurements were performed on each sample to obtain the mean value.

Wear resistance was evaluated by a Ball-on disk test (ASTM G99-03) and a Rubber-wheel test (ASTM G65-00) for the sliding friction and abrasive effects, respectively. In the former, the sliding counterpart is a ∅11mm WC-Co ball that slides over the polished sample with a circle track of 16mm up to a full distance of 1000m and with an applied normal load of 5N; whereas the rotating rubber wheel moves at a constant speed of 139 rpm on the specimen, while silica particles flow by gravity between the two surfaces. A normal load of 50 N is applied and the mass loss is measured up to 30 min. The friction wear rate ($mm^3 N^{-1} m^{-1}$) was calculated from the volume loss obtained by means of white light interferometry (SWLI) using a surface analysis microscope (Zygo New View 100); the abrasive wear rate was calculated from the mass loss per test time.

Finally, oxidation behavior was assessed in two ways. First, the oxidation kinetics were tested through thermogravimetric measurements carried out for small pieces of debonded coating, under continuous air flow in TA Instruments SDT 2960 DSC-TGA equipment with a heating rate of 10ºC/min. The isothermal tests were carried out for 72h at 500ºC and 900ºC to explore their performance at moderate and high temperatures. Second, to examine the performance of as-sprayed deposits, these were placed in a furnace under oxidizing conditions and left for 72h at the same temperatures (500ºC and 900ºC). Furthermore, as we were aware of the oxidation damage caused by pesting, one set of samples was tested for 1h under oxidating and low-oxidating conditions (with Ar flux) in order to clarify what happens at early stages of oxidation.

3   Results and discussion

3.1   Feedstock powder characterization

Figure 1 shows the main characteristics of Fe40Al powder; it has angular-shape topography (Fig 1a) as a result of the milling. As has already been discussed in other studies in which such powder has been used, the milling step pursued two goals: first, intense plastic deformation induces nanocrystallization within the structure, as can be seen from the broad x-ray peaks (Fig. 1c) and last-minute yttria addition was intended to reinforce grain boundaries. Figure 1b shows homogeneous particle size distribution with d_{90} below 31 microns, which made them suitable because of their good flowability and suggested a good powder for spraying.

Second, Figure 2 shows the main features for niobium aluminide powder. A first examination at low magnification showed that there were really different particle sizes. Some can even reach 50 microns, whereas there are also very small particles that tend to agglomerate. According to the particle size plot, instead of good symmetrical distribution, such as was found for FeAl powder, $NbAl_3$ leads to a very broad low-size range. As could be expected from this, the powder showed no flowability at all, which would mean many difficulties for spraying. The x-ray trace shows that it is formed by predominantly $NbAl_3$ phase with a trace of Nb_2Al (Fig. 2c).

3.2   Coating microstructures

The characteristics of the Fe40Al coating have been discussed in detail elsewhere [9]. It can be seen from Figure 5a that it consists of a homogeneous and quite dense coating with good adherence and intersplat cohesion. At higher magnification, the microstructure features grey and dark contrasts associated with the intermetallic phase and oxidation. Oxide phases are mainly encountered at the splat boundaries as a result of particle oxidation during particle in-flight; some light contrast also indicates that these areas have been depleted in Al (Fe-rich zones). According to the X-ray scan, there is the intermetallic phase as well as the spinel $FeAl_2O_4$ oxide (Fig. 5c). Here, it is worth noting that, while the initial powder just showed the characteristic fundamental lines of the B2 lattice (h+k+l=even), indicating it had a disordered structure, the spraying process leads to the appearance of super-lattice lines (h+k+l=odd). The ordering effect is attributed to the high temperatures, which made it possible to rearrange atoms to some extent. However, Al depletion, as well as the partial melting of particle cores, prevents the achievement of an ordered B2 structure.

$NbAl_3$ powder often blocked the nozzle, making it difficult to achieve a uniform coating. Despite these problems, a 92 ± 5 microns-thick deposit was achieved (Fig. 6a). Figure 6b shows its microstructure with characteristic lamellas (fully melted particles), surrounded by open porosity, dark grey and light contrasts corresponding to oxidation and Nb-rich zones, according to EDS microanalysis. In both iron and niobium aluminides, propylene was used as fuel; however, the much lower value for the iron aluminide coating left much more fuel unused, which served as cooling. These conditions also helped to minimize oxide content. In a previous study, various conditions were tested, leading to the conclusion that these were among the optimum ones [9]. The $NbAl_3$ alloy, with a higher melting point, i.e. 1680ºC against 1250ºC for FeAl, made us change the spraying parameters to a higher oxygen/fuel ratio for good efficiency. With up to ~4.2 ratio, propylene has in this case a negligible effect on cooling particle temperatures and high oxygen flux leads to considerable oxidation.

3.3   Mechanical properties: hardness, friction and abrasive behavior

The Vickers indentation test gives greater hardness for the niobium aluminide coatings with HV_{200} 666 ± 28, whereas the iron aluminide sample had around 434 ± 48. The hardness value is influenced by all the phases included in the indentation print, which means that 434 HV_{200} is the mean hardness value between FeAl and $FeAl_2O_4$ phases, whereas 666 HV_{200} is in there among $NbAl_3$, NbO and NbO_2.

Previous thermal-sprayed FeAl coatings obtained by other authors reached hardnesses of 520 HV at most, because of the lower porosity and oxidation spraying at the highest particle velocities [10, 11]. Although it might not be reliable to compare two different techniques; just for reference, a recent study reported the formation of a niobium aluminide overlay using Plasma Transferred Arc (PTA), which consists of a welding process to produce dense coatings but with a high influence on dilution, this is, the participation of the substrate in the coating alters the chemical composition [12]. On analysis of different intermetallic Ni-Al, Fe-Al and Nb-Al mixtures, greater hardness was also achieved for the niobium aluminide coating processed with the richer Al (40wt.%) powder, obtaining a hardness value over 620HV. It also exhibited the highest abrasive resistance, as abrasive damage is normally dependent on material hardness [13]. However, Table 2 shows that, despite being harder, our niobium aluminide coating has the lowest abrasive resistance. A possible explanation for this is that so much oxidation at the interlamella

boundaries might have produced an embrittlement effect favoring crack nucleation and detachment of particles rather than plastic deformation.

In terms of friction wear, the ball-on-disc tests showed that the iron aluminide coating possessed a higher friction coefficient (Fig. 5), but lower wear rate (Table 3). This could be explained by assuming that the embrittlement effect associated with the intersplat oxidation explained above facilitates the delamination mechanism by which the material is removed. It causes much more severe damage in the niobium aluminide coating. However, examination of the wear tracks shows that iron aluminide debris is formed by plate-like shapes corresponding to oxidized areas (Fig. 6a), whereas the niobium aluminide coating shows scratch wear scars with some fractured regions (Fig. 6b). Thus, FeAl shows an adhesive mechanism, but, instead of forming a transfer layer on the counterface, the wear debris is rather removed to the laterals of the wear track. In contrast, the morphology of the niobium aluminide wear track seems to have been the result of an abrasive mechanism, which is possible if wear debris remained between the two surfaces, producing a third-body abrasion effect.

3.4   Oxidation performance

Figure 7 shows the heat flow and mass gain-temperature dependence for the as-sprayed coatings. It should be noted that, while the iron aluminide coating shows continuous weight increase as a result of oxidation without any change in the heat flow curve, the niobium aluminide coating gains considerable weight at the same time as the heat flow curve demonstrates that some change is occurring. The two overlapping peaks with respective peak temperatures at approximately 595ºC and 710ºC correspond to severe oxidation processes, as the final product is a white powder-like material. As can be seen in the enlargement of Figure 8, the curve of the as-sprayed Fe40Al can be interpreted as an approximately linear function, while $NbAl_3$ shows more complex behavior: there is a first linear stage from 400ºC to 500ºC followed by an almost exponential function, thus suggesting that it has different oxidation mechanisms above and below 500ºC.

As a result of such observations, oxidation temperatures of 500ºC and 900ºC were chosen for the isothermal oxidation measurements, in order to study the kinetics of the medium- and high-temperature oxidation separately. The results of these measurements are shown in Figures 9 and 10. Fairly logarithmic-like behavior can be clearly seen at 500ºC of isothermal oxidation in the niobium aluminide coating (Fig. 9). The logarithmic-scale plot shows that the main oxidation at 500ºC starts early at about 20 min and that, at approximately 30 min, starts its acceleration up to 3,000 min, where near saturation level is reached. At 900ºC (Fig. 10), the iron aluminide coating shows a logarithmic oxidation rate that increases its weight asymptotically up to approximately 3% during the first 360 min (6h), at which moment its weight remains almost constant. In contrast, the as-sprayed $NbAl_3$ attains a 40%wt. increase in the first hour. With the logarithmic scale, one can see that both start their oxidation at about 20 min from the test's start, but $NbAl_3$ increases sharply from 20 to 50 min, beyond which moment it is stabilized. This time range corresponds to the interval from 400ºC to 900ºC, where it was already seen that it suffered the main oxidation processes.

In terms of microstructural phase formation, both iron and nickel aluminides have very different oxidation mechanisms from those for refractory metal compounds such as $MoSi_2$ or $NbAl_3$. In Ni- and Fe-based compounds with high Al content, the formation of a protective alumina layer prevents the formation of

the thermodynamically less stable but more rapid-growing oxides. Nevertheless, in Nb- and Ti-base systems, it should be taken into account that: (1) the base metal oxides (e.g. TiO_2 and NbO_2) are of comparable stability to alumina and have much higher growth rates than NiO or FeO, making the formation of a homogeneous Al_2O_3 layer difficult, (2) whenever the activity of Al is reduced, the stability of the oxide scale is considerably diminished. In particular, $NbAl_3$ and $MoSi_2$ [14] show Nb and Mo linear oxidation kinetics, promoting the removal of any sign of growth of protective oxide nuclei. In addition, $NbAl_3$ and $MoSi_2$, unlike $TiAl_3$, exist in a narrow composition range, so that a lower stoichiometric phase is formed beneath the oxide in the Al or Si depleted zone, which influences the subsequent stability and adherence of the protective oxide . An extensive study, which examined the oxidation properties of iron aluminide coating at 900, 1000 and 1100ºC, also reported this [15]. Oxidation at 900ºC featured the formation of a layered oxide scale consisting of a thin alumina layer and the formation of transient oxides on the top, e.g. $FeAl_2O_4$ and Fe_2O_3. This behavior is normally observed when Al concentration is low and the alumina is formed as internal oxide precipitates: this is not at all protective and allows the formation of rapidly growing iron oxide. However, as the oxide scale was fairly dense, oxidation resistance was reasonably good. Such an oxidation mechanism in the coating is based on the assumption of the Al-depletion of the powder material when building up the coating and the presence of internal coating defects that behave as additional paths for ion diffusion. The only problems then reported for the iron aluminide coating in terms of its oxidation resistance at 900ºC depend on the oxide scale adherence. Therefore, the extent of spallation will determine the oxidation rate.

Above 1000ºC, however, although the formation of a compact adherent α-alumina scale is reported for bulk materials, intrinsic Al depletion within the as-sprayed coating becomes critical and the presence of voids in the coating-oxide scale interface, as well as the mismatch of expansion coefficients, are the source of poor adherence and the trigger for rapid oxidation.

With regard to the oxidation of the niobium aluminide-coated specimen at 500ºC, it resulted in a light grey powder-like material, similarly to that observed after the TGA experiment inndicating that oxidation had alredy begun.

On the temperature being increased to 900ºC, the coating transformed into a thick white brittle layer, showing that $NbAlO_4$ had formed, as confirmed by XRD (Fig. 11a). When the scale was smashed, we also detected iron oxides (Fig. 11b), indicating that the steel substrate had oxidized beneath the coating. The top surface morphologies included the formation of some porous iron niobium oxide nodules and needle-like oxides typical of NbO_z (Fig. 12b) [16]. These iron niobium oxides, not observed at 500ºC, might be formed by Fe outwards diffusion. Finally, the difference in the expansion coefficients induced the detachment of the oxide scale.

However, when the coated sample was tested for 1h in the same oxidizing atmosphere at 900ºC, the scale was thinner and completely white, also with a powder-like morphology and with no signs of the presence of iron niobium oxides as in the oxidation at 500ºC. The experiment with an argon continuous flux did not even show that the coating turned white: it still conserved its dark grey color. Nevertheless, the X-ray (Fig. 13) already notices the beginning of the oxidation process shown by the presence of $NbAlO_4$ and $Fe_4Nb_2O_9$, indicating that the small remaining oxygen content within the atmosphere has already promoted slight oxidation. The formation of $NbAlO_4$ is one of the critical steps indicating that lower Nb-

Al binary compounds have been formed. In addition, examination of the top surface showed the cracking initiation process (Fig. 14a) and the formation of $NbAlO_4$ (Fig. 14b).

According to the above results and knowing that only the $NbAl_3$ "line compound" forms continuous alumina layers, the oxidation of the thermal sprayed coating could be summarized as follows: Al-depleted intersplat boundaries oxidize easily without giving time to the $NbAl_3$ parts to form any protective layer and, even if alumina was formed, it would have left a $NbAl_2$ sub-surface area that produced cracking, causing further oxygen penetration that would also oxidize this lower aluminide rapidly. At the same time as this is happening, there is an outward Fe diffusion that combines with niobium to form mixed oxides and inward oxygen penetration that results in steel substrate corrosion.

4   Conclusions

In all senses, iron aluminide coating behaves better than $NbAl_3$. Whether in the abrasion and friction or oxidation tests, niobium aluminide shows more damage and premature failure. The explanation for its worse wear properties may be related to the structure of the coating itself rather than the material, as it possesses much greater hardness, usually related to wear resistance. In oxidation analysis, despite the high melting point of $NbA1_3$, it suffers from "pesting" (intergranular disintegration) at moderate temperatures. This is favored by the high oxidation and coating defects that facilitate oxygen diffusion inwards and Al-depletion in the as-sprayed coating itself. With regard to the wear results, further damage is caused in the niobium coatings by both sliding and abrasive mechanisms, which is attributed to a brittle effect that leads to interlamellar cracking and easy decohesion.
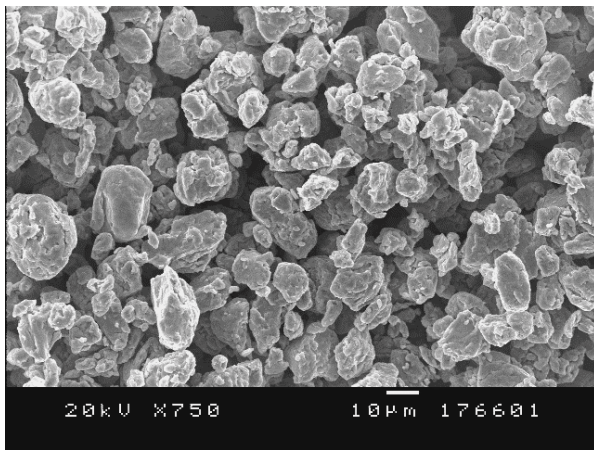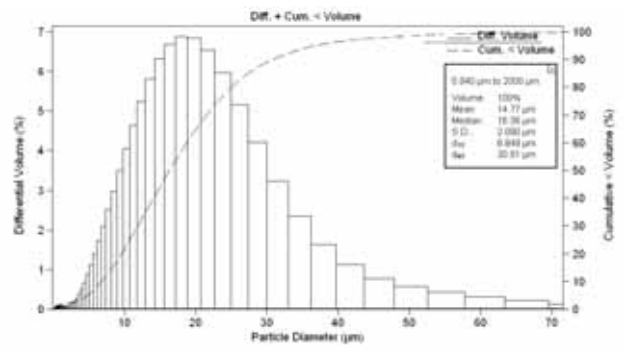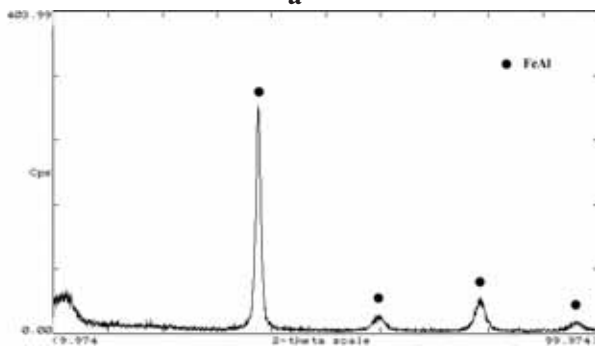
FIGURES

Figure 1. (a) Morphology, (b) particle size distribution and (c) x-ray scan of the Fe40%at.Al powder.
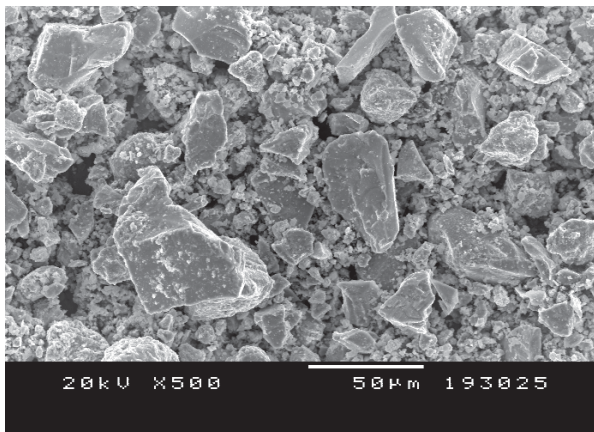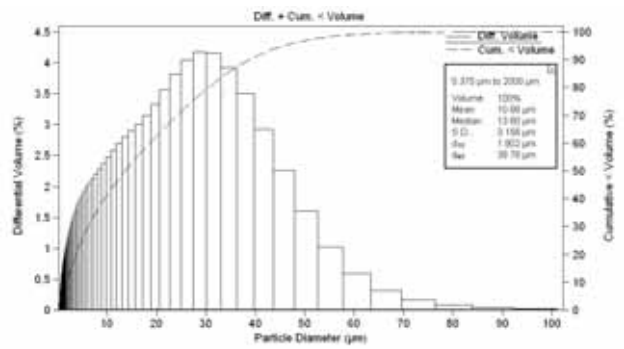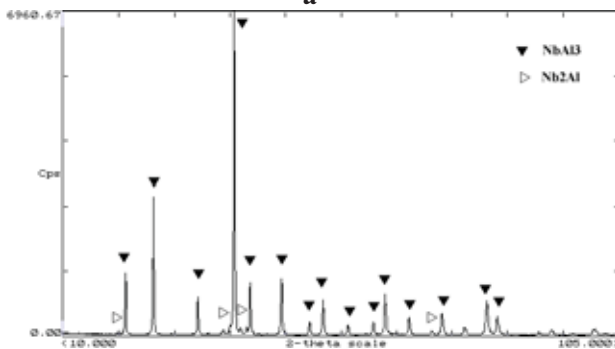
Figure 2. (a) Morphology, (b) particle size distribution and (c) x-ray scan of the NbAl₃ powder.
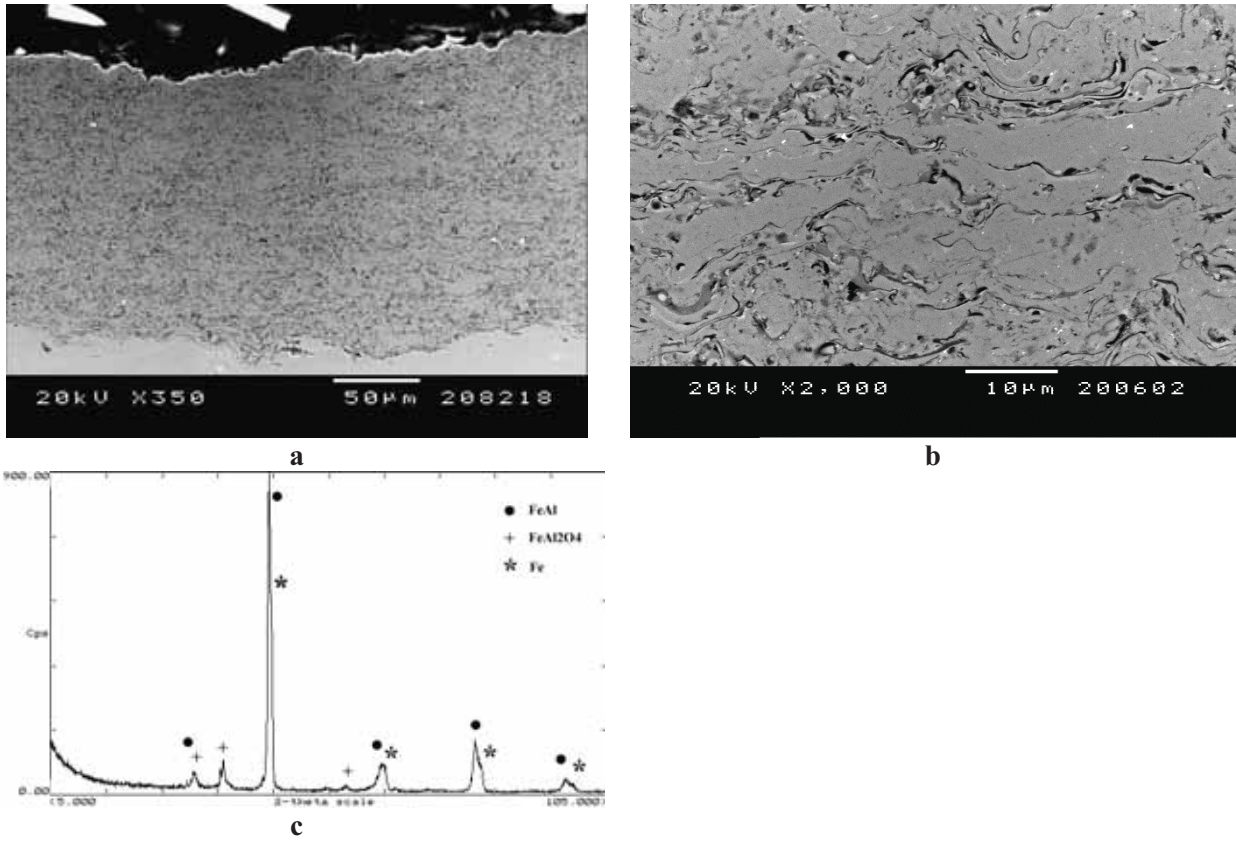
Figure 3. (a) General view and (b) magnification of the as-sprayed cross section Fe40Al coating and, (c) X-ray spectrum.

c
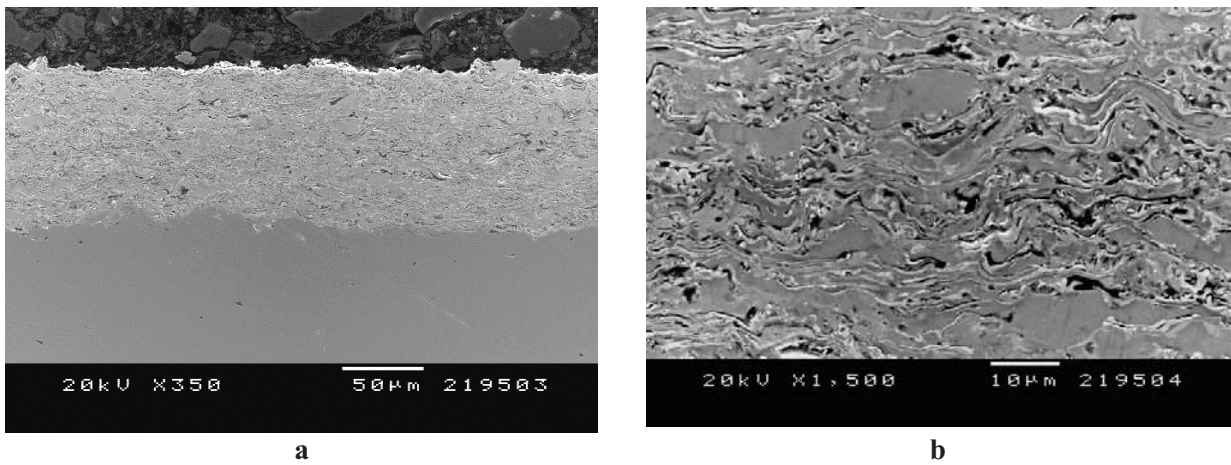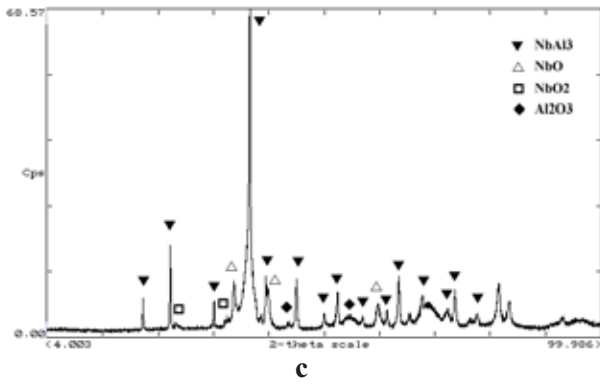
Figure 4. (a) General view and (b) magnification of the as-sprayed cross section NbAl$_3$ coating and, (c) X-ray spectrum.
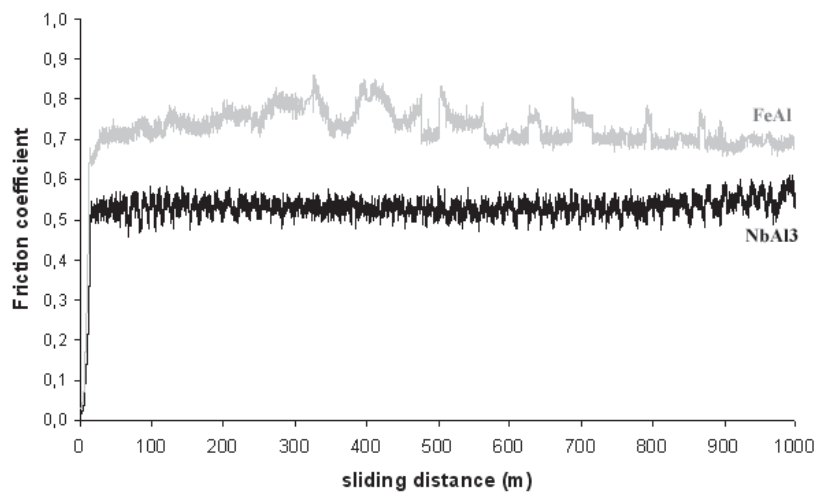
Figure 5. Friction coefficient of iron- and niobium aluminide coatings.
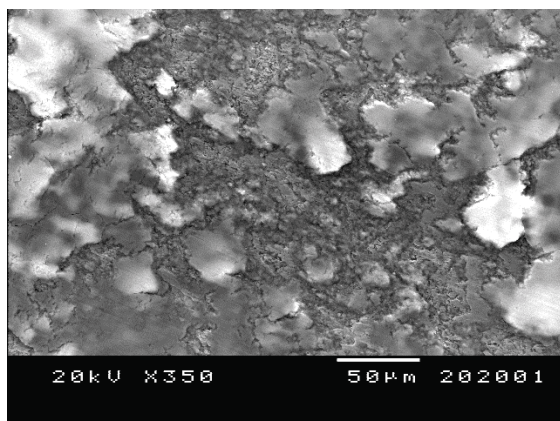
a
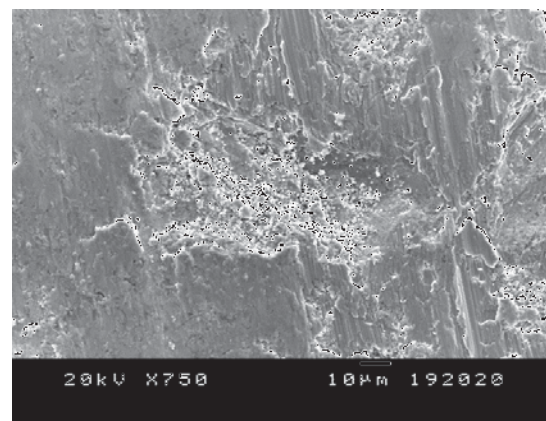
b

Figure 6. Debris morphologies on the wear track of (a) iron- and (b) niobium aluminide coatings.
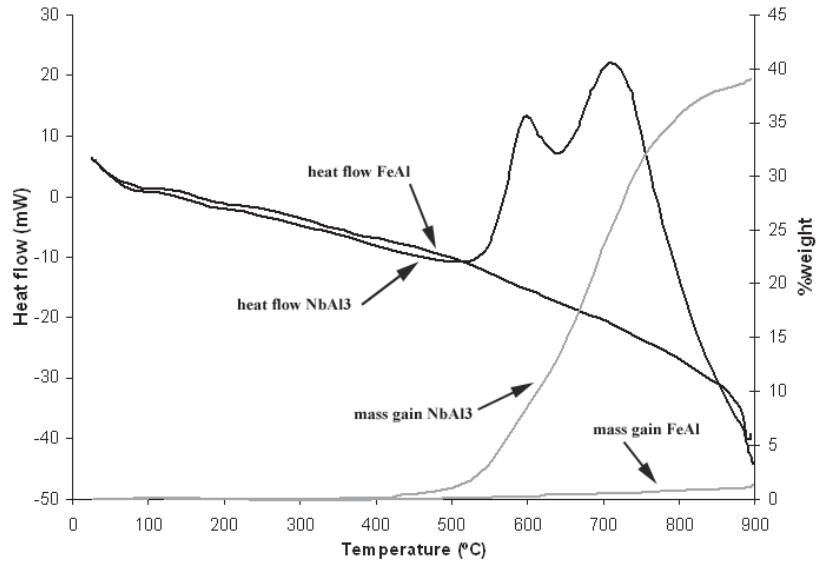
Figure 7. Heat flow and mass gain-temperature dependence for the as-sprayed coatings.
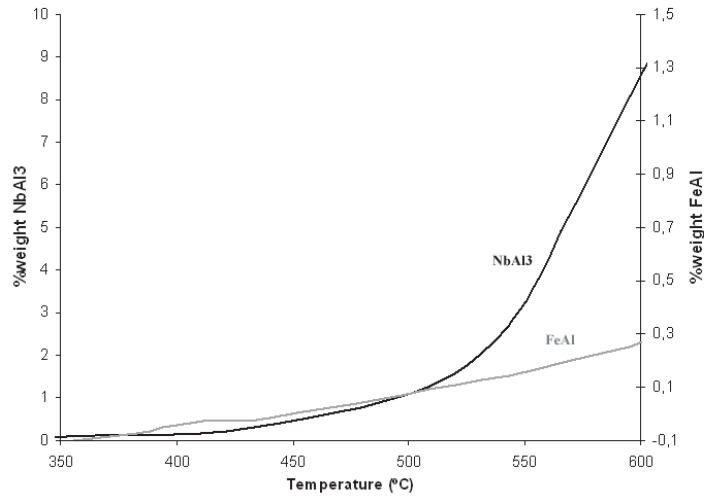
Figure 8. Magnification of the DSC-TGA measurements within the temperature range 350-600ºC.
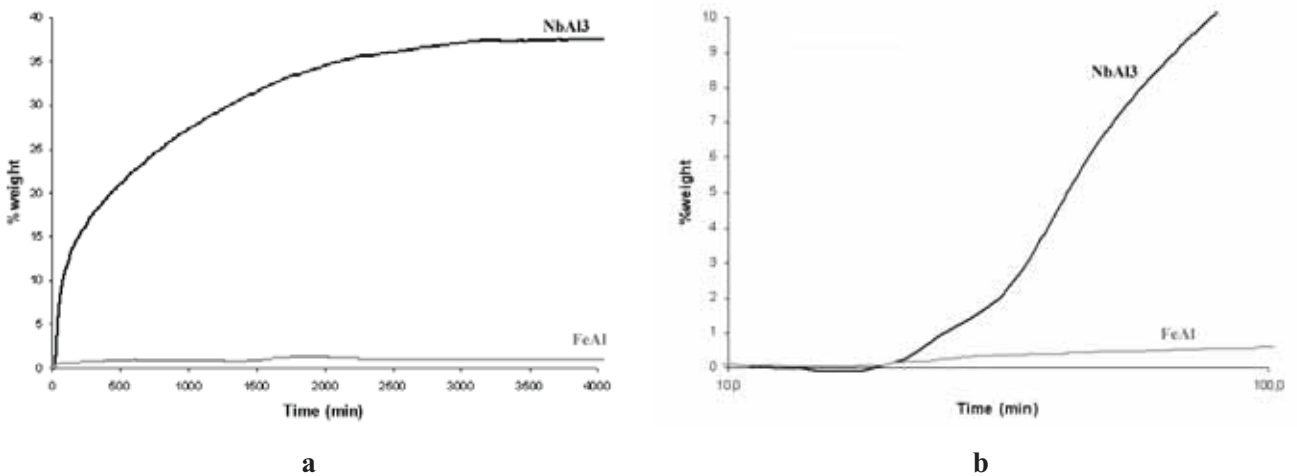
Figure 9. (a) Comparison of the mass change of the iron- and niobium aluminide specimens tested at

500ºC for 72h, (b) logaritmic scale.
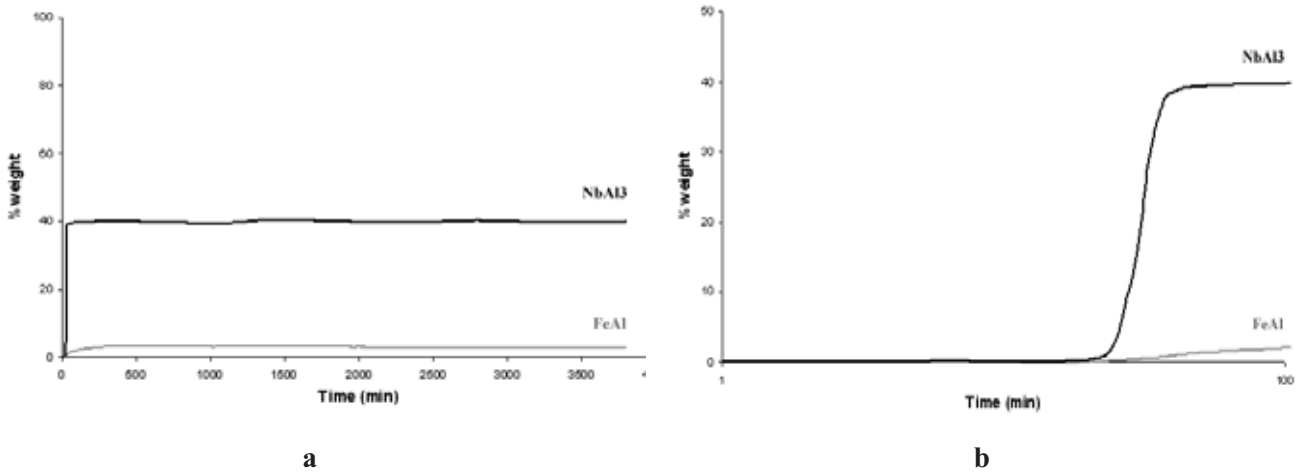
Figure 10. (a) Comparison of the mass change of the iron- and niobium aluminide specimens tested at 900ºC for 72h, (b) logaritmic scale.
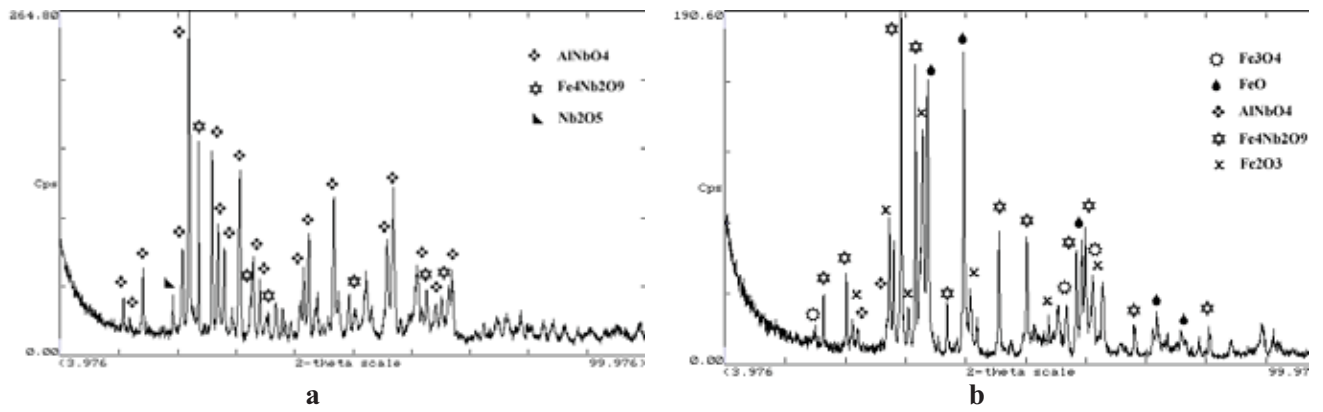
Figure 11. XRD spectra of the (a) top surface and (b) smashed oxide scale of the niobium aluminide coating oxidized for 72h at 900ºC in an air atmosphere.

153
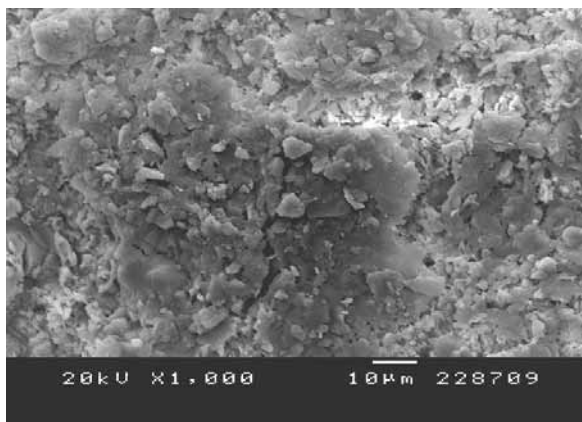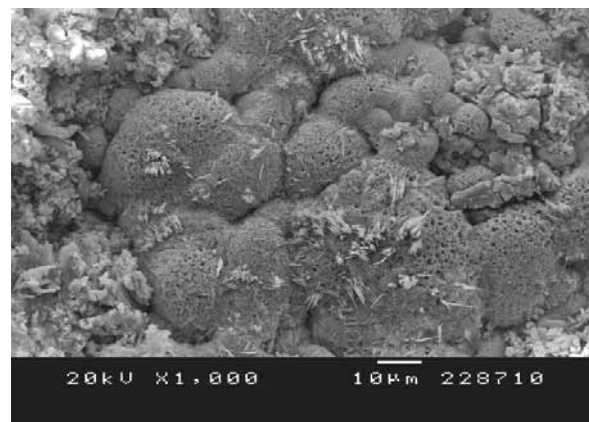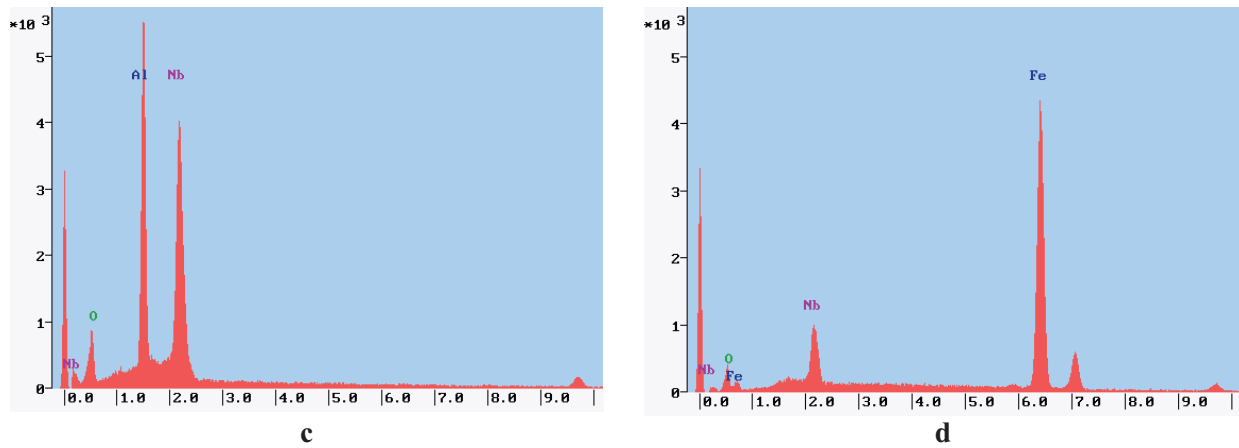
Figure 12. (a) and (b) Oxide morphologies on the top surface of the oxidized niobium aluminide coating for 72h at 900ºC in an air atmosphere and, (c), (d) their respective EDS microanalysis.
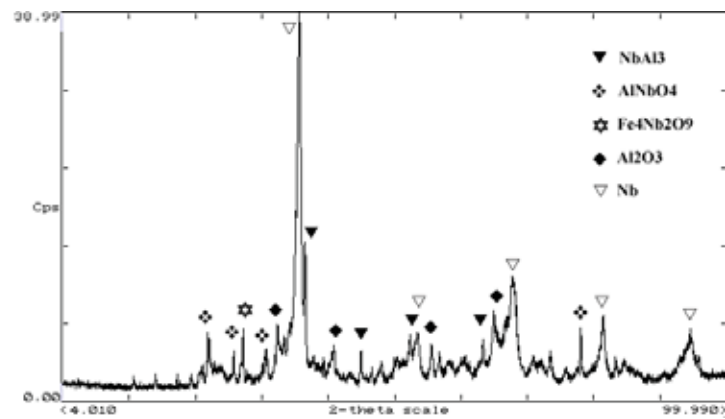
Figure 13. XRD spectrum of the oxidized niobium aluminide coating under low oxygen pressure conditions for 1h at 900ºC.
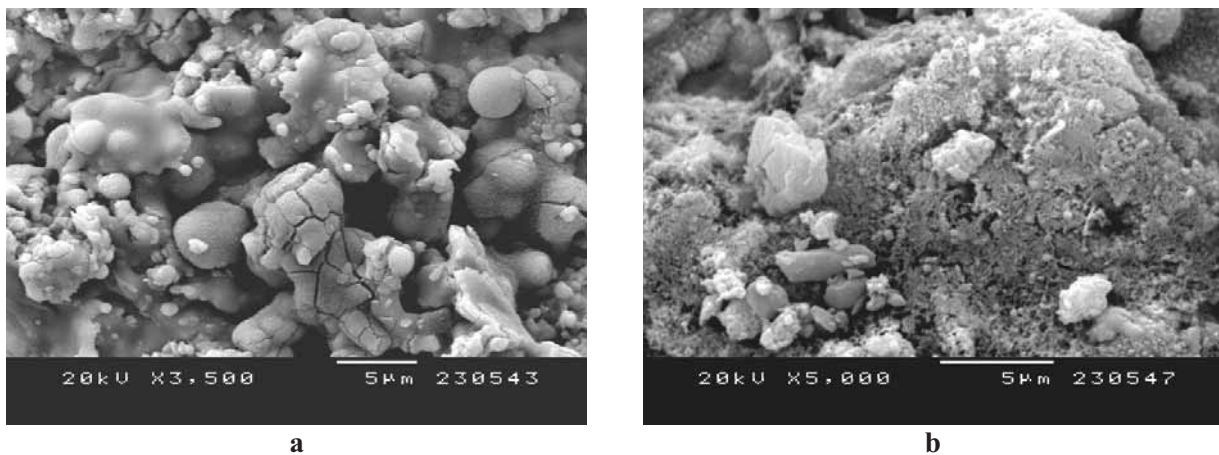
Figure 14. (a) and (b) Oxide morphologies on the top surface of the oxidized niobium aluminide coating under Ar flow at 900ºC for 1h.

154

TABLES

Table 1. Thermal spraying parameters.

	FeAl	**NbAl$_3$**
Oxygen flow rate (l/min)	180-190	250-260
Propylene flow rate (l/min)	80-90	70-80
Carrier gas (l/min)	300-310	370-380
Oxygen/fuel ratio	2.8	4.2
Feeding rate (g/min)	20	15
Spraying distance (mm)	250	240

Table 2. Abrasive wear rates.

	Abrasive wear rate (mm^3 /N m)
Fe40Al	3.7 10^{-5}
NbAl$_3$	1.2 10^{-4}

Table 3. Friction wear rates.

	Wear rate (mm^3/Nm)
Fe40Al	5.9 10^{-6}
NbAl$_3$	3.6 10^{-4}

References

[1] Westbrook J. H., Applications of Intermetallic Compounds, MRS Bulletin Vol. 21, Issue 5 (1996), 26-28.

[2] Deevi S. C., Sikka V. K., Liu C. T., Processing, properties and applications of nickel and iron aluminides, Progress in Materials Science, Vol. 42 (1997) 177-192.

[3] George E. P., Yamaguichi M., Kumar K. S., Liu C. T., Ordered intermetallics, Annual Review in Materials Science, Vol. 24 (1994) 409-51.

[4] Liu C. T., Stringer J., Mundy J. N., Horton L-L., Angelini P., Ordered intermetallic alloys: an assessment, Intermetallics, Vol. 5 (1997) 579-596.

[5] Hanada S., Niobium Aluminides, Institute for Materials Research, Tohoku University.

[6] www.cbmm.com.br/portug/sources/techlib/science_techno/table_content/sub_3/images/pdfs/016.pdf

[7] www.cbmm.com.br/portug/sources/techlib/science_techno/table_content/sub_3/images/pdfs/016.pdf

[8] Gauthier V., Bernard F., Gaffet E., Munir Z. A., Larpin J. P., Synthesis of nanocrystalline NbAl$_3$ by mechanical and field activation, Intermetallics, Vol. 9 (2001) 571-580.

[9] Guilemany J. M., Cinca N., Lima C. R. C., Miguel J. R., Studies of Fe40Al coatings obtained by High Velocity Oxy-Fuel. Surf & Coat Tech, 201 (2006) 2072-2079.

[10] Totemeier T., Wright R., Swank W. D., FeAl and Mo-Si-B intermetallic coatings prepared by thermal spraying, Intermetallics, 12 (2004), 1335-1344.

[11] Ji G., Grosdidier T., Liao H. L., Morniroli J., Coddet C., Spray forming thick nanostructured and microstructured FeAl deposits, Intermetallics, 13 (2005) 596-607.

[12] D'Oliveira A., de Christo A., Vaz D. S., Curitiba BR., Evaluation of intermetallic coatings processed by PTA, ITSC 08.

[13] Hutchings I. M., Tribology: Friction and Wear of engineering materials, Metallurgy and Materials Science Series, ISBN 0-340-56184-x.

[14] Kircher T. A., Courtright E. L., Engineering limitations of $MoSi_2$ coatings, Materials Science and Engineering A, Vol. 155 (1992) 67-74.

[15] Guilemany J. M., Cinca N., Dosta S., Lima C.R.C, High temperature corrosion of Fe-40Al coatings, Intermetallics, Vol. 15 (2007) 1384-1394.

[16] Huijbregts W.M.M, Brabers M.J., Oxidation of niobium coated with aluminium in steam-air mixtures, Journ. Intern d'étude sur l'Oxydation des metaux (1965) 61-69.

4.3   Ni-Ti system results

4.3.1   Powder characterization

Some of the experiments carried out with this powder have been published in the following paper: "Study of NiTi Metastable Powders and Coatings Obtained by Plasma Spraying" (*Appendix VII*). This work concludes that APS-quenching of a Ni-Ti powder mixture leads to the formation of the intermetallic NiTi phase but also TiO; starting from a prealloyed (atomised) powder, the oxidation was reduced and the intermetallic phase remains in a metastable structure given by its lattice parameter changes.

Therefore, owing to the already alloyed composition and the rounded particle morphology, which facilitates the spraying process, the atomised powder was chosen for coating deposition and further characterization. Although few aspects of powder and coating characterization have already been explained in the previous paper and, some others will be included in the paper entitled "Corrosion behaviour of thermal sprayed nitinol coatings", these will be briefly presented in the next section in order to have a global view.

a)   Particle size distribution and flowability

Figure 4.37 shows the particle size distribution of the alloyed powder. The curve shows an asymmetric peak with a broad right end which corresponds to the small amount of particles above 80 microns. According to this distribution, it appears that there are no particles below 10 microns, differently to what was observed in the iron aluminide powders, where the curve started from zero and was progressively increased in a more or less Gaussian shape. Due to the absence of small particle agglomeration and very large particles that might be responsible of injector blocking, this powder showed a fairly good flowability.
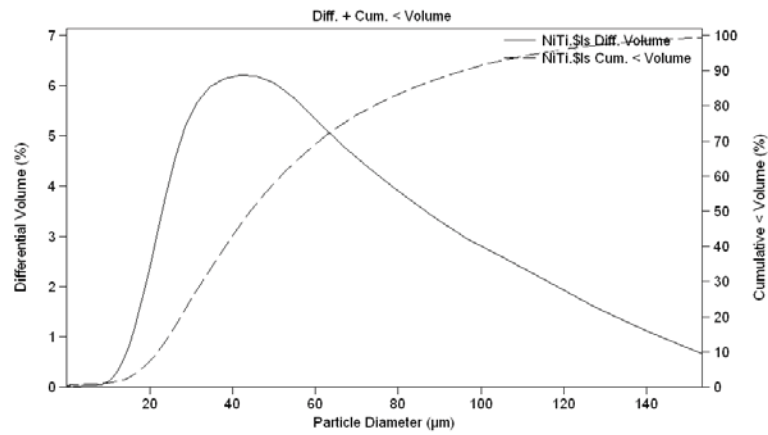
Figure 4.37. Particle size distribution for the alloyed NiTi powder.

b)   Morphology and phase analysis

This powder was obtained by gas atomization, thus its morphology is also spherical (fig. 4.38) as that exhibited by the unmilled Fe40Al.
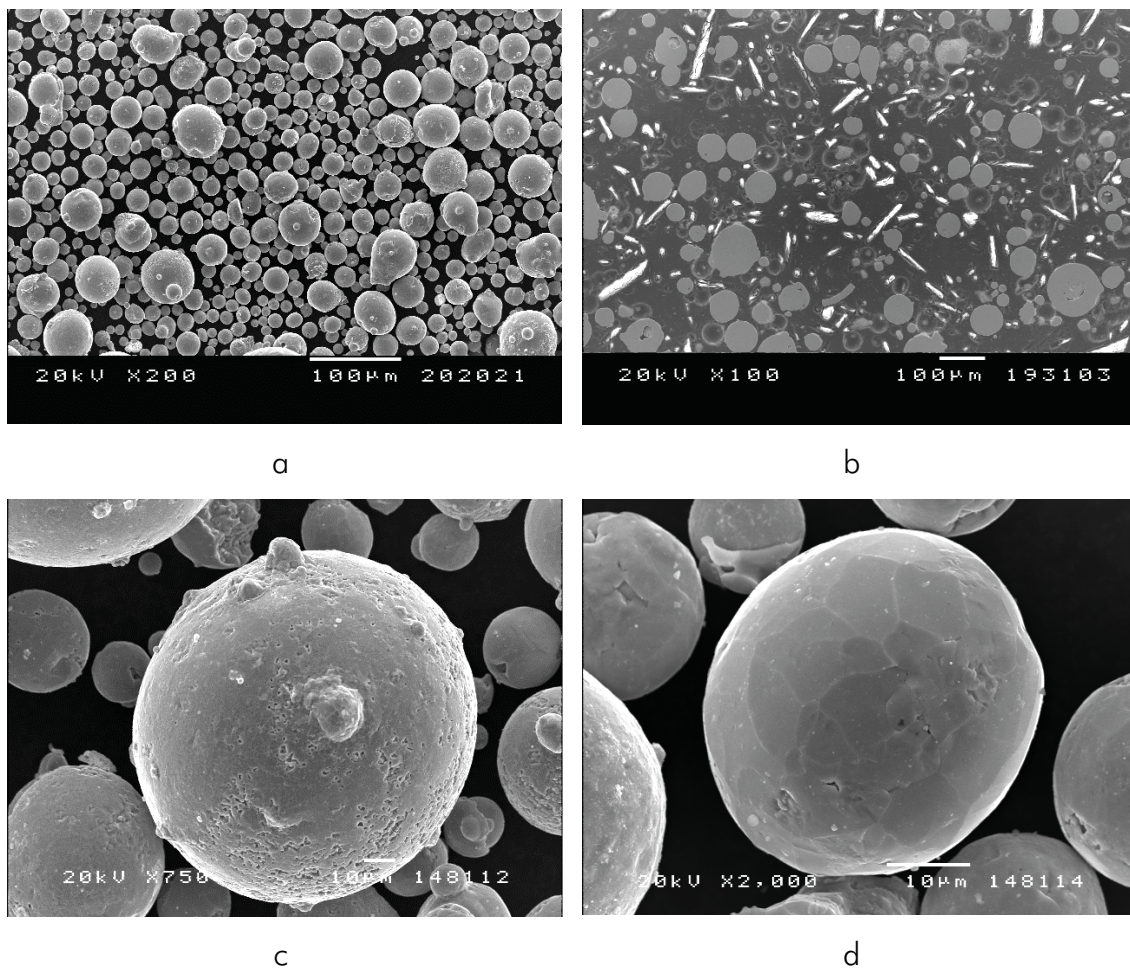
Figure 4.38. SEM micrographs of the NiTi powder (a) morphology and (b) cross section –general views– and, (c), (d) enlargements of a coarse and small particle respectively.

The larger particles in this powder have a rougher surface (fig. 4.38c) than the smaller ones (fig, 4.38d). By etching, one can see the existence of fine precipitates (fig. 4.39a), which can be identified as $NiTi_2$ or Ti_4Ni_2O –the peak positions of these two phases are identically the same [38]– (fig. 4.39b) in a matrix of austenitic-NiTi phase. Both phases could actually have formed: $NiTi_2$ is found beside the NiTi intermetallic compound in the Ni-Ti diagram and, this latter, in turn, exists in a narrow composition range so, when cooling from the liquid state, a small change in composition might lead to this Ti-rich side; also, due to the easy reaction of NiTi with oxygen, the small solubility limit might have been surpassed leading to the formation of Ti_4Ni_2O.
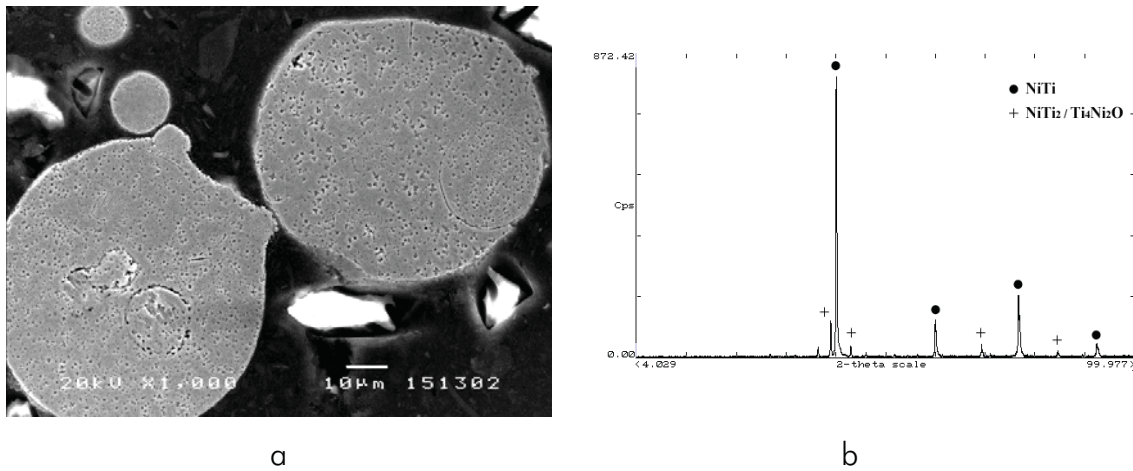
Figure 4.39. (a) Detail of the etched NiTi powder and (b) X-ray spectrum

The elemental analysis justifying the presence of oxygen might lead to the conclusion that those peaks correspond to the mixed oxide. Such particles are visible by etching the alloy with a mixture of $HF:HNO_3$ solution. Combinations of hydrofluoric acid, nitric acid, and water give some of the most useful solutions for chemical surface treatment of TiNi [39, 40, 41].

c)   Advanced studies on thermal stability

As it is known, the most important property in NiTi alloys is the shape memory effect and pseudoelasticity. Figure 4.40 plots heat flow versus time and versus

sample temperature during the following cicles: (i) cooling from room temperature to –125°C, (ii) heating from –125 to 100°C (x2). It is more common to see it versus temperature but, since the endothermic peak is clearer in the representation versus time, the parameters were recorded from these ones. Such peak is supposed to correspond to the transformation of the austenite phase which, having transformed to martensite when cooling, turns to austenite when heating. However, the reverse transformation was not appreciated. Some authors also did not observe any peak in the DSC at the cooling curve of the as-received NiTi solid solution [42, 43]. Miyazaki et al. have attributed the absence of peaks to the large hysteresis of such transformations [44].

a   b
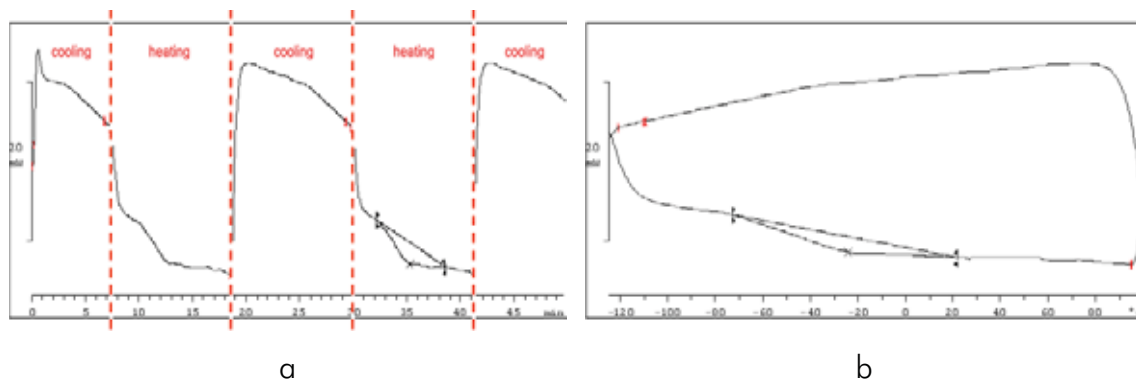
Figure 4.40. DSC of the NiTi powder.

4.3.2   Microstructural coating characterization

a)   Spraying parameters optimization

Due to the high reactivity of this alloy with oxygen to form TiO_x, the main technique to form thick coatings has been Vacuum Plasma Spray (VPS); our attempt has been to further explore the feasibility of other techniques such as HVOF and APS-quench.

- ▪ The optimization for VPS spraying was carried out in the Center for Thermal Spray Research (University of Stony Brook, NY); first, different splat runs were performed at 1g/min with a gun transverse speed

10mm/sec. There must be a precise control of the vacuum chamber and pressure conditions as otherwise the coatings exhibit a bluish surface finish indicating oxidation has taken place. The optimal parameters are given in table 4.7.

- The APS-quenching procedure has already been exposed in section 3.3.1. The plasma conditions were slightly modified, just the hydrogen flow and the spraying distance (table 4.8).

- The less porosity as possible is preferable for this type of alloy, especially because its corrosion resistance will be one of the most important properties to be evaluated and it requires a good sealing able to prevent the electrolyte path. Therefore, hydrogen was used to produce reasonable melting with minimum oxidation (table 4.9).

Table 4.7. Thermal spraying parameters for VPS.

Primary Argon plasma gas flow (l/min)	50
Secondary Hydrogen plasma gas flow (l/min)	8
Arc current (A)	600
Gun voltage (V)	72
Carrier Argon gas flow (l/min)	4
Chamber Vacuum Pressure (mbar)	60
Spraying distance (mm)	300

Table 4.8. Thermal spraying parameters for APS-quenching.

	Parameter set 1 (T1)	Parameter set 2 (T2)	Parameter set 3 (T3)
Argon (L/min)	35		
Hydrogen (L/min)	13	13	14
Arc current (A)	500		
Carrier gas, Ar (L/min)	4,5		
Spraying distance (mm)	120	110	120

Table 4.9. Thermal spraying parameters for HVOF.

	Parameter set
Oxygen flow rate (l/min)	214
Hydrogen (l/min)	635
Carrier gas (l/min)	344
Spraying distance (mm)	220
Oxygen-fuel ratio	0,445

b)   Structure morphologies and phase composition analysis

As already said, the paper entitled "Corrosion behaviour of thermal sprayed nitinol coatings", includes the characterization of the previous coatings, but these are here briefly reviewed in order to follow the same logical sequence as in FeAl.

-       *Scanning Electron Microscopy and X-ray diffraction*

Figure 4.41, 4.42 and 4.43 show the coating microstructures of the parameters presented in the former tables.

Neither porosity nor oxidation can be observed in the VPS coating and the splat morphology is only revealed by etching, leading to two distinct kind of areas (fig. 4.41); it is not actually clear why ones have been preferentially etched than the others but it seems that the rougher ones are slightly Ti-richer [45].
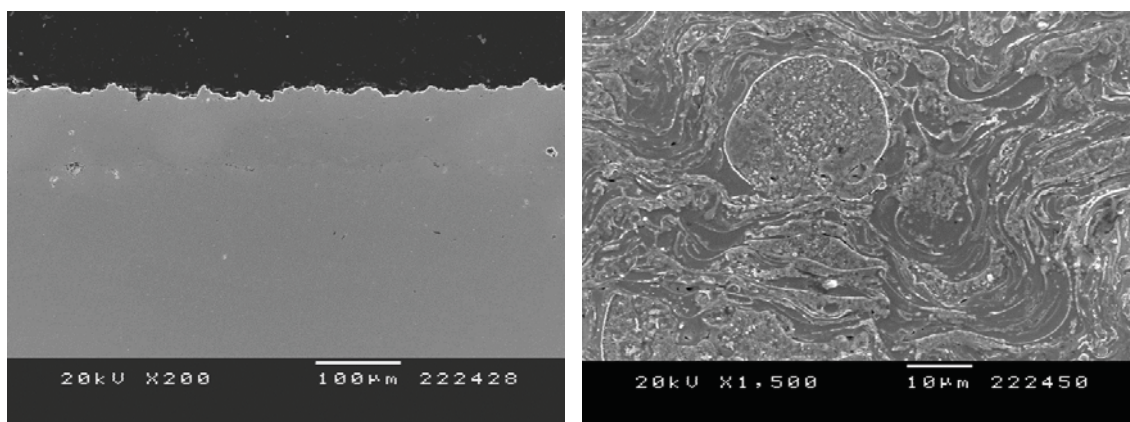
a   b

Figure 4.41. (a) General micrograph of the unetched VPS coating, (b) magnification of the revealed microstructure after etching.

Among the conditions in table 4.8, no big differences were observed; therefore, these were selected according to the fewer cracks within the structure (T3 conditions- fig. 4.42). Such cracks are perpendicular to the plane of splat deposition and are attributed to the rapid solidification when using the N_2 cooling device. In the XRD included in our articles about these NiTi-based

coatings, the oxide phase of the APS-quenching deposit was identified as TiO (fig. 4.44).
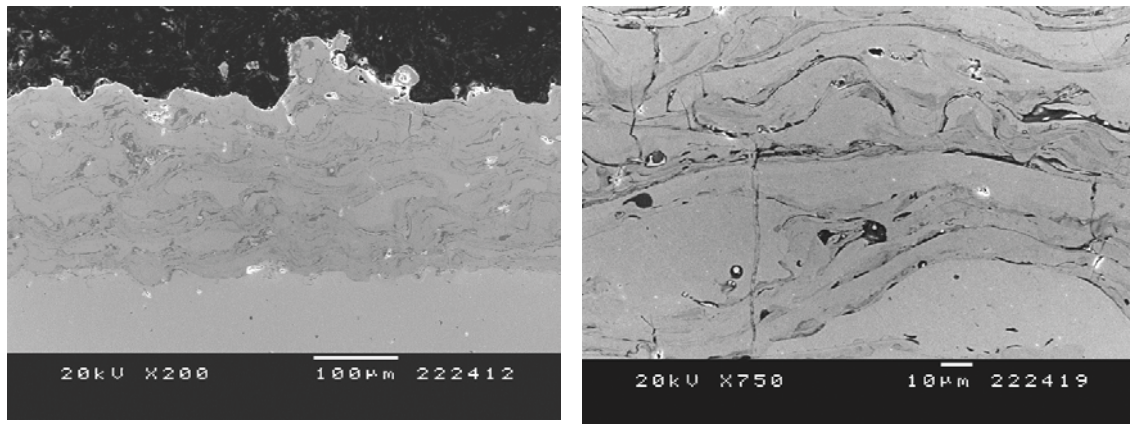
a   b

Figure 4.42. (a) General micrograph of the APS+Q coating (T3), (b) higher magnification.
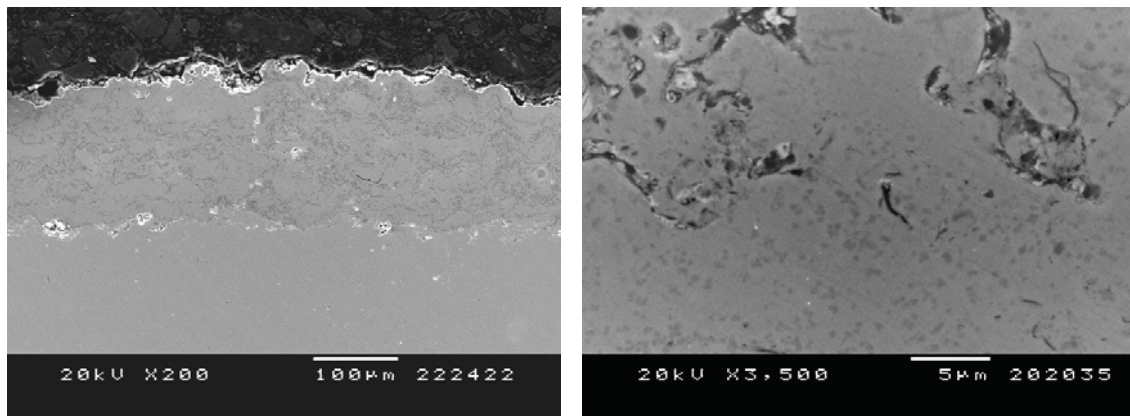
a   b

Figure 4.43. (a) General micrograph of the HVOF coating, (b) higher magnification.

By using HVOF, the coating still preserves the powder structure in the coarser particles which are non-fully molten (fig. 4.43b). The microstructure here is a little bit more complex than the other two: apart from the powder phases, Ni-rich zones and Ti_2O_3 have been also detected. The Ti-depleted areas can be attributed to the oxidation of this element, similarly as observed with the Fe-rich in FeAl due to the formation of Al-rich oxides.
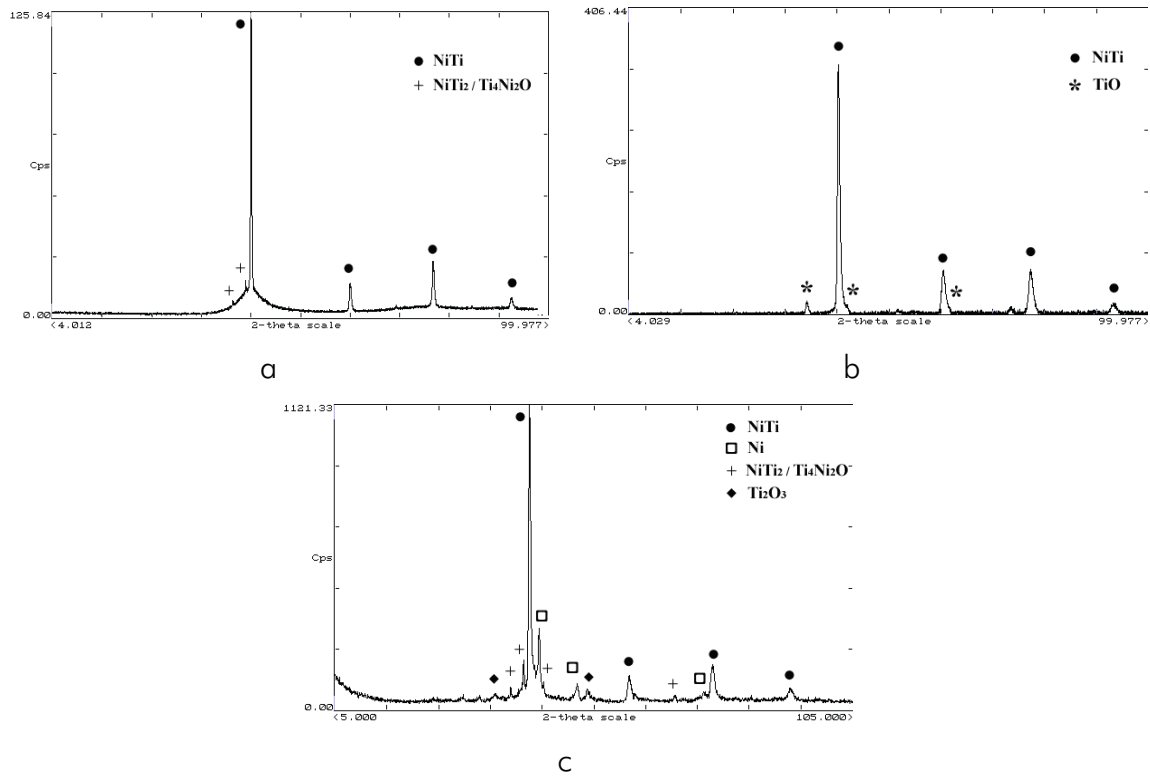
Figure 4.44. X-ray spectra of the (a) VPS, (b) APS+Q and (c) HVOF- NiTi coatings.

Figure 4.45 shows the top surface of the three coatings, which gives an idea of the degree of melting in each case. It is worth noting the cracks in the APS+Q coating (fig. 4.45b).
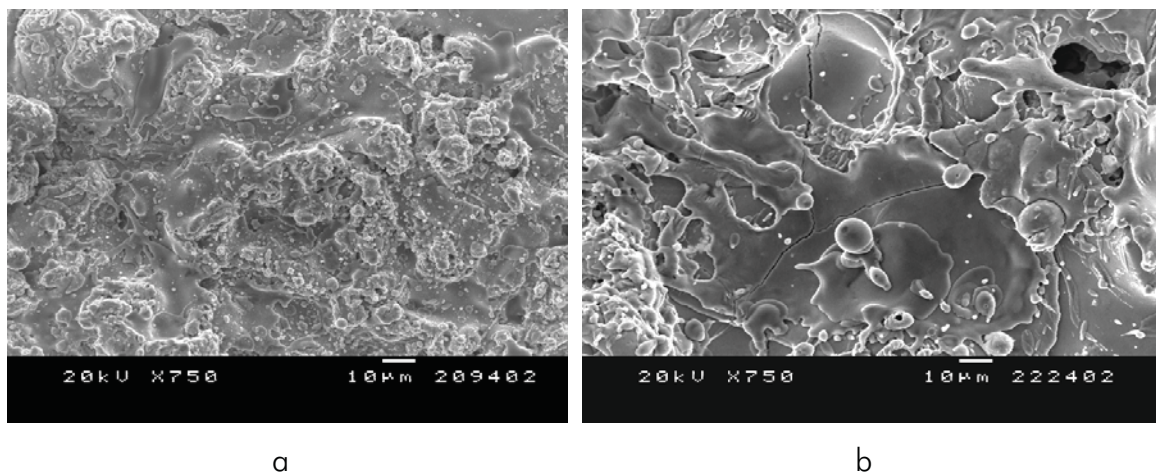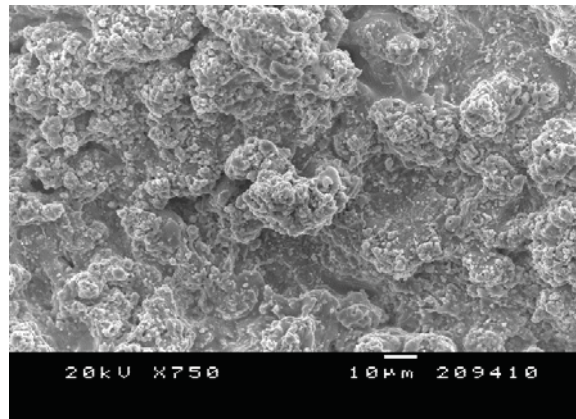
c

Figure 4.45. Surface morphologies of the (a) VPS, (b) APS+Q and (c) HVOF- NiTi coatings.

-        *Transmission Electron Microscopy*

Figure 4.46 shows the TEM features of the VPS coating; it was found that there were large amorphous zones (fig. 4.46a), polycrystalline regions with grain sizes in the microscale or some hundreds of nanometers (fig. 4.46b) and, grains in the nanoscale as in figure 4.46c [46]. The identification of the corresponding SAED patterns indicated that the coarser grains have a NiTi cubic structure (austenite) while in the nanocrystalline areas the monoclinic NiTi (martensite) phase might have formed by the rapid cooling from high temperatures during spraying (figs. 4.46b and d). According to several EDX analyses, the amorphous area appeared to have higher Ni content but no association could be found with the two different phases revealed when etching (fig. 4.41b).

a   b

c   d
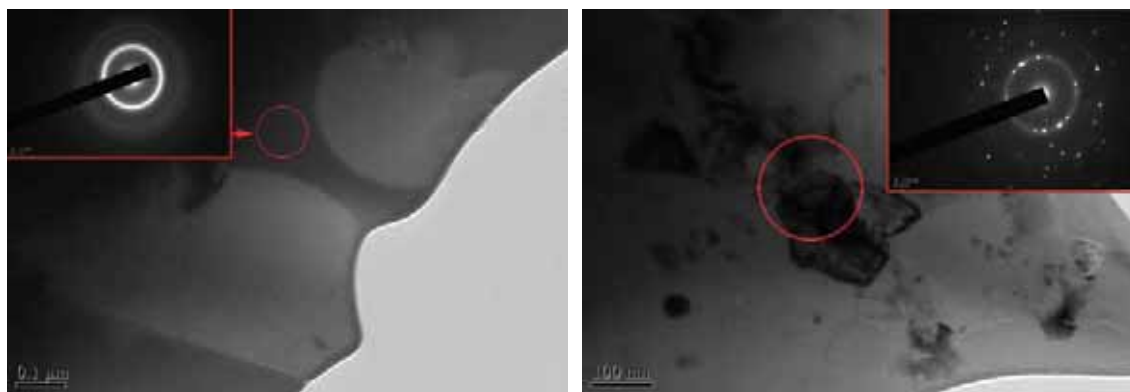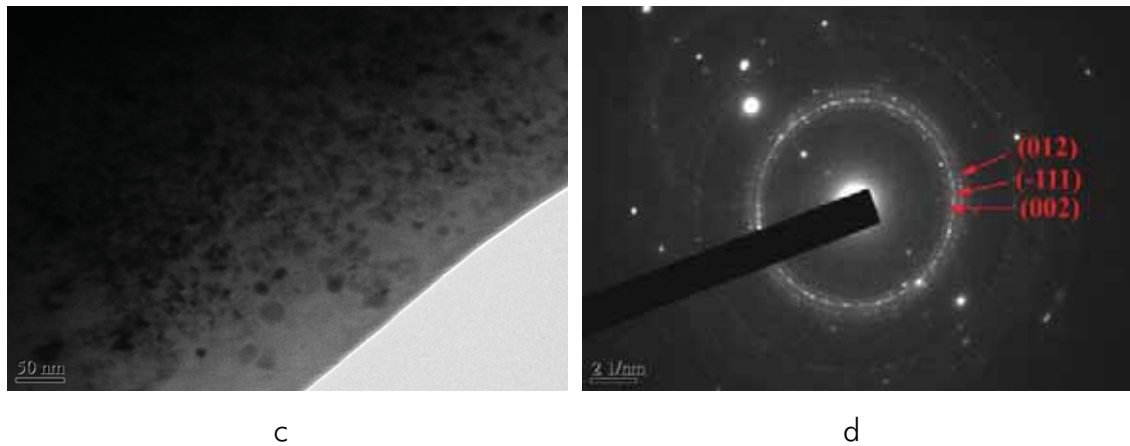
Figure 4.46. TEM images of the VPS-NiTi coating showing: (a) amorphous areas, (b) micro and (c) nanograins with a monoclinic phase.

The APS-quenching deposit exhibited many features demonstrating that it has a strained and non-equilibrium structure. Figure 4.47a shows two different zones with columnar grains with a SAED pattern exhibiting many spots of the monoclinic phase. Actually, many columnar grains were found within the structure; these are common of the APS+Q deposits where the temperature difference between the fused particle and the substrate is high. The fact that no columnar grains were observed within the examined area of the VPS deposit does not mean that they were not formed but rather these could not be found in the as-prepared zone.

Figure 4.47b shows the same area observed with different tilt: in the picture on the left, several columnar grains within the rounded area can be observed, whereas in the picture on the right, there is a nanostructure with grains even smaller than 10nm. Such observation agrees with the XRD of this coating, which exhibitted broad peaks corresponding to the occurrence of a nanocrystalline structure. This area was found to have also a monoclinic phase. Figure 4.47c illustrates the electron diffraction of the area marked with the arrows. Surprisingly, many of these spots seem to correspond to the $NiTi_2$ phase, which was not observed in the X-ray diffraction of the coating.
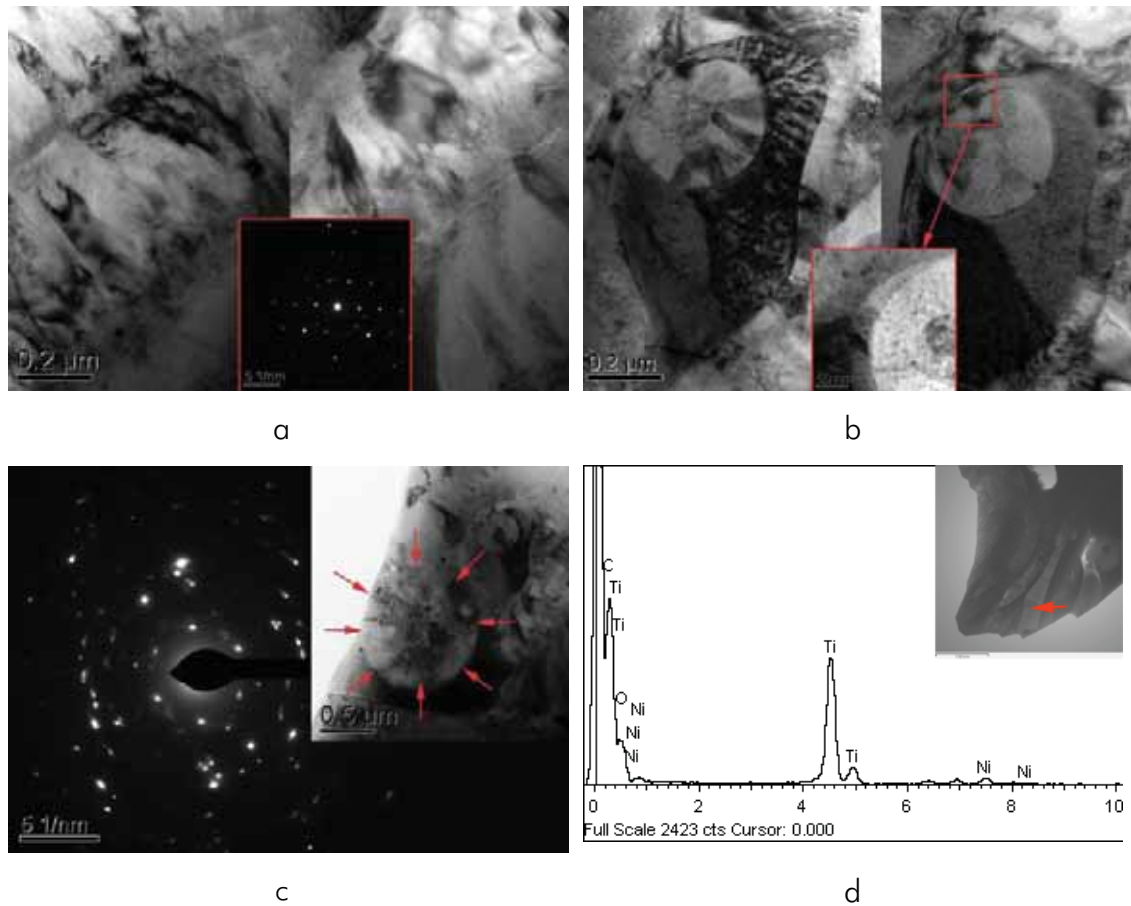
Figure 4.47. TEM images of the APS+Q NiTi coating showing: (a) columnar grains, (b) nanocrystalline structure, (c) Ti-enriched area and (d) TiO oxide band.

Finally, the HVOF coating is featured by equiaxed and columnar grains, as well as amorphous and oxidized bands. Figure 4.48b displays the ring pattern of a columnar zone with many spots corresponding to the cubic NiTi phase (austenite). Other encountered grains of above 1 micron size (figs. 4.48c and d) also matched to a cubic lattice. Here, it could not be proved the occurrence of monoclinic phase. This difference with what was obtained with the VPS and APS+Q deposits might be due to the moderate heat input in the HVOF technique; as observed by SEM, the powder microstructure remains in the coating leading to the same NiTi phase.
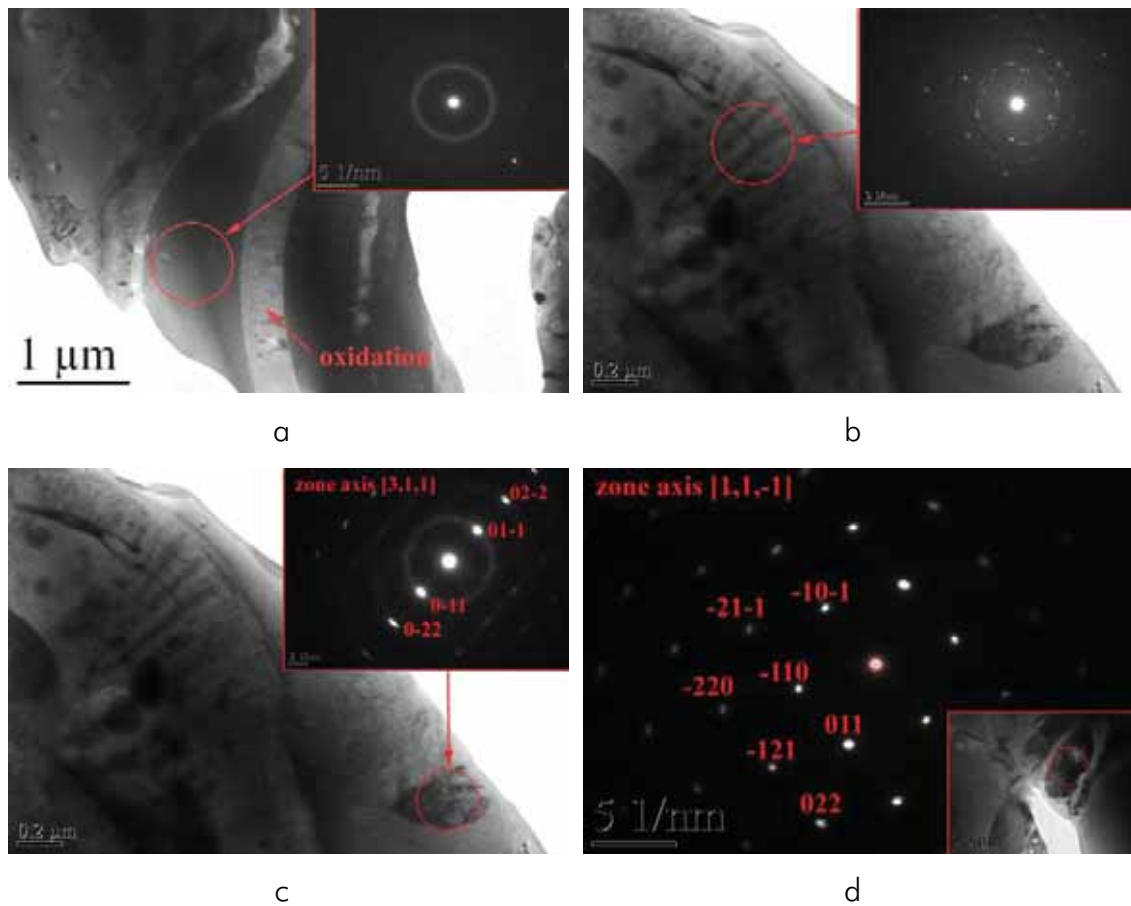
Figure 4.48. TEM images of the HVOF-NiTi coating showing: (a) oxide bands and amorphous areas, (b) columnar austenie NiTi grains and (c), (d) equiaxed micro-scale grains with also austenite phase.

c)   Calorimetric analyses

Figure 4.48 shows the calorimetries of the three as-sprayed NiTi powders and table 4.10 shows their peak temperatures as well as that of the powder. It can be observed that there are differences of about 20°C if such temperature is measured either from the heat flow vs time plot or from the heat flow vs temperature. These differences are not noticeable considering that the whole transformation (A_S-A_f) occurs in a temperature range of above 60°C. It is worth noting that there is a certain tendency: powder<HVOF≈APS+Q<VPS, which might be due to all the factors that produce a shift to higher or lower temperatures.

a   b

c   d

e   f
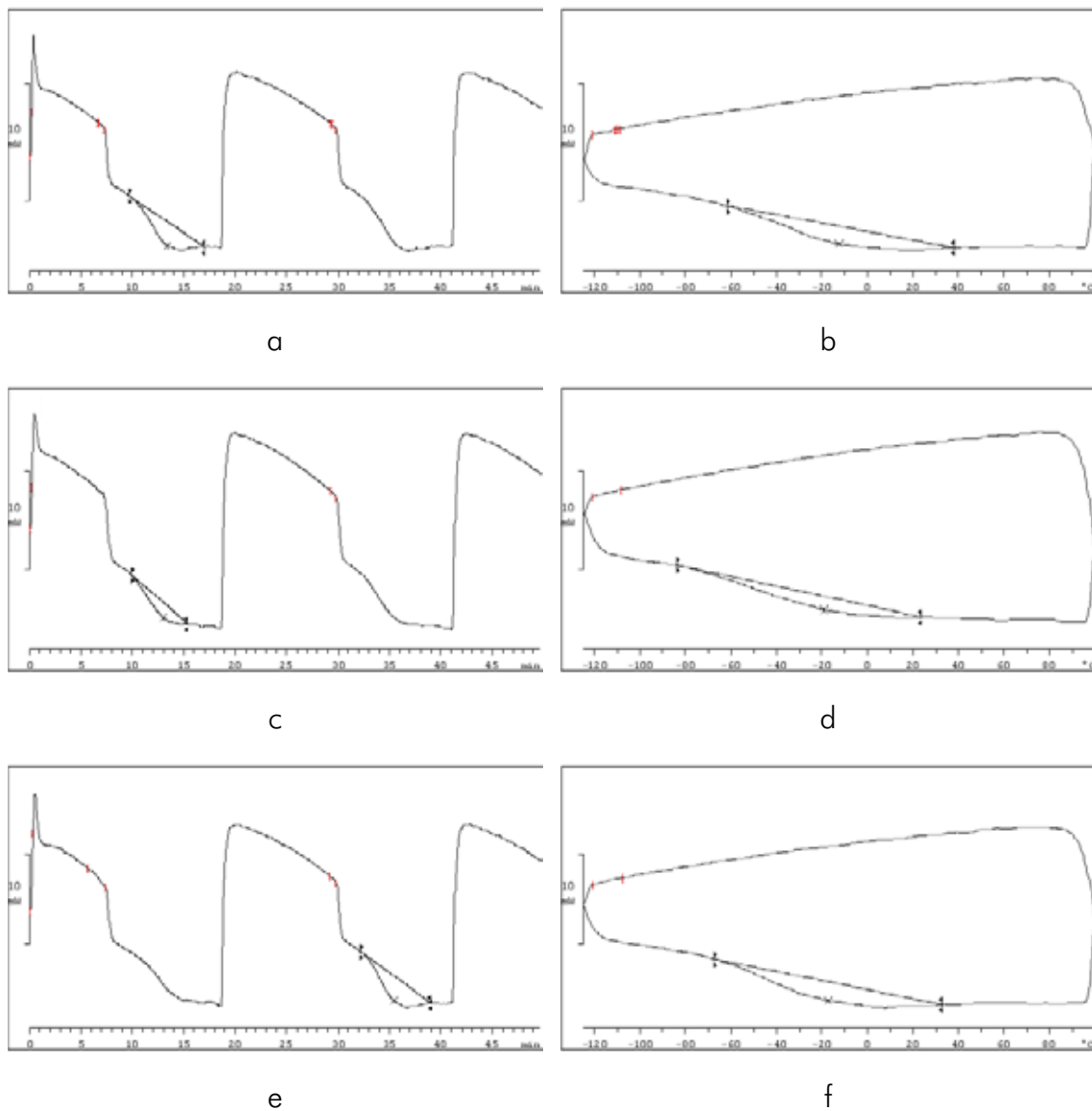
Figure 4.49. (a), (c), (e) heat flow versus time and (b), (d), (f) heat flow versus temperature of the VPS, APS-quenching and HVOF deposits respectively.

Table 4.10. Transformation temperatures detected when heating in the DSC experiments.

Sample	Transformation peak M→A (°C) (versus time test)	Transformation peak M→A (°C) (versus sample temperature)
Powder	5.6	-23.96
HVOF	8.4	-17.19
APS+Q	9	-19.13
VPS	18.4	-12.40

4.3.3   Characterization of coating properties

a)   Mechanical properties

With regard to the tensile strength, the three coatings showed failure in the coating, with fairly similar values to those of FeAl. Table 4.10 also shows their microhardness and elastic moduli: the lowest microhardness corresponds to the VPS coating; the highest values of the APS are likely due to the presence of intersplat oxidation and the low material ductility as result of the fast cooling.

Table 4.10. Tensile strength, Vickers microhardness and elastic modulus for the as-sprayed NiTi powder.

	Adherence, MPa	Vickers microhardness, HV_{200}	Elastic modulus, GPa
VPS	75,3 ± 5,1	496 ± 20	105 ± 8
APS-quenching	43,1 ± 4,2	549 ± 43	86 ± 10
HVOF	45,4 ± 2,9	539 ± 39	91 ± 10

b)   Wear resistance

Some studies report that NiTi alloys exhibit a wear resistance in sliding conditions, water jet, slurry and cavitation erosion, as good as that of hastelloy and stellite alloys [47, 48, 49, 50]. Some have ascribed such wear properties to work-hardening [47], whereas others attribute it to pseudoelasticity [48, 51, 52]. Pseudoelasticity (austenite phase) can be achieved by adjusting the composition and performing heat treatments; however, the occurrence of pseudoplastic state (martensitic) seems to be also promising for improving wear resistance [53, 54]. Liang et al. [54] outlined that wear resistance depends on the sum of the pseudoplastic and pseudoelastic strain limits and, explained the micromechanisms that occur in each case, whenever the material is in one state or the other. They also exclude a possible work-hardening effect owing to the different plastic deformation mechanisms of conventional alloys with that of NiTi. Stella et al. examined the erosion properties of vacuum plasma sprayed coatings and, although they did not demonstrate that coatings had shape memory, they assumed that despite porosity and second phases not showing this effect, the pseudoelasticity of

stoichiometric NiTi phase played some role on improving the wear resistance [55].

Table 4.6 shows the main wear parameters resulting of the abrasive and friction tests. Regarding the three-body abrasion, fairly similar values are obtained and, as in the case of iron aluminide coatings, the tendency is the same as that of the material hardness: the hardest deposit (APS-quenching) possessess the lowest wear rate. In a simple model then, the material hardness is one of the main influencing factors through the abrasive hardness to surface hardness ratio, the wear rate being more sensitive when H_a/H_s is lower than about 1. However, in predicting three-body abrasive rates, one must also consider other factors as particle angularity, shape of abrasive and so on [56, 57].

With regard to the dry sliding behavior, the highest friction coefficient is that of the VPS coating and the lowest wear rate corresponds to APS-quenching.

Table 4.6. Wear rates comparison for the iron aluminide coatings.

	Abrasion	Friction		
	Wear rate $(mm^3 \ N^{-1} \ m^{-1})$	Friction Coefficient	Track width (μm)	Wear rate $(mm^3 \ N^{-1} \ m^{-1})$
VPS	$1,4 \ 10^{-4}$	$0,88_6$	1118 ± 20	$5,7 \ 10^{-5}$
APS-quenched	$9,1 \ 10^{-5}$	$0,74_6$	793 ± 33	$1,8 \ 10^{-5}$
HVOF	$2,2 \ 10^{-4}$	$0,81_0$	1599 ± 54	$4,2 \ 10^{-4}$

By examination of the worn surfaces (figs. 4.50, 4.51 and 4.52), one can see that the APS-quenching is formed by fresh coating and cracking, which made think that the wear mechanism was by fatigue; cracking expansion might be facilitated by continuous cycles of the ball sliding over the coating. By contrast, VPS and HVOF deposits exhibitted carbide particles coming from the worn counterface (WC-Co). According to this, these particles behave as abrasive between the moving surfaces leading to a more damaging wear effect. In addition, these two coatings also show the largest contact area as seen by ball prints, where it seems that material transference from the sprayed NiTi has

taken place. The smallest contact area corresponds to APS+Q deposit, and this has in turn, the narrowest wear track and the lowest friction coefficient.

a

b

c
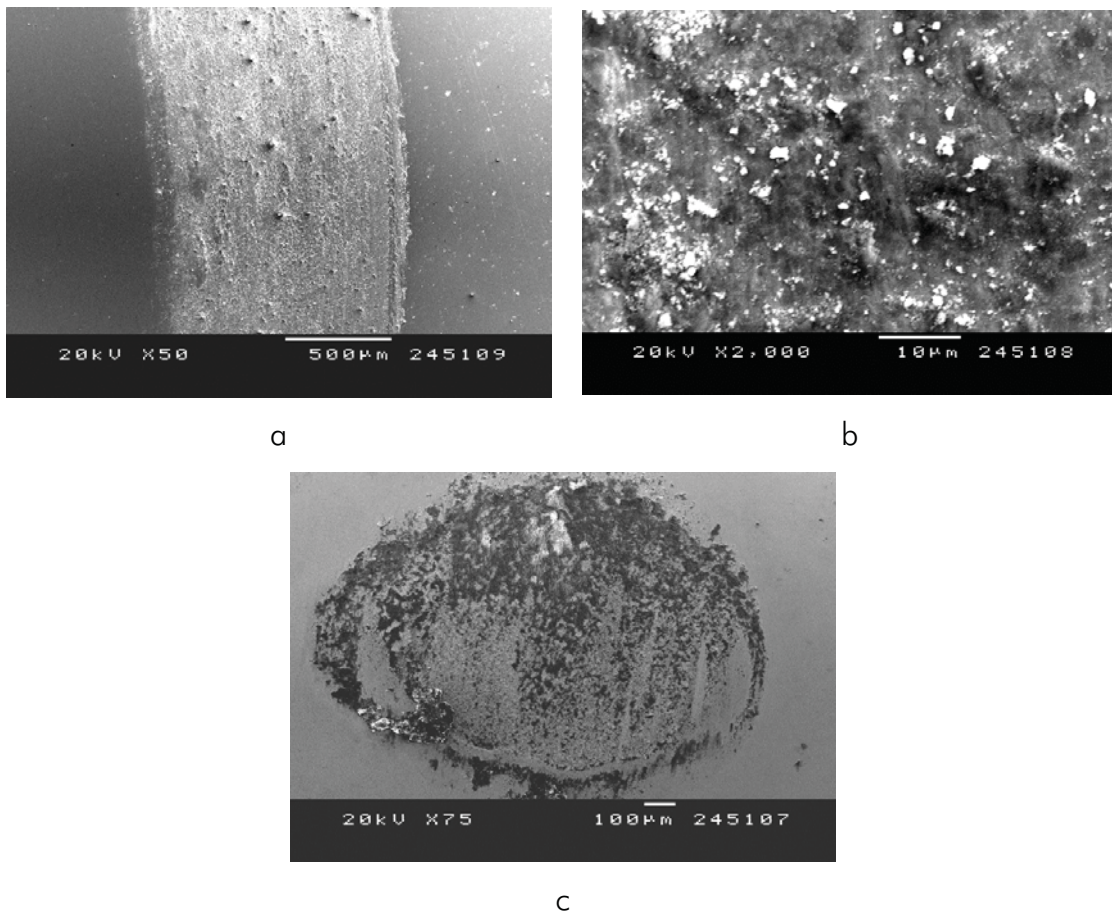
Figure 4.50. Wear track features of after the sliding test for the VPS NiTi coating.

a

b
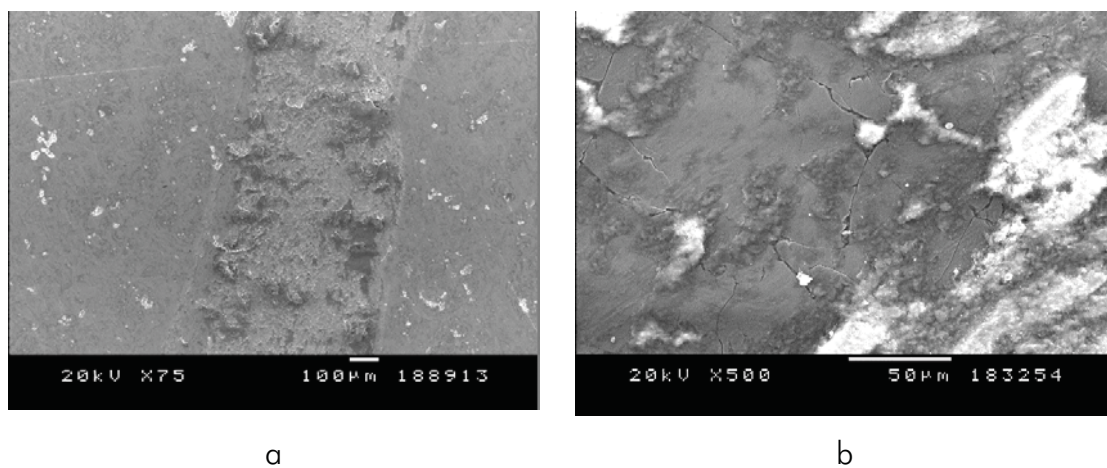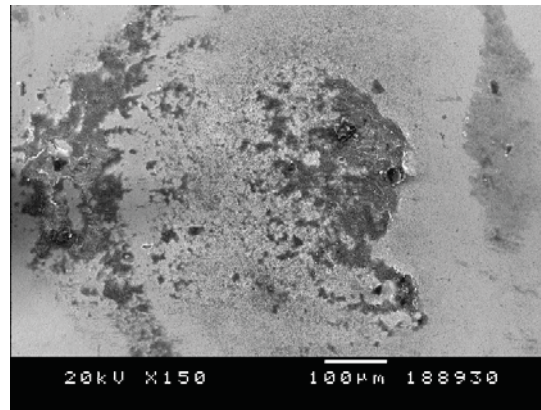
c

Figure 4.51. Wear track features of after the sliding test for the APS-quenching NiTi coating.
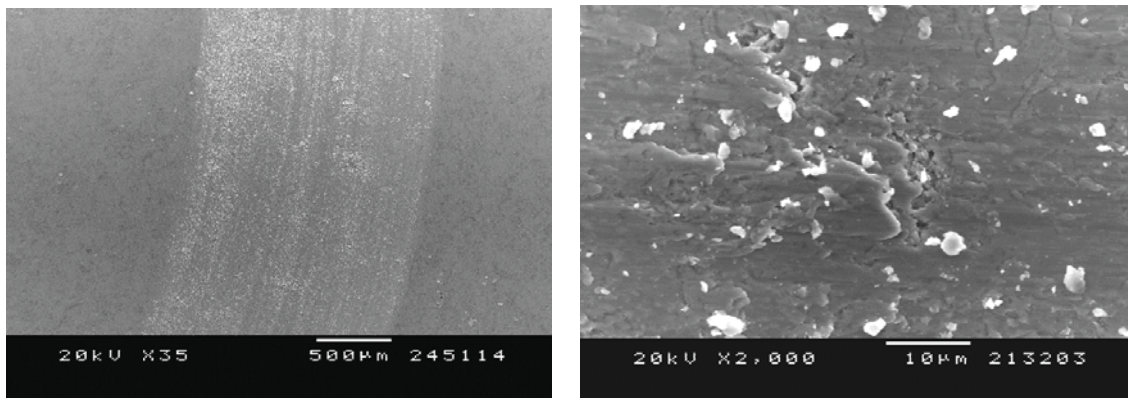
a   b
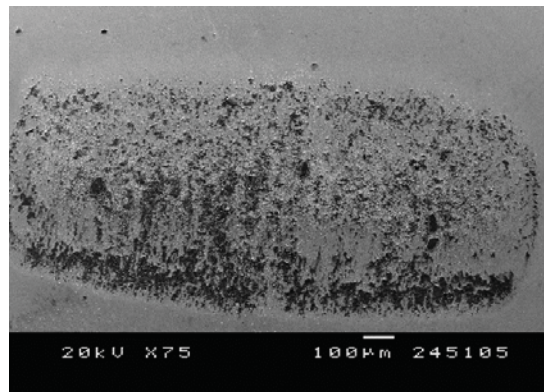
c

Figure 4.52. Wear track features of after the sliding test for the HVOF NiTi coating.

c)   Corrosion resistance

-    *Electrochemical tests*

Corrosion behavior of NiTi alloys has been largely examined in physiological conditions but it has been poorly studied in aggressive chloride solutions

where they can exhibit localized corrosion. Some authors have suggested that the presence of chloride ions in solution can produce extensive localized attack by their absorption on weak parts of the oxide film, forming soluble complexes [58]. Cheng et al analysed the influence of Cl⁻ ion concentration and pH and concluded that the corrosion resistance decreases with increasing [Cl⁻] and pH value, being the main form of corrosion by pitting [59]. The mechanism might include accelerated corrosion by retarding film repair. Since the surface oxide layer is not perfectly uniform, the defects within the structure of the oxide would be preferentially occupied by chloride ions by adsorption. In his review, Shabalovskaya pointed out the significance of surface finish of NiTi in the corrosion behavior [60].

With regard to theses studies, the thermal sprayed NiTi coatings, especially VPS and HVOF show similar corrosion potential values. However, these results are difficult to compare as the corrosion behaviour depends first on the processing route e.g. the microstructure of a thermal spray coating is completely different to that of a bulk material (second-phase particles and inclusions [61, 62] and surface finish [62]) and, seconly, it depends on the type of corrosion tests and test conditions employed.

Paper 6: J. M. Guilemany, N. Cinca, S. Dosta, A.V. Benedetti, Corrosion behaviour of thermal sprayed nitinol coatings, *Corrosion Science* (accepted with minor revisions).

According to the open circuit tests, the electrolyte penetration within the APS+Q proceeds straight to the substrate through the cracks and pores. The VPS and HVOF coatings however, show non-uniform wettability that produces preferential corrosion near the oxides, at the Ti-depleted areas or even, in the case of HVOF, the precipitates observed in the starting powder may also act as potential sites for corrosion.

By the potenciodynamic curves, it is observed that the highest anodic passive current corresponds to the APS-quenched sample and the other two (VPS and

HVOF) are fairly similar with slightly differences. These results obviously indicate that the APS+Q specimen has increased tendency for corrosion mainly ascribed to the easy electrolyte penetration to the substrate rather than the coating composition. Besides, as the passive potential range of HVOF is lower than the VPS, the first one shows more tendency for pitting initiation.

Corrosion behaviour of thermal sprayed nitinol coatings

J. M. Guilemany[1], N. Cinca[1], S. Dosta[1], A.V. Benedetti[2]

[1]Thermal Spray center, Department of Materials Science and Engineering, University of Barcelona.

SPAIN

[2]UNESP-Universidade Estadual Paulista, Instituto de Química, CP.355, 14801-970 Araraquara, SP,

Brasil

Abstract

NiTi alloy is here investigated as an alternative coating to stainless steel since it is considered to possess good corrosion properties. Three different thermal spray techniques (High Velocity Oxy-Fuel –HVOF–, Vacuum Plasma Spray –VPS– and modified Atmospheric Plasma Spray –APS–) have been used for building the coatings, and electrochemical tests have been carried out for corrosion evaluation. Open-circuit tests have revealed that the VPS-coating shows fairly good corrosion resistance, both in the as-sprayed and polished forms. The HVOF specimen however, showed a strong dependence on the surface conditions and APS is dominated by electrolyte penetration through coating cracks. As expected therefore, this latter one possesses a higher i_{corr}.

1. Introduction

Near equiatomic Ni-Ti composition is especially world-wide known for its shape memory effect (SME) and superelastic behaviour [1]. Such properties have already been exploited in biomedical applications. In such field, corrosion performance is hampered by Ni ions release, which can cause toxicity [2, 3, 4]. Other important applications related to SME are for sealing requirements [5, 6] or as microactuators [7, 8, 9, 10].

Apart from medical devices, Ni-Ti also accomplishes other requirements which make it of technological interest. Its promising wear and erosion-corrosion properties make it also a material to be investigated [11, 12, 13]. The erosion resistance is mainly due to its superelasticity [14, 15] while its corrosion performance (slightly more noble than AISI 316 stainless steel) is due to a TiO_2 passive film formation. Nevertheless, manufacturing of large components made entirely of NiTi is complicated and expensive; therefore, their use as coatings has been proposed as a good alternative [16, 17, 18, 19, 20].

Within the field of thin films, magnetron sputtering [8, 19, 21, 22] has been largely investigated, whereas in the range of thicker coatings, the most used processing method is Vacuum Plasma Spraying [4, 23, 24, 25, 26, 27, 28]. In such process, the spray chamber is filled with inert gas and maintained at low pressure (~100mbar) during spraying to allow coatings of reactive materials to be produced without oxidation. Especially in the NiTi case, this is interesting because the alloy is susceptible to react rapidly with oxygen, hydrogen and nitrogen during exposition to high temperature; the presence of such impurities would limit the shape memory behaviour. Apart from its attractiveness for the low oxidation content, in VPS, the high droplet impact velocities permit the manufacture of dense coatings.

The present work has also focused on two other spraying techniques for comparison with vacuum plasma sprayed NiTi alloy. These are HVOF (High Velocity Oxy-Fuel) and APS (Atmospheric Plasma Spray)-quenched respectively. Instead of a plasma produced by an arc discharge, High Velocity Oxy-Fuel Spraying involves a continuous gas combustion in a chamber under high pressure; the highly accelerated particles and their lower particle in-flight time compared to that of common PS processes, produce exceptionally dense metal sprayed coatings with excellent adhesion and, commonly, with low oxidation and partially melted particles [29].

APS-quenched, by contrast, follows the same rules as Atmospheric Plasma Spraying with the unique difference that an inert atmosphere is simulated by the addition of a liquid nitrogen cooling system. Such procedure was developed and patented by our group to obtain nanostructures from thermally treated metastable structures, which are produced by rapid solidification from the liquid state [30].

As well as stainless steel, bronze, tin and more exotic materials, NiTi coatings are cathodic relative to the steel substrate; they act as a barrier as long the electrolyte path to the substrate is prevented. Chiu et al. [31] attempted to modify the surface of an AISI 316L stainless steel with NiTi using different laser treatments. These samples were tested in a saline solution and showed that pitting potentials of the laser-treated samples were comparable to that of the AISI 316L substrate, but the protection and corrosion potentials were somewhat lower. A laser surface modification was also used by Man et al. [32], but with the idea of melting the surface of a bulk NiTi alloy in order to produce a crack- and porosity-free layer. These authors claim that a significant corrosion improvement was achieved by lowering the I_{corr} one order of magnitude with respect to the untreated sample.

The main goal of the present work is to study the corrosion behaviour in a marine environment of different NiTi deposits obtained by the above mentioned thermal spray techniques. This approach has been carried out by means of electrochemical tests.

2. Experimental procedure

2.1   Powders and coatings preparation

NiTi powders were manufactured using the gas atomization technique. The alloy was melted in a CaO crucible; this is normally preferred instead of other crucible materials such as alumina or magnesia as these contaminate the molten nitinol with oxygen. An Al_2O_3 tube coated with ZrO_2 was used to plug the hole of the delivery tube fixed at the bottom of the crucible. The melt was atomized under highly pure Ar atmosphere. The oxygen content found in the powder is due to the reaction between Ti and the plug tube (an Al_2O_3 tube coated with ZrO_2).

For the production of the coatings, a low alloyed carbon steel G41350 UNS (Fe-0.34C-0.65Mn-0.27Si-0.02P-0.02S-0.2Ni-0.96Cr-0.16Mo-0.42Cu wt.%) was used as substrate. The samples were previously degreased in acetone and sandblasted until reaching a roughness about 4Ra to provide mechanical bonding. The coatings were produced using a VPS Plasma System (Sulzer Metco) with F4VB plasma gun; an HVOF system (Diamond Jet Hybrid -DJH2700), and an Air Plasma Spraying gun (F4) from Sulzer Metco with a liquid nitrogen cooling system [33]. This last system allows more rapid solidification

reaching cooling velocities as high as 10^6 K/s. Tables 1, 2 and 3 present the spraying parameters and conditions according to the different techniques.

For their examination, a cross-section of each coating was prepared and these were polished until 1 μm diamond suspension. Some of them were etched with a HF:HNO$_3$ solution (10 mL HF, 25 mL HNO$_3$, 150 mL H$_2$O) to reveal the microstructure and afterwards observed in a Scanning Electron Microscope (JEOL 5510) operated at 20 kV with an EDS for microanalysis. All x-ray diffractograms were performed on a Bragg Brentano θ/2θ Siemens D-500 diffractometer with Cu Kα radiation.

2.2   Electrochemical corrosion tests

The corrosion resistance was evaluated by means of electrochemical measurements in 80 mL of an aerated and unstirred 3.4% NaCl solution. The three coatings were first evaluated in the as-sprayed form but, as the surface nature is known to affect considerably the electrochemical response, they were also tested after being polished below 1 μm Ra. A conventional three-electrode cell was used, with an Ag/AgCl/KCl$_{saturated}$ as reference electrode, a Pt-wire as counter electrode and the as-sprayed and polished samples as the working electrode. All potential values are referred to Ag/AgCl/KCl$_{saturated}$ electrode. The coated sample was placed at the bottom of the electrochemical cell exposing a geometric area of 1cm^2 to the solution; it is worth noting however, that this area can be very different from the real one exposed to the solution, since it depends on the electrolyte penetration, surface roughness and defects within the coating structure (cracks, porous, oxides, etc.) [34, 35]. A PC-programmed EG&G 263A potentiostat/galvanostat (Princeton Applied Research, UK) was employed. For all the specimens, the following procedure was applied: once the open-circuit potential was stabilised, a linear polarization was performed in the small potential range around the open-circuit potential, E_{OC}, (±5 mV/ E_{OC}) at a scan rate of 0.05 mV/s and finally, the potentiodynamic curves were recorded starting at –150 mV / E$_{OC}$ up to +1000 mV / E_{OC} at a 0.166 mV/s.

From the classical Tafel analysis, i_{corr} was estimated by plotting the linear anodic and cathodic curves in the E (mV Ag/AgCl) *vs.* log *(i* /A cm^{-2}) curve. At least two samples have been tested for each system.

The corrosion current density value was compared with the one calculated from Stern-Geary relationship [36], equation (2), using the estimated Tafel slopes and the polarisation resistance, which was calculated from the linear fitting of the *E-I* curve obtained around the open-circuit potential. Rigorously, this procedure can be only applied for generally corroded surfaces and also whenever the conditions to deduce the Butler-Volmer equation are valid. For instance, it means that R_p should be equal to the charge transfer resistance (R_{ct}) of the corrosion reaction [37]. However, other resistances can compose R_p such as diffusion resistance, adsorption resistance, ohmic resistance (caused by an oxide or salt film with passive characteristic) and, so on. So many simplifications must be accepted in practical using of Stern-Geary equation, since many times, all conditions for its correct use are not present. Here, the i_{corr} was just estimated using equation (1) so that we could compare the same coating materials with different surface finishing or preparation. The discussion of the corrosion mechanism based on electrochemical reactions was ruled out.

(1) $$\frac{1}{R_p} = 2.3\frac{b_a + b_c}{b_a b_c} i_{corr}$$

3. Results and discussion

3.1   Powder characterization

Figure 1 shows the typical spherical morphology of the feedstock Ti-50.01%atNi powder. The backscattered micrograph of the powder reveals a microstructure with two phases according to the different grey contrasts: a dark one which is dissolved into the light matrix. By etching the cross-sections, the light matrix seems to be in relief with respect to the precipitates as if those were preferentially etched (figure 2). Figure 3 shows the XRD of the atomised powder. From the pattern data list, it is difficult to distinguish whether the less intense peaks correspond to $NiTi_2$ phase or Ti_4Ni_2O because their lattice parameters are very similar, both around 11,278 Å. However, as the chemical analysis reports an oxygen content of 7000 ppm, the presence of Ti_4Ni_2O is fairly probable. Since solid solubility of oxygen is very small (0.045%at), alloys with oxygen contents exceeding this limit solidify, on cooling from a melt, transforming into primary NiTi and, an eutectic mixture of a NiTi solid solution and the Ti_4Ni_2O oxide. In addition however, the presence of $NiTi_2$ cannot be ruled out at all; although NiTi has negative Gibbs free energy over a wide temperature range, the driving forces for the formation of $NiTi_2$ and Ni_3Ti are stronger. Furthermore, the formation of NiTi is highly exothermic between 500 and 900 ºC, resulting in a severe sample temperature increase up to the $NiTi_2$ eutectic (942 ºC). Such phase can even be formed by a peritectic reaction at 984 ºC. Therefore, melting step is critical and chemical composition and temperatures must be controlled very accurately [38].

3.2   Coatings characterization

The coatings were sprayed having in mind that minimal oxidation and porosities are required to produce dense coatings for optimal cathodic protection. The Vaccum Plasma Sprayed coating shows high density and good adherence (fig. 4). No different contrasts are distinguished at first examination; hence, in order to reveal some kind of feature within the structure, the sample was etched with the same etchant as used for the powder. Surprisingly, not only splat boundaries are perfectly delimited, but it also seems that there are two different phases. The inset in figure 4 illustrates the etched microstructure where some areas have been further attacked. The smooth zones correspond to areas depleted in titanium (fig. 5). According to the micrograph, this phase is not encountered in the intersplat boundaries or specific coating features; it alternates randomly within the coating.

The x-ray profile presents sharp NiTi peaks and broad tails at both sides of the main intense peak, which seem to hidden $NiTi_2$ or Ti_4Ni_2O lines (fig. 6). This could be explained by the presence of amorphous areas after rapid solidification. Such fact would not be surprising as Thermal Spraying are non-equilibrium processes where diffusion is inhibited because of the high cooling rates.

In opposite to VPS coatings, some oxidation was exhibited in the APS-quenched overlays. Despite the liquid nitrogen atmosphere, certain oxidation was inevitable. Such oxidation is illustrated by more dark contrasts and, it has been associated to TiO formation identified by XRD (fig. 7a and b). The initial purpose of such cooling system (within the frame of NAMAMET [39, 40]) was to retain a metastable structure that could evolve to a nanocrystalline material after a proper heat treatment. As it can be seen,

the X-ray trace displays all NiTi lines broader than the VPS coating but there are no signs of amorphous phase; the broadening can indicate a reduction of grain size or microstrain effects. Actually, Transmission Electron Microscopy studies have enabled to see that large nanocrystalline areas are present within the APS coating, which agrees with the broadening of the X-ray lines, whereas in the VPS, there are fewer nanocrystalline areas but much larger amorphous zones. These differences are associated to the different thermal history of particles and the rapid cooling rates. Furthermore, the $NiTi_2$ or Ti_4Ni_2O phase no longer appears in APS. Etching treatment of such cross-sections did not provide more information. It is also worth saying that cooling with nitrogen produced some perpendicular cracks across the splats. Although a modification of the spraying parameters was attempted to minimise such phenomena, they could not be avoided. This fact was presumed to be detrimental for the corrosion analysis.

Finally, HVOF coatings showed a completely different microstructure (fig. 8). Due of the moderate heat input in the HVOF technique, the material undergoes only slight metallurgical changes as a result of the spray process. Figure 8b shows a magnification which reminds the microstructure of the powder; this is because there are large non-fully melted areas. Apart from the starting phases, the spraying has also lead to the formation of Ti_2O_3 and Ni-rich zones (fig. 9) with some porosity especially around the smallest particles. It is also worth noting that while the VPS and APS deposits exhibited a yellow gold surface colour as that of the feedstock powder, the HVOF coating had a more grey tonality due to oxidation. Such observation may be ascribed to be associated to the other different phases encountered in the coating.

3.3   Corrosion tests

Open-circuit curves

Figure 10 shows the open-circuit potential-time curves for three as-sprayed (fig. 10a) and as-polished (fig. 10b) samples in aerated and unstirred chloride solution. As the potential at each time was not locally measured, it only represents an average potential value of all contributions of the sample in contact with the electrolyte; it may inform on the evolution and degradation of the coating and / or substrate. For unpolished samples and at short immersion times, the curve profiles were as follows: some potential decaying for APS, decaying followed by increasing for HVOF and, increasing for VPS. Then, for all as-sprayed samples, steady-state potential values were reached after around 2 h of immersion at: -600 mV Ag/AgCl (APS), -177 mV Ag/AgCl (VPS) and –88 mV Ag/AgCl (HVOF), indicating that both, VPS and HVOF samples, presented more noble corrosion potentials. VPS and HVOF coatings show corrosion potential values comparable to AISI 316 steel, which gave an $E_{corr} \approx –113$ mV Ag/AgCl in the same solution. The potential changes at the beginning of the test are strongly influenced by the state of the coating surface and finishing, and can be related to oxides formation and dissolution, ions adsorption, electrolyte penetration and so on. The APS-quenched sample did not present potential fluctuations, while VPS and HVOF samples showed such fluctuations during the time course test. The reason why the APS-quenched specimen did not show potential oscillations can be related to the penetration of the electrolyte direct to the substrate through the cracks, causing a homogeneous wetability of the whole system; then, the final potential value tends to the one measured for the substrate (-690 mV Ag/AgCl) as discussed by Guilemany et al. [41].In the previous referenced work, the authors observed that the potential oscillations for a cermet coating disappeared after long immersion times when the electrolyte had reached the

substrate.The large cracks produced in APS are the main responsible for the open-circuit potential behaviour rather than some nickel oxide formation and dissolution. This feature will be better observed in the polarization curve where no passive behaviour is expected.

Potential oscillations observed for VPS and HVOF coatings can be related to irregular electrolyte penetration and / or a depassivation / repassivation process as a consequence of a pitting attack of chloride to the regions near oxides or new phases, where localized attack is favoured [41]. In the case of the VPS coating, some amorphous areas and titanium depleted zones were observed, while for the HVOF coating, large non-fully melted areas, pores and oxides were found. Therefore, Ti-depleted zones in VPS probably work as water and / or oxygen reduction area and, the enriched Ti zones may behave as oxidation sites to form Ti-based oxides; these oxides undergo pit attack, leading to a depassivation / repassivation process. For HVOF specimens, the dissolution of oxidized zones (chloride attack) and electrolyte penetration through the pores can be the main cause of the potential oscillations. Also, probably due to the same reason, for both VPS and HVOF samples, a large and well-defined passive behaviour will be not evident in the polarizations curves.

Another aspect to take into account is that corrosion properties are also asumed to be considerably affected by the surface roughness since the roughness of the coatings promotes a better solution contact in certain areas; this might be also the cause of the unstable VPS and HVOF E_{OC}. All these features can be responsible of the observed potential oscillations.

The electrochemical tests were also conducted with as-polished samples in order to evaluate the influence of surface roughness -coating thicknesses after polishing: APS (186 ± 9 µm), VPS (66 ± 4 µm) and HVOF (87 ± 5 µm)-. As it can be seen in figure 10b, E_{oc} curves for as-polished APS and VPS samples showed a potential evolution analogous to that of as-sprayed specimens. These results suggest that electrolyte penetration through the cracks is still the main mechanism for potential evolution as far as APS is concerned while, for the VPS coating, the potential oscillations are ascribed to a depassivation / repassivation mechanism. Surprisingly, however, the as-polished HVOF NiTi coatings led to somewhat different behaviour; they displayed a less noble potential with an E_{corr} of about -433 mV Ag/AgCl, the same as that of bulk laser-untreated NiTi alloy in the study carried out by Man et al. [32]. The lower E_{oc} value measured for as-polished compared with unpolished samples may be due to mechanical polishing action which leaves open porosity and even crack formation (fig. 11) or surface oxide removal (after polishing the surface, it has a metallic bright finish) facilitating the electrolyte access.

To sum up, the higher potential value for the as-sprayed HVOF sample compared to that of the VPS one is due to its higher oxidation level, while the lowest E_{oc} measured for the APS sample is related to the substrate oxidation. For the as-polished samples, only the E_{oc} value of HVOF changed, being lower than that of VPS due to cracking after mechanical polishing.

Potentiodynamic curves

In order to estimate the corrosion current density, anodic and cathodic curves were recorded around the corrosion potential (E_{corr}) for both as-sprayed and as-polished samples (fig. 12 and table 5). From the intercept between the anodic and cathodic linear plots and, by interpolating to the y and x axis, both E_{corr} and i_{corr} are respectively estimated. According to these Tafel-plots, for both unpolished and polished

samples, the observed corrosion potentials (table 5) are fairly similar to those obtained from the *E vs.* time curves. This means that the cathodic polarization did not cause appreciable change to the electrode surface. The slight differences between E_{oc}(2 h) and E_{corr} values might be associated to the fact that the polarization curves started at -150 mV / E_{oc}; the cathodic branch can be then shifted to lower potential values due to the reduction of some corrosion products formed during the open-circuit potential. As a consequence, the corrosion potential may shift to negative values and the anodic polarization curve may be modified to a less resistive response.

For both unpolished and polished samples, the i_{corr} values (table 5) decrease as follows: APS-quenched > HVOF ≈ VPS, being the values slightly lower for the polished samples probably due to the little decrease in the surface area. Thus, the results indicated that the APS specimen is the most easily corroded; no passive region was observed, the current density continuously increased up to ca. 10^{-3} A cm^{-2}, and followed increasing monotonically. By contrast, as-polished VPS and HVOF NiTi alloys exhibited a slight passive-like behaviour. Their curves possess an inflexion point at high anodic potentials (around 80 mV Ag/AgCl and -30 mV Ag/AgCl for un- and polished HVOF coatings, respectively and, around 90 mV Ag/AgCl for both un- and polished VPS) and the correspondent current values (around 10^{-6} and 10^{-5} A cm^{-2} for un- and polished HVOF coatings and around 10^{-6} A cm^{-2} for both un- and polished VPS) could be attributed to the breakdown of the thin passive film. Such effect has been associated to the faster diffusion of small Cl^{-} ions than that of oxygen through defects, which makes difficult for the surface to be homogeneously passivated and enables that pitting and crevice corrosion take place. The effect of surface conditions had been already noticed by other authors [42, 43]. They claimed that it is very difficult for a metal to form a high quality passive film on a rough surface [32].

According to the above comments, the APS deposit exhibits a different corrosion mechanism than the others, and the polarization curve resembles the anodic curve of the substrate since the electrolyte penetrates through cracks to reach the steel.

Tafel slopes are those expected for the reduction and oxidation processes above described, except for the following: b_c of the polished-VPS sample is very high and could be associated to the oxygen diffusion resistance or a mass transport control and, b_a of the polished-HVOF specimen is also higher than the others probably due to the ohmic resistance or a very low anodic charge transfer coefficient.

Finally, the examination of the specimens after the corrosion tests states that there have been some preferential sites for corrosion. Figure 13 shows the corrosion prints in the as-polished specimens. The APS coating was attacked, as expected, when the electrolyte reached the substrate through the cracks; figure 13 c includes an EDS analysis where Fe has been identified. It is better illustrated by the analysis through the cross-section by means of Electron Microprobe Analysis (fig. 14). Actually, this is one of the problems of those coating-substrate pairs where the coating is nobler than the substrate; in such case, the substrate is protected whenever the integrity of the coating is maintained. Therefore, there is a strong dependence on raw materials and spraying parameters in order to achieve a good coating quality.

By contrast, VPS and HVOF have been corroded but the substrate did not seem to be reached or severely corroded during the experimental time. This might be explained by the interlamellar cohesion, which is quite good in both cases and therefore, electrolyte penetration is not direct.

Differently from the corrosion in bulk materials, the corrosion in coatings can be more easily extended. For bulks, chemical inhomogeneities are known to be common preferred sites for pitting initialisation. It is in these sites where the passive film is imperfect and breakdown occurs preferentially. According to the nature of inhomogeneities, the common susceptible sites for pits are known to be the inclusions, second phase precipitates, grain boundaries, processing defects such as pores, cracks, etc. The occurrence of such features is inherent within many sprayed materials. Creus et al. [44] evaluated the porosity effect as a critical parameter in the corrosion resistance of deposited materials with emphasis to the role of open porosity. Even also worth noting, intersplat boundaries have to be also taken into consideration with regard to coatings corrosion; these can be depleted in the most oxidizable elements by particle oxidation occurring during deposition (in the gas jet or immediately after impact, before a new layer is deposited): this depletion results in reduced passivating ability in those interlamellar regions where corrosion initiation is more likely, as mentioned above [45, 46]. Apart from interlamella gaps, open or interconnected porosity, oxides also produce an embrittlement of the coating and an additional possible internal path for the electrolyte. This might be the explanation why the corrosion in VPS and HVOF NiTi has not been homogeneous when the pitting phenomenon has occurred; it rather seems that NiTi alloy zones have remained.

4. Conclusions

The main drawback encountered when spraying NiTi-alloys to form coatings is the high sensitivity to oxidation and easy depletion as it is a "line compound"; both facts prevent the complete formation of the intermetallic. The present work has explored other routes apart from the most used Vacuum Plasma spraying; HVOF and modified-APS have been used for comparison. The resulting microstructures lead to a dense and low oxide VPS-coating due to the fully melting at a low pressure atmosphere, while HVOF and APS show some oxidation and porosities.

With regard to their corrosion properties, a chloride solution was employed for the electrochemical tests simulating an aggressive corrosion medium; the three coatings were examined in their as-sprayed and as-polished form in order to evaluate the surface conditions. As result of the E vs time and potenciodynamic curves, one can see that the VPS coating has the highest E_{corr} and shows no differences whether it is polished or not; also both APS-quenched tend to the same E_{corr} but in the opposite, reaching the most negative values of the three coatings because of the facility of the electrolyte penetration to the substrate through the coating defects. By contrast, HVOF shows potential values similar to that of VPS in the as-sprayed form but decrease considerably in the as-polished, which has been attributed to crack formation after polishing oroxide removal of the top layer. In summary, according to the above results and under the experimental conditions of this work, the VPS coating presented the best corrosion resistance.
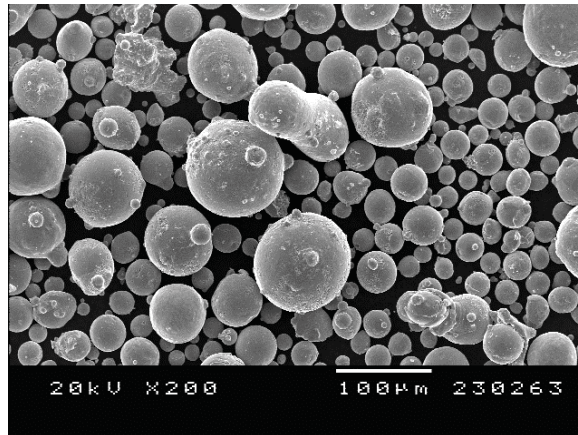
FIGURES

Fig 1. Spherical morphology of the as-atomized Ni-45%wt.Ti powders.
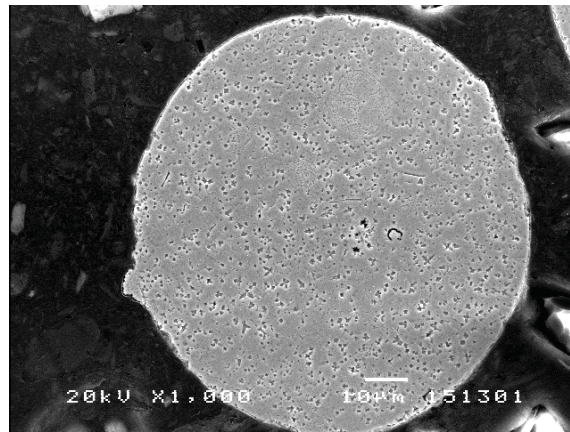
Figure 2. SE micrograph of the cross-section etched atomized powder.
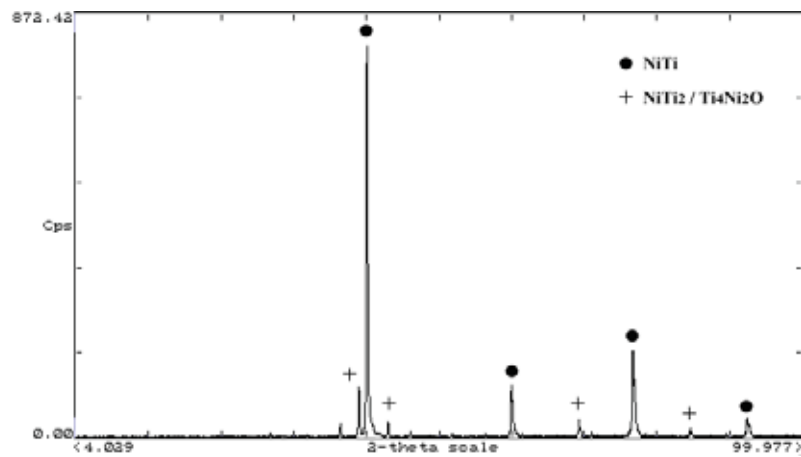
Figure 3. XRD scan of the atomized NiTi powder .
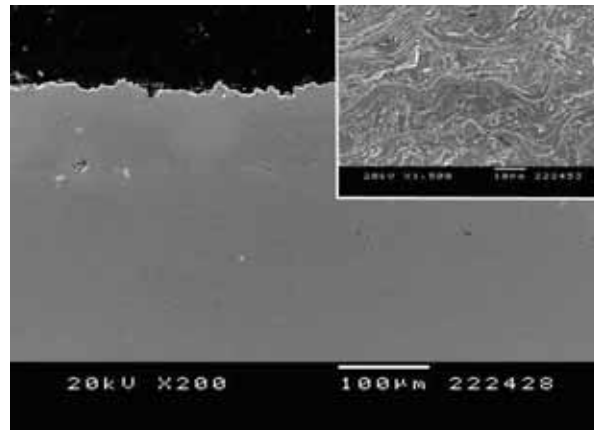
Figure 4. General micrograph of the unetched VPS coating, with a magnification of the revealed microstructure after etching.
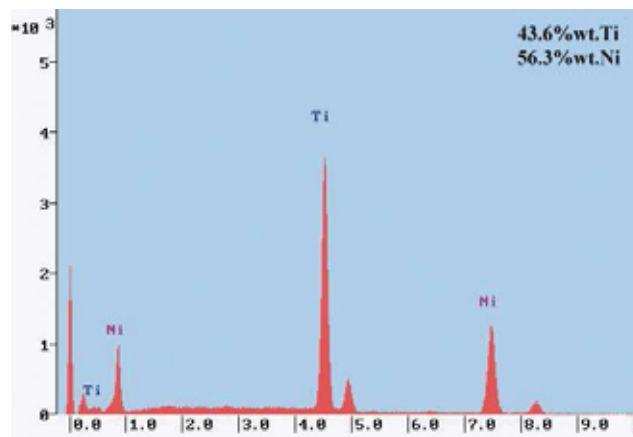
Figure 5. EDS microanalysis of the smooth etched VPS coating.
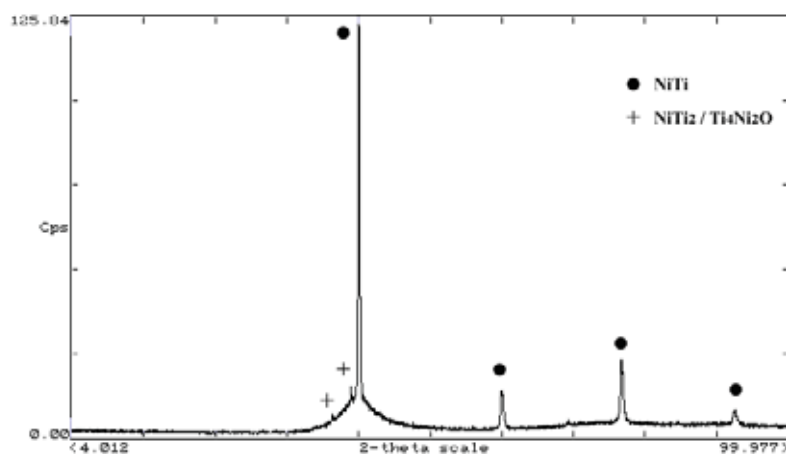
Figure 6. X-ray scan of the VPS coating surface.

a   **b**
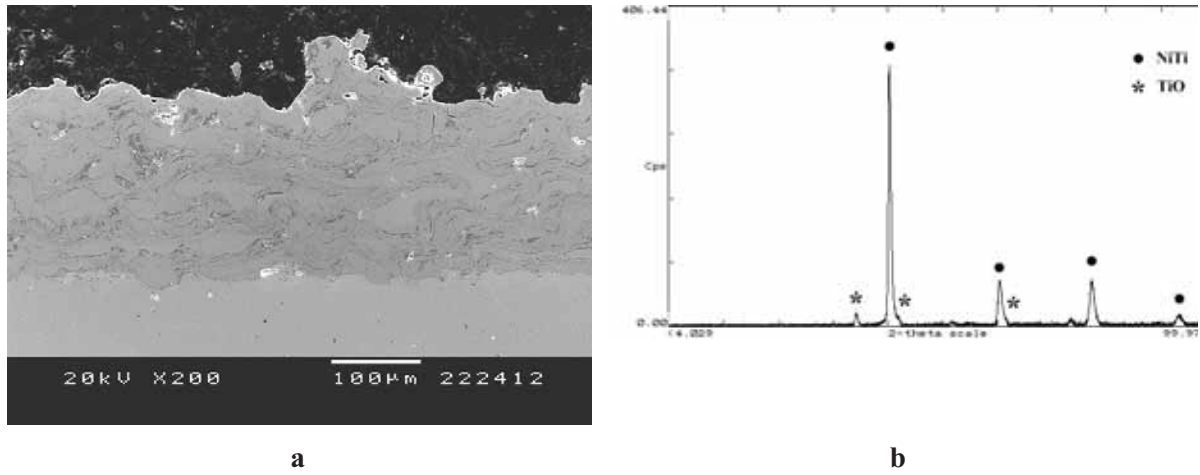
Figure 7. (a) General micrograph of the APS-quenched cross-section and (b) x-ray scan of the coating surface.
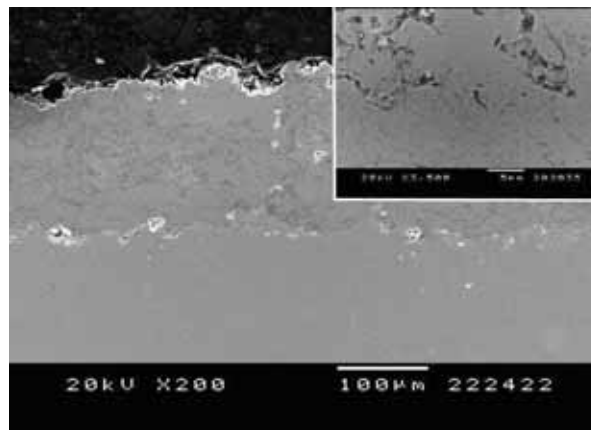
Figure 8. General micrograph of the HVOF sample cross-section and magnification of its microstructure.
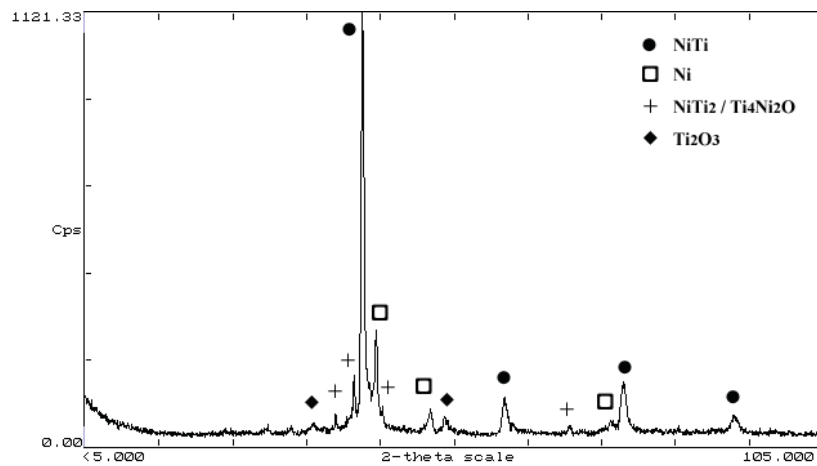
Figure 9. X-ray scan of the HVOF coating surface
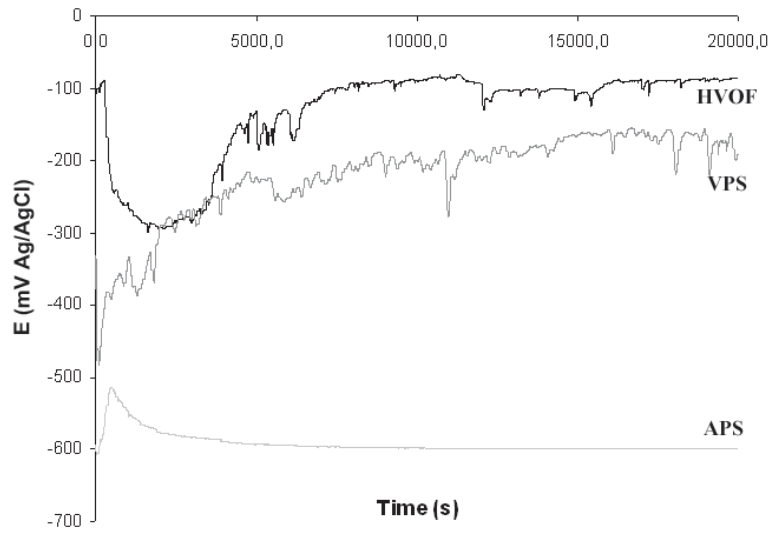
a
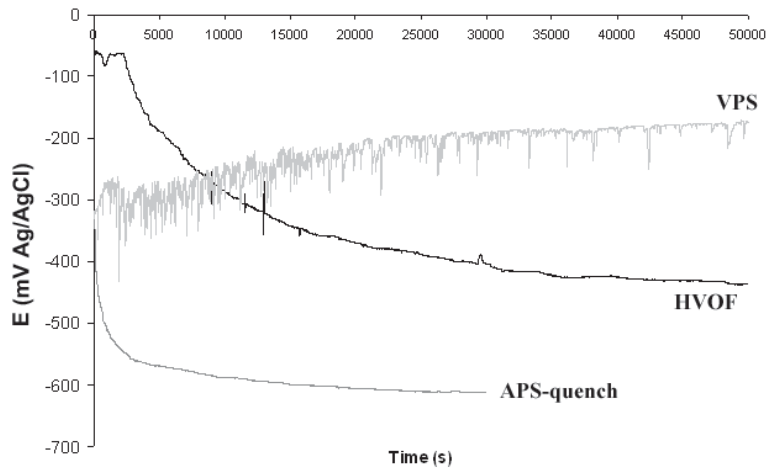
b

Figure 10. Open-circuit potentials of (a) as-sprayed and (b) as-polished coatings in chloride solution.
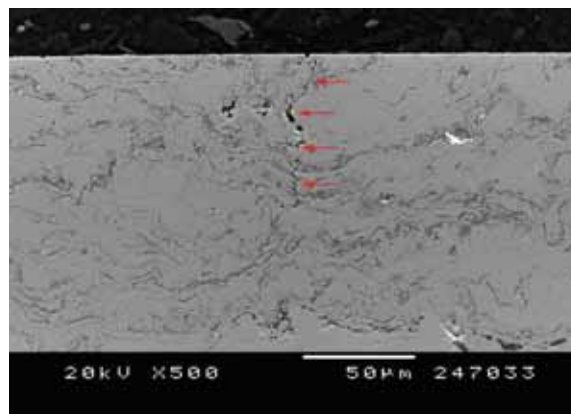
Figure 11. Cross section of the as-polished HVOF coating.

a

b
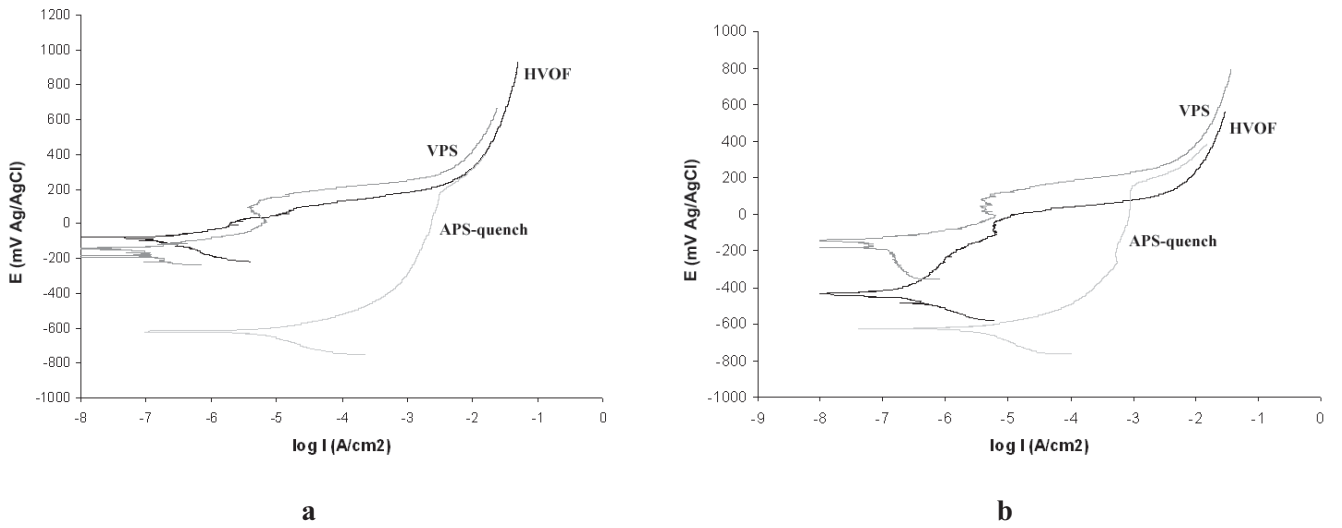
Figure 12. Potentiodinamic curves of the three coatings recorded in chloride solution at 0.166 mV s-1: (a) as-sprayed and (b) as-polished amples.

a

b

c

d
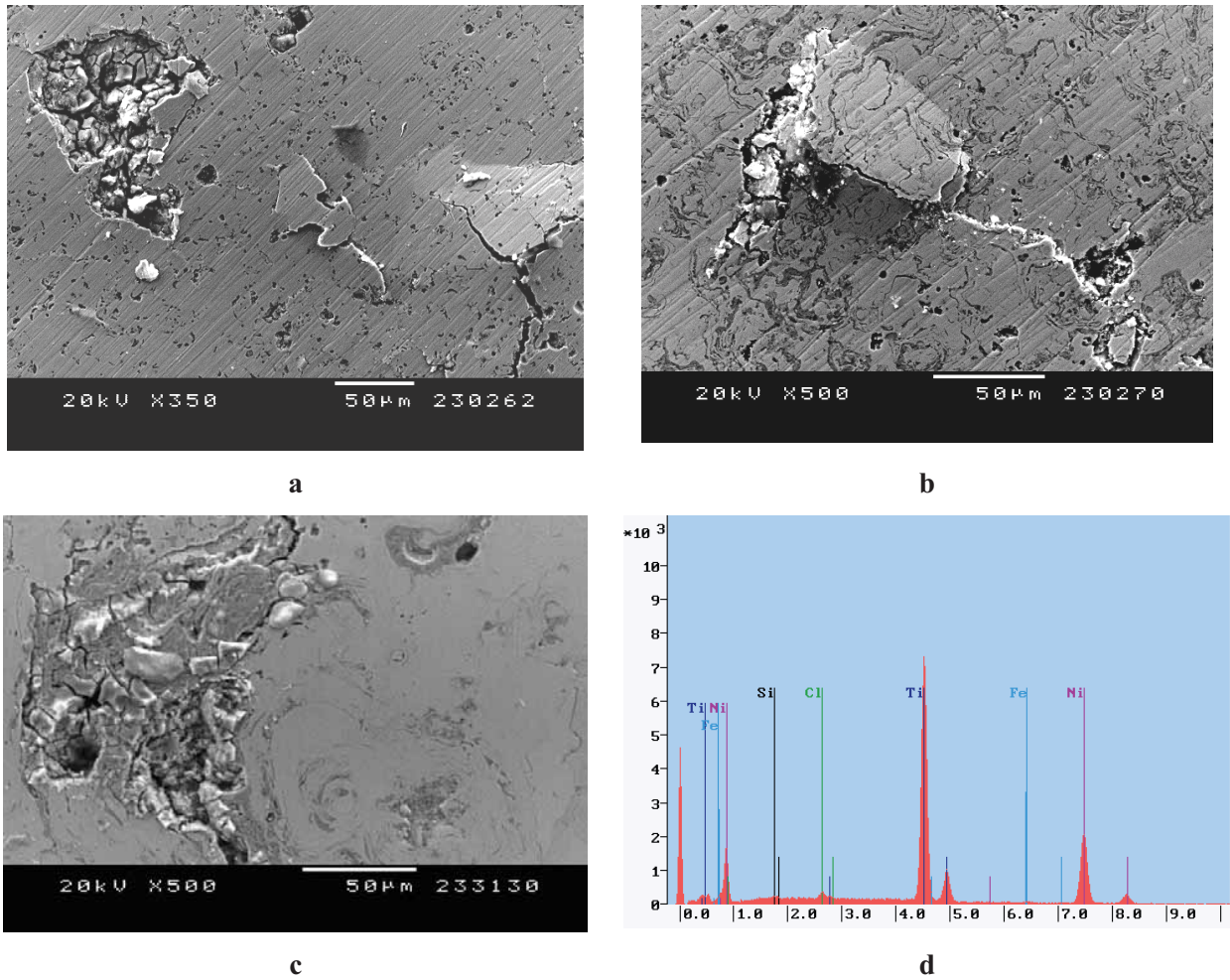
Figure 13. (a), (b) and (c) pitting phenomena on the VPS, HVOF and APS coatings respectively; (d) EDS of the corrosion products on the APS sprayed coating.

189
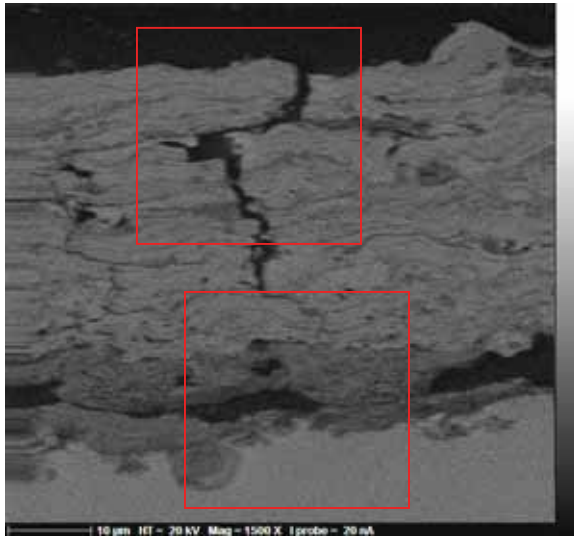
a
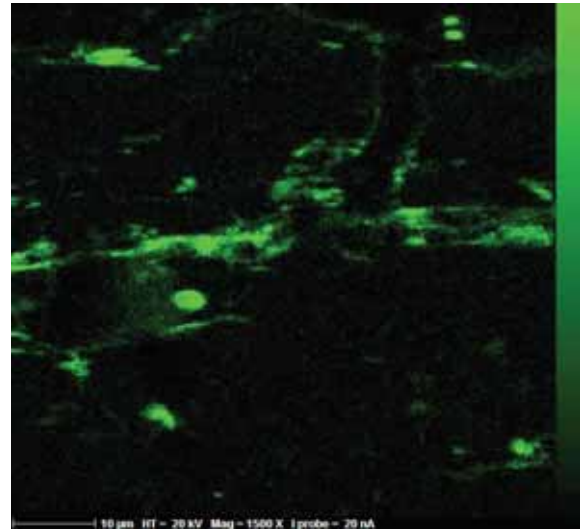
b
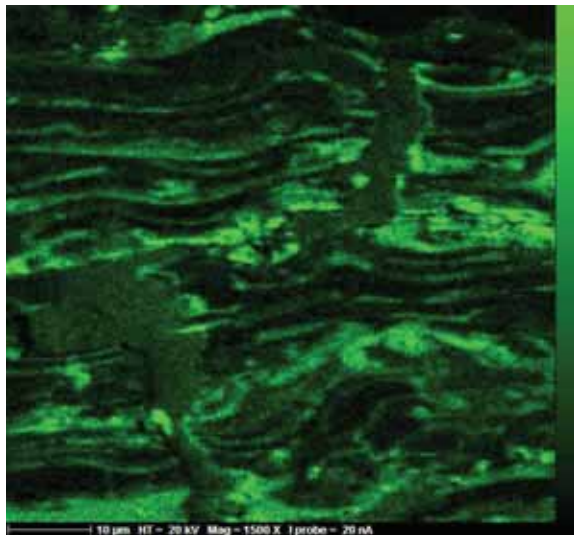
c
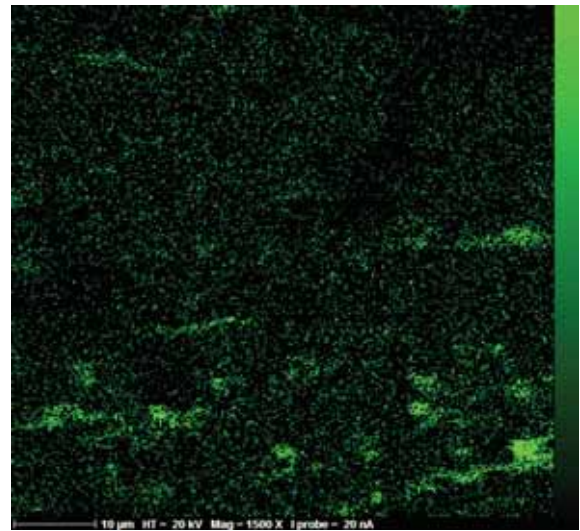
d
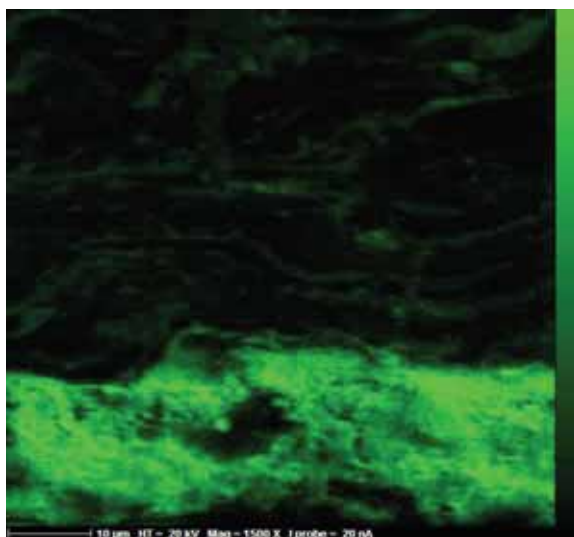
e
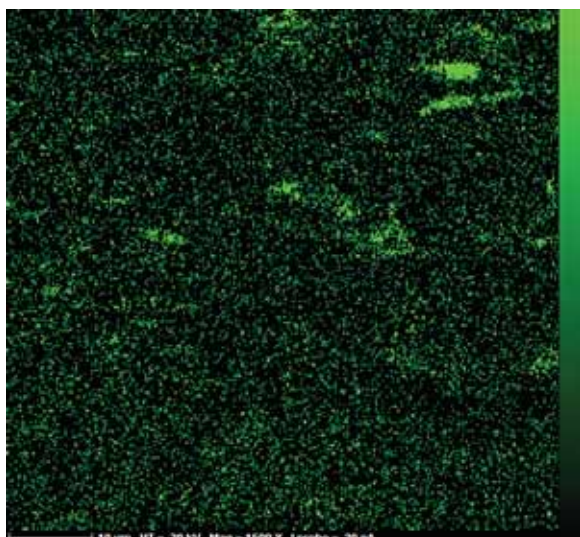
f
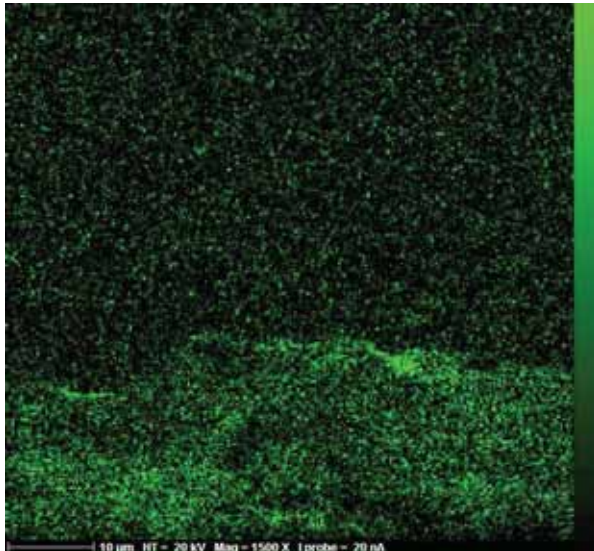
g

Figure 14. (a) Cross-section general micrograph of the crack, (b) Fe, (c) O and (d) Cl analysis of the upper part of the crack; (e) O, (f) Cl and (g) Na analysis of the down section of the crack.

TABLES

Table 1. Thermal spraying parameters for APS-quenching.

Argon (L/min)	30-40
Hydrogen (L/min)	10-15
Arc current (A)	600
Carrier gas, Ar (L/min)	4.5-5.0
Spraying distance (mm)	120

Table 2. Thermal spraying parameters for VPS.

Primary Argon plasma gas flow (L/min)	45-55
Secondary Hydrogen plasma gas flow (L/min)	5-10
Arc current (A)	600
Gun voltaje (V)	72
Carrier Argon gas flow (L/min)	4-5
Chamber Vacuum Pressure (mbar)	60
Spraying distance (mm)	300

Table 3. Thermal spraying parameters for HVOF.

Oxygen flow rate (L/min)	210-215
Hydrogen flow rate (L/min)	630-640
Carrier gas (L/min)	340-350
Spraying distance (mm)	220

Table 4. Roughness and thickness of the coatings.

	Roughness, Ra	**Thickness, μm**
APS-quenched	13.1 ± 1.7	201 ± 19
VPS	4.8 ± 0.6	85 ± 7
HVOF	8.2 ± 0.9	154 ± 14

Table 5. Corrosion parameters estimated from the potenciodynamic curves.

	APS-quenched		VPS		HVOF	
	As-sprayed	**polished**	**As-sprayed**	**polished**	**As-sprayed**	**polished**
i_{corr} (A cm^{-2})*	$2.6 \cdot 10^{-5}$	$4.8 \cdot 10^{-5}$	-	$3.7 \cdot 10^{-8}$	$1.0 \cdot 10^{-5}$	$7.6 \cdot 10^{-7}$
i_{corr} (A cm^{-2})**	$3.3 \cdot 10^{-6}$	$1.7 \cdot 10^{-6}$	$5.2 \cdot 10^{-8}$	$9.2 \cdot 10^{-8}$	$8.5 \cdot 10^{-8}$	$1.2 \cdot 10^{-7}$
bc, (mV Ag/AgCl) /decade	-85	-63	-123	-475	-60	-76
ba (mV Ag/AgCl) /decade	44	53	48	49	52	173
Rp (ohm cm^2)	$1.5 \cdot 10^{3}$	$3 \cdot 10^{3}$	-	$6 \cdot 10^{5}$	$1.6 \cdot 10^{4}$	$7.7 \cdot 10^{4}$
E_{corr} (mV Ag/AgCl)	-619	-628	-140	-140	-79	-436

* Stern-Geary estimation

** From polarization curves estimation

References

[1] http://www.uib.es/depart/dfs/apl/rsm/Tesis%20(2%20of%208).pdf

[2] Shabalovskaya S. A., Physicochemical and biological aspects of nitinol as a biomaterial, International Materials Review 46 (4) (2001) 1-17.

[3] Huang H., Chiu Y., Lee T., Wu S., Yang H., Su K., Hsu C., Ion release from NiTi orthodontic wires in artificial saliva with various acidities, Biomaterials 24, Issue 20 (2003) 3585-3592.

[4] Okuyama M., Kobayashi J., Take S., Itoi Y., Effect of Plasma Spray and Surface Sealing Treatment of Ni-Ti Shape Memory Alloy Applying to Biomaterials 45, Issue 4 (2004) 1045-1053.

[5] Sickinger A., Teter J. P. Superleastic shape memory alloy for seal applications produced by low pressure thermal spray technology. Mat Res Soc Symp Proc. 604 (2000) Materials research Society.

[6] Friske W. H., Schwartzbart H., Shape memory alloy seals for geothermal applications. U. S. Department of Energy database, Technical report.

[7] Seguin J.-L., Bendahan M., Isalgue A., Esteve-Cano V., Carchano H., Torra V. Low temperature crystallised Ti-rich NiTi shape memory alloy films for microactuators, Sensors and Actuators 74 (1999) 65–69.

[8] Kohl M., Dittmann D., Quandt E., Winzek B., Thin film shape memory microvalves with adjustable operation Temperature. Sensors and Actuators 83 (2000) 214–219.

[9] Fu Y., Huang W., Du H., Huang X., Tan J., GaoX., Characterization of TiNi shape-memory alloy thin films for MEMS applications, Surface Coatings and Technology 145 (2001) 107–112.

[10] Krulevitch P., Lee A. P., Ramsey P. B., Trevino J. C., Hamilton J., Northp M. A., Thin Film Shape Memory Alloys as microactuators, Journal of microelectromechanical systems 5, Issue 4 (1996) 270-282.

[11] Cheng F. T., Shi P., Man H. C.. Correlation of cavitation erosion resistance with indentation-derived properties for a NiTi alloy. Scripta Materialia 45 (2001) 1083-1089.

[12] Liang Y. N., Li S. Z., Jin Y. B., Jin W., Li S. Wear behaviour of a NiTi alloy. Wear 198 (1996) 236-241.

[13] Lin H. C., Wu S. K., Yeh C. H.. A comparison of slurry erosion characteristics of TiNi shape memory alloys and SUS304 stainless steel. Wear 249 (2001) 557-565.

[14] Richman R. H., Rao A. S., Hodgson D. E., Cavitation erosion of two NiTi alloys. Wear 157 (1992) 401 – 407.

[15] Cheng F. T., Shi P., Man H. C., Cavitation erosion resistance of heat-treated NiTi, Materials Science and Engineering A 339 (2003) 312 - 317.

[16] Hiraga H., Inoue T., Shimura H., Matsunawa A.. Cavitation erosion mechanism of NiTi coatings made by laser plasma hybrid spraying. Wear 231 (1999) 272-278.

[17] Ni W., Cheng Y., Grummon D. S., Wear resistant self-healing tribological surfaces by using hard coatings on NiTi shape memory alloys. Surface & coatings technology 201, 3-4 (2006) 1053-1057.

[18] Richman R. H., Rao A. S., Kung D.. Cavitation erosion of NiTi explosively welded to steel. Wear 181-183 (1995) 80-85.

[19] Girardeau T., Bouslykjane K., Mimault J., Villain J. P., Chartier P., Wear improvement and local structure in nickel-titanium coatings produced by reactive ion spouttering. Thin Solid Films 283 (1996) 67-74.

[20] Hiraga H., Inoue T., Shimura H., Kamado S., Kojima Y., Matsunawa A.., Matsunawa A., Fabrication of NiTi intermetallic compound coating made by laser plasma hybrid spraying of mechanically alloyed powders. Surface and Coatings Technology 139 (2001) 93-100.

[21] Ho K. K., Carman G. P., Sputter deposition of NiTi thin film shape memory alloy using a heated target. Thin Solid Films 370, Issue 57 (2000) 18-29.

[22] Yang Y. Q., Jia H. S., Zhang Z. F., Shen H. M., Hu A., Wang Y. N., Transformations in sputter-deposited thin films of NiTi shape memory alloy. Materials Letterns 22, Issues 3-4 (1995) 137-140.

[23] Bram M., Ahmad-Khanlou A., Buchkremer H. P., Stöver, Vacuum plasma spraying of NiTi protection layers. Materials Letters 57 (2002) 647-651.

[24] Siegmann S., Halter K., Wielage B.. Vacuum plasma sprayed coatings and freestanding parts of Ni-Ti shape memory alloy. ITSC 2003 pp 589-595.

[25] Halter K., Sickinger A., Zysset L., Siegmann S., Low Pressure Wire Arc and vacuum Plasma Spraying of NiTi Shape Memory alloys, Thermal Spray 2003: Advancing the Sicence & Applying the Technology. Ed C Moreau and B. Marple. Ohio USA. pp 589-595

[26] Siegmann S., Halter K., Wielage B. Vacuum plasma sprayed coatings and freestanding parts of nit-it shape memory alloy. ITSC 2002 pp 357-361.

[27] Sickinger A., Thermal Spraying of NiTi alloys, SMST-2003: The International Conference on Shape Memory and Superelastic Technologies; USA; (2004) 153-162.

[28] Halter K., Sickinger A., Siegmann S., Zysset L., Thermal Spray forming of NiTi shape memory alloys, SMST-2003: The International Conference on Shape Memory and Superelastic Technologies; USA; (2004) 163-172.

[29] Sobolev V.V., Guilemany J.M., Nutting J., High velocity oxy-fuel spraying, W.S. Maney and Son Ltd., Leeds, UK, 2004.

[30] Cano I.G., Dosta S., Miguel J.R., Guilemany J.M., Journal of Materials Science 42 (2007) 9331-9335.

[31] Chiu K. Y., Cheng F. T., man H. C., Corrosion behaviour of AISI 316L stainless steel surface-modified with NiTi, Surface & Coatings Technology 200 (2006) 6054-6061.

[32] Man H. C., Cui Z. D., Yue T. M., Corrosion properties of laser surface melted NiTi shape memory alloy. Scripta materialia 45 (2001) 1447-1453.

[33] Guilemany J.M., Miguel J.R., Fernández J., Dosta S., Cano I.G., Tntellectual Property Protection of Plasma+quench Process (APS+Q), iPP (AVCRI 040)

[34] Suegama P. H., Espallargas N., Guilemany J. M., Fernández J., Benedetti A., Electrochemical and Structural Characterization of Heat-Treated Cr_3C_2–NiCr Coatings. J. Elec. Soc. B, 123 (2006) 434-445.

[35] Suegama P. H., Fugivara C. S., Benedetti A. V., Fernández J., Espallargas N., Delgado J. M., Guilemany J. M., Microstructure and electrochemical studies of Cr_3C_2–NiCr Coatings obtained by HVOF. In: Vargus, E. P. (Ed.) New researchers on electrochemistry, New York: Nova Science publishers, Chapter 4 (2007).

[36] Stern, M., Geary, A. L., Electrochemical Polarization: I. A Theoretical Analysis of the Shape of Polarization Curves. J. Electrochem. Soc., 104 (1957) 56-63.

[37] V. Feliu, J. A. González, C. Andrade, S. Feliu, Equivalent circuit for modelling the steel-concrete interface. II. Complications in applying the Stern-Geary equation to corrosion rate determinations. Corros. Sci., 40 (1998) 995-1006.

[38] Gaffet E., Ni-Ti: State of the Art, in: NAMAMET, NanoMaterials Research Group (2004).

[39] Cano I.G., Cinca N., Dosta S. , Guilemany J.M.. On the NiTi Metastable Powders and Coatings Obtained by Plasma Spraying. Primer Congreso Español sobre Pulvimetalúrgia, julio 2006.

[40] Final Activity Report: Nano–technologies and nano–sciences, knowledge–based multifunctional materials, and new production processes and devices – 'NMP', SIXTH FRAMEWORK PROGRAMME (Processing of NAnostructured MAterials through Metastable Transformations) 2008.

[41] Guilemany J.M., Espallargas N., Suegama P.H., Benedetti A.V., Comparative study of Cr_3C_2–NiCr coatings obtained by HVOF and hard chromium coatings. Corros. Sci., 48 (2006) 2998-3013.

[42] Shabalovskaya, Surface, corrosion and biocompatibility aspects of nitinol as an implant material, Bio-Med Materials Engineering 12 (2002) 69 –109.

[43] Matthews B., Broszeit E., Aromaa J., Ronkainen, Hannula H., Leyland S., Matthews A., Corrosion performance of some titanium-based hard coatings. Surface and coatings technology 49 (1991), 489-495.

[44] Creus J., Mazille H., Idrissi, Porosity evaluation of protective coatings onto steel, through electrochemical techniques. Surface and Coatings Technology 130 (2000) 224.232.

[45] Lister T.E., Wright R.N., Pinhero P.J., Swank W.D., Corrosion of thermal spray hastelloy C-22 coatings in dilute HCl, Journal of Thermal Spray Technology 11 (2002) 530-535.

[46] Zhang D., Harris S.J., McCartney D.G., Microstructure formation and corrosion behaviour in HVOF-sprayed Inconel 625 coatings. Materials Science and Engineering A 344 (2003) 45-56.

- *Corrosion in a marine environment*

The previous electrochemical tests were used to identify the corrosion behaviour of the material in aqueous solutions of chloride ions at the laboratory scale. However, the tests that can better reproduce a marine atmosphere are salt fog chambers.

Figure 4.53 shows the different samples after being removed from the chamber; VPS and HVOF NiTi alloys lasted to the end of the test (1500h), whereas the APS-quenching exhibited some pitting initiation at 700h. Therefore, as well as in electrochemical tests, this sample possesses the lowest corrosion resistance.

| a | b | c |
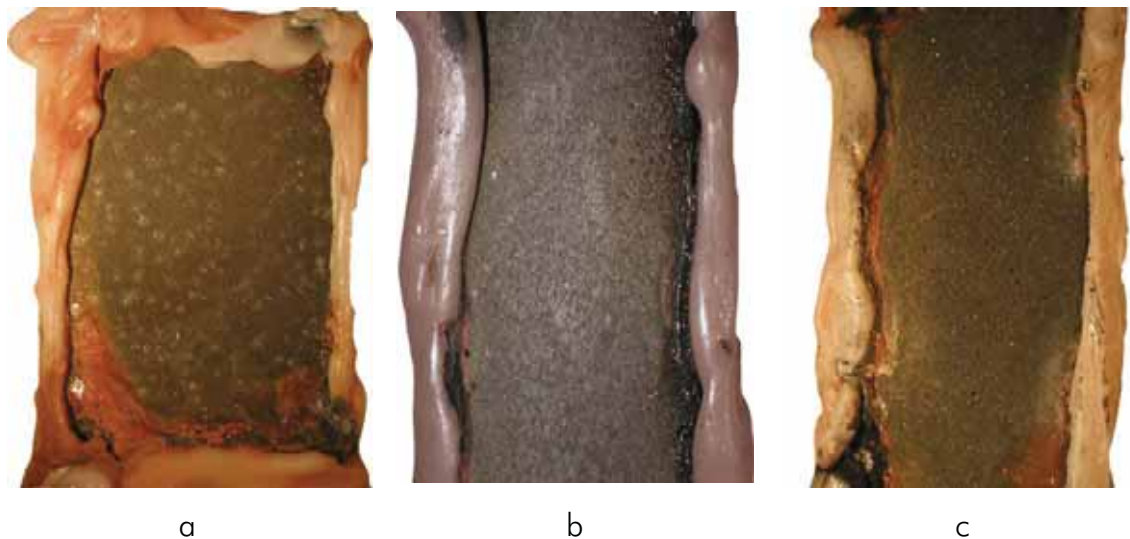
Figure 4.53. Salt fog testing for the NiTi coatings (a) VPS, (b) APS-quenching and (c) HVOF.

The corrosion is considered to start when oxidation occurs in the middle of the coating, as the edge corrosion is normal due to the presence of the wax surrounding the samples to leave just the sprayed surface exposed to the corrosive atmosphere. Finally, figure 4.54 shows the X-ray scans with some of the identified oxidized products.
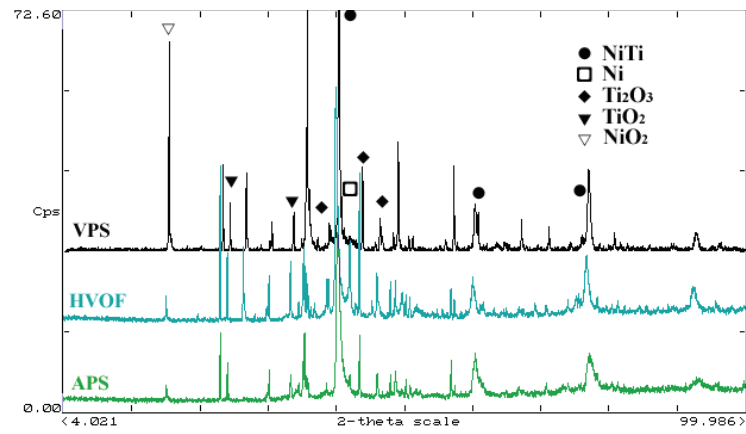
Figure 4.54. X-ray scans after the salt fog tests.

REFERENCES

[1]   S. Launois, A. Fraczkiewicz, Environmental effect on mechanical behavior of reinforced FeAl (40 at. % Al) alloy, Journal de physique IV, Vol. 6, Issue 2 (1996) pp. C2.223-C2.228.

[2]   T. Grosdidier, G. Ji, F. Bernard, Sébastien Launois , Synthesis of FeAl Hetero-Nanostructured Bulk Parts via Spark Plasma Sintering of Milled Powder, MRS Bulletin (2007).

[3]   D. B. Witkin, E. J. Lavernia, Synthesis and mechanical behaviour of nanostructured materials via cryomilling, Progress in Materials Science, Vol. 51 (2006) pp. 1-60.

[4]   B. J. M. Alkin, M. G. Hebsur, J. D. Whittenberger, Reproducibility of NiAl cryomilling, Proceedings of the 2nd International Conference on Structural Applications of Mechanical Alloying, Canada, 1993.

[5]   B. Huang, J. Vallone, M. J. Luton, The effect of nitrogen and oxygen on the síntesis of B2 NiAl by cryomilling, Nanostructured Materials, Vol. 5, Number 6 (1995) pp. 631-642.

[6]   C. Suryanarayana, Mechanical alloying and milling, Progress in Materials Science, Vol. 46 (2001) pp. 1-184.

[7]   Ji G., Grosdidier T., Liao H. L., Morniroli J., Coddet C., Spray forming thick nanostructured and microstructured FeAl deposits, Intermetallics, Vol. 13 (2005) pp. 96-607.

[8]   M. Krasnowski, A. Grabias, T. Kulik, Phase transformations during mechanical alloying of Fe50%Al and subsequent heating of the milling product, Journal of alloys and compounds, Vol. 424, Issue 1-2 (2006) pp. 119-127.

[9]   B. D. Cullity, Elements of X-ray diffraction, Ed. Addison-Wesley, 2a ed, cop. 1978.

[10]   J. Gang, J. Morniroli, T. Grosdidier, Nanostructures in thermal spray coatings, Scripta Materialia, Vol. 48 (2003) pp. 1599-1604.

[11]   J. Gang, T. Grosdidier, H. L. Liao, J. Morniroli, C. Coddet, Spray forming thick nanostructured and microstructural FeAl deposits, Intermetallics, Vol. 13, Issue 6 (2005) pp. 596-607.

[12]   S. Desphande, S- Sampath, H. Zhang, Mechanisms of oxidation and its role in microstructural evolution of metallic thermal spray coatings- Case study for Ni-Al. Surface & coatings Technology, Vol. 200 (2006) pp. 5395-5406.

[13]   L. Pawlowski, The science and engineering of Thermal Spray coatings, John Wiley & Sons, New York, NY (1995).

[14]   G. H. Meier, Research on oxidation and embrittlement of intermetallic compounds in the U.S., Materials and Corrosion, Vol. 47 (1996) pp. 595-618.

[15] C. D. Ngoc Chan, C. Hujier, J. F. Dinhut, High temperature corrosion of some B2 iron aluminides, Intermetallics, Vol. 9 (2001) pp. 817-826.

[16] F. Lang, Z. Yu, S. Gedevanishvili, S. C. Deevi, T. Narita, Isothermal oxidation behavior of a sheet alloy of Fe40at.Al, at temperatures between 1073 and 1473K, Intermetallics, Vol. 11 (2003) pp. 697-705.

[17] A. Mignone, S. Frangini, A. La Barbera, O. Tassa, High Temperature corrosion of B2 iron aluminides, Corrosion Science, Vol. 40, Issue 8 (1998) pp. 1331-1347.

[18] H. Hindam, D. P. Whittle, Microstructure, adhesion and growth kinetics of protective scales on metals and alloys, Oxidation of metals, Vol. 18, Numbers 5-6 (1982) pp. 245-283.

[19] C. H. Xu, W. Gao, S. Li, Oxidation behaviour of FeAl intermetallics- the effect of Y on the scale spallation resistance, Corrosion Science, Vol. 43 (2001) pp. 671-688.

[20] S. Vladimirovich Klinkov, V. Fedorovich Kosarev, M. rein, Cold spray deposition, Aerospace Science and technology, Vol. 9 (2005) pp. 582-591.

[21] F. Raletz, M. Vardelle, G. Ezo'o, Critical particle velocity under cold spray conditions, Surface & Coatings technology, Vol. 201 (2006) pp. 1942-1947.

[22] H. Wang, C. Li, G. Yang, P. Gao, Q. Zhang, Deposition characteristics of Fe/Al composite coating fabricated by cold spraying, International Thermal Spray Conference (2008).

[23] J. W. Koger, M. Marietta, Molten salt corrosion, Metals Handbook. ASM International. Tenth Edition, Vol. 13: Corrosion (1990) pp. 216-219.

[24] Corrosion in Fossil Fuel Power Plants, Metals Handbook. ASM International. Tenth Edition, Vol. 13: Corrosion (1990) pp. 985-1001.

[25] H. Singh, B. S. Sidhu, D. Puri, S. Parkash, use of plasma spray technology for deposition of high temperature oxidation/corrosion resistant coatings- a review, Materials and Corrosion, Vol. 58, Number 2 (2007) pp. 92-102.

[26] T. Mäntyla, M. Uusitalo, P. Vuoristo, Hot corrosion and hot erosion resistant thermal spray coatings, 2 Rencontres Internacionales sur la Projection Thermique (2005) pp. 244-246.

[27] Y. S. Li, M. Spiegel, Models describing the degradation of FeAl and NiAl alloys induced by $ZnCl_2$-KCl melt at 400-450°C, Corrosion Science, Vol. 46 (2004) pp. 2009-2023.

[28] Y. S. Li, M. Spiegel, Internal Oxidation of Fe-Al alloys in a KCl-air atmosphere at 650°C, Oxidation of metals, Vol. 61, Numbers 3-4 (2004) pp. 303-312.

[29] Magnetic Alloys for technological applications. Landolt-Börnstein. Numerical data and functional relationship in science and technology. Group III, Vol. 19. Magnetic Properties of Metals, subvolume I-1.

[30] R. J. Harrison, A. Putnis, The magnetic properties and crystal chemistry of oxide spinel solid solutions, Surveys in Geophysics, Vol. 19 (1999) pp. 461-520.

[31] X. Amils, J. Nogués, S. Suriñach, J.S. Muñoz, L. Lutterotti, S. Gialanella, M.D. Baró, Structural, mechanical and magnetic properties of nanostructured FeAl alloys during disordering and thermal recovery, NanoStructured Materials, Vol. 11, No. 6 (1999) pp. 689–695.

[32] Q. Zeng, I. Baker, The effects of local versus bulk disorder on the magnetic behaviour of stoichiometric Ni_3Al, Intermetallics, Vol. 15 (2007) pp. 419-427.

[33] D. Wu, I. Baker, Strain-induced ferromagnetism in FeAl single crystals, Materials Science and Engineering A, Vols. 329-331 (2002) pp. 334-338.

[34] M. Cherigui, N. E. Fenineche, A. Gupta, G. Zhang, C. Coddet, Magnetic properties of HVOF thermally sprayed coatings obtained from nanostructured powders, Surface & Coatings Technology, Vol. 201 (2006) pp. 1805-1813.

[35] M. Cherigui, N. E. Fenineche, G. Ji, T. Grosdidier, C. Coddet, Microstructure and magnetic properties of Fe-Si-based coatings produced by HVOF thermal spraying process, Journal of Alloys and Compounds, Vol. 427 (2007) pp. 281-290.

[36] N. E. Fenineche, R. Hamzaoui, O. El Kedim, Structure and magnetic properties of nanocrystalline Co-Ni and Co-Fe mechanically alloyed, Materials Letters, Vol. 57 (2003) pp. 4165-4169.

[37] V. Gauthier, C. Josse, J. P. Larpin, M. Vilasi, High-Temperature Oxidation Behavior of the Intermetallic Compound $NbAl_3$: Influence of Two Processing Techniques on the Oxidation Mechanism, Oxidation of Metals, Vol. 54, Nos. 1/2 (2000) pp. 27-45

[38] M. H. Mueller, H. W. Knott, The crystal structures of Ti_2Cu, Ti_2Ni, Ti_4Ni_2O, and Ti_4Cu_2O, Transactions of the Metallurgical Society of Aime, Vol. 227 (1963) pp. 674-678.

[39] Hhttp://www.aerofit.com/SMA/corrwref.pdfH

[40] M. J. Vestel, D. S. Grummon, Precipitates and lamellar microstructures in NiTi films, HMaterials Science and Engineering AH, HVol. 378, Issues 1-2H (2004) pp. 437-442.

[41] M . Vestel, Effect of temperature on the devitrification kinetics of NiTi films, Acta Materialia, Vol. 51, Issue 18, pp. 5309 – 5318.

[42] M. Târcolea, A. E. Dumitru, A. M. Sandu, F. Miculescu, C. M. Cotrut, N. Miculescu, Investigations on precipitation phenomena in a SMA (Ni-Ti), European Cells and Materials, Vol. 16, Suppl. 1 (2008) pp. 57.

[43] A. J. Muir Wood, J-H You, T. W. Clyne, Nanoindentation response of superelastic materials, Smart Materials, Nano- and Micro-Smart Systems: Smart Materials III, Proceedings of SPIE 5648.

[44] J. I. Kim, Y. Liu, S. Miyazaki, Ageing-induced two-stage R-phase transformation in ti-50.9at%Ni, Acta Materialia, Vol. 52 (2004) pp. 487-499.

[45] J. M. Guilemany, N. Cinca, S. Dosta, A.V. Benedetti, Corrosion behaviour of thermal sprayed nitinol coatings, *Corrosion Science* (submitted).

[46] E. J. Young,U, E. Mateeva, John J. Moore, B. Mishra, Michael Loch, Low pressure plasma spray coatings, Thin Solid Films, Vols. 377-378 (2000) pp. 788-792

[47] A. Ball, On the importance of work hardening in the design of wear-resistant materials, Wear, Vol. 91 (1983) pp. 201-207.

[48] Y. Shida, Y. Sugimoto, Water jet erosion behavior of Ti-Ni binary alloys, Wear, Vol. 146 (1991) pp. 219-228.

[49] P. Clayton, Tribological behavior of a titanium-nickel alloy, Wear, Vol. 162 (1993) pp. 202-210.

[50] J. Singh, A. T. Alpas, Dry sliding wear mechanisms in a $Ti_{50}Ni_{47}Fe_3$ intermetallic alloys, Wear, Vol. 181-183 (1995) pp. 302-311.

[51] H. C. Lin, S. K. Wu, C. H. Yeh, A comparison of slurry erosion characteristics of TiNi shape memory alloys and SUS304 stainless steel, Wear, Vol. 249 (2001) pp. 557-565.

[52] F. T. Cheng, P. Shi, H. C. Man, Cavitation erosion resistance of heat-treated NiTi, Materials Science and Engineering A, Vol. 339 (2003) pp. 312-317.

[53] R. H. Richman, A. S. Rao, D. Kung, Cavitation erosion of NiTi explosively welded to steel, Wear, Vols. 181-83 (1995) pp. 80-85.

[54] Y. N. Liang, S. Z. Li, Y. B. Jin, W. Jin, S. Li, Wear behavior of a TiNi alloy, Wear, Vol. 198 (1996) pp. 236-241.

[55] J. Stella, E. Schüller, C. Heissing, O. A. Hamed, M. Pohl, D. Stöver, Cavitation erosion of plasma-sprayed NiTi coatings, Wear, Vol. 260 (2006) pp. 1020-1027.

[56] V. Imbeni, C. Martini, D. Prandstraller, G. Poli, C. Trepanier, T. W. Duerig, Preliminary study of micro-scale abrasive wer of a NiTi shape memory alloy, Wear, Vol. 254 (2003) pp. 1299-1306.

[57] G. B. Stachowiak, G. W. Stachowiak, The effects of particle characteristics on three-body abrasive wear, Wear, Vol. 249 (2001) pp. 201-207.

[58] M. Pourbaix, Electrochemical corrosion of metallic biomaterials, Biomaterials, Vol. 5 (1984) pp.122.

[59] Y. Cheng, W. Cai, L. C. Zhao, Effects of Cl- ion concentration and pH on the corrosion properties of NiTi alloy in NaCl solution, Journal of Materials Science Letters, Vol. 22 (2003) pp. 239-240.

[60] S. A. Shabalowskaya, Surface, corrosion and biocompatibility aspects of Nitinol as an implant material, Bio-Medical Materials and Engineering, Vol. 12 (2002) pp. 69-109.

[61] R. S. Dutta, K. Madangopal, H. S. Gadiyar, S. Banerjee, Biocompatibility of Ni-Ti shape memory alloy British Corrosion Journal, Vol. 8 (1993) pp. 217-221.

[62] P. P. Traskoma, Corrosion, in : R. K. Everett, R. J. Arsenault Eds, Metal-Matrix Composites: Mechanisms and Properties, Academic Press, California, USA, 1991, pp. 383-403.

CHAPTER 5: DISCUSSION

The previous chapter explained the results obtained for various intermetallic coatings (FeAl, NbAl$_3$ and NiTi) and discussed in detail the problems involved. This discussion chapter looks at all the above alloys and tackles each property in terms of its material composition and deposit structure.

5.1   Pre-deposition

The manufacturing processes by which the raw powder material is produced, have a strong influence on the final deposited composition. Hence, for instance, the supplied iron aluminide Grade-3 powders were produced by atomising + ball-milling, which gives an angular shape to the powder and introduces a strained structure with refined grain size. Such a decrease in grain size is aimed at improving material properties over those obtained with just as-atomized powders. In the paper entitled "Ordering and disordering processes in MA and MM intermetallic iron aluminide powders", the degree of disorder of the powder was evaluated and was compared to that of the atomized (unmilled) and annealed powder. It was observed, however, that a full ordered structure could not be achieved, as the initial composition deviates slightly from the stoichiometry.

In this case, however, the alloy was already formed, with a disordered lattice and, despite the occurrence of more or less oxidation during the spraying process, the intermetallic phase was predominant in the composition of the deposited material. It was then proceeded to evaluate the feasibility of the mechanical alloying technique, starting from a Fe+Al powder mixture. The alloying was performed in a cryogenic medium, since the intention was to strengthen the material by AlN formation, even to the detriment of complete alloying (milling by this method led to a solid solution phase). Although the presence of such dispersed particles has not yet been demonstrated, the compositional analysis indicates the presence of elemental N.

Although the previous powders were angular in shape, they did not show any flowability problem, not even the cryomilled powder, which does not show a Gaussian distribution.

For the commercial niobium aluminide ($NbAl_3$) alloy, the lower aluminide $NbAl_2$, though in trace quantities, was also found in the starting composition. This powder agglomerated easily and had asymmetric particle size distribution. Finally, NiTi powder is a gas-atomized powder with perfect flowability and it consists basically of Austenite phase with some $NiTi_2$/Ti_4Ni_2O precipitates. As mentioned above, this alloy is known for its pseudo-elasticity and shape memory effect. Such changes result from a series of Martensite transformations between these three phases: B2 (CsCl-type) Austenite **A** phase, B19' (monoclinic), Martensite **M** phase and the **R** (rhombohedral) phase. The three transformations A↔M, A↔R and R↔M are possible. All three transformations involve lattice distortions and are sensitive to variations in metallurgical and mechanical conditions as well as chemical composition. Specifically, A↔M and R↔M are characterized by large lattice distortion and large transformation hysteresis, as well as introducing structural defects into the microstructure. The reversible and diffusionless martensite-austenite transformation takes place in the temperature range from 50 to 100°C as a function of the Ni content of the matrix (usually 48-51at.%). Other factors may also influence the transformation temperature:

- According to the phase diagram, Ti-rich and Ni-rich compositions show respectively $NiTi_2$ and Ti_3Ni_4 precipitates, with different effects on the shape memory effect. Excess nickel strongly depresses the transformation temperature and increases the yield strength of the austenite; actually, a variation of the Ni content by 0,1at.% changes the transformation temperature by approximately 10°C. Many works have claimed that the occurrence of Ti_3Ni_4 precipitates resulting of ageing treatments, yields to the appearance of the A↔R transformations.

- Common contaminants such as oxygen and carbon ($Ti_4Ni_2O_X$ and TiC_XNi_{1-X}) can also shift the transformation temperature and degrade the mechanical properties.
- The elimination of local stresses after a heat treatment produces an increase of the transformation temperature.

Then, the presence of Ti-rich phases, either $NiTi_2$ or $Ti_4Ni_2O_X$, leaves a matrix rich in nickel that makes the transformation temperature fall below room temperature. In addition, the fact that no sign of the A→M process is evident on cooling, might be due to the large hysteresis of such transformation.

5.2   As-sprayed coatings

All the above powders show a compact structure that leads to a temperature gradient from the external particle to the core during the spraying process. This hinders total particle fusion by preventing oxidation, as higher energy or in-flight times would be necessary. This is especially important when using HVOF, which involves lower flame temperatures.

– *Iron aluminide*

In line with the references found in the literature, iron aluminide powder was sprayed by HVOF and different spraying parameters were tested. These preliminar tests were performed with the FeAl grade 3 powder and consisted on modifying fuel gases (propylene and hydrogen) and their fluxes as well as those of oxygen and air.

According to the parameters used with propylene, all the oxygen/fuel ratios were below the stoichiometry (4.5), having F3 the closest to that corresponding to the maximum flame temperature. This is why F1 and F2 microstructures exhibit more partially molten areas than in F3, where there is a

clear lamellar structure with oxidation at the intersplats. The much higher oxygen/fuel ratio in F3 comes from the larger oxygen flow rate, whereas the oxygen difference between F1 and F2 comes from the 20% in the air. This higher air flow rate in F1, compared to F2, also affects to the stream velocity since there is a larger amount of gases.

When comparing among the different HVOF spraying conditions, by using hydrogen as fuel, less oxygen is needed for combustion according to the stoichiometry. Thus, the reaction is less competitive with particle oxidation and the entire oxygen mainly reacts with hydrogen. Then, the coatings produced with hydrogen should have less oxidation. Surprisingly, the results showed the opposite. A possible explanation might be that the higher thermal efficiency and so larger melting when using hydrogen, leads to increased surface to volume ratios compared to combustion with propylene. Larger surface to volume ratios would produce more oxidation. As result of such oxidation, there is Al-depletion beneath the surface of the splat, which appears as the light grey area right below the oxide layer.

Among the three microstructures sprayed with hydrogen, F5 presents the higher oxygen/hydrogen ratio yielding to a more effective combustion, more melting and more reactive droplet surface to be oxidized. In F4, the oxygen comes from the higher air flow rate. Finally, F6 conditions reached the coolest and more reductive conditions among the three.

The cryomilled powders also led to coatings with molten and almost fully molten splats with oxidized bands. The TEM studies were supported by X-ray patterns, which showed that these two strained and disordered powders (coming from either the disordered B2 lattice or Fe(Al) solid solution) evolve to a coating structure of recrystallized grains. Nevertheless, in the CEA (F2) coating referred to, the super-lattice spots are already visible, while in the CRYO coating they are not. The reason for this might be that the high spraying temperatures facilitated the further alloying of the Fe(Al) to produce

FeAl, but these were not sufficient to achieve such a degree of order as that observed in CEA.

TEM studies also examined the structure of those coatings obtained by using a feedstock powder of 40-60 particle size (MEC40-60 coating). Some other works using nanocrystalline powders claim that the origin of a nanocrystalline structure in the coating remains to be established. It is not certain whether it results from retention of a nanocrystalline structure in feedstock powders or from the formation of nanocrystalline structure during spraying of the powders. Here we assume the latter explanation, as otherwise the (100) reflection would not be detected. Then, the annealing of this powder resulted in a coating with an ordered FeAl lattice and coarser grain sizes within the microscale. The higher grain size of such annealed powder was shown by its narrower X-ray peaks.

Spraying such larger particles also produced different coating microstructure with no signs of oxidation in the X-ray scans. Oxidation was internal, as identified in the electron diffraction patterns.

— *Niobium aluminide*

The microstructure of Nb-Al coatings resemble that of the iron aluminide coatings obtained by spraying the prealloyed MM powder and the cryomilled one, in the sense that they are composed of a lamellar structure with the $NbAl_3$ core regions and oxidized splat boundaries. However, the Al-depleted areas resulting of such oxidation will be detrimental for oxidation resistance.

Among the niobium aluminides within the Nb-Al diagram phase, NbAl3 is known to have the best properties for high-temperature resistance, the others degrade easily. Thus, it would have been desirable to produce a microstructure without oxidation since it prevents the formation of Al-depleted areas. However, considering the higher melting point of $NbAl_3$ compared to FeAl, higher flame temperatures were necessary; in addition, regarding the

broad distribution of the feedstock powder and its low flowability, the final microstructure was considered to be a good achievement.

− *Nickel titanium*

There are few studies of the use of nitinol alloy obtained by thermal spray as a coating. Because of material oxidation, other authors only attempted to use Vacuum Plasma Spray as oxygen changes its transformation temperatures. Nevertheless, the objective of additional spraying by HVOF and APS+Q was to evaluate other properties such as corrosion and wear. Because of its corrosion resistance, this alloy in its bulk form has been extensively investigated, mainly for biomedical use, but also for use in aggressive environments such as marine atmospheres.

Therefore, oxidation was here critical. Vacuum Plasma Spray, as expected, did not show intersplat oxidation but the other techniques presented a contribution of both in-flight and/or after splat impact oxidation. In HVOF, reduction of in-flight oxidation is associated to lower particle temperature, which makes the viscosity increase and the relative velocity between flame gas and particle lower, thus giving internal oxides within particle and a thin oxide shell but no segregation at the front end of the particle, as commonly shown in APS. On the other hand, the impinging gas jet can cause oxidation of splat surface before the arrival of the new molten droplet; the length of time for which post-impact oxidation occurs is determined by the time lag between two successive splats and this, in turn, depends on the powder feed rate, torch transverse speed and deposition efficiency of the process. Also in HVOF, because of the thin splats, the increased surface to volume ratio is suitable for oxidation but exposure time is reduced because of larger particle velocities. This leads to a reduced number of oxide bands in a given coating thickness.

Apart from oxidation the different thermal history of particles in the three techniques (HVOF, VPS and APS+Q) led to the formation of different phases. In VPS, the material revealed two phases with different Ni and Ti contents. The

rapid cooling in this technique induced the formation of amorphous and nanocrystalline regions with a monoclinical (non-equilibrium) structure. This is not surprising, as the heat treatments that particles undergo during Thermal Spraying do not follow phase diagram rules. Thus, amorphous metallic materials can be obtained by this rapid quenching procedure. One can then obtain materials with a disordered structure beyond some inter-atomic distances.

In both the VPS- and APS-sprayed materials, the monoclinic phase occurred in the nanocrystalline areas. In contrast, HVOF coating showed a predominantly Austenite phase due to moderate heat input.

Several factors, such as the content of amorphous or metastable phases or oxidation, may affect the variation of transformation temperatures. Nevertheless, the peak observed during the heating step cannot be related solely to the transformation of the Austenite phase, as Martensite nanocrystals might also transform.

5.3   Characterization

5.3.1   Mechanical properties
a)   Tensile strength

Tensile bond strength has already been defined as the adhesion between a substrate and a coating and the cohesion between the particles. The strength of adhesion of the impinging particle to the substrate is dependent on mechanical, metallurgical-chemical and physical mechanisms: (i) an impinging particle is mechanically bonded when it flattens and conforms to a suitably prepared surface; (ii) subsequently, diffusion or alloying may occur, forming intermetallic compounds, which is known as the metallurgical-chemical adhesion mechanism; and (iii) physical bonding results from particle adhesion to the substrate by Van der Waals forces.

Apart from the deposition process employed, bond strength also depends on the cleanliness (without oxides and other foreign elements), adequate roughness and adhesion to a substrate surface, along with the plastic deformation of the particle on it. Optimization of the deposition process is thus important, to ensure that both the bond and cohesive strengths of the coating are at a maximum, thus producing a quality coating.

Regarding the currently available thermal spraying techniques, High Velocity Oxygen-Fuel offers one of the highest bond strengths, normally in the range of 40-96 MPa. The results of the tensile bond strengths demonstrate that, in all cases, glue strength is much higher than bond strength (coating-substrate interface) or cohesive strength (within the coating).

For iron aluminide coatings, influencing factors are: (i) the higher melting of the particles in the as-sprayed FeAl grade 3 (CEA) and cryomilled (CRYO) powders, which easily promotes deformation when these impact on the substrate, leading to improved adhesion due to stronger mechanical bonding; and (ii) higher oxidation at the intersplat boundaries, which lowers the cohesive strength, so inducing the cohesive failure these samples underwent.

Another variable is the thickness of the coating, which matters especially for porous coatings sprayed with the less vigorous flame spray techniques. The resin can penetrate into the interconnected pores, reinforce the coating and even, by contacting with the substrate, increase adhesion. The coatings sprayed with AS, APS, VPS, D-gun or HVOF are less porous and the resin does not penetrate deeply.

Due to its lower pressure, Vacuum Plasma Spray can also reach bond strengths beyond 70 MPa, as its particle velocities are much higher than conventional plasma and there is no oxidation. This was confirmed for the as-sprayed VPS coating which had a much larger bond strength than the other ones.

b)   Hardness

Thermal spray coatings generally include voids and oxides within the coating structure. Thus, macro-hardness levels are less than those of the equivalent material in its wrought or cast form. Oxides are known to improve coating hardness, although they reduce its internal strength. Thus, for example, of iron aluminide coatings, CEA and CRYO have the highest values, whereas the two MEC40-60 types resemble a densified structure. The argument as to why the as-sprayed annealed coarse particles (MEC40-60$_{ANN}$) show improved hardness was ascribed to internal oxidation of particles rather than any other explanation.

As far as the NiTi alloy is concerned, the greatest hardness is that of the APS deposit, which is associated with the presence of oxidation and the formation of the Martensite phase as a result of high cooling rates. HVOF hardness values may also be ascribed to oxidation and second-phase precipitates. The absence of oxide phases might be the cause of the lower hardness in the VPS alloy.

5.3.2   Wear resistance

The friction and wear response of thermally sprayed materials is difficult to analyze. Many authors have striven to develop models able to predict such behavior, but it is still unpredictable, as not only the common material properties such as elastic modulus, yield strength, hardness or fracture toughness affect behavior, but the random occurrence of metastable phases, oxides, cracks or pores also do. However, although various micro-mechanisms may be involved, the dominant one in each case depends on the particular situation.

−   *Sliding friction*

The microscopic mechanisms that are involved, to varying degrees, in generating friction are: (i) adhesion, (ii) mechanical interaction of surface

asperities, (iii) ploughing of one surface by asperities on the other, (iv) deformation and/or fracture of surface layers such as oxides and (v) interference and local plastic deformation caused by third bodies, mainly agglomerated wear particles, that are trapped between the moving surfaces.

Many studies are based on the principle that contact occurs only at discrete points, emphasizing an existing roughness at the microscale level. Thus, friction might be caused by mechanical interlocking of asperities which might adhere or deform plastically. Adhesion can also be seen as a component of the plastic deformation of asperities that strongly influences the amount and nature of the deformation. Such a mechanism was observed after the ball-on-disk test for the CEA coating. Actually, to be more accurate, material removal is helped by the splat structure that facilitates delamination by crack nucleation at the intersplat boundaries.

One must also remember that local contact areas may be under conditions quite different from the rest of material. They may be heated by friction to temperatures that cause significant softening or even recrystallization, and that may promote local oxidation. Significant oxidation was observed on the sliding CRYO coating, with debris remaining on the wear track.

The delamination mechanism, however, was discarded in view of the results obtained for the MEC40-60 coatings, since the absence of a typical lamellar structure does not favor the occurrence of such a mechanism. Rather, this structure resembles a bulk sintered material. Another variable that might have some effect on this coating is the interaction of FeAl with moisture in the air[7]. Thus, water vapor molecules can adsorb to the surface, making friction drop because surface sites become covered with adsorbed atoms or even thin layers of oxide, and thus the surface area available for cold welding decreases.

---

[7] It is known that poor ductility of iron aluminides is attributed to environmental brittleness due to the interaction of aluminium with water vapor present in the atmosphere: $2\ Al + 3\ H_2O \rightarrow Al_2O_3 + 6\ H$.
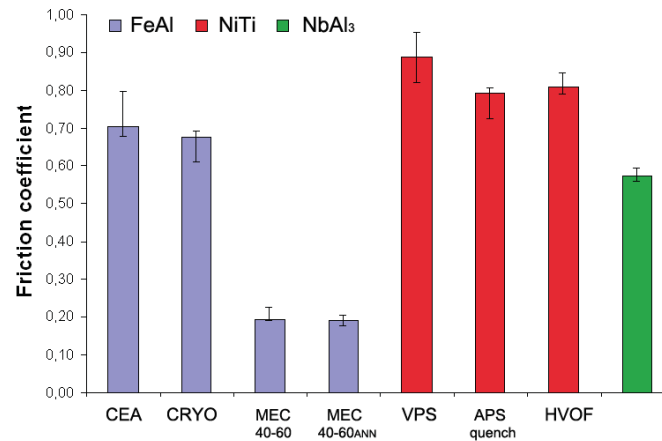
FigureCC 6.1. Friction coefficient of the thermal sprayed coatings.

Figure 6.1 shows the friction coefficient for the different intermetallic coatings and each particular spraying condition. The highest values correspond to the NiTi alloy. It is considered that friction has three components ($\mu = \mu_{asp} + \mu_{plow} + \mu_{part}$): (i) deformation of asperities, (ii) ploughing effects and (iii) wear particles that remain in the wear zone and may agglomerate, harden severely and act as third bodies that deform the contact surfaces. This last effect makes the friction rise and was found to be predominant in track wear examination of the as-sprayed and polished VPS and HVOF NiTi surfaces.

Therefore, although friction is often considered to be directly caused by adhesive wear, other mechanisms must be taken into account.

Actually, according to the theory, adhesion is proportional to the sliding distance and the load, and is inversely proportional to the hardness and independent of the apparent area of contact. As the tests have been carried out for the same distance and load, we can analyze the effect of material hardness. However, according to figure 6.2 and what has been explained in the above paragraphs, it is difficult to evaluate the influence of coating hardness. One could think that, the softer the material is (FeAl), the more damage it should suffer, but it must be remembered that the third-body effect observed in the NiTi and $NbAl_3$-based alloys facilitates aggressive removal of material.
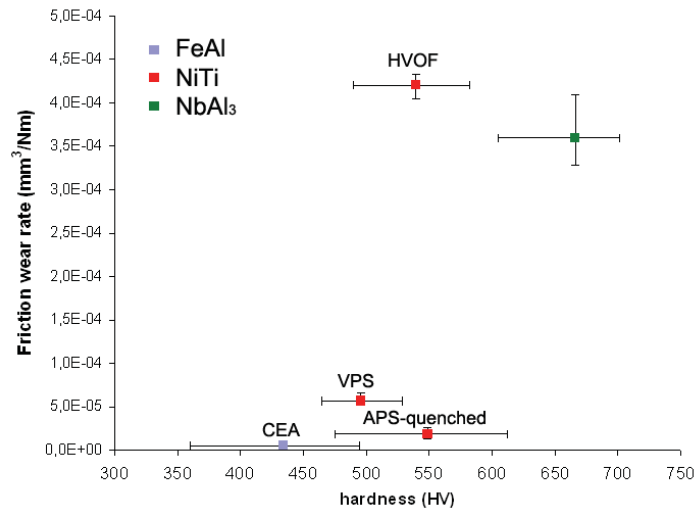
Figure 6.2. Friction wear rate *versus* hardness of the thermal sprayed coatings (the iron aluminide and CEA coating values correspond).

—   *Abrasion*

It is known that abrasive wear occurs at the contact of hard particles or asperities of a hard surface of a second body (two-body abrasion) or in the presence of hard particles (three-body abrasion). A variety of material characteristics, such as hardness, elastic modulus, yield strength, crystal structure, microstructure and composition, either form a correlation with abrasive wear or have some effect on it.

It has been proved experimentally and theoretically that the hardness of a material correlates with its abrasion rate. According to figure 6.3, the tendency for iron aluminide coatings, except for the CRYO, shows that the harder the coating is, the lower the abrasion wear rate is. For the NiTi coatings, APS+Q has lower abrasion damage than VPS, which is consistent with the greater hardness of the former. However, no explanation was found for the greater abrasion wear rate of HVOF.

216
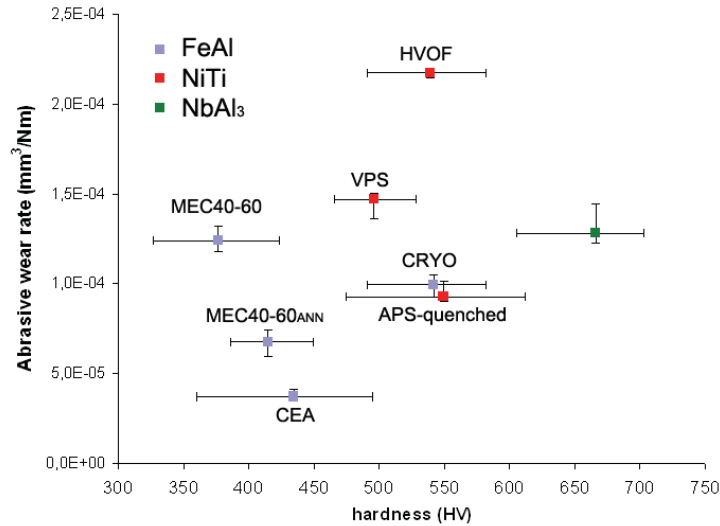
Figure 6.3. Abrasion wear rate *versus* hardness of the thermal sprayed coatings.

It is generally believed that the surface of a material is work-hardened during the process of abrasion. Thermal spraying introduces oxides and metastable or amorphous phases that may result in large increases in hardness and yield strength. One would expect this to lead to large decreases in abrasive wear. Figure 6.4 plots the abrasive wear rates for the different coatings in order to see if there is some influence on the material composition, but except for the HVOF-NiTi alloy, which possesses much higher abrasion damage than the others, no reasonable tendency in the different alloys can be discerned.
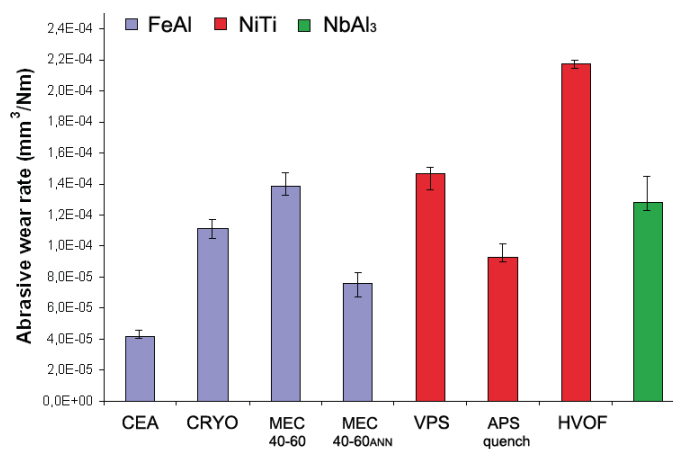
Figure 6.4. Abrasion wear rate of the thermal sprayed coatings.

−   *Erosion*

Erosive wear takes place when the coating surface is subjected to the impingement of solid particles. As a result of impact, part of the tested surface is removed. The response of the material depends on the class material and its properties (thermal history, exposure to previous stresses or surface tensions), and the environmental parameters associated with the erosion process, such as impact velocity, impact angle and particle size/type. Normally, there is an inverse relationship between erosion wear rate and hardness. This has also been observed for the iron aluminide coatings: MEC40-60 presents the lowest abrasion wear rate while CRYO shows the highest. The mechanism has already been explained in paper 3.

5.3.3   Corrosion properties

−   *High-temperature oxidation*

Under most conditions, this resistance derives from the establishment and maintenance of an adherent oxide layer. Consequently, the performance of iron aluminides under different aggressive high-temperature environments can be related to fundamental factors that affect the development, adhesion and durability (lifetime) of the alumina scale. Overall corrosion resistance depends not only on the thermodynamic stability of the reaction product in a particular environment and its growth kinetics, but also on scale integrity and morphology, the chemical and physical nature of the oxide-metal interface, alloy strength and the specific composition of the iron aluminide.

The aluminium levels present in bulk iron aluminides are well in excess of the critical concentrations for forming a surface layer of almost pure alumina. However, what occurs in thermal-sprayed iron aluminides is very different, as Al-depleted areas and oxides play an important role. According to the results in Chapter 4, the oxidation of FeAl coatings at 900°C mainly led to the formation of spinel and metastable alumina phases in the CEA sample and further α-Al$_2$O$_3$ contents in MEC40-60 specimens. Thus, in the first case, as

these transient oxides are known to contain a high number of defects, they make Al and Fe diffusion through the oxide to the outer surface possible. Some α-Al_2O_3 is formed, preventing further growth of iron oxides, but due to the Al-depletion within the coating, the oxide growth rate decreases. Such Al-depletion is more effective if spallation of the scale occurs, as eventually the aluminium concentration in the overall coating falls below that needed to maintain the effective surface activity to form alumina.

Oxidation to α-Al_2O_3 is more effective in MEC40-60, because its composition is closer than that of the intermetallic coating, but the performance, as shown by thermogravimetric analysis and laboratory tests, indicates that CEA has better oxidation resistance. This might be associated with a more strained structure in MEC40-60 and its intrinsic structure, which means that, once oxygen penetrates, the spallation of large particles results in a greater decrease in coating thickness. Hence, thermal stresses would induce scale cracking, leaving fresh coating ready for further oxidation.

For oxidation behavior beyond 900°C, low resistance was shown for the different coatings. CEA showed great density of voids at the coating-scale interface early in the test. These would presumably lead to more rapid scale failure and spallation. At such temperatures, scale stresses became critical. These normally arose during oxide growth and during cooling from the oxidation temperature, because of the differences in the respective coefficients of thermal expansion of the alloy and alumina. Another factor is the roughness of the sprayed coating, as interfacial cavities are more promptly formed and the scale appears to be more wrinkled than on a polished surface. Then, all the iron aluminide coatings showed accelerated oxidation at 1100°C, even resulting in substrate oxidation. Therefore, improving alumina scale adherence is the key to extended lifetimes.

Among the intermetallics in the Nb-Al system, Nb_3Al and $NbAl_2$ are lacking in oxidation resistance, while $NbAl_3$ can form an Al_2O_3 scale. Results on the oxidation performance of the as-sprayed powders indicated however that their

practical use is impeded by the selective oxidation of Al and deterioration by pesting. Therefore, although no success has yet been obtained on this question, now that the powder can be sprayed, we should focus on what can be done to minimize its rapid disintegration.

- *Corrosion in molten salts*

This kind of test was conducted in order to evaluate the corrosion performance of such alloys in boilers fuelled with municipal refuse, for comparison with the results of a previous thesis where other Ni- and Fe-based compositions were used.

The corrosion problems here that are different from those encountered with fossil fuels stem from the fact that chlorine rather than sulfur is primarily responsible for the attack. Such chlorine content is present either as plastic or as inorganic substances, principally NaCl. The chlorine in the plastic is converted to hydrochlorine acid, HCl, in the combustion process. The inorganic chlorides are vaporized in the flame and ultimately condense in the boiler deposits or pass through the boiler with the flue gases. Zinc, lead and tin in the refuse can react with the HCl to form the metal chlorides and/or eutectic mixtures with melting points low enough to cause molten salt attack at wall tube metal temperatures.

Most of the methods for preventing incinerator wall tube corrosion have some penalty in boiler efficiency. This is why thermal spraying offers a good alternative. Although capital costs might be greater, the extended tube life resulting from the use of more resistant alloys compensates for the initial expense and is a cost-effective solution to the problem.

Corrosion resistance in such environments is normally evaluated as the capacity of the coating to form an oxide scale good enough to minimize its dissolution by molten salts and prevent its mechanical rupture, allowing inward electrolyte flux. Once the fused salt has penetrated, corrosion resistance will be determined by the material and the splat boundary oxides.

As has been observed, although there is still coating after 240h, the oxide scales are porous and spallation is important, thus exposing the rest of the coating to further oxidation. Fe-based (Austenitic) coatings[8] showed similar behavior: apparently, increased thickness was promoted by the expansion produced by the growing oxides at the intersplat boundaries, which reduced coating cohesion. The same tests performed for different Ni-based compositions showed that less porous and more protective oxide scales were formed, thus achieving greater corrosion resistance.

–   *Corrosion in saline environments*

As in high-temperature corrosion, corrosion in the electrochemical and salt-fog tests also depends on the nature of the protective oxide scale formed on the alloy. As far as is known, chloride ions in solution produce extensive localized attacks on NiTi alloys, which are influenced by several factors, such as the environment (pH), surface conditions, microstructure and so on.

It was found that VPS coating possesses the greatest corrosion resistance, with a much lower current density than APS-quenching forms. APS+Q allowed electrolyte penetration through the cracks produced during the spraying process, which made it have a corrosion potential near that of the steel substrate. Corrosion parameters of HVOF are more like those of VPS than of APS+Q, because the corrosion is dependent on the microstructural features such as Ti-depleted areas, precipitates and so on, leading to depassivation/repassivation processes.

---

[8] M. Torrell, THESIS: Mejora de la resistencia a la degradación de intercambiadores de calor en plantas IRSU mediante recubrimientos de Proyección Térmica HVOF (2008).

CHAPTER 6: CONCLUSIONS

With regard to the Fe-Al system

1.   High Velocity Oxygen Fuel process has been employed to obtain dense and adherent coatings from mechanically milled (MM) and mechanically alloyed (MA) iron aluminide powders. The optimum parameters have been achieved by using propylene as fuel. This allowed the obtention of compact deposits with minimized oxidation and porosity.

2.   An ordered structure of the FeAl intermetallic was achieved from spraying the prealloyed (MM) powder, while the mechanical alloyed in a cryogenic atmosphere led to the formation of the FeAl but with a disordered structure.

3.   Coatings obtained from coarse particles of the mechanically milled powder, yielded to a structure ressembling to that of sintered materials presenting a nanocrystalline structure. This was associated to a partial recrystallization of the particle in-flight time.

4.   Pre-annealing of powder induced the ordering of structure as well as a grain size increase. Hence, spraying such particles result in a more ordered lattice that was desirable for thermal stability.

5.   The as-sprayed mechanically alloyed (whole particle size distribution) and cryomilled powders led to the coatings with largest oxide content. As consequence, these possessed higher hardness.

6.   A higher hardness value was found to be correlated with a higher abrasion resistance. The as-sprayed FeAl grade 3 powder possessed the highest wear resistance; its wear rate was three times lower than the deposit obtained from the coarse particles.

7. The as-sprayed MM powder showed an enhanced friction coefficient and the highest wear rate when compared with the two as-sprayed coarse particles, both with and without annealing. These two latter coatings exhibited negligible friction damage due to the absence of delamination mechanisms.

8. Iron aluminide coatings have shown to have a fairly good oxidation resistance up to 900°C. The uniform oxide scale without significantly spallation guarantees a reliable performance in high temperature applications enabling the use of a less oxidation resistant substrate but with a higher load-carrying capability.

9. Along the test time at 900°C, the as-sprayed prealloyed powder (whole particle size distribution) with propylene showed a uniform and stable oxide scale, whereas the same powders sprayed with hydrogen and the as-sprayed cryomilled powders, formed an oxide scale that exhibitted a slow growing during the test.

10. The two coatings obtained by spraying the coarse particles (unannealed and previously annealed) seemed to be promising regarding their microstructure and higher aluminium content; actually, these formed more α-Al_2O_3 on the top surface, but the the thermal stresses are thought to be the cause of coating failure.

11. The corrosion in molten salts shows that spallation is more important in the as-sprayed prealloyed powder than by just spraying the coarse particles. In this latter case coating thickness reduction is noticeable, while in the first case, rather than a decrease, there is an increase attributed to the oxidation inside the coating.

With regard to the Nb-Al system:

12.   HVOF is a flexible alternative to produce compact Nb-Al based coatings without the influence of the substrate as it occurs in diffusion aluminide coatings.

13.   A higher oxygen/fuel ratio enabled the attainment of higher flame temperatures that facilitated the alloy melting.

14.   The niobium aluminide coating is between 20-23% harder than the hardest nitinol and iron aluminide coatings.

15.   Nb-Al based deposits displayed more wear damage than iron aluminides. Despite being harder, their abrasion rate has the same order of magnitude as the softest iron aluminide coatings. The explanation for its worse wear properties might be related to the structure of the coating itself rather than the material. However, they are more abrasion resistant than some of the nitinol coatings.

16.   The sliding wear rate of niobium aluminide coatings is two orders of magnitude higher than the as-sprayed iron aluminide prealloyed powders.

17.   When these coatings are oxidized, they follow a logarithmic behaviour but with a much more rapid kinetics than the iron aluminide coatings. At 900°C, whereas the steady state is reached for a weight increase below 10% in the different Fe-Al coatings, the corresponding to the Nb-Al coatings increases up to 40% due to the pesting phenomenon.

With regard to the Ni-Ti system:

18.   HVOF and APS-quenching (APS+Q) techniques have been evaluated as alternatives to the much more expensive VPS procedure.

19.   The new method APS-Q was employed for spraying NiTi powders in a low oxygen atmosphere. Also, HVOF spraying parameters were optimized to obtain the less oxidation as possible.

20.   Detailed TEM studies revealed the phase differences (autenite/martensite) in the three coatings (HVOF, APS+Q and VPS). Both, VPS and APS+Q coatings were formed by large amounts of nanocrystalline areas with a monoclinic phase as well as columnar grains and amorphous zones. By contrast, HVOF-NiTi is almost fully formed by austenitic equiaxed and columnar grains, as well as oxide phases in the intersplat boundaries.

21.   A transformation from martensite to austenite was detected for the powder and as-sprayed specimens when heating, but no reverse transformation was appreciated when cooling which is ascribed to the large hysteresis these kinds of transformations have.

22.   The hardness of the NiTi coatings is much higher than that of the iron aluminide coatings obtained from the prealloyed powders. However, it is comparable to that of the deposit obtained by spraying the cryomilled FeAl powder.

23.   The abrasion resistance of the APS-quenched NiTi coating is comparable to that of the Fe-Al and Nb-Al coatings. In the case of the VPS and HVOF specimens, these values are lower.

24.   The sliding behaviour of the nitinol coatings leads to increased wear rates owing to the different mechanisms that influence material removal. The VPS and APS-quenching deposits are have an order of magnitude higher than the as-sprayed iron aluminide prealloyed powders, while HVOF-nitinol is two orders of magnitude higher.

25.   The as-sprayed VPS and HVOF coatings exhibit superior corrosion resistance than APS+Q in terms of corrosion potentials and current densities. Thus, as the NiTi alloy is actually expensive, the total costs can be reduced by using HVOF instead of VPS since the process is more economical. The corrosion behaviour in the salt fog tests also proved their improved corrosion resistance and their promising application for coating components surrounded by a marine environment. Thus, they are thought to possess a good cathodic protection in these and other aggressive conditions.

APPENDIX I: FAMILIES OF COMPOUNDS

Most reviews on intermetallics within the literature deal with those compounds based on aluminides owing to their attractive properties for structural use at elevated temperatures in hostile environments. Many of these exist over a range of compositions and, in such case, the degree of order decreases as the deviation from stoichiometry increases. Usually metal-metalloid compound such as silicides, arsenides or tellurides are also included in the category since the phenomenology of most such compounds is similar to that of metal-metal compounds [1, 2].

➢   Laves-phase alloys

This group includes a large number of intermetallics with high melting points which crystallize with the AB_2 stoichiometry. In binary refractory metal-chromium systems such as Cr-Ti, Cr-Zr, Cr-Hf, Cr-Nb and Cr-Ta, these Laves phases are in equilibrium with chromium and frequently with the refractory metal as well, via eutectic reactions. Alloy compositions in the two-phase regions where the intermetallic is the predominant phase may be damage-tolerant at room temperature and yet be sufficiently creep-resistant at elevated temperatures.

➢   Beryllides

The Be-rich phases with Ti, Zr, Hf, Nb, Ta, or Mo, also called transition-metal beryllides have good properties for applications as structural, high-temperature materials, high melting temperatures, high stiffness and strengths, and high oxidation resistances.

They have generally low densities, between 2 and 5 g/cm³, complex cubic, tetragonal, or hexagonal crystal structure.

The formation of a BeO layer on the surface of the material comported a good oxidation resistance, therefore Be-rich phases are also used as

protective coating. Brittle-to-ductile transformation temperature is about 1000°C.

The challenge for this group of intermetallic compounds in view of their application is to increase the low-temperature toughness by optimisation of the mechanical properties.

➢ Silicides

Silicides can be seen as a transition from intermtallics with predominantly metallic bonding to non-metallic compounds since silicon is a semiconductor, rather than a metal. However, they are usually comprised within the intermetallics group. They were thought to be appropriate for high-temperature applications because of their capability to form, in oxidizing environments, oxide scales that are often compact and protective. Other general properties are the following: hard and brittle, with high electrical and thermal conductivities, a positive temperature coefficient of resistivity and paramagnetism.

At the beginning, silicides were used for their high strength and oxidation resistance. Now, the electrical properties allow them to be used for important applications as thin films in microelectronic devices.

The most famous silicides for application are M_3Si, M_2Si, M_5Si_3, MSi phase compounds and disilicides. Especially $MoSi_2$ has perhaps received most attention.

➢ Rare-earth compounds

Mostly of the rare-earth compounds are line compounds, so that they have only narrow composition ranges. The production of these compounds is very difficult because of the high affinity with oxygen that leads to reaction with other common materials.

Magnetic properties are the most important in rare-earth compounds and these depend on the composition and crystal structure.

Recent studies claim that ductile intermetallic compounds with a CsCl lattice type have been identified by combining a rare earth element with certain main group or transition metals e.g YAg, YCu, CeAg, ErAu and so on [3]. This is particularly important because brittleness is the main drawback intermetallics possess for their use as structural materials.

For example, YAg proved to have an elongation of 25%, compared to 2% or less for many other intermetallics. The reason why these materials deform while other IMCs do not is not quite clear, but theoretical calculations show that they possess much lower unstable stacking-fault energies which enable then to plastically deform instead of fracturing.

MISCELLANEOUS APPLICATIONS

So versatile are intermetallic compounds in all areas of materials application that examples of their use in industrial, medical, consumer and military products are almost limitless. We will briefly attempt to identify some of the more important of these applications. In some cases, the IMC is present as a precipitate or dispersed particle that provides strengthening or other property modifications while in other examples, the IMC is employed in bulk form [4, 5, 6, 7, 8].

High-temperature applications

- Aerospace applications

From an engineering point of view, their primary function has been to provide strengthening of alloys through precipitation of constituent phases. The main example is the Ni-based superalloys consisting of a solid-solution matrix surrounding Ni_3Al precipitates.

A great research is being currently done on the replacement of these alloys in the hot sections of the gas-turbine engines for aircraft propulsion systems. This

means to find new materials with high melting temperatures and good specific properties with low densities, since the weight of the propulsion system as a whole decreases rapidly with decreasing weight of the rotating components. Obviously, good oxidation resistances and cost considerations are important to be reviewed.

Tables 1 and 2 show the attractive applications of intermetallics in aerospace field and the best candidates to be used. Notice the high melting temperatures imposed by their ordered structures and low densities when compared to other metals.

Table I.1. Potential aerospace applications

Turbines	Airframes	Other
- turbine blades - discs - cases - transition pieces - compressor blades	- NASP - fasteners	- diesel engine component - high temperature sprays - turbo charges

Table I.2. Properties of intermetallics for aerospace applications

Compound	Crystal structure	Melting point, °C	Density, g/cm^3	Modulus, GPa
Ni_3Al	$L1_2$	1390	7.50	178
NiAl	B2	1640	5.86	200
TiAl	$L1_0$	1460	3.91	175
$NbAl_3$	$D0_{22}$	1600	4.54	-
$TaAl_3$	$D0_{22}$	1550	6.90	167
$MoSi_2$	C_{11}	2030	6.30	359
$TiAl_3$	$D0_{22}$	1325	3.40	-

However, still low ductility and toughness, some lack of knowledge on creep properties and environmental stability are the main limitations for an immediate and widespread displacement of Ni-based superalloys. Therefore, use of new intermetallic-based alloy candidates will be very selective and gradual.

- Heat storage at elevated temperature

Here, IMCs find application on trying to balance powder generation and power consumption. The idea is to employ some form of off-peak storage of energy that can then be tapped as additional power capacity in peak hours. Specially IMCs based on eutectic systems offer advantages over earlier systems such as higher thermal conductivity, much smaller volume change on melting, and high entropy of fusion. Some studies concentrated on intermetallics based on Al, Ca, Cu, Mg, Na and Zn with the nonmetals C, P and S. Other alloys studied more recently are Ni, Ge, Ga and Sb IMCs.

Electronics and sensors

The silicides compounds are widely used as superconductors, ohmic contacts for integrated circuits, for growth of epitaxial films and as infrared detectors and sensors. Other intermetallics are now being studied for electronic applications.

Also some problems have been encountered in thin-film semiconductor devices. The diffusion of one specie into another causes degradation of the performance of contacts and conduction lines. IMCs are used as diffusion barriers to limit reaction with either the substrate or the overlayer e.g. Al_3Ti, Al_3Hf, Co_2Si, $NiSi$ and WSi_2.

Magnets

Several intermetallic compounds, including FeCo and rare earth compounds, have been used as permanent mangets. One of the most interesting compounds is $Nd_2Fe_{14}B$, which has the highest energy product of commercial permanent magnets. Current development is focused on reaching greater machinability, easier handling and use as a structural element by improving fracture stress and toughness.

Improved mechanical properties are needed to produce electric vehicle wheel motors. The use of improved permanent magnets in heat pump compressors and fan motors could provide substantial energy savings.

<u>Shape-memory alloys</u>

An important subset of intermetallics exhibits a property called "shape memory": this term encompasses a number of phenomena. One version is the ability of an object made of such an intermetallic to accept a substantial shape change imposed by external loading, and then to return to its original shape when it is mildly heated, even against a restraining stress which tries to prevent that return. Phases which behave like this are capable of martensitic transformation under stress; "martensitic" here implies a phase transformation that takes place by shear, without the involvement of any diffusion. Within the most important SMA alloys, NiTi, CuAlNi and CuZnAl are those which have achieved the commercial status.

The applications for SMAs can be divided in two categories: (1) one-way devices that provide permanent coupling or fastening action and (2) two-way devices that are usually in the form of an actuator that provides force and motion in response to a temperature change. The former class includes: hydraulic tube couplings for military aircraft, couplings for ship pipping systems and pipping and tubing in chemistry and petroleum-plant equipment and in biomedicine as well.

<u>Tribology applications</u>

The presence of IMCs in a metal matrix is usually beneficial for its wear resistance. Here are some examples: lead-based babbits owes its resistance to SbSn and, in later versions, with the addition of Cu, Cu_6Sn_5 was recognized.

For bearings that operate under high loads, bronze bearing alloys based on copper-tin compositions are considered more suitable. The main intermetallic

phase they posses is $Cu_{31}Sn_8$. Lead is usually added for its lubricity, giving the bearing bronze its resistance to seizure.

In recent years, NiAl and Ni_3Al have been studied for their use as high temperature applications as well as their potential as bearing materials for use in unlubricated or boundary-lubricated high temperature systems.

Metal-matrix composites

A good alternative to polymer matrix systems in the search for improved high-temperature composites for airframe and aerospace structures, is a metal-matrix composite structure produced by directional solidification of a eutectic or quasieutectic system in which one phase is an IMC that grows as continuous fibers. These systems have higher compatibility than polymer-based composites. Interesting results have been observed in systems such as Al_2Cu, Al_2CuMg or Al_3Ni in an aluminium matrix. Ni matrix composites have also been studied using Nb_3Al or Ni_3Nb as the fiber-reinforcing IMC.

REFERENCES

[1]   E. P. George, M. Yamaguichi, K. S. Kumar, C. T. Liu, Ordered intermetallics, Annual Review in Materials Science, Vol. 24 (1994) pp. 409-51.

[2]   G. Sauthoff, State of intermetallic development, Materials and corrosion, Vol. 47 (1996), pp. 589-94.

[3]   Hhttp://www.sciencedaily.com/releases/2003/09/030916073616.htmH

[4]   D. P. Pope, R. Darolia, High-temperature applications of intermetallic compounds, MRS Bulletin, Vol. 21, 5 (1996), pp. 30-36.

[5]   J. H. Westbrook, Metallurgical and chemical applications of intermetallics, MRS Bulletin, Vol. 21, 5 (1996), pp. 37-43.

[6]   L. McD. Schetky, Miscellaneous applications of intermetallic compounds, MRS Bulletin, Vol. 21, 5 (1996), pp. 50-55.

[7]   N. S. Stoloff, C. T. Liu, S- C- Deevi, Emerging applications of intermetallics, Intermetallics Vol. 8 (2000) pp. 1313-20.

[8]   D. J. Duquette, N. S. Stoloff, Aerospace applications of intermetallics, Key Engineering Materials, Vols. 77-78 (1992) pp. 289-300.

APPENDIX II: Refinement of x-ray data

The XRD data was processed in many ways in order to get information from the FeAl powder diffractograms, first to analyse the grain size and strain evolution in the experimental mechanically alloyed Fe25wt.Al powder (evaluation along the processing time when milling at cryogenic temperatures) and afterwards, to carry out the whole assessment on the ordering processes when annealing the powders.

In the first case, in order to evaluate the strain increase and grain size decrease as result of the high deformation produced in the ball milling process of the Fe and Al blend powder, two procedures were primarily investigated: individual x-ray peak fitting and, whole x-ray spectrum fitting by Rietveld method. This latter method was also employed for the second case. There is an extensive mathematic background around these methods but here, it will be explained briefly introducing just the most important formula.

a   b
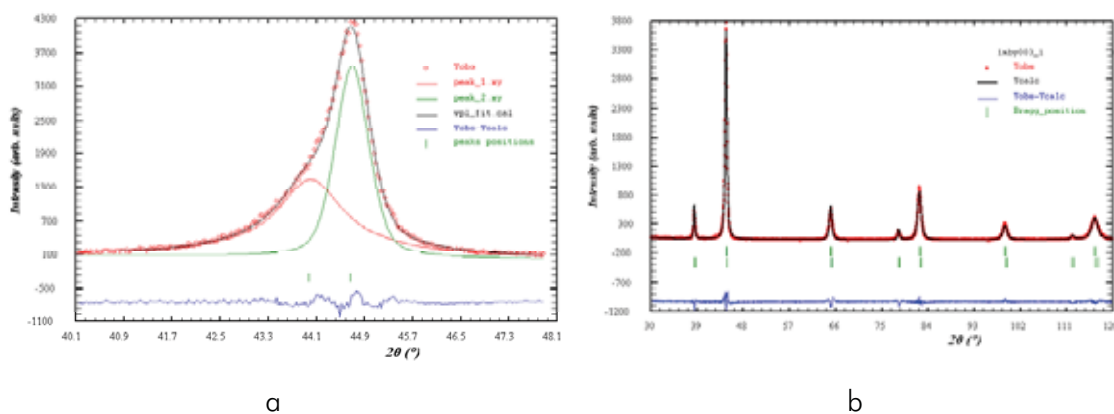
Figure II.1. (a) Individual X-ray peak fitting and (b) the Rietveld method where the red points are the experimental data, the black line is the calculated profile and the blue line the difference.

Basically, the as-called individual x-ray peak fitting is a free-profile fitting were neither structural nor crystallographic information is taken into account, whereas the Rietveld method requires as input data, the crystalline structure of each phase.

Figure II.1 shows an example of the output profiles obtained with the two methods.

Free-profile fitting

One or some of the peaks of the analysed x-ray spectra are fitted without using any structural information by means of the pseudo-Voigt (pV) function included in the XRFit program (WinPLOTR software pack). Assuming linear background, such function is a linear combination of the two possible peak shape functions: Gaussian (G) and Lorentzian (L). Hence, pV results in:

$$pV = \eta G + (1-\eta)L \quad \text{(Equation II.1)}$$

Both G and L depend directly on the full width at half maximum of the peak (FWHM) and (2θ-$2\theta_h$). The best fit sought is the best least-squares fit to all y_i's simultaneously. The quantity minimized in the least-squares refinement is the residual X^2:

$$X^2 = \sum_i w_i (y_i^{obs} - y_i^{calc})^2 \quad \text{(Equation II.2)}$$

Where y_i^{obs}, y_i^{calc} and w_i are observed and calculated intensities at the ith step and weigth respectively.

The output data consists of the angular position ($2\theta_h$) for a certain reflection, the integrated intensity, FWHM, η and H_G and H_L contributions to the global breadth H. A continuous refinement is carried out until the convergence criterion is reached, achieving a minimum for X^2.

By using the Bragg law, the d_{hkl} reflections are calculated and these are introduced in the Scherrer formula (Eq II.3).

Equation II.3: $\beta = \dfrac{C\lambda}{D\cos\theta}$, where β is the full width at half maximum of the peak, λ is the wavelength of the x-ray, θ is the Bragg angle, C is a unit cell geometry-dependent constant whose value is typically between 0.85 and 0.99 and, D is the grain size.

However, Scherrer has some limitations, especially for our purpose. It only considers that x-ray peak broadening comes from the small crystallite size and misses the strain effect. Considering the high plastic deformation induced in a ball-milling process, the strain introduced cannot be negligee (table II.1 actually shows all the possible factors inducing broadening or shifting in peak profiles). The microstrain effect has been hampered by using the Williamson-Hall equation:

Equation II.4: $\beta = \dfrac{1}{D} + 2\varepsilon Q = \dfrac{\beta\cos\theta}{C\lambda} + \dfrac{4\sin\theta\cdot\varepsilon}{\lambda}$ (Williamson Hall), where D is calculated from equation II.3 and $Q = 1/d_{hkl}$ (Bragg's law). When $1/D$ is plotted versus Q the intercept gives particle size and the slope gives the strain. By using the Bragg law, the d_{hkl} reflections can be also employed to calculate the lattice constant, a, for a cubic lattice e. g. FeAl (CsCl-type).

Equation II.5: $a = d\sqrt{h^2 + k^2 + l^2} = \dfrac{\lambda}{2\sin\theta}\sqrt{h^2 + k^2 + l^2}$

Table II.1. Correlations between peak profile features (broadening, shifts, …), and the different microstructure elements.

peak profile features / microstructure properties	peak shift	peak broadening	peak assymmetry	aniosotropic peak broadening	peak shape
Dislocations		+	+	+	+
Stucking faults	+	+	+	+	+
Twinning		+	+	+	+
Microstresses		+			
Long-range internal stresses	+		+	+	
Grain boundaries	+	+			
Sub-Boundaries	+	+			
Internal stresses	+				
Coherency strains	+	+	+	+	
Chemical heterogeneities	+	+	+		
Point deffects					+
Precipitates and inclusions	+		+		
Crystallite or subgrains		+		+	+

The RIETVELD METHOD

One of the most important things before defining the refinement strategy is having very good resolute data; hence, data collection implies fitting the experiment to the need. Then, particular best fit obtained will depend on the adequacy of the model and on the attainment of the global minimum.

In the previous method, we refined profiles, here we refine crystal structures. The things actually being refined are parameters in models for the structure and for other specimen and instrument effects on the diffraction pattern. In the Rietveld method the least-squares refinements are carried out until the best fit is obtained between the entire observed powder diffraction pattern taken as a whole and the entire calculated pattern based on the simultaneously refined models.

Analytical reflection profile functions available in some of the most widely used programs include conventional pseudo-Voigt and *Thomson, Cox-Hastings* pseudo-Voigt functions, the Pearson VII function, and Gaussian, Lorentzian and modified Lorentzian functions. We used *Thomson-Cox-Hastings* pseudo-Voigt because it seems the most suitable in this case. In this function, FWHM of the corresponding Gaussian and Lorentzian contributions are calculated according to:

Equation II.6: $H_G{}^2 = U \cdot tg^2\theta + V \cdot tg\theta + W$

Equation II.7: $H_L = X \cdot tg\theta + \dfrac{Y}{\cos\theta}$

where *U, V, W, X* and *Y* are the parameters to be refined.

Individual parameters were refined one by one in order to discern the adequacy of the value and update the model at each step. First, global parameters such as scale factors and background were defined; then, lattice parameter and peak shapes. Finally, for refinement of the occupational factor, there have been imposed some restraints taking into account that with the

composition $Fe_{60}Al_{40}$, 10at.% of Fe will occupy Al positions in the case of the perfect ordered lattice.

Table II.2 presents the main advantages of this method and the limitations when trying to quantify.

Table II.2. Advantages and limitations of Rietveld method

Advantages	Limitations
- Whole spectrum fitting	- Long time for measurements
- Deconvolution of overlapping peaks	- Difficulties on data processing
- Correction of preferent orientation	- Microabsortion
- Control of results reliability	

APPENDIX III: MOSSBAUER SPECTROSCOPY

Mössbauer spectroscopy is a versatile technique that can be used to provide information in many areas of science such as Physics, Chemistry, Biology and Metallurgy. It can give very precise information about the chemical, structural, magnetic and time-dependent properties of a material.

The changes produced in the energy levels associated with the emission or absorption of a gamma ray can provide information about the atom's local environment within a system. There are, however, two major obstacles in obtaining this information: the 'hyperfine' interactions between the nucleus and its environment are extremely small, and the recoil of the nucleus as the gamma-ray is emitted or absorbed prevents resonance. To achieve resonance the loss of the recoil energy must be overcome in some way.

In a free nucleus during emission or absorption of a gamma ray, it recoils with a recoil energy E_R. The emitted gamma ray has E_R less energy than the nuclear transition but, to be resonantly absorbed, it must be E_R greater than the transition energy due to the recoil of the absorbing nucleus. This means that the two energies (emitted and absorbed) observed in figure III.1 should overlap. This is not observed for freely moving atoms or molecules, i.e. in gaseous or liquid state. Key to the success was the discovery of recoilless gamma ray emission and absorption, referred to as the *Mössbauer effect*. Basically, when the atoms are within a solid matrix (crystalline or non-crystalline), a recoilless emission and absorption of gamma ray is possible, and the essentially unshifted transition lines can (partially) overlap and nuclear resonance absorption can be observed. The recoiling mass is now effectively the mass of the whole system, making E_R and Γ_0 very small. If the gamma-ray energy is small enough the recoil of the nucleus is too low to be transmitted as a phonon (vibration in the crystal lattice) and so the whole system recoils, making the recoil energy practically zero. Hence, if the emitting and absorbing

nuclei are in a solid matrix, the emitted and absorbed gamma-ray is the same energy (resonance).
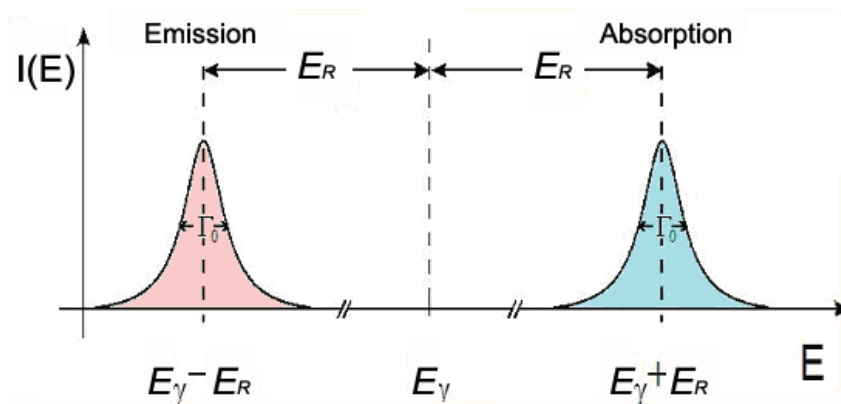
Figure III.1. Intensity as function of the transition energy for emission and absorption of gamma ray.

As resonance only occurs when the transition energy of the emitting and absorbing nucleus match exactly, the effect is isotope specific. The relative number of recoil-free events (and hence the strength of the signal) is strongly dependent upon the gamma-ray energy and so the Mössbauer effect is only detected in isotopes with very low lying excited states. Similarly, the resolution is dependent upon the lifetime of the excited state. These two factors limit the number of isotopes that can be used successfully for Mössbauer spectroscopy. The most used is ^{57}Fe, which has both a very low energy gamma-ray and long-lived excited state, matching both requirements well.

As the environment of the nuclei in the studied system will almost certainly be different to the source, the hyperfine interactions between the nucleus and its environment will change the energy of the nuclear transition. To detect this it is necessary to change the energy of the probing gamma-rays. The energy levels in the absorbing nuclei can be modified by their environment in three main ways: by the Isomer Shift, Quadrupole Splitting and Magnetic Splitting.

– **Isomer shift (δ)**

It is the interaction of the nuclear charge distribution with the electron cloud surrounding the nuclei in both the absorber and source. The isomer shift arises due to the non-

$$E_A - E_S = \delta$$
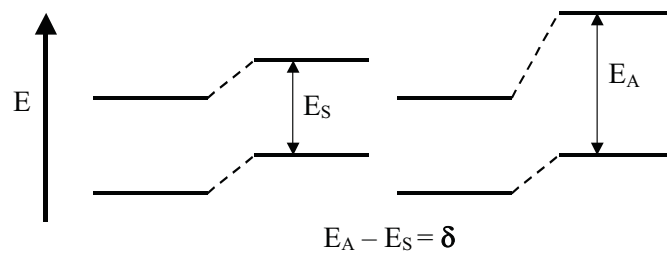
Fiaure III.2. Isomer shift illustration.

zero volume of the nucleus and the electron charge density due to s-electrons within it (figure III.2). This leads to a monopole (Coulomb) interaction, altering the nuclear energy levels. Any difference in the s-electron environment between the source and absorber thus produces a shift in the resonance energy of the transition. This shifts the whole spectrum positively or negatively depending upon the s-electron density, and sets the centroid of the spectrum.

As the shift cannot be measured directly it is quoted relative to a known absorber. For example ^{57}Fe Mössbauer spectra will often be quoted relative to alpha-iron at room temperature.

The isomer shift is useful for determining valency states, ligand bonding states, electron shielding and the electron-drawing power of electronegative groups.

– **Quadrupole Splitting (Δ)**

It is the interaction of the nuclear electric quadrupole moment with the electron field gradient and the nucleus. This arises where the nucleus has a spin of more than 1/2, either in the ground state or in the metastable state. There is a non-spherical charge distribution and this produces a nuclear
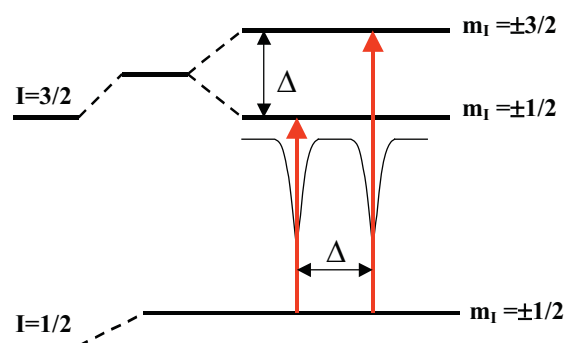
Figure III.3. Quadrupole splitting illustration.

247

quadrupole moment. The nuclear quadrupole moment interacts with electric field gradients at the nucleus (produced by an asymmetric electronic charge distribution or ligand arrangement), and thus the quadrupole coupling indicates the degree of departure from sperical summetry at the nucleus. A further interaction which may be detected in the Mössbauer effect is the splitting of nuclear energy levels in a magnetic field.

In the case of an isotope with a I=3/2 excited state, such as ^{57}Fe or ^{119}Sn, the excited state is split into two substates $m_I=\pm1/2$ and $m_I=\pm3/2$. This is shown in figure III.3, giving a two line spectrum or 'doublet'.

–   *Magnetic Splitting*

In the presence of a magnetic field the nuclear spin moment experiences a dipolar interaction with the magnetic field i. e. Zeeman splitting. There are many sources of magnetic fields that can be experienced by the nucleus. The total effective magnetic field at the nucleus, B_{eff} is given by:

$$B_{eff} = (B_{contact} + B_{orbital} + B_{dipolar}) + B_{applied}$$

Where the first three terms are due to the atom's own partially filled electron shells: $B_{contact}$ is due to the spin on those electrons polarising the spin density at the nucleus, $B_{orbital}$ is due to the orbital moment on those electrons, and $B_{dipolar}$ is the dipolar field due to the spin of those electrons. This magnetic field splits nuclear levels with a spin of I into (2I+1) substates.

Therefore, the requirements for magnetic dipole interaction to be observed are that (i) the nuclear states involved possess a magnetic dipole moment and (ii) a magnetic field is present at the nucleus. A nuclear state with spin
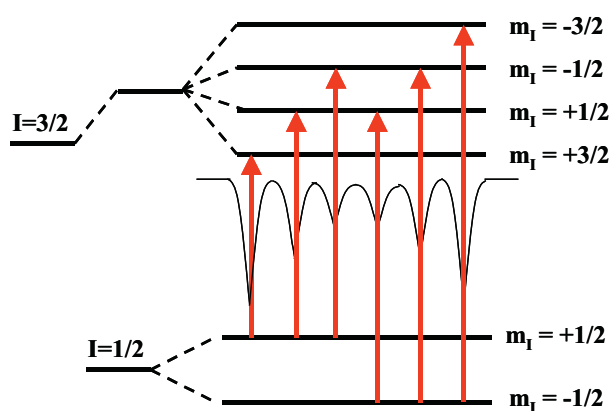
Figure III.4. Magnetic splitting illustration.

I > 1/2 possesses a magnetic dipole moment μ. This is the case for both the ground state with I = 1/2 and the first excited state with I = 3/2 of ^{57}Fe. Magnetic dipole interaction (visualized as the precession of the magnetic dipole moment vector about the axis of the magnetic field) leads to splitting of the states into 2I+1 substates characterised by the magnetic spin quantum numbers m_I. Thus the excited state with I = 3/2 is split into four, and the ground state with I = 1/2 into two substates.

This is shown in figure III.4 for ^{57}Fe. Transitions between the excited state and ground state can only occur where m_I changes by 0 or 1. This gives six possible transitions for a 3/2 to 1/2 transition, giving a sextet with the line spacing being proportional to B_{eff}.

These interactions, Isomer Shift, Quadrupole Splitting and Magnetic Splitting, alone or in combination are the primary characteristics of many Mössbauer spectra. Hence, in practice, Mössbauer spectra can be really complex depending on the iron oxidation state, ordering of crystal lattice, and so on.

APPENDIX IV: HVOF AND APS

HIGH-VELOCITY OXY-FUEL (HVOF)

Both flame spraying and high velocity oxy-fuel are based on the heat generated by the combustion of an oxygen-fuel flame to melt the spray materials. Combustion flame temperatures are around 3000°C although they may vary somewhat depending on specific gas and fuel ratios. However, while particle velocities in flame spraying are low, typically around 40 to 100 m/s, the high gas velocities in HVOF can reach particle velocities of around 400 to 800m/s.

As shown in figure IV.1, the powder is injected axially into the jet as suspension in the carrier gas. The gases are burnt in the combustion chamber and flow through the nozzle out of the torch. The combustion chamber and the nozzle are water cooled.
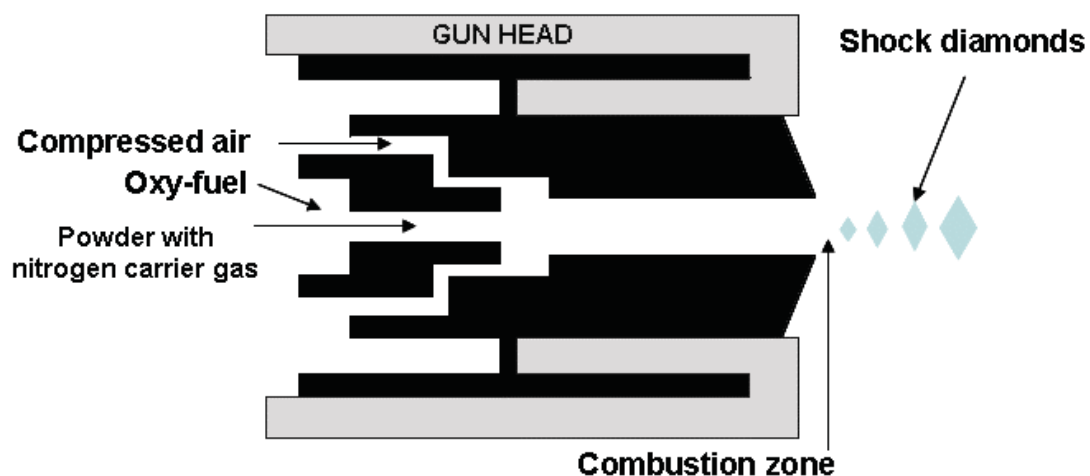
Figure IV.1. Schematic cross-section of Diamond Jet spray gun.

Within the high-velocity combustion processes, one can distinguish between HVOF and D-gun systems; the detonation process is based on repetitive explosions or detonations of oxygen-fuel gas mixtures rather than continuous burning of a combustion flame, as in HVOF. The main HVOF processes are

those developed by Sulzer Metco company and, PRAXAIR Surface technologies and TAFA Incorporated: the Diamond Jet and the DJ Hybrid (water cooled) guns were developed by the first ones; the most known are two types: DJ2600 which mainly uses hydrogen as fuel gas, and the DJ2700 uses propane or propylene as fuel gas. Among those developed by PRAXAIR, there are: JP-5000, HV-2000, etc.

The newest high-velocity oxy-fuel guns generate an internal combustion jet with gas velocities that can exceed 2100 m/s compared to the older systems that approach 1360 m/s. The major advantage of this higher kinetic energy process is that coatings with greater density are achieved. Other benefits include increased thickness capability, smoother surface finishes, lower oxide levels, and less effect on the environment (reduced oxidation and loss of key elements by vaporization).

A characteristic of most HVOF guns is the multiple shock-diamond pattern that is visible in the flame. As combustion products pass through the nozzle, the jet expands because the static pressure in the nozzle is greater than the ambient pressure and expansion and compression waves occur in the free jet. The intersection of these waves (from up to the bottom edge) form bright regions (diamond shape as a result of the N-type shock wave) in the jet stream, the as-known as shock diamonds.

As explained earlier, oxygen and a fuel gas are mixed under pressure in the gun before entering the combustion zone, then on ignition, a chemical reaction takes place and releases heat energy. Pressure increases with the increase in temperature, which produces high gas velocities. Combustion fuels include propylene, propane, natural gas, hydrogen, acetylene and kerosene and, the chemical reaction of the gases is the following:

fuel gas + oxygen + nitrogen $\rightarrow$ water + carbon dioxide + nitrogen + heat

As can be seen, the nitrogen remains unaffected, the fuel gas and oxygen form water and carbon dioxide. In practice, this reaction does not usually reach the stoichiometry; in such case, the process is incomplete and some reactants may remain in excess. Because of the excessively high deposition temperatures the water evaporates. The energy from the chemical reaction is converted to heat and pressure, which is used to melt and accelerate the individual powder particles together with the emerging gases.

During flight these particles are subjected to the supersonic shock waves produced by the flow gases. The temperatures of these particles decrease with increase flight distance, and their velocities decrease due to the viscous shear effects exhibited at the outer boundaries of the flame. The velocities vary axially depending on the pressure at each distance away from the nozzle outlet.

The thermal efficiency of the process also varies according to the fuel gas. Table IV.1 shows the main characteristics of the different flames depending on the fuel used for the combustion. It can be noticed that the oxygen/fuel ratio for the maximum temperature flame never coincides with that of the stoichiometry.

Table IV.1. Fuel characteristics.

Fuel gas	Max flame T (°C)	Heat of combustion (MJ/m^3)	O_2/fuel ratio		
			Max flame T	Neutral flame (stoichiometry)	HVOF application
Propane	2828	93.2	4.5	5	3.0-8.0
Propylene	2896	87.6	3.7	4.5	3.5-7.0
Hydrogen	2856	10.8	0.42	0.5	0.3-0.6
Etylene	2924	59.5	2.4	3.0	2.0-5.0
Acetylene	3160	56.4	1.5	2.5	1.3-4.0
Kerosene	2760	37.3 MJ/l	2.9	3.4	2.8-4.8

Finally, regardless of the gun system, the benefits of HVOF technology are many. Applications that had shown few benefits from thermal spray coatings years ago, are now achieving success through HVOF technology.

Table IV.2. Benefits of using HVOF technology.

coating benefit	main reasons for this benefit
• higher density (lower porosity)	• higher impact energy
• improved corrosion barrier	• less porosity
• higher hardness ratings	• better bonding, less degradation
• improved wear resistance	• harder, tougher coating
• higher bond and cohesive strengths	• improved particle bonding
• lower oxide content	• less in-flight exposure time to air
• fewer unmelted particle content	• better particle heating
• greater chemistry and phase retention	• reduced time at higher temperatures
• thicker coatings	• less residual stress
• smoother as-sprayed surfaces	• higher impact energies

ATMOSPHERIC PLASMA SPRAY (APS)

In the plasma process, an electric arc (usually operated at either 40kW or 80kW) is generated between a water-cooled tungsten electrode and an annular water-cooled copper anode. A primary gas such as nitrogen or argon, in combination with a secondary gas such as hydrogen or helium is heated and ionized to create the plasma "flame". Plasma guns run on direct current; when an arc is formed between the electrode and the nozzle to complete the circuit, gases are typically dissociated and ionized, forming a plasma. The thermal energy of the plasma is utilized in the melting and projecting of the deposit material onto the substrate.
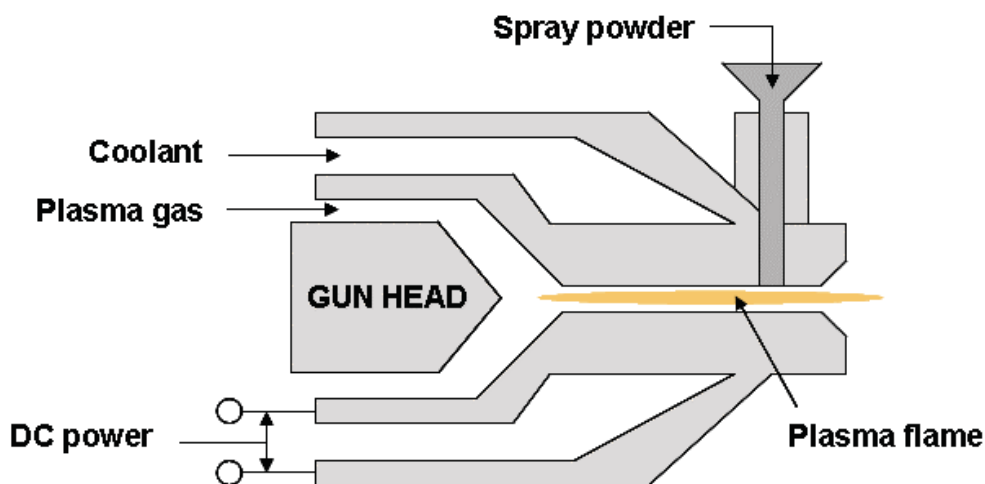
Figure IV.3. Schematic cross-section of a plasma spraying gun.

Although either nitrogen or argon can serve as the primary plasma gas, each has its own unique characteristics, which may play a role in the success of an application. Figure IV.4 shows the main dissociation and ionization of the mainly used thermal spray gases; this plot is normally used for the calculation of plasma temperature in case that there is a mixture of gases. A secondary gas (typically hydrogen or helium) may be added to raise heat content and/or maintain constant voltage. It results in typical mixtures such as Ar + H_2, Ar + He, Ar + N_2 or N_2 + H_2. The choice of gases is dictated mostly by the ability

255

to melt the sprayed particles. This ability is higher for molecular gases (especially H_2) due to greater thermal conductivity, than for atomic gases. On the other hand, the monoatomic gases jets reach a higher velocity. That is why mixtures of monoatomic gas with a molecular one have been often used in order to assure melting of the particles as well as their high velocity while spraying.
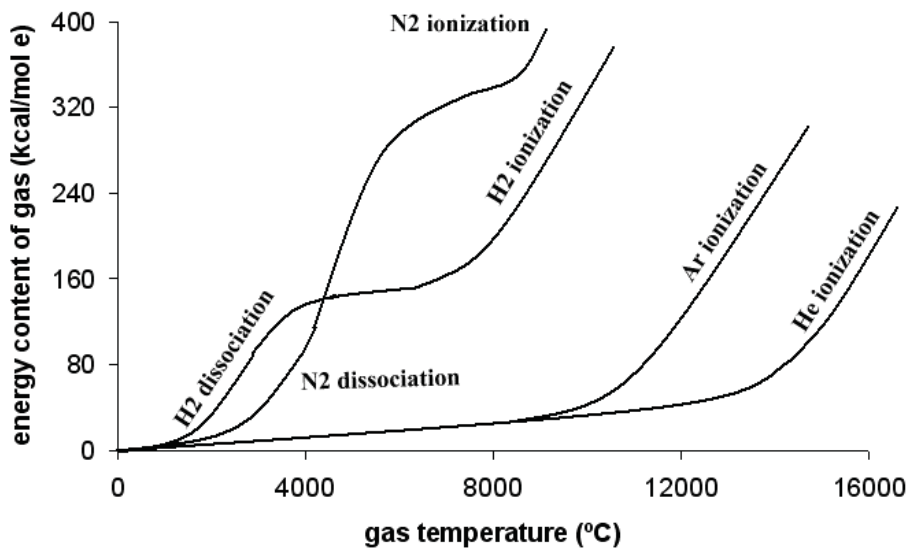
*Figure IV.4.*Energy content of primary plasma spray gases versus gas temperature.

Apart from plasma gas temperatures and particle velocities, other variables that affect melting include are: nozzle diameter, powder particle size and injection angle, gas velocity, feed rate and power settings (amperage and voltage).

The newest guns from Sulzer Metco:

- F4-MB: high spray rates of up to 100 g/min and high particle velocities up to 760 m/s.

- TriplexPro™-200: high spray rates of up to 200 g/min assure lowest operational costs per unit of material applied and high particle velocities up to 380 m/s.

- 3MB: Low capital cost and, small overall size goes into tight locations

- iPro-90: Robust design for high volume production and long spray runs.

- SM-F210: Excellent deposit efficiencies and spray rates.

A benefit of the plasma process is its versatility in changing flame temperatures, particle velocities and conditions. The main use of this system is to generate high temperatures for the spraying of materials with high melting temperatures. Because of the high propulsion of the individual particles, high bond strengths may be achieved in the coatings.

Vaccum Plasma Spray (VPS) specifications have already been included in chapter 3. VPS basically consists of a conventional plasma spraying enclosed in a vacuum tank, where the powder is injected into a hot gas plasma (~10,000K) that melts and projects the molten droplets at high velocity onto a substrate to form a coating. The use of an inert chamber serves for two purposes: to restrict the formation of oxides which may be associated with open air spraying and secondly, to confine the expelled hazardous materials. LPPS/VPS coatings typically have high bond strengths with very low levels of porosity and oxides.

APPENDIX V: J. M. Guilemany, N. Cinca, C. R. C. Lima, J. R. Miguel. Studies of Fe40Al coatings obtained by High Velocity Oxy-Fuel. *Surface and Coatings Technology*.

Studies of Fe–40Al coatings obtained by high velocity oxy-fuel

J.M. Guilemany [a], C.R.C. Lima [b], N. Cinca [a,*], J.R. Miguel [a]

[a] Thermal Spray Centre (CPT), Dpt. Ciència dels Materials i Enginyeria Metal.lúrgica, Universitat de Barcelona, C/Martí i Franqués, 1. 08028 Barcelona, Spain
[b] Unimep — Methodist University of Piracicaba, College of Engineering, SP, Brazil

Abstract

Interesting properties that intermetallics possess have made them to be promising materials to be used either as bulk materials or as coatings, both at medium or elevated temperature environments. This group of materials possesses a long-range order, which can be kept by some intermetallics until their melting point, which is the main reason why they possess a good stability at high temperatures. Some other properties can be summarized as follows: high thermal conductivity; low density; great strength, particularly at high temperatures; good oxidation resistance at high temperatures (because of the formation of oxide films); low ductility, brittle fracture at room temperature.

FeAl coatings from powder of nominal composition Fe–40Al–0.05 Zr (at.%) with 50 ppm B and 1 wt.% Y_2O_3 have been prepared using high velocity oxy-fuel (HVOF) technique. Several standard spraying conditions have been assessed; some parameter variations from those standards intend to find optimal spraying conditions. The characterization has been carried out by DRX, EDS and Scanning Electron Microscopy. The results conclude that a major intermetallic FeAl phase has been obtained.

Microhardness and wear properties have been evaluated for those coatings obtained with optimal conditions. Compared to room temperature sliding wear behaviour, the friction coefficient is reduced when the test is performed at 400 °C.
© 2006 Published by Elsevier B.V.

Keywords: Iron aluminide coatings; High velocity oxygen fuel

1. Introduction

FeAl intermetallics have been intensively studied as potential substitutes for high temperature superalloys in some applications both as bulk materials or coatings. Like general intermetallic compounds, they possess high melting points, high thermal conductivity, lower density compared to conventional Fe- and Ni-based alloys, good mechanical strength/mass ratios as well as oxidation and corrosion resistance to high temperatures. The major drawbacks of this family of compounds are low ductility and creep resistance [1,2]. The brittleness can be solved by adding some alloying elements such as boron, which modifies the fracture mode from intergranular to transgranular [1,3–6], or by reducing the grain size [3,7]. The poor creep resistance can be improved by precipitation and solid solution hardening [8] or even by dispersing particles [9–12].

Iron aluminides are especially attractive due to their low cost and availability of raw materials and also due to their excellent

oxidation and sulphidation resistance (better than that of any other iron or nickel base alloys). Such oxidation and sulphidation resistance are credited to the formation of an adherent alumina layer

Fig. 1. Console and HVOF flame torch used in this work.

* Corresponding author. Tel./fax: +34 934021297.
E-mail address: nuria.cinca@ub.edu (N. Cinca).

Table 1
Thermal spraying parameters

	Parameter set 1 (F1)	Parameter set 2 (F2)	Parameter set 3 (F3)
Oxygen flow rate, $1\,min^{-1}$	189	189	253
Oxygen pressure, bar	10.3	10.3	10.3
Carrier gas (air), $1\,min^{-1}$	385	305	305
Air pressure, bar	6.9		
Fuel (propylene), $1\,min^{-1}$	87		
Propylene pressure, bar	6.9		
Spraying distance, mm	250		

Fig. 3. X-ray diffraction trace from milled powder compared with Fe and FeAl patterns.

on the surface when exposed to air or oxygen atmospheres [1,2,13]. The difficulties in shaping have focused many efforts on these materials as coatings [14].

In the present work, FeAl coatings from powder of a nominal composition Fe–40Al–0.05 Zr (at.%) with 50 ppm B and 1 wt.% Y_2O_3 have been prepared using high velocity oxy-fuel spraying (HVOF).

HVOF spraying enables to obtain coatings with low porosity and oxide content, with a good adherence and beneficial compressive stresses [15]. Moreover, as FeAl coatings are thought to exhibit poor wear-resistance at room temperature, wear (sliding and abrasive) tests have been carried out onto the system with lower oxidation content.

As far as wear behaviour is concerned of WC-40 vol.% FeAl composites has also been investigated by other authors comparing it with the typical WC-10 vol.% Co. It concludes that FeAl intermetallic is a promising binder; these type of composites, with lower WC content, provide similar wear rates compared to WC-Co as long as the materials have equal hardness values [16].

2. Experimental procedure

The starting powder with a nominal composition of Fe–40Al–0.05Zr (at.%) and 50 ppm B, was atomised under argon atmosphere and ball milled for several tens of hours. During this later stage of mechanical alloying, yttrium was introduced to

create about 1 wt.% of finely dispersed Y_2O_3, which provides particle and grain boundary strengthening [12].

These Fe–40Al powders were sprayed by high velocity oxy-fuel spraying [17] on flat and circular samples of low alloyed carbon steel G41350 UNS, previously grit blasted to provide mechanical bonding.

The equipment used for powder deposition is a Diamond Jet Hybrid (DJH) model 2600/2700 (Sulzer Metco) shown in Fig. 1. The equipment consists of a control panel, a power supply, a system of gas metering, a mass hopper for powder feeding, a water cooling system and a flame torch. In order to avoid significant heating during the experiments, the substrates were cooled on their back sides using compressed air.

Different parameters' combinations have been tested to assess the optimal ones with regard to intermetallic content, minimal oxidation rate and porosity. The spraying parameters are shown in Table 1. The console has been programmed for the deposition of 9 layers that approximately results in a 120-micron thick deposit. The characterization has been carried out by XRD, Scanning Electron Microscopy-EDS and microhardness evaluation.

Dry sliding wear resistance at room and high temperatures of the F1 deposit has been investigated using a ball-on-disk (ASTM G99-90) equipment. It consists of a ball subjected to an
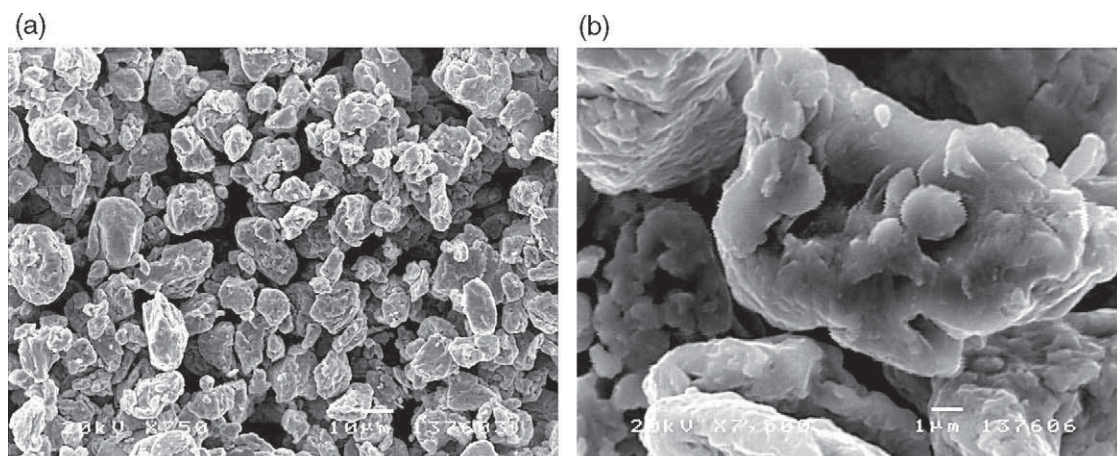
Fig. 2. Secondary electron SEM micrographs showing the morphology of the milled powder: (a) general and (b) detailed view.

3
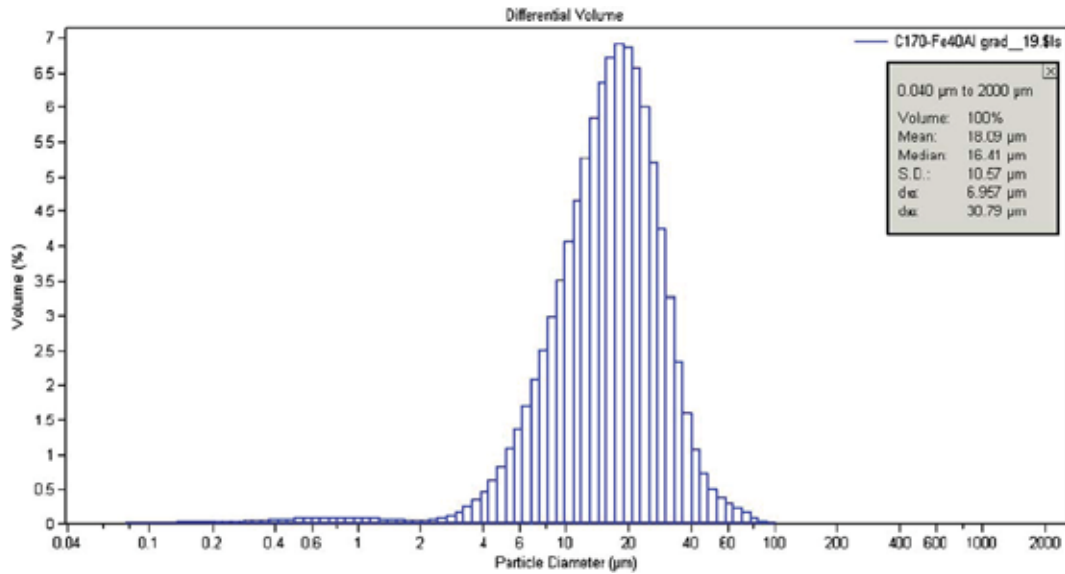
Fig. 4. Distribution particle size of the feedstock FeAl powders.

arm that has load cell that is able to measure the tangential load. The sample is rotated with a speed so that the ball draws up a furrow in the coating.

The abrasive wear behaviour has been studied by means of a test, which consists of a rubber wheel rotating at a constant speed of 139 rpm on the studied deposit. A normal force of 50 N
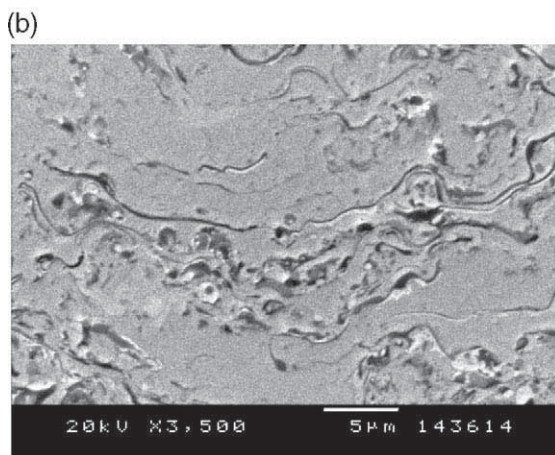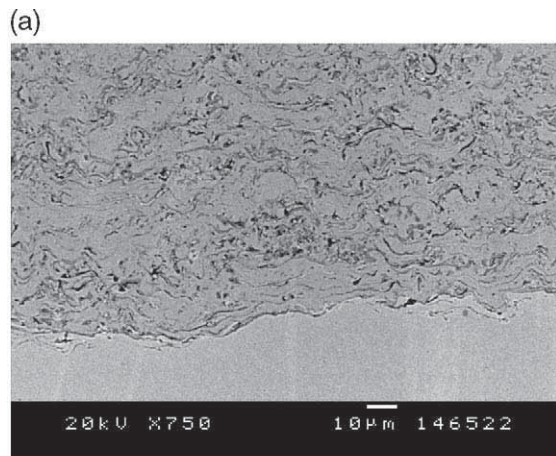
Fig. 5. Backscattered scanning electron micrographs of the coating cross-section F1 (a) X750 and (b) X3500.
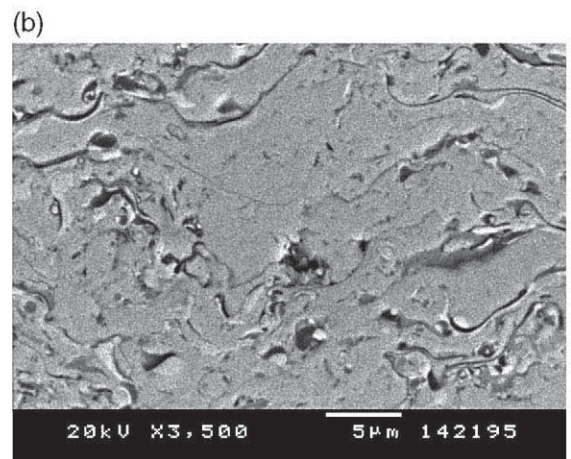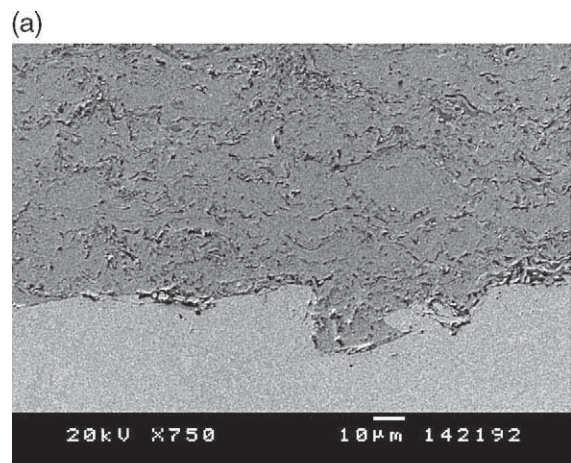
Fig. 6. Backscattered scanning electron micrographs of the coating cross-section F2 (a) X750 and (b) X3500.

is applied and an abrasive agent (SiO_2) is introduced by gravity between the wheel and the coating.

3. Results and discussion

3.1. The feedstock powder

Fig. 2 shows the morphology of obtained powder after ball milling stage. Scanning electron microscopy does not provide enough resolution to evidence the nanograin structure of the powder as reported by Grosdidier et al. [18,19].

Besides inducing a nanocrystalline structure, mechanical milling, according to Gang et al. [20], also creates a non-equilibrium microstructure in the powder particles. This is confirmed by diffraction studies as shown in Fig. 3, where XRD trace for the powder is compared with the typical Fe and FeAl patterns. It can be noticed that peaks agree with the Fe bcc phase (a_{Fe}=2.8664 Å) but with a different lattice parameter owing to the presence of aluminium atoms which have an atomic radii larger than that of Fe (a_{powder}=2.919 Å). As far as FeAl lattice parameter is concerned (a_{FeAl}=2.8954 Å), it is closer to the powder than that of alpha-Fe.

Both alpha-Fe and B2-type FeAl have a cubic crystal system but while alpha-Fe belongs to Im-3m space group, B2 FeAl has

Fig. 8. EDS general composition analysis of coatings: (a) F1, (b) F2, (c) F3.

Fig. 7. Backscattered scanning electron micrographs of the coating cross-section F3 (a) X750 and (b) X3500.

a long-range ordered structure, which belongs to Pm-3m. Consequently, if our feedstock powder had an ordered FeAl phase, more peaks should be shown in the experimental pattern because a primitive (P) system does not present systematic extinctions. Under those circumstances, it is demonstrated that powder crystalline structure can be defined by a disordered FeAl phase rather than an ordered B2-type.

Another aspect to notice is the broadening of the peaks owing to the small fraction size.
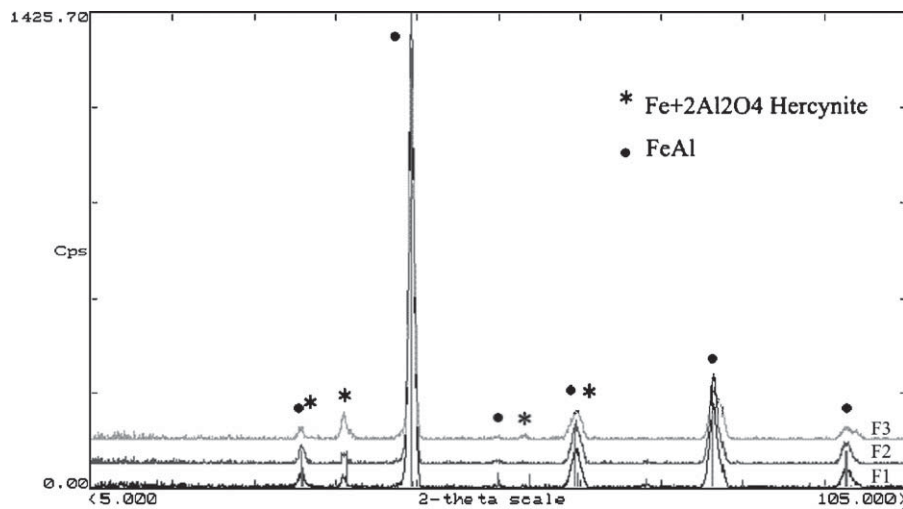
Fig. 9. X-ray diffraction: traces coatings (F1, F2, F3) in comparison with Fe and FeAl patterns.
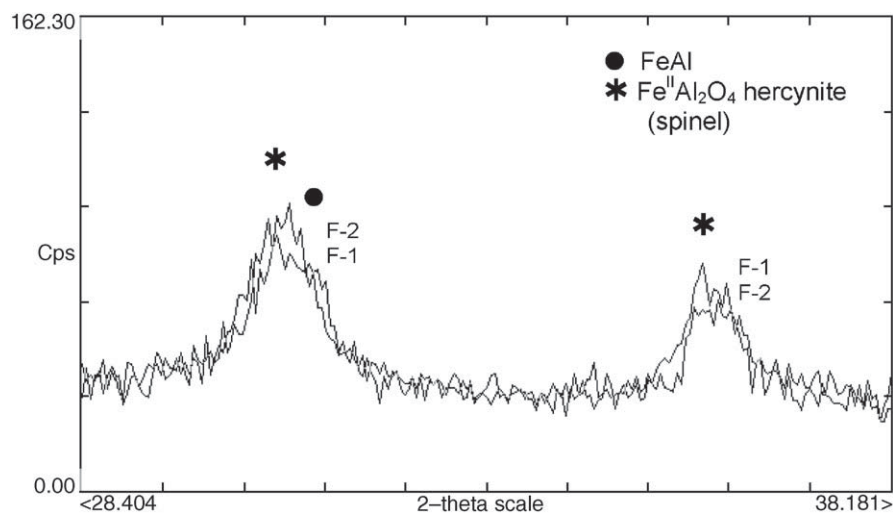
Fig. 10. X-ray diffraction amplification: comparison between traces coatings F1 and F2.

Fig. 4 shows the powder size distribution. The size fraction of this feedstock powder is $-30+7$ μm.

3.2. Microstructure of as-deposited coatings

Figs. 5, 6 and 7 show cross-sectional micrographs of the FeAl deposits obtained by SEM under backscattered conditions. These are the coatings obtained using propylene as fuel and with parameter sets 1, 2 and 3, respectively, referred as F1, F2 and F3 deposits. The main grey contrast has been identified as FeAl intermetallic phase by EDS analysis, while some dark and light grey contrasts, present essentially at the periphery of non-molten particles or at intersplats boundaries, correspond to oxides and phases with lower Al content, respectively.

Whereas F1 and F2 do not exhibit much difference, it can be observed and confirmed by area SEM/EDS analysis of the cross-sections (Fig. 8), a further oxidation in F3 sample due to the larger oxygen flow rate, which allows to reach higher temperatures. This is the reason why the microstructure contains a majority of fully melted particles. There is another reason for the major melting, which is the air flow rate, lower than F1; this contributes to a larger residence time of the particles in the flame. This reasoning is confirmed by oxygen/propylene values because whereas those rates used for F1, F2 and F3 deposits correspond to 3.06 and 2.87 and 3.61 respectively, the theoric oxygen/propylene rate value for the maximal temperature flame is 3.7.

In contrast, F1 and F2 contain more particles than F3 that did not fully melt in the flame as it can be observed at lower magnification (Figs. 5a and 6a) and few of which melted and

Table 2
Microhardness values of the as-deposited coatings

Sample reference	Microhardness (HV$_{200}$)
F1	475±31
F2	434±48
F3	468±26
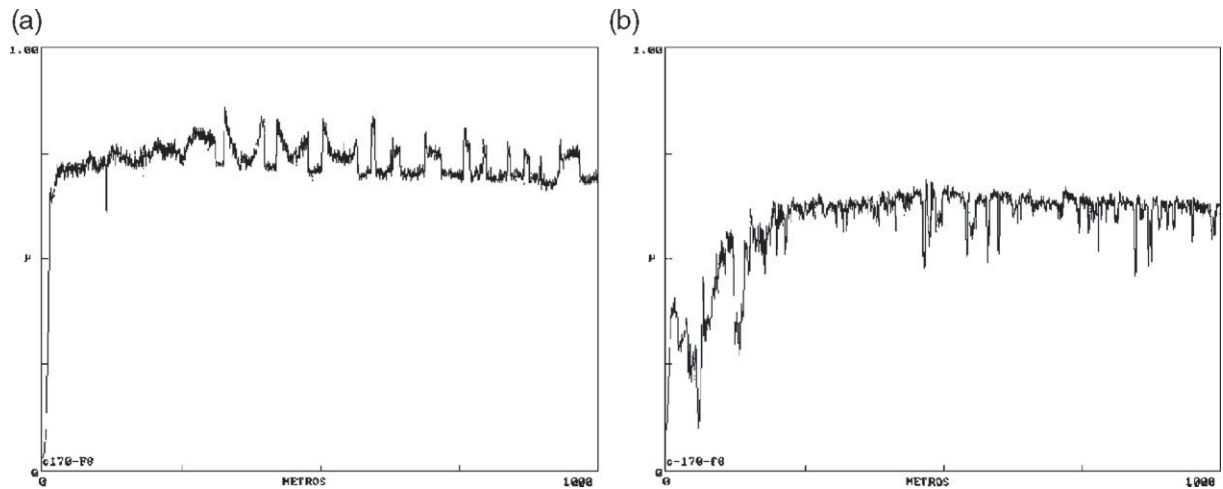
Fig. 11. Effect of load on the friction coefficient vs. sliding distance: (a) at room temperature and (b) at 400 °C.

flowed on impact to form the splats. The lower oxidation content in these deposits permits the presence of the main FeAl intermetallic phase in those particles not fully melted. As reported by Ji et al., this phase is a disordered FeAl structure while the B2-type FeAl is obtained in those actually melted zones [19].

As far as the microstructure concerns, no great difference can be observed between F1 and F2.

3.3. X-ray diffraction

X-ray diffraction was performed by means of a Bragg–Brentano $\theta/2\theta$ Siemens D-500 diffractometer (radius=215.5 mm) with Cu Kα radiation, selected by means of a secondary graphite monochromator. The divergence slit was of 1° and the receiving slit of 0.15°. The starting and the final 2θ angles were 10 and 105° respectively. The step size was 0.05° 2θ and the measuring time of 3 s per step.

Fig. 9 shows XRD scans for F1, F2 and F3 coatings. While F1 and F2 show apparently the same, in F3 some peaks seem to be split in two. The reason for this phenomenon will be accurately studied by Rietveld method. Fig. 10 shows an amplification of those two peaks observed at lower angle values. It can be appre-

ciated that the right one only corresponds to oxide phase; it means that oxide content is higher in F1 coating. According to this, the other peak which shows both contribution to FeAl and hercynite phases, indicates that F2 contains greater amount of intermetallic phase than F1.

3.4. Coating microhardness

Microhardness was measured through the whole deposit cross-sections using 200 g load. The final values in Table 2 were obtained from the average of 20 measurements.

The average values are included in the range of 400–500 HV_{200}, higher than those reported by Gang et al. [21]: 307 HV with a fraction of powder size ($-40+20$ μm), 395 HV with a fraction of powder size ($-63+40$ μm) and 349 with the coarsest powder ($-100+20$ μm). It is difficult to accurately compare different coatings obtained with different systems but these values can be used at least as a reference.

3.5. Sliding wear behaviour

Few studies have been carried out with regard to wear properties of FeAl coatings. Many authors have striven for reaching
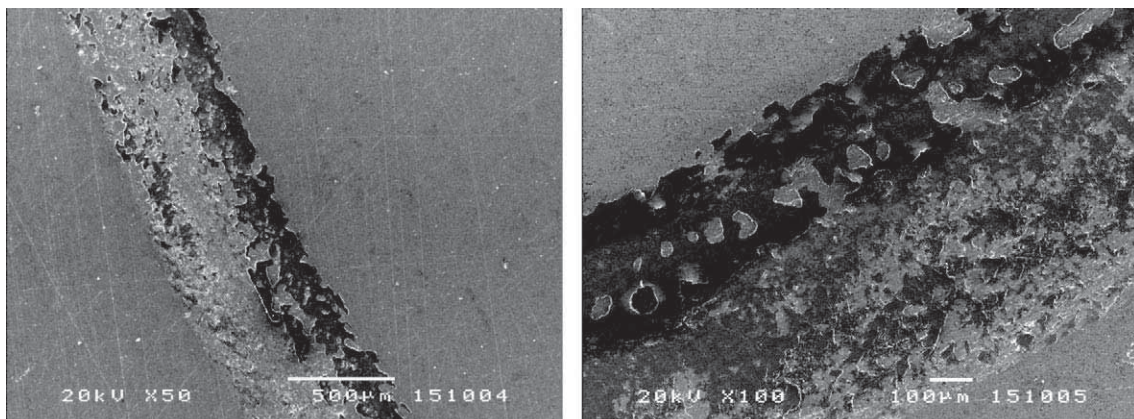
Fig. 12. SEM morphologies of the wear track at room temperature.
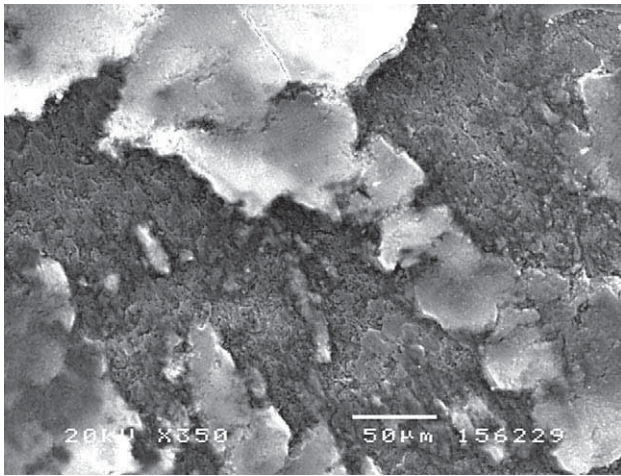
Fig. 13. SEM morphology of an area covered by wear debris.

Fig. 15. Mass loss during the whole Rubber-Wheel test.

a better wear behaviour by introducing WC particles embedded in the FeAl matrix [22].

We have been investigating the wear properties both at room and high temperature using a ball-on-disk test. The tests are made in a closed camera to control temperature and humidity ($T = 25$ °C and HR 20%). The used ball has been a cermet made from WC-6Co with 11 mm of diameter, the load of the arm was of 5 N and the diameter of route of the ball is of 16 mm, with speed of 0.11 m/s). The number of cycles is 19,895, which corresponds to a total distance of 1000 m.

Fig. 11a and b show the variation of friction coefficient of the Fe–40Al coating sprayed under F1 conditions, which permits a low oxide content. At room temperature, the friction coefficient ($\mu = 0.706$) is higher than that at 400 °C ($\mu = 0.617$), which was somewhat predictable due to the reported better properties at high temperature environments. Both values are calculated from the latest 200 m. Bin-shi et al. [23], who obtained FeAl coatings by High Velocity Arc Spraying (HVAS), also performed similar tests with different wear variables at different temperatures.

Fig. 12 shows the SEM morphologies of the worn FeAl coatings surface after sliding at room temperature. At room temperature, the darkest zones observed on the wear track correspond to oxide films

formed by friction heating during sliding, while the lighter ones are associated to fresh coating. A higher magnification in Fig. 13 shows some of this wear debris remaining on the wear track.

The relative high friction coefficients indicate that probably the principal wear mechanism is adhesive due to the larger real surface of contact. The smooth surfaces required for this test (Ra < 0.8) would permit the formation of more local microwelding zones which are susceptible to plastic deformation; this phenomenon would produce an increase in the contact area as well as in the coefficient of friction. This hypothesis is confirmed by EDS analysis in the wear track where it can be observed elemental transference of W and C from the ball.

Furthermore, the absence of furrows on the wear track rules out the possibility of an abrasive mechanism. Yang et al. also mentioned the presence of those cracks in bulk materials after different ball-on-disk tests to study the influence of several variables [24]. With a sliding speed of 0.03 m/s, the large amount of tracks observed is said to indicate a severe microfracture mechanism, while at 0.1 m/s, fewer cracks indicate a fatigue wear mechanism. However, fatigue cracks tend to be perpendicular to the sliding direction and no cracks of this kind are observed under our conditions; therefore, we would conclude that fatigue does not have any influence.

Fig. 14 shows the SEM morphologies of the worn FeAl coatings surface after sliding at 400 °C, where a higher oxidation level is observed. Such oxide could behave as lubricant responsible for the decrease in the coefficient friction.
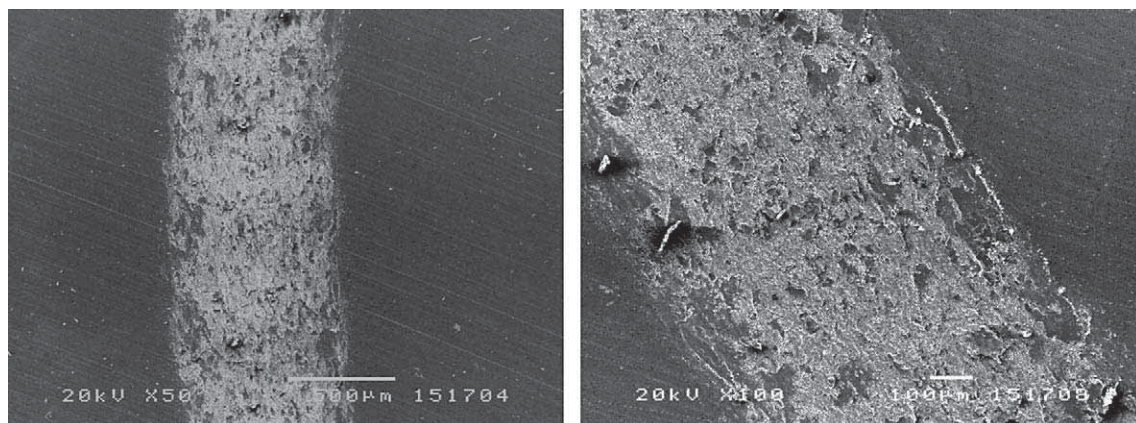
Fig. 14. SEM morphologies of the worn deposits at 400 °C.
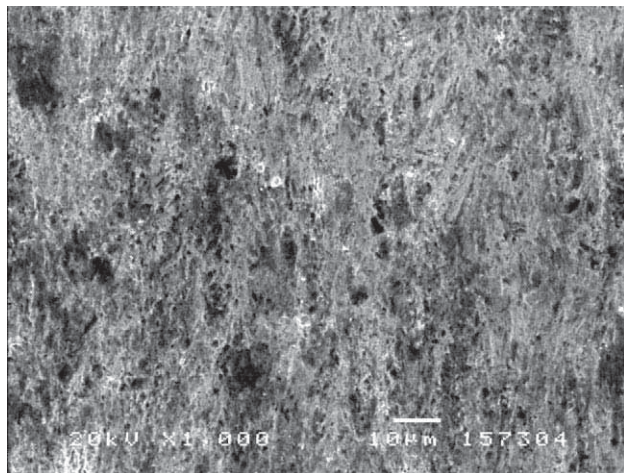
Fig. 16. Morphology of the worn surface by means of Rubber-Wheel test.

However, in the near future a more detailed study on wear will be done by means of interferometry and confocal microscopy, where a three-dimensional image of the sample can be obtained. It is worth to study the topography.

3.6. Abrasive wear behaviour

The abrasive wear resistance of iron aluminide F1 coating has been investigated using a Rubber-Wheel test through the measurement of the loss of weight. Three analogue tests have been carried out with a time test of 30 min. In all the cases it has not reached the substrate. Fig. 15 shows the evolution of the mass loss during the test. It is observed that during the first 10 min the wear rate (pendent) is slightly higher due to the beginning of the wear process. After this while, the wear rate is estimated to be $4.14 \ 10^{-3} \ mm^3 \ min^{-1} \ N^{-1}$.

In Fig. 16, the furrows produced by the silica performing as the abrasive agent between the rubber wheel and the coating can be observed. It is said to be a three body wear because SiO_2 particles remain between the two surfaces producing the abrasive effect.

4. Conclusion

Microstructural and compositional investigations have been carried out on cross-sections of FeAl coatings obtained by HVOF spraying with different oxygen-propylene rates. Under those conditions, the conclusions of the study can be summarized as follows:

1. Composition studies by EDS and X-ray diffraction revealed that used thermal spray conditions have allowed the formation of a FeAl phase in a closer B2-type state compared to the structure of the feedstock powder.
2. As far as microstructure and EDS analysis are concerned, the higher oxidation content is observed for F3 coating, obtained with the oxygen/propylene ratio closer to that of the ones corresponding to higher temperature of flame. Such conditions allow a larger melting and oxidation of the particles during the spraying process.

3. Rather high microhardness values have been obtained for the three studied deposits.
4. As far as tribological properties concern, the friction coefficient obtained by ball-on-disk test at 400 °C is lower than that at room temperature. The wear debris on the wear track and EDS analysis indicate that it is controlled by an adhesive mechanism.
5. The abrasive wear rate is $4.14 \ 10^{-3} \ mm^3 \ min^{-1} \ N^{-1}$.

Acknowledgements

References

[1] C.T. Liu, J.O. Stiegler, Ordered intermetallics. Properties and selection: nonferrous alloys and special purpose materials, Metals Handbook, Tenth edition ASM International, 1990.
[2] S.C. Deevi, V.K. Sikka, Intermetallics 4 (1996) 357.
[3] M.M. Rico, J.M. Greneche, G.A. Perez, J. Alloys Compd. 398 (2005) 26.
[4] C.T. Liu, E.P. George, P.J. Maziasz, J.H. Scneibel, Mater. Sci. Eng., A Struct. Mater.: Prop. Microstruct. Process. 258 (1998) 84.
[5] L. Pang, K.S. Kumar, Mater. Sci. Eng., A Struct. Mater.: Prop. Microstruct. Process. 258 (1998) 161.
[6] J. Bystrzycku, R.A. Varin, Mater. Sci. Eng., A Struct. Mater.: Prop. Microstruct. Process. 270 (1999) 151.
[7] H. Skoglund, M. Knutson, B. Karlsson, Intermetallics 12 (2004) 977.
[8] W.J. Zhang, R.S. Sundar, S.C. Deevi, Intermetallics 12 (2004) 893.
[9] E. Arzt, R. Behr, E. Göhring, P. Grahle, R.P. Mason, Mater. Sci. Eng., A Struct. Mater.: Prop. Microstruct. Process. 234–236 (1997) 22.
[10] D.G. Morris, S. Gunther, Mater. Sci. Eng., A Struct. Mater.: Prop. Microstruct. Process. 208 (1996) 7.
[11] R. Baccino, K. Wolsky, F. Thevenot, J. le Coze, F. Moret, Proprietes mecaniques d'alliages ODS a base fer elabores par mecanosynthese et consolidation a chaud, CEA/CEREM, Département d'Etude des Matériaux, Grenoble, France.
[12] M.A. Muñoz-Morris, C. Garcia Oca, D.G. Morris, Acta Mater. 51 (2003) 5187.
[13] P. Adeva, Revista de la Asociación Española de Científicos, vol. 1, 1999, p. 1.
[14] S.C. Deevi, V.K. Sikka, C.T. Liu, Prog. Mater. Sci. 42 (1997) 177.
[15] T. Totemeier, R. Wright, W.D. Swank, Intermetallics 12 (2004) 1335.
[16] A.Y. Mosbah, D. Wexler, A. Calka, Abrasive wear of WC-FeAl composites, Wear 258 (2005) 1337.
[17] V.V. Sobolev, J. Guilemany, J. Nutting, High Velocity Oxy-fuel Spraying, Maney Publishing1-902653-72-6, 2004.
[18] T. Grosdidier, A. Tidu, H. Liao, Scr. Mater. 44 (2001) 387.
[19] J. Gang, J. Morniroli, T. Grosidider, Scr. Mater. 48 (2003) 1599.
[20] J. Gang, T. Grosdidier, H.L. Liao, J. Morniroli, C. Coddet, Intermetallics 13 (2005) 596.
[21] J. Gang, O. Elkedim, T. Grosdidier, Surf. Coat. Technol. 190 (2005) 406.
[22] B. Xu, Z. Zhu, S. Ma, W. Zhang, W. Liu, Wear 257 (2004) 1089.
[23] X. Bin-shi, Z. Zi-xin, Z. Wei, M. Shi-ning, ITSC (2004) 19.
[24] Y. Yang, P. La, W. Liu, Q. Xue, Wear 257 (2004) 104.

APPENDIX VI: J. M. Guilemany, N. Cinca, S. Dosta, C. R. C. Lima, Oxidation behaviour of HVOF-sprayed ODS-Fe40Al Coatings at 900ºC. ITSC (2007)

Oxidation Behavior of HVOF-sprayed ODS-Fe40Al Coatings at 900°C

J. M. Guilemany, N. Cinca , S. Dosta
Thermal Spray Centre (CPT). Dpt. Ciència dels Materials i Enginyeria Metal.lúrgica. Universitat de Barcelona, Spain

C.R.C. Lima
Unimep – Methodist University of Piracicaba, College of Engineering, SP, Brazil

Abstract

This study examines the oxidation performance of two different iron aluminide coatings obtained by means of High Velocity Oxygen Fuel spraying starting from the same feedstock powder but using propylene and hydrogen as fuels. The isothermal oxidation tests were carried out at 900°C for 4, 36 and 72 hours. After detailed observation a more rapid oxide scale growth is obtained for that coating obtained under hydrogen conditions. It leads to the assertion that propylene-coatings would perform better under high temperature environments.

Introduction

Thermal Spraying technologies have been extensively used to produce intermetallic coatings. These sort of materials are potential for high temperature structural applications due to the thermal stability of their ordered superlattice. As far as the near stoichometric intermetallic FeAl (40%at.) is concerned, many results have been reported involving High Velocity Oxy-Fuel-sprayed powders [1-5] with regard to their wear and oxidation resistance. As already known HVOF is specially an interesting processing method to form dense deposits [6].

High melting points, low relative densities, high thermal conductivity, high mechanical strength at high temperatures despite poor ductility at room temperatures and good corrosion resistance [7, 8] provide to high-temperature intermetallic compounds excellent properties for their use as a protective medium in hostile atmospheres.

Apart from the previous general properties which intermetallics posses, aluminides have a good strength/mass ratio and excellent oxidation resistance at elevated temperatures. Specially, FeAl appears to be interesting due to the low cost raw materials and excellent oxidation and sulphidation resistance [9].

Under the circumstances exposed above, the present investigation is focused on four different directions: one is to use HVOF as a consolidation processing technique to produce dense coatings from milled powders; second, to evaluate the coating structures using two different fuels and third, to assess the oxidation behavior of the previous coatings after carrying out oxidation tests at 900 °C at different times. Finally, as so many efforts have been made to understand the effect of yttria to improve the performance of bulk iron aluminides at high temperatures, it has been strived for clarifying its role on the as-sprayed ODS-FeAl powders exposed to oxidizing environments.

Experimental Procedure

A Diamond Jet Hybrid (DJH) model 2600/2700 (Sulzer Metco) system has been used in this work to produce dense iron aluminide coatings. The starting atomized powders with a composition of Fe-40Al-0.05Zr (at.%) + 50 ppm B and then milled to reduce grain size and introduce 1%wt. Y_2O_3 as dispersoids to improve strength, were supplied by CEA (Commissariat a` l'Energie Atomique).

In a previous study by Guilemany et al. [10], some results testing different spraying parameters using propylene as fuel were already reported, which can be found elsewhere [10] and is not explained here in detail Primarily, the present study deals with that coating referenced as F-2 there, which was observed to present lower oxidation content. For the performance of isothermal tests, it has then been compared with that coating obtained under hydrogen conditions which also showed lower oxidation. Table 1 shows the spraying conditions for both coatings (P-Fe40Al is the same as F-2 in [10]).

	Parameter set	
	P- Fe40Al *	H- Fe40Al **
Oxygen flow rate , l min⁻¹	189	147
Carrier gas (air), l min⁻¹	305	344
Fuel, l min⁻¹	87	717
Spraying distance , mm	250	

* Using propylene as fuel
** Using hydrogen as fuel

The microstructure characterization of the coatings was performed by a Scanning Electron Microscope (SEM) JEOL 5510, to which detector is connected for the semiquantitative analysis by means of Energy Dispersive Spectroscopy. The X-ray diffraction patterns were obtained using a Bragg-Brentano θ/2θ Siemens D-500 diffractometer with Cu Kα radiation.

After the deposition onto grit-blasted even rectangular steel samples, several specimens were cut out and edge covered with cement so that the preferential interface substrate-coating oxidation is minimized. The isothermal tests were carried out in a furnace under air atmosphere. After samples were oxidized for 4, 36 and 72h, they were cooled in air.

Results

Coatings Characterization
Microstructural observation and XRD analysis of the starting powder and the as-deposited coatings under propylene conditions were already discussed in our previous work [10]. Thus, they will be compared to those features observed for the coatings deposited using hydrogen as fuel. All of them showed a lamellar structure resulting from mostly fully melted particles in a grey contrast surrounded by dark and light contrasts in the intersplats.

As already did for propylene, for the hydrogen several spraying conditions were used in order to deposit the coating with a major phase of intermetallics. For the optimization of oxygen, carrier gas and hydrogen flow rate combinations, three oxygen/hydrogen ratios of 0.327, 0.445 and 0.301 were selected for deposition of the coatings which were referred to as F-4, F-5 and F-6, respectively. The later one corresponding to the cooler conditions was the one chosen for comparison with F-2 to evaluate the high temperature resistance.

With the higher oxygen flow rate (O_2/H_2 ratio 0.445), the more efficient combustion was created and thus, the particles were heated to higher temperatures. Moreover, it leads to more oxide phase. No appreciable differences were observed when the hydrogen and air flow rates were increased and the oxygen was decreased. However, if instead of increasing, the air flow rate is also decreased, cooler and more reductive conditions are reached. The former case corresponds to the parameter set of H-Fe40Al sample.

Compared to propylene, the thermal efficiency of the flame using hydrogen is higher, which leads to higher degree of melting of particles. Figure 1 shows the microstructure of those coatings obtained with the conditions exhibited in Table 1, which were used for the isothermal oxidation tests. While in P-Fe40Al it could be said that particles are just melted to enable to form the deposit, which led to a high percentage inclusions of unmelted or partially melted particles in the deposits. In H-Fe40Al coating more flattened particles were present with oxide at the interfaces between them. As revealed by EDS, the dark grey features correspond to a spinel oxide phase whereas the lighter contrasts between splats were assigned to Fe-rich zones. The presence of such phases was also appreciated by XRD (Fig. 2). The major grey zones are assigned to the FeAl alloy.
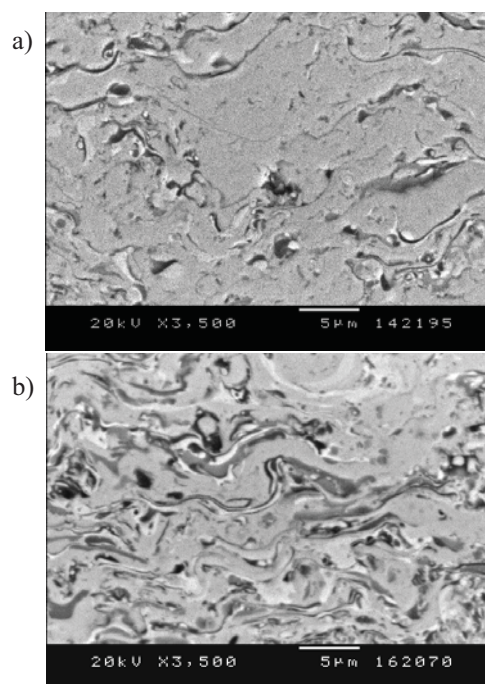
Figure 1: BSE micrographs of the coating cross section (a) P-Fe40Al and (b) H-Fe40Al.

After an study of the structure factor for a disordered and ordered B2-phase, it was found the occurrence of the intermetallic phase in the as-sprayed deposits at some extend by the presence of the as-denominated superlattice lines in the XRD scans of the coatings. By contrast, only fundamental lines appeared in the XRD scan of the powder indicating that it is a disordered alloy. This can be asserted considering that the powder comes from a ball-milling route.
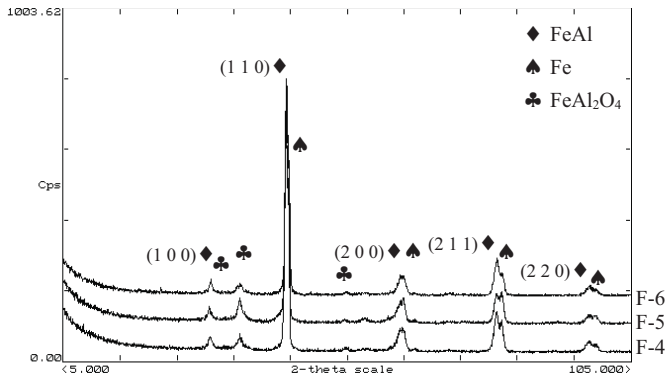
Figure 2: XRD patterns of the as-sprayed coatings under hydrogen conditions.

Table 2 shows the angles for both coatings and the powder. Those values for which h+k+l is an uneven number correspond to the superlattice lines of FeAl phase indicating the presence of the ordered B-2 phase, which was claimed to be in the melted zones as suggested by other authors [2]. By the peak lines in H-Fe40Al, it can be clearly appreciated the presence of the before mentioned Fe-rich zones.

Table 2: 2θ angles corresponding to the phases included in the starting powder and coatings compared to the patterns of the Fe and B2-FeAl phases.

Fe	FeAl	Powder	P-Fe40Al	H-Fe40Al
	30.819 (1 0 0)		30.750	30,971
	44.187 (1 1 0)	43,867	44.261	44,356
44,711 (1 1 0)				44,673
	54.858 (1 1 1)		54.949	54,896
	64.318 (2 0 0)	63,777	64.558	64,414
65,080 (2 0 0)				64,959
	81.339 (2 1 1)	80,607	81.429	81,488
82,413 (2 1 1)				82,294
	97.596 (2 2 0)	96,574	97.733	97,785
99,053 (2 2 0)				98,937

Isothermal Tests

After undergoing oxidation tests for both coatings during 4, 36 and 72 h of exposure in air atmosphere, the formation of an adherent oxide layer was observed above the deposits. Figure 3 shows both coating cross sections after 72 h oxidation. However, it can be noticed that the growth rate is clearly slower in the case of P-Fe40Al. Furthermore, no voids were present in the coating-oxide layer interface.

Although the slightly difference in the oxide scale thickness observed, the coating still remains almost intact. Actually, another test for 300 h was carried out for H-Fe40Al sample in order to prove whether the continuous growing of oxide scale reduce the thermal sprayed coating. But no differences were

observed. Thus, for both deposits the oxide layer protects effectively the coating from corrosion. However, less uniform scales are formed for H-Fe40Al and some spallation was observed.

XRD of the oxide scales indicated the major presence of iron oxide with some trace of aluminium oxide in the P-Fe40Al sample, which must be the reason why the protection is more effective in this case (Fig. 4). Although no alumina was detected by XRD in the H-Fe40Al sample, according to SEM observations and EDS analysis of the oxide-coating interface, some mixed oxides must have been formed beneath the hematites top layer. For both cases, with increasing the exposure time, the intensity of FeAl peaks decreased.

Moreover, several micrographs taken at the same magnification as Fig. 1 did not reveal so many different grey contrast features. Thus, for instance, no light grey intersplats zones were appreciated indicating a diffusion process between those initial Fe-rich areas and inner partially melted particles when the samples were exposed to 900°C [11].

Figure 5 shows the nodular and some whisker-like morphology of the iron oxide formed on the surface. While most of the P-Fe40Al surface contains oxide nodules, H-Fe40Al exhibits more whisker-like features indicating a more oxidation step process.
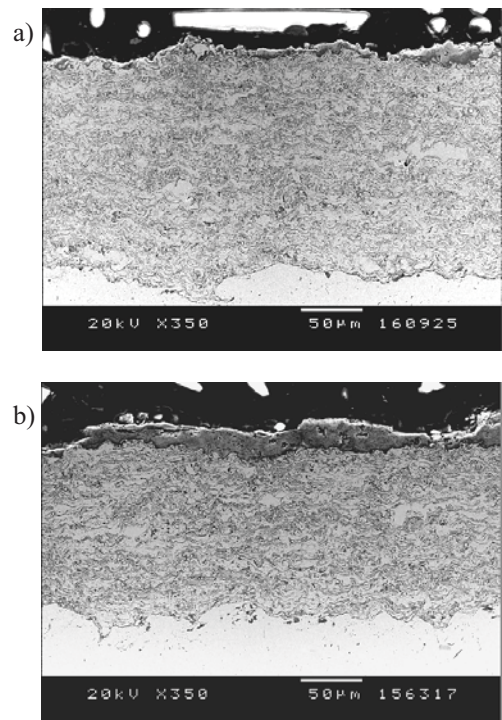
Figure 3: Cross section micrographs after 72h of exposure at 900C in oxidizing atmosphere (a) P-Fe40Al and (b) H-Fe40Al.

Figure 4: XRD patterns of the top surface of two coatings after 4, 36 and 72h: (a) P-Fe40Al and (b) H-Fe40Al.

Figure 5: Top surface features after 72h of exposure at 900C in oxidizing atmosphere (a) P-Fe40Al and (b) H-Fe40Al.

Analysis and Discussion

In view of the results presented above, both as-sprayed powders with propylene and hydrogen led to dense coatings. However, the first one exhibits more fraction deposited by partially melted particles and less oxidation than the latter one. The type of oxides characterized in these coatings, specially in H-Fe40Al, appeared to be the result of oxidation during the particle flight in the spraying chamber and the occurrence of Fe-rich areas are known to be formed because of the aluminium evaporation during the deposition process [2, 4].

Despite not having carried out exhaustive TEM analysis to determine grain size and yttria particles distribution in the milled powders, other authors using the same feedstock powders claim that mechanical alloying leads to particles with small nanocrystalline domains less than 20 nm which permit to obtain the so called 'nano-deposits' [2]. After producing the coatings, interestingly, the same authors did not find any trace of Y_2O_3 neither in the unmelted nor the fully melted zones.

As already claimed by many authors, the oxidation behavior of pure and ODS bulk iron aluminides follows a parabolic kinetics [12-18]. By examination of the scale growth, it can be seen it reaches a nearly steady state; however, as no mass gain measurements have been undertaken, it is not reliable to assert that the oxidation of the coating follows also a parabolic rate. Detailed studies on diffusivities through the "bulk" coating should be carried out and compared to the bulk material.

With regard to the results obtained after the isothermal tests, it can be concluded that after reaching a certain thickness, the oxide scale remained almost in the same value, without the presence of cracks that would permit a continuous inward oxygen diffusion and thus an accelerated oxidation. Furthermore, apparently, the stresses on the scales are not large enough to produce an extended spallation which would leads to a decrease in the oxidation resistance. This feature has been largely reported to occur in bulk FeAl. In the present case, the thickness of the oxide scale reaches a steady state causing a protective effect on the coating and consequently on the substrate as this one seems not to have been affected.

Nevertheless, considering the high aluminium content in the alloy and the alumina oxide layers for similar tests undergone for bulk materials, the little alumina content in P-Fe40Al and its absence on H-Fe40Al coatings after the tests, are surprising. The reason remains unclear and it can only be speculated that the fast growing nucleation of iron oxide leads to the formation of a Fe_2O_3 top layer which is mainly detected by XRD. Under such layer, alumina or some spinel oxides may have formed as corrosion products.

The formation of an uniform oxide layer has also been obtained by Szczucka-Lasota et al. [19] who proposed a model for that. They also obtained Fe_2O_3 as one of the main
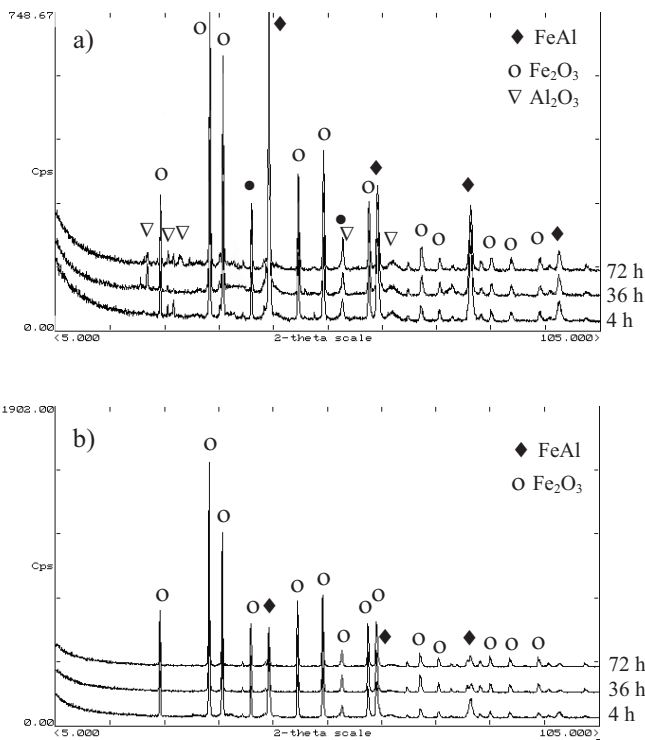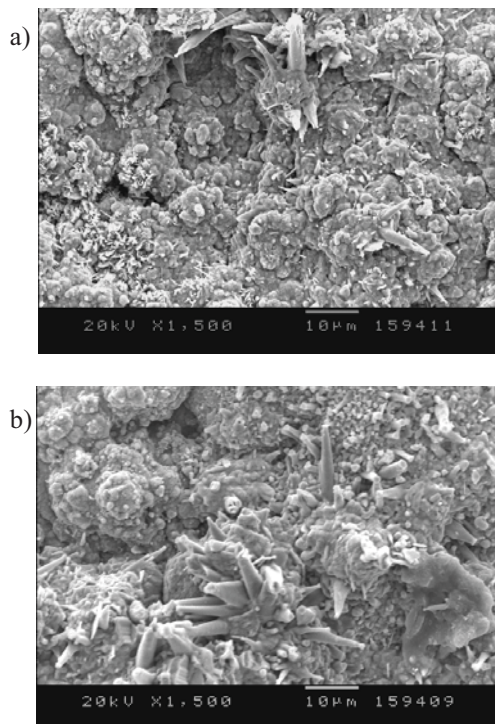
corrosion products at 950ºC and, according to their observations, the amount of such iron oxides decreases when aluminium oxides increase. This argument can also justify the present results for P-Fe40Al which do not show a notable morphology change in the surface from short to long exposition time, where the nodular structure persists on the majority of the surface coating. By contrast, the absence of alumina on H-Fe40Al facilitates the growing of the iron oxides. In this former case, it has been likely produced by a reaction as the following: $Al_2O_3 + \frac{1}{2} O_2 + Fe \rightarrow FeAl_2O_4$.

It is also worth noting that a more homogeneous composition is obtained after the tests owing to the diffusion processes which equilibrate FeAl and iron rich zones. For bulk materials, apart from the inwards oxygen diffusion, the outwards Al ions diffusion has been claimed to justify an stable alumina scale [18, 20]. In the present study, the presence of Fe atoms and the complex coating microstructure itself produces the features characterized above.

These conclusions appear to be opposite as the results obtained by Pedraza et al. [21], who observed an inner $FeAl_2O_4$ layer but a predominant alumina at the outermost surface. They claim a possible reaction between iron and aluminium oxides to form the spinel structure and a rapid diffusion of Al atoms which would allow the formation of the alumina scale.

Apart from improving mechanical properties [22-24], the presence of yttria in many alloys is said to modify the growth process of the oxide protective film [25, 26]. Several authors have presented their results on the base of different Y_2O_3 percentages. Many studies dealing with the same composition as presented here, report their results with a 1%wt. Y_2O_3, specially at temperatures above 1000 ºC, when the stable alumina phase is likely to form [12, 27, 28]; at 900 ºC, Pedraza et al. found the spinel-alumina sequence structure explained above [21]; others, used lower contents as 0,5% concluding that a decrease in yttria content allowed an earlier alumina formation [29], earlier studies indeed claimed no differences between oxidation behaviour for ODS and and FeAl alloys [26]. However, its role in as-sprayed coatings cannot be well understood if even no signs of such dispersoids are found in the coating microstructure.

Summary and Conclusions

Iron aluminides have been proposed for their service at high temperature environments. The performance of bulk materials has been extensively studied. However, few investigations have addressed to coatings oxidation resistance. Thus, this paper has evaluated the possible service of iron aluminide thermally sprayed coatings at elevated temperatures.

After testing different spraying conditions regarding the type of fuel and the flow gases rates, Fe40%at.Al intermetallic coatings containing 1%wt. Y_2O_3 were deposited and characterized under the exposure at 900ºC. After the microstructural observations of the oxidized samples for 4, 36 and 72 h, a fairly good oxidation resistance is accomplished. Although the main corrosion product in both cases is Fe_2O_3 and not Al_2O_3, the integrity of both tested coatings obtained using propylene and hydrogen as fuels remained allowing the protection of the substrate. It might be due to an initial thin alumina or spinel layer under the iron oxide. Then, it is clear that diffusion processes take place but the slow growing of the oxide scale appears to denote that the failure of the coating is not foreseen at an early stage.

References

1. T. Totemeier, R. Wright, W. D. Swank, FeAl and Mo-Si-B intermetallic coatings prepared by thermal spraying, *Intermetallics*, 2004, 12, p. 1335-1344.
2. G. Ji, T. Grosdidier, H. L. Liao, J. Morniroli, C. Coddet, Spray forming thick nanostructured and microstructured FeAl deposits, *Intermetallics*, 2005, 13, p. 596-607.
3. B. Szczucka-Lasota, B. Formanek, A. Hernas, Growth of corrosion products on thermally sprayed coatings with intermetallic phases in aggressive environments, *J. Mater. Process. Technol.*, 2005, 164-165, p. 930-934.
4. C. Xiao, W. Chen, Sulfidation resistance of CeO2-modified HVOF sprayed FeAl coatings at 700 °C, *Surf. Coat. Technol.*, 2006, in press.
5. Y. Wang, M. Yan, The effect of CeO2 on the erosion and abrasive wear of thermal sprayed FeAl intermetallic alloy coatings, *Wear*, 2006, in press.
6. V. V. Sobolev, JM Guilemany, J Nutting, *High Velocity Oxyfuel Spraying. Theory, Structure – Property Relationships and Applications.* Maney. Leeds (UK) 2004.
7. C. T. Liu, J. O. Stiegler, Ordered Intermetallics, Properties and selection: nonferrous alloys and special purpose materials, *Metals Handbook*, ASM International 10th ed., 1990.
8. M. Yamaguichi, H. Inui , K. Ito, High Temperature Structural Intermetallics, *Acta Mater.*, 2000, 48, p. 307-322.
9. N. S. Stoloff, Iron aluminides: present status and future prospects, *Mater. Sci. Eng. A*, 1998, 258,p. 1-14.
10. J. M. Guilemany, C. R. C. Lima, N. Cinca, J. R. Miguel, Studies of Fe-40Al coatings obtained by High Velocity-

Oxy Fuel, *Surf. Coat. Technol.*, 2006, 201 (5), p. 2072-2079.

11. J. A. Hearley, J. A. Little, A. J. Sturgeon, Oxidation properties of NiAl intermetallic coatings prepared by High Velocity Oxy-Fuel thermal spraying, *Proceedings of the 15th Thermal Spray Conference*, vol. 1, Christian Coddet, 25-29 May 1998 (Nice, France), ASM International, p. 89-94.

12. F. Lang, Z. Yu, S. Gedevanishvilib, S. C. Deevib, T. Naritaa, Isothermal oxidation behavior of a sheet alloy of Fe–40at.%Al at temperatures between 1073 and 1473 K, *Intermetallics*, 2003, 11, p. 697–705.

13. F. Langa, Z. Yub, S. Gedevanishvilic, S. C. Deevic, T. Naritad, Cyclic oxidation behavior of Fe-40Al sheet, *Intermetallics*, 2004, 12, p. 451–458.

14. P. F. Tortorelli and J. H. DeVan, Behavior of iron aluminides in oxidizing and oxidizing/sulfidizing Environments, *Mater. Sci. Eng., A* 1992, 153, p. 573-577.

15. M. Berlanga, J.L. Gonzalez-Carrasco, M.A. Montealegre, M.A. Munoz-Morris, Oxidation behaviour of yttria dispersion strengthened Fe40Al alloy foils, *Intermetallics*, 2004, 12, p. 205–212.

16. C.H. Xu, W. Gao, H. Gong, Oxidation behaviour of FeAl intermetallics, The effects of Y and/or Zr on isothermal oxidation kinetics, *Intermetallics,* 2000, 8, p. 769-779.

17. M.A. Montealegre, J.L. Gonzalez-Carrasco, M.A. Morris-Munoz, J. Chao, D.G. Morris The high temperature oxidation behaviour of an ODS FeAl alloy, *Intermetallics,* 2000, 8, p. 439-446.

18. C. Dang Ngoc Chan , C. Huvier , J. F. Dinhut , High temperature corrosion of some B2 iron aluminides, *Intermetallics*, 2001, 9, p. 817-826.

19. B. Szczucka-Lasota, B. Formanek, A. Hernas, Oxidation models of the growth of corrosion products on the intermetallic coatings strengthened by a fine dispersive Al$_2$O$_3$, *J. Mater. Process. Technol.*, 2005, 164-165, p. 935-939.

20. H.J. Grabke, Oxidation of NiAl and FeAl, *Intermetallic,* 1999, 7, p. 1153-1158.

21. F. Pedraza, J. L. Grosseau-Poussard , J. F. Dinhut, Evolution of oxide scales on an ODS FeAl intermetallic alloy during high temperature exposure in air, *Intermetallics*, 2005, 13, p. 23-33.

22. K. Wolski, F. ThCvenot, J. Le Coze, Effect of nanometric oxide dispersion on creep resistance of ODS-FeAl prepared by mechanical alloying, *Intermetallics,* 1996, 4, p. 299-307.

23. T. Grosdidier, G. Ji, N. Bozzolo, Hardness, thermal stability and yttrium distribution in nanostructured deposits obtained by thermal spraying from milled—Y2O3 reinforced—or atomized FeAl powders, *Intermetallics,* 2006, 14, p. 715–721.

24. M. A. Muñoz-Morris, C. Garcia Oca , D. G. Morris, Microstructure and room temperature strength of Fe-40Al containing nanocrystalline oxide particles, *Acta Mater.*, 2003, 51, p. 5187-5197.

25. E. Arzt, R. Behr, E. Göhring, P. Grahle, R. P. Mason, Dispersion strengthening of intermetallics, *Mater. Sci. Eng. A*, 1997, 234-236, p. 22-29.

26. A. Mignone, S. Frangini, A. La Barbera, O. Tassa, High Temperature corrosion of B2 iron aluminides, *Corros. Sci.*, 1998, 40, p. 1331-1347.

27. M.A. Montealegre, G. Strehl, J.L. Gonzalez-Carrasco, G. Borchardt, Oxidation behaviour of novel ODS FeAlCr intermetallic alloys, *Intermetallics*, 2005, 13, p. 896–906.

28. C.-H. Xu, W. Gao, S. Li, Oxidation behaviour of FeAl intermetallics ± the effect of Y on the scale spallation resistance, *Corros. Sci.*, 2001, 43, p. 671±688.M.A.

29. M. A. Montealegre, J.L. Gonzalez-Carrasco, Influence of the yttria content on the oxidation behaviour of the intermetallic Fe40Al Alloy, *Intermetallics,* 2003, 11, p. 169–175.

APPENDIX VI: I.G. Cano, N. Cinca, S. Dosta and J.M. Guilemany. Study of NiTi

Metastable Powders and Coatings Obtained by Plasma Spraying. *Revista de Metalúrgia*.

Estudio de polvos y recubrimientos metaestables de NiTi obtenidos por proyección térmica de plasma(•)

I.G. Cano*, N. Cinca*, S. Dosta* y J.M. Guillemany

Resumen
El compuesto intermetálico de NiTi es conocido por su capacidad de memoria de forma así como por su pseudoelasticidad. Debido, además, a su alta resistencia a corrosión (biocompatiblidad), la gran mayoría de estudios se centran en su uso para aplicaciones médicas. Dentro del conjunto de las tecnologías de superficie, las investigaciones actuales utilizan la técnica de Proyección Térmica de Plasma al Vacío para producir recubrimientos de NiTi con contenidos mínimos de porosidad y de óxidos.El Centro de Proyección Térmica se planteó como objetivo la obtención de polvos y recubrimientos metaestables de NiTi a través de la técnica de Proyección de Plasma acoplado a un sistema de refrigeración con nitrógeno líquido. Se estudiaron dos polvos con diferentes características, pero de la misma composición nominal (Ni-45 % peso Ti). Uno de ellos, es el resultado de una mezcla directa de partículas de níquel y de titanio, mientras que el otro consiste en una aleación obtenida a través de un proceso de atomización por gas. Ambos polvos fueron proyectados, obteniéndose mejores resultados para el polvo atomizado, ya que ha permitido la obtención de recubrimientos en los que la fase de NiTi es la mayoritaria con un mínimo contenido en óxido. Para lograrlo, se ensayaron diferentes parámetros de proyección.La caracterización microestructural se llevó a cabo mediante microscopía electrónica de barrido con un sistema de microanálisis acoplado. Además, los estudios de difracción de rayos X permiten concluir que el ensanchamiento de los picos puede demostrar la existencia de metaestabilidad en los recubrimientos obtenidos.

Palabras clave
Metaestabilidad. Nanotecnología. Solidificación rápida. Proyección térmica.

Study of metastable NiTi powders and coatings obtained by plasma spraying

Abstract
NiTi intermetallic is widely known for its shape memory effect and pseudoelasticity. Due to its high corrosion resístanse (biocompatibility), most of the studies carried out deal with its use for medical applications. With regard to surface technologies, many reported investigations focus on Vacuum Thermal Spray to provide NiTi coatings with minimal oxide content.The Thermal Spray Center has attempted to obtain metastable NiTi powders and coatings by means of Atmospheric Plasma Spraying with a liquid nitrogen cooling system. Starting from two different Ni-45wt%Ti feedstock powders. One powder is a blend of Ti and Ni particles, whereas the other has been alloyed by gas atomization. Both powders were sprayed obtaining better results starting from the gas atomized powder resulting in a final deposit where NiTi was the main phase with minimal oxidation. Different spraying parameters were tested and microstructural characterization was performed by SEM-EDS. XRD patterns showed some peak broadening; that seems to be produced by structural metastability of the coatings.

Keywords
Metastability. Nanotecnology. Rapid solidification. Thermal spray.

1. INTRODUCCIÓN

Durante las últimas décadas ha tenido lugar un incipiente interés por el mundo de la nanotecnología; este auge enfocado al estudio de las escalas comprendidas entre 10 y 100 nm se debe a la mejora de propiedades que presentan los materiales. Un procedimiento para obtener materiales nanocristalinos es a partir de fases metaestables, es decir, estructuras de no-equilibrio. La obtención de dichas fases a través de procesos de alta temperatura y su posterior evolución hacia materiales con tamaño de grano comprendido

entre 20 y 50 nm, es el objetivo del proyecto europeo Processing of NAnostructured MAterials through MEtastable Transformations (NAMAMET)[1]. Otros autores, también han destacado el proceso de aleación mecánica para la obtención de estructuras nanométricas[2].

El Centro de Proyección Térmica de la Universidad de Barcelona ha aplicado tecnologías de Proyección Térmica (plasma y enfriamiento rápido), las cuales involucran altas temperaturas y rápidas velocidades de enfriamiento, lo que permite la obtención de estructuras metaestables, como ya se ha comprobado en diferentes sistemas[3]. La solidificación rápida de metales y aleaciones constituye un método destacable para la formación de fases metaestables, lo cual se encuentra asociado, generalmente, con la rápida cinética de enfriamiento generada desde el estado fundido. La evolución microestructural durante este proceso depende de la velocidad de enfriamiento y de solidificación.

Dentro de esta línea de investigación se han desarrollado otros procesos de solidificación rápida para la obtención de fases metaestables en sistemas cerámicos [4-6].

Mediante Proyección por Plasma (APS), el material de partida en forma de polvo de tamaño micrométrico llega a la fase líquida donde, fases inicialmente inmiscibles se homogeneizan y solubilizan en estado líquido durante el pequeño intervalo de tiempo que permanecen en el haz de proyección, formándose así las fases metaestables tras un enfriamiento rápido[2].

Uno de los sistemas metálicos encuadrado en este marco, interesante en cuanto a sus aplicaciones como materiales funcionales y en el campo de la biomedicina, es la aleación NiTi (nitinol). Estas aleaciones, con composiciones cercanas a la equiatómica, presentan dos propiedades básicas por las cuales son conocidas: el efecto de memoria de forma, conocido como la capacidad que tiene un material para deformarse mediante un esfuerzo aplicado y recuperar posteriormente su forma original mediante un simple calentamiento, y la superelasticidad, por la cuál es posible inducir una transformación martensítica por esfuerzo cuando el material presenta fase austenítica (fase de alta temperatura).

Esta aleación ofrece una amplia gama de posibilidades: en cuanto a aplicaciones para ortopedia (placas de osteosíntesis, clavos de fijación intramedular para fractura de huesos, grapas par unir huesos y espaciadores para cirugía de columna vertebral, *stents*), para cirugía cardiovascular (filtros para vena Cava, *stents*, músculos artificiales, grapas para aneurismas craneales, instrumentos clínicos) y en recubrimientos protectores y resistentes a la erosión. Otras aplicaciones a destacar son las siguientes: controladores

de temperatura, equipos de seguridad en aparatos domésticos y, en radiadores, entre muchos otros[7].

El presente estudio explora la posibilidad de obtención de polvos con estructuras fuera del equilibrio en el sistema Ni-Ti a través de Proyección por Plasma en una atmósfera de baja temperatura. Hasta el momento, se han obtenido resultados con éxito para otros sistemas, especialmente cerámicos[8], en dónde, realizando tratamientos térmicos posteriores, se obtienen las estructuras predichas por el diagrama de fases pero con estructuras de tamaño de grano fino. Asimismo, se realizó un análisis microestructural de los recubrimientos obtenidos con el fin de evaluar, en posteriores estudios, el comportamiento a desgaste de dichos recubrimientos y comparar los resultados obtenidos con otras técnicas de obtención de recubrimientos[9].

2. PROCEDIMIENTO EXPERIMENTAL

Para la realización de este estudio, se partió de dos polvos de composición Ni-45 % peso Ti. El primero consiste en una mezcla directa de polvos de níquel y de titanio, mientras que el otro consiste en partículas de la aleación ya formada por fusión y atomización en atmósfera de argón, por lo cual se parte del intermetálico equiatómico presentado en el diagrama de fases de la figura 1. Como ya se desarrolla en la presentación y discusión de resultados, para mejorar la fluidez del polvo de mezcla, se activó mecánicamente, molturando durante 2h a 300 rev/min y utilizando bolas de zircona.

Se utilizó un equipo F4 de Sulzer Metco con mezclas de argón e hidrógeno como gases para la proyección por plasma atmosférico (APS y enfriamiento rápido), obteniéndose polvos y recubrimientos de Ni-Ti. En ambos casos, el polvo se proyectó sobre un sustrato de cobre (*splat quenching*) enfriado con N_2 líquido (Fig. 2), consiguiendo velocidades de enfriamiento del orden de $\sim 10^6$ K/s; con estos coeficientes de enfriamiento se pueden conseguir estructuras de no equilibrio que posteriormente evolucionan a nanoestructuras.

Ambos polvos han sido caracterizados estructuralmente mediante la técnica de Microscopía Electrónica de Barrido (SEM), acoplado a un sistema de microanálisis de rayos X (EDS) y por Difracción de Rayos X (XRD). Asimismo, el análisis morfométrico de éstos se realizó por difracción láser con el equipo BECKMAN COULTER LS, que utiliza un láser de 5 mW con una longitud de onda de 750 nm, que permite analizar partículas desde los 200 nm hasta los 2 mm. Los resultados se obtienen a partir de una ponderación en volumen. Es importante la elección del
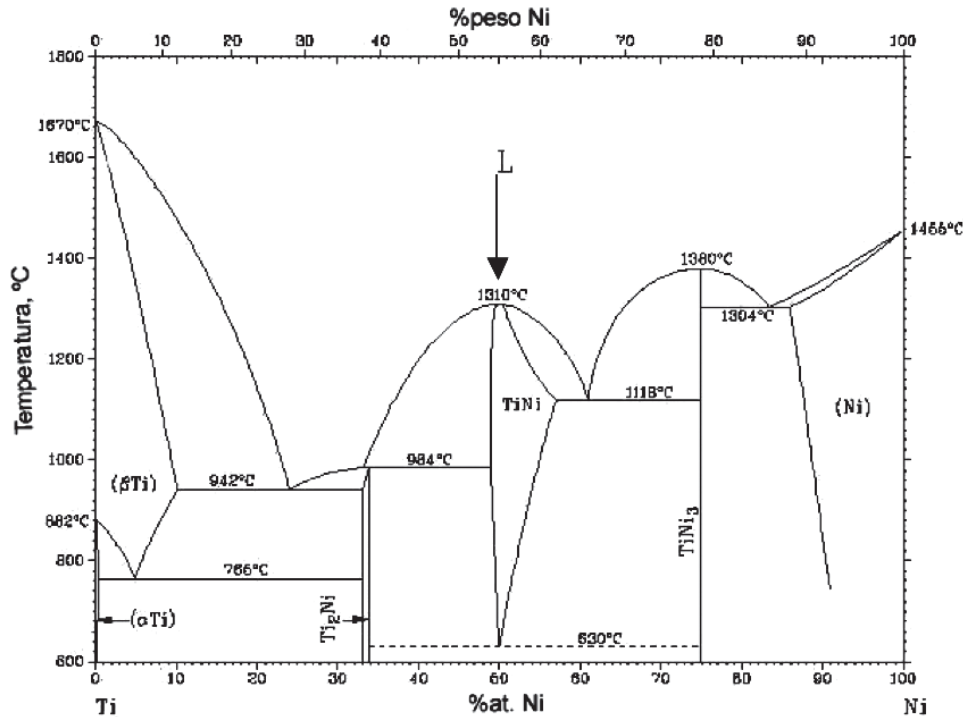
Figura 1. Diagrama de fases del sistema Ni-Ti.

Figure 1. Phase diagram of Ni-Ti system.

Figura 2. Esquema del sistema de proyección.

Figure 2. Scheme of the spraying process.

disolvente para producir la correcta dispersión de las partículas de polvo, puesto que su aglomeración en un disolvente no adecuado falsearía los resultados. Para el presente caso, se estableció como disolvente idóneo el aceite.

Se realizaron ensayos de fluidez bajo norma ASTM B-213-30 que permiten conocer la capacidad de fluir de un polvo bajo la única acción de la gravedad. Para determinar la fluidez se determina el tiempo necesario para que 50 g del polvo fluyan a través de un embudo tipo Hall.

La caracterización estructural de los recubrimientos incluye el estudio de la sección transversal mediante Microscopía Electrónica de Barrido (SEM) y el uso de Microanálisis de Rayos X por Separación de Energías (EDS) para analizar la composición de las distintas fases observadas.

Finalmente, el espesor de los recubrimientos obtenidos se calculó mediante análisis de imagen de la sección transversal con el software MATROX INS-PECTOR Image Analysis.

La determinación de la microdureza se realizó siguiendo la norma UNE 7-423/2. Se utilizó un microdurómetro MATSUZAWA MXT-a, con cargas de 100 g para la sección transversal de los recubrimientos y un tiempo de indentación de 15 s. Se realizaron 20 medidas aleatorias en todo el recubrimiento.

3. RESULTADOS Y DISCUSIÓN

3.1. Caracterización del polvo inicial

La figura 3 muestra una imagen de la morfología en superficie libre que presenta el polvo de mezcla. Puede apreciarse la presencia de partículas esféricas, así como partículas angulosas. El difractograma presentado

Figura 3. Superficie libre del polvo de mezcla inicial.

Figure 3. Morphology of the initial blended powder.

en la figura 4 confirma la existencia de níquel y titanio, separadamente, y el estudio detallado mediante EDS revela que las partículas esféricas están compuestas de níquel mientras que las segundas corresponden a las de titanio. Estas diferencias en la morfología de las partículas hacen que el polvo presente una mala fluidez en el embudo Hall. Asimismo, entre otras razones, también cabe destacar la distribución de tamaños. La figura 5 muestra la distribución granulométrica del polvo inicial; éste, presenta dos distribuciones: una centrada en, aproximadamente, 15 µm, mientras que la otra se encuentra alrededor de los 40 µm. En este caso, el 90 % de las partículas
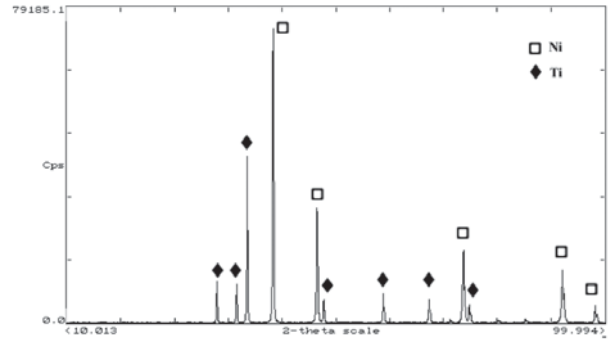
Figura 4. Difractograma del polvo de mezcla Ni-Ti.

Figure 4. XRD pattern of Ni-Ti blended.

están por debajo de los 65 µm. La presencia, aunque mínima, de partículas excesivamente grandes por encima, incluso, los 100 µm, juntamente con la posible formación de aglomerados de partículas pequeñas, es un factor limitante de la fluidez. Se intentó mejorar, entonces, la fluidez del polvo en vistas al proceso de proyección, para lo que se procedió a una activación mecánica de dicho polvo mediante molturación. La distribución observada después de dicho proceso es la que se muestra en la figura 6, donde el 90 % se encuentra por debajo de los 55 µm. Se puede observar una distribución igualmente de doble pico aunque con menos cantidad de partículas grandes y consiguiendo, a su vez, reducir los dos máximos esta vez centrados en 10 y 30 µm. En todo caso, el pico que aparece a menor tamaño corresponde
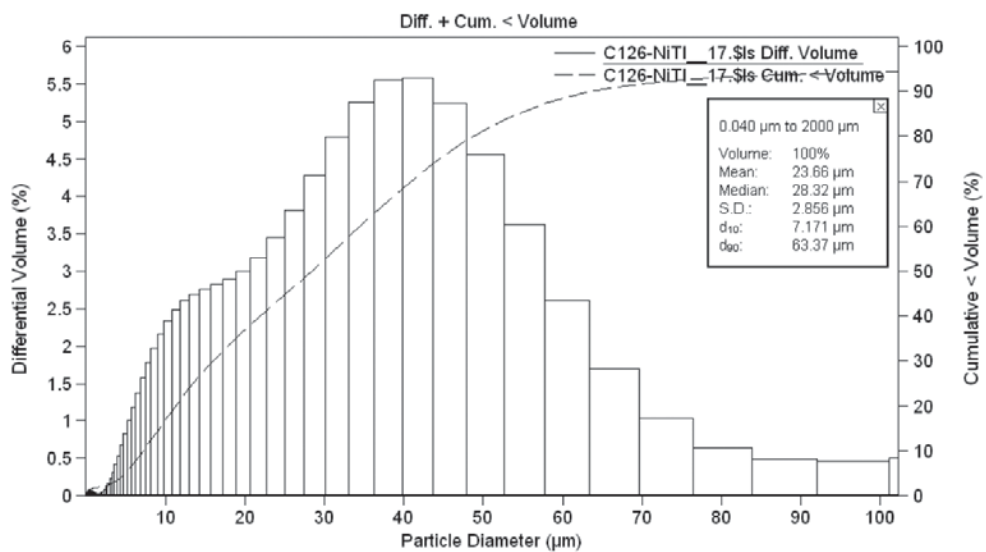
Figura 5. Distribución granulométrica del polvo de mezcla Ni-Ti.

Figure 5. Particle size distribution of NiTi blended.
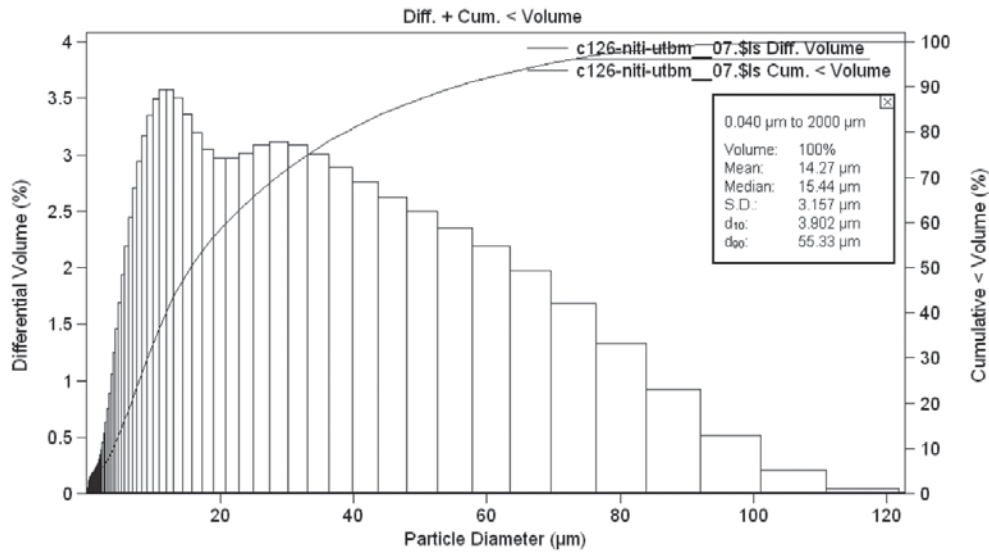
Figura 6. Distribución granulométrica del polvo de mezcla Ni-Ti después de molturar.

Figure 6. Particle size distribution of NiTi blended after milling.

a las partículas esféricas de níquel, mientras que el otro se asocia a las partículas de titanio. Habiendo reducido el tamaño de las partículas, se ha conseguido una mayor homogeneidad del polvo y es más probable que el rendimiento durante la proyección sea mayor, ya que con el polvo inicial lo más probable es que las partículas grandes de titanio no hubieran llegado a fundir saliendo así rebotadas.

El segundo polvo presenta una morfología esférica tal y como se muestra en la figura 7; ésta, es típica de los procesos de obtención por atomización por gas, lo cuál favorece la fluidez del polvo. La figura 8 muestra el difractograma del polvo con presencia de las fases NiTi y $NiTi_2$. La distribución granulométrica

Figura 8. Difractograma del polvo aleado Ni-Ti.

Figure 8. XRD pattern of Ni-Ti atomised .

indica una curva tipo gausiana, adecuada para el proceso de proyección, con un tamaño medio centrado en 81,92 µm (Fig. 9). Este polvo, a diferencia del anterior, presenta una fluidez aceptable y no hubo problemas durante su proyección.

3.2. Obtención de estructuras metaestables

El objetivo del proceso de proyección era llegar a un estado líquido donde las fases de equilibrio que se encontraban en el polvo inicial (NiTi y $NiTi_2$) se solubilizaran. De este modo, durante el proceso de enfriamiento rápido, podría esperarse una evolución a

Figura 7. Superficie libre del polvo aleado.

Figure 7. Morphology of the initial atomised powder.
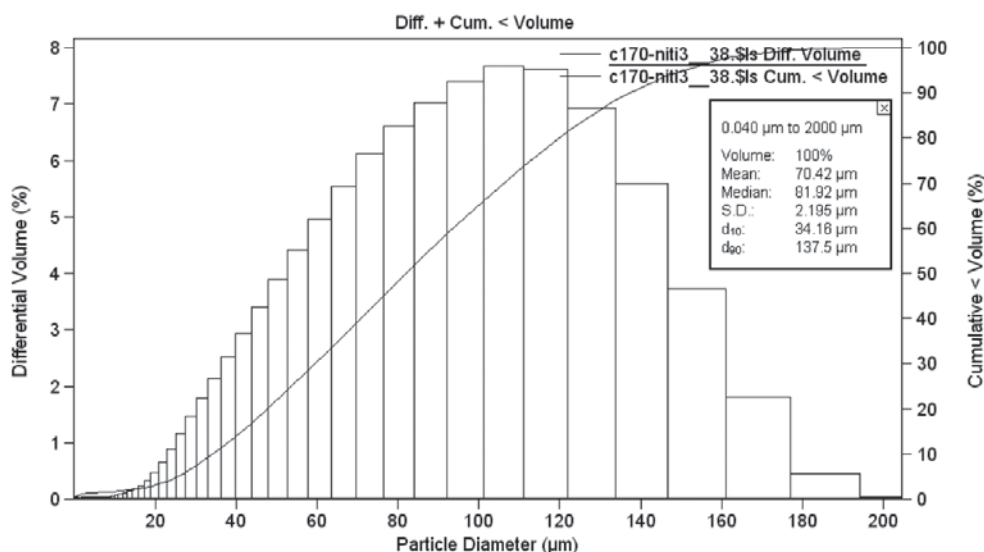
Figura 9. Distribución granulométrica del polvo aleado Ni-Ti.

Figure 9. Particle size distribution of NiTi atomised.

una única fase fuera del equilibrio (metaestabilidad), como ya se ha comprobado en otros sistemas, especialmente cerámicos[10]. Esta fase, dado el rango de composiciones del polvo inicial, debería ser la de NiTi. En el presente estudio, lo que se observa es la desaparición de la fase $NiTi_2$ por la fusión mayoritaria del polvo, indicando que el enfriamiento ha sido suficientemente rápido para no dar lugar a las fases de equilibrio. Por el contrario, se aprecia un ensanchamiento en los picos del espectro de difracción y un desplazamiento a ángulos mayores; teniendo en cuenta que el parámetro de red teórico para las fases cúbicas NiTi y $NiTi_2$ es de 2.998 y 11.310, respectivamente, a partir de los difractogramas experimentales se ha encontrado que estos valores corresponden a 3.009 y 11.318 para el polvo inicial, mientras que en cuanto al recubrimiento, a= 2.992 para la fase esteyquiométrica. Por lo tanto, todo esto llevaría a la conclusión de que la metaestabilidad asociada al presente sistema se traduce a una deformación de la red con respecto al polvo inicial. Es conocido que, otros sistemas intermetálicos que también presentan una estructura ordenada tipo B2 (LRO-long range order), como la fase austenítica del NiTi, presentan temperaturas de ordenación próximas a su punto de fusión; por tanto, sería necesario comprobar si el NiTi, después de fundir durante la proyección, conserva un cierto grado de orden (SRO-*short range order*) de manera que al enfriar rápido se obtenga NiTi con una estructura ligeramente diferente. Para poder asegurar la existencia de estos cambios se están realizando estudios de microscopía electrónica de transmisión, TEM.

Por otro lado, se observó la presencia de óxidos siendo, ésta, menor en el caso de la utilización de polvo aleado (Figs. 10 y 11); aún y favoreciendo una atmósfera baja en oxígeno por la presencia del nitrógeno, es inevitable una mínima oxidación de las partículas, inherente al proceso de APS.

Los recubrimientos obtenidos se molturaron con molino de bolas, obteniéndose un polvo cuyas características se muestran en las figuras 12 y 13. La figura 12 muestra la morfología de dicho polvo; su distribución granulométrica muestra que el 90 % de las partículas se encuentran por debajo de los 65 μm . Este polvo se pretende estudiar como material inicial en procesos de densificación. En la actualidad, se esta
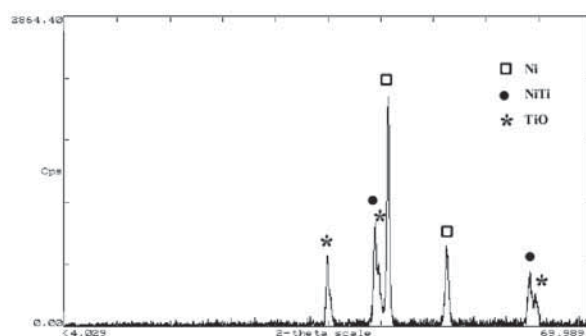
Figura 10. Difractograma del polvo de mezcla proyectado Ni-Ti.

Figure 10. XRD pattern of the splat quenched Ni-Ti blended powder.
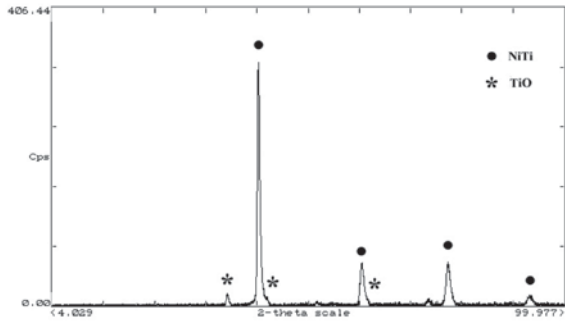
Figura 11. Difractograma del polvo aleado una vez proyectado Ni-Ti.

Figure 11. XRD pattern of the splat quenched Ni-Ti atomised powder.

analizando la viabilidad de procesos como HT_HP, SPS, *dinamic compactation*, etc. Se están llevando a cabo estudios sobre el efecto que esta fase metaestable causa a la estructura final del material denso.

Con el fin de observar la microestructura del recubrimiento proyectado, se partió de un sustrato previamente granallado donde la rugosidad superficial inducida por el choque de un haz de partículas de corindón a alta presión, permite el anclaje mecánico de las partículas de NiTi fundidas. La figura 14 presenta una sección transversal del mismo, mostrándose cierto grado de oxidación y porosidad. Los microanálisis (EDS) indican que las zonas de contraste oscuro, señaladas como EDS 2, en la figura 14, revelan un mayor porcentaje en peso de oxígeno
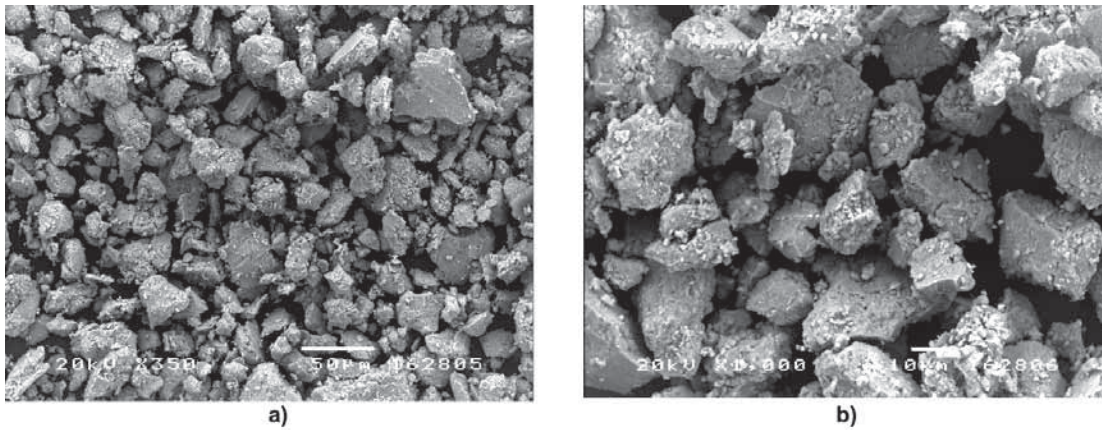
Figura 12. Morfología del polvo resultante de la etapa de molturación del recubrimiento obtenido.

Figure 12. SEM images of the ball-milled splat-quenched powder.
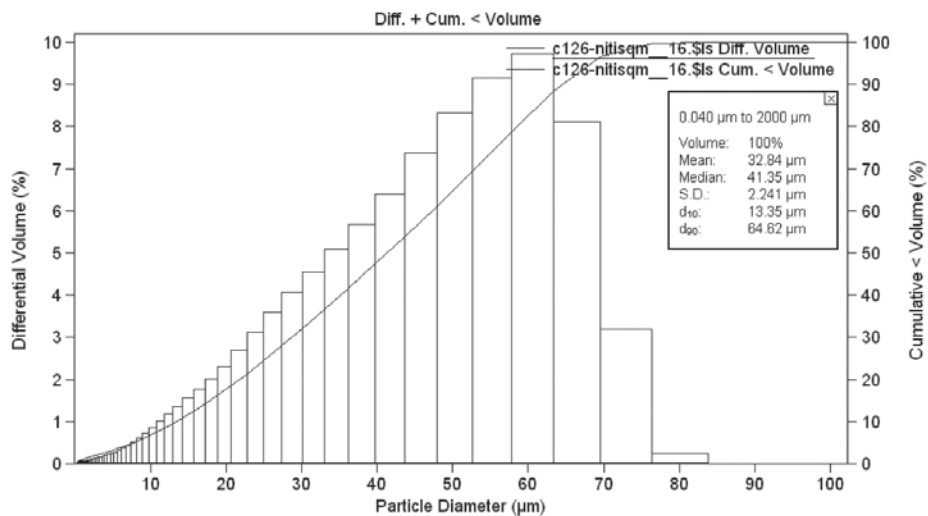
Figura 13. Distribución granulométrica del polvo obtenido de la molturación del recubrimiento.

Figure 13. Particle size distribution of the ball-milled coating.

Figura 14. Imágenes de la superficie transversal obtenida por microscopía electrónica de barrido del recubrimiento de NiTi refrigerado con N2.

Figure 14. Cross-sectional SEM images of NiTi coating cooled with the N2 feeders.

(62,31 % Ti, 24,78 % Ni, 12,90 % O), así como un mayor contenido en titanio, mientras que las zonas de contraste claro marcadas como EDS1 presentan una menor diferencia entre los porcentajes de níquel y titanio y el contenido en oxígeno es inapreciable (46,48 % Ti, 53,52 % Ni wt %).

Respecto a ensayos preliminares de dureza Vickers realizados en dichos recubrimientos, los resultados obtenidos presentan unos valores HVN_{100} de 549 ± 43 que, comparados con materiales densos, presentan un aumento aproximado del 45 % (296 y 349 Vickers[11 y 12]). Este aumento puede deberse al efecto reforzante por parte del óxido de níquel. De todas maneras, a través de los estudios de microscopía de transmisión, también se pretende profundizar en este tema.

4. CONCLUSIONES

— Se ha logrado la formación de fase intermetálica NiTi en la proyección del polvo a través del proceso APS + enfriamiento rápido. En el caso del uso del polvo aleado, los resultados muestran mayores contenidos de NiTi y menor grado de oxidación, formándose solamente, en ambos casos, la fase NiO.

— El ensanchamiento y desplazamiento de los picos, mostrado en el difractograma del polvo aleado una vez proyectado, denota un cambio en la estructura de la aleación de NiTi.

— La oxidación, tanto en el polvo como en el

Figura 14. Imágenes de la superficie transversal obtenida por microscopía electrónica de barrido del recubrimiento de NiTi refrigerado con N2.

Figure 14. Cross-sectional SEM images of NiTi coating cooled with the N2 feeders.

(62,31 % Ti, 24,78 % Ni, 12,90 % O), así como un mayor contenido en titanio, mientras que las zonas de contraste claro marcadas como EDS1 presentan una menor diferencia entre los porcentajes de níquel y titanio y el contenido en oxígeno es inapreciable (46,48 % Ti, 53,52 % Ni wt %).

Respecto a ensayos preliminares de dureza Vickers realizados en dichos recubrimientos, los resultados obtenidos presentan unos valores HVN_{100} de 549 ± 43 que, comparados con materiales densos, presentan un aumento aproximado del 45 % (296 y 349 Vickers[11 y 12]). Este aumento puede deberse al efecto reforzante por parte del óxido de níquel. De todas maneras, a través de los estudios de microscopía de transmisión, también se pretende profundizar en este tema.

4. CONCLUSIONES

— Se ha logrado la formación de fase intermetálica NiTi en la proyección del polvo a través del proceso APS + enfriamiento rápido. En el caso del uso del polvo aleado, los resultados muestran mayores contenidos de NiTi y menor grado de oxidación, formándose solamente, en ambos casos, la fase NiO.

— El ensanchamiento y desplazamiento de los picos, mostrado en el difractograma del polvo aleado una vez proyectado, denota un cambio en la estructura de la aleación de NiTi.

— La oxidación, tanto en el polvo como en el

RESUM EN CATALÀ

La idea de fer una tesi sobre recobriments de compostos intermetàl·lics sorgí després de dur a terme una recerca bibliogràfica, que va fer adonar-nos de què aquests compostos estaven despertant, en els últims anys, un interès creixent dins de la comunitat científica.

El document està estructurat en diferents capítols, bàsicament: introducció, presentació de resultats, discussió de dits resultats i conclusions. A la vegada, aquesta tesi s'ha realitzat com a compendi d'articles; no obstant, donat que els temes estudiats són força variats, dits articles s'inclouen oportunament al llarg del text, enmig doncs d'altres anàlisis i resultats que s'han dut a terme.

1.   Breu introducció

Els compostos intermetàl.lics són senzillament materials formats a partir d'una mescla, en una proporció definida, de dos o més metalls formant una estructura cristal.lina diferent a l'observada en els elements originals. Es diferencien de les solucions sòlides convencionals en què, aquestes consisteixen essencialment en aliatges desordenats de diferents elements metàl·lics, no tenen una formula química que les identifiqui i es poden descriure fàcilment com un material base al qual se li han afegit altres elements. Per contra, un compost intermetàl.lic té una fórmula química definida i sol trobar-se comprès dins d'un marge fix i estret de composicions.

De la seva ordenació atòmica i la força dels enllaços se'n deriven propietats com els alts punts de fusió, les altes resistències mecàniques (sobretot a altes temperatures) i les baixes ductilitats; aquests trets els assimilen molt als ceràmics però, a diferència d'aquests, tenen brillantor metàl·lica, són bons conductors tèrmics i elèctrics i, poden ser processats generalment per les tècniques convencionals comunes en metalls.

De tots els compostos intermetàl.lics que es coneixen, ens hem centrat com ha estudi dins de la present tesi en els aluminurs i en el nitinol (Ni-Ti). El grup dels aluminurs és bastant estudiat actualment a nivell de materials en volum degut a les expectatives que suposa poder disposar d'unes aleacions amb alta resistència, baixa densitat (degut a la presència de l'alumini) i bon comportament a alta temperature (degut a la formació d'una capa compacta d'alúmina). Com a representació dins d'aquest grup, bàsicament cal fer menció als sistemes Fe-Al, Ni-Al i Ti-Al, als quals se'ls està intentant millorar la poca ductilitat que tenen a través de variar el mètode de processat, reduir el tamany de gra o introduir tercers elements aleants. Actualment, tot i que encara no són comercialitzats, poden trobar aplicació en elements tèrmics i s'espera, que en les properes dècades el seu estudi sigui prou avançat com perue puguin arribar a substituir als superaliatges. Els seus elevats punts de fusió, claus per aquestes aplicacions deriven de la naturalesa del seu enllaç. Es coneixen, fins i tot, intermetàl.lics, anomenats refractaris amb punts de fusió per sobre dels 1600ºC; dos exemples en són el $MoSi_2$ i el $NbAl_3$. Per això, a fi de comparar dos tipus d'aluminurs, es va escollir el FeAl, com a representant del primer gruo i, el $NbAl_3$, com a representant del segon grup.

Pel que fa al nitinol, aquest es va escollir com a compost curiós i realment interessant en el món dels materials ja que té el què es coneix com a efecte memòria de forma i pseudoelasticitat a través d'una transformació entre dues fases: la martensita (fase de baixa temperatura) i l'austenita (fase d'alta temperatura). L'efecte memòria de forma consisteix en el següent: si el material, inicialment a baixa temperatura, es deforma, a l'escalfar recupera la seva forma original; mentre està a alta temperatura, el material és superelàstic, és a dir, que en fase austenítica, qualsevol deformació que se li apliqui, sempre acabarà tornant a la posició inicial. Aquestes propietats, juntament amb la bona resistència a la corrosió, fan que sigui un material molt estudiat sobretot en el camp de la biomedicina.

Per altra banda, cal plantejar perque s'han aplicat tots aquests compostos com a recobriments. Pel que fa als aluminurs, les causes són varies: (i) els mètodes de processat convencionals a través de la fusió poden donar problemes d'exotermicitat i d'oxidació de l'alumini, (ii) conformar materials en volum resulta complicat degut a la seva extrema fragilitat, (iii) aconseguir un material amb unes bones propietats a oxidació però que a la vegada tingui una alta resistència mecànica no és fàcil de compaginar. En les aleacions actuals, els nivells d'alumini i crom s'han de mantenir per sota d'uns percentatges crítics ja que d'altra manera no podrien soportar les càrregues per a les aplicacions a què estan destinades. Per tant, l'opció de disposar d'un substrat amb les prestacions mecàniques desitjades protegit amb un recobriment que pugui proporcionar-li una bona resistència a l'oxidació a alta temperatura, sembla una bona opció.

En el cas del nitinol, un dels principals impediments és l'econòmic ja que fabricar peces en volum d'aquest material pot resultar molt car. Algunes de les prestacions que es tenen en ment per l'ús dels recobriments obtinguts a partir d'aquesta aleació són la resistència a la corrosió i, si es pot aconseguir, un bon comportament també a desgast.

Per a aquest fi, el conjunt de tecnologies de la Projecció Tèrmica ofereix grans avantatges ja que pot arribar a permetre la reparació in-situ de peces danyades elevant així el seu temps de vida fent que, a la llarga, això suposi una reducció de costos de manteniment. Dins d'aquest grup, les principals tècniques que s'han utilitzat són: projecció per Alta Velocitat (HVOF, High-Velocity Oxy-Fuel), projecció per Plasma Atmosfèric (APS, Atmospheric Plasma Spraying) i projecció per Plasma al Buit, (VPS, Vacuum Plasma Spraying). Bàsicament, la primera es fonamenta en una combustió mentre que la segona es basa en la formació d'un plasma a través d'un arc elèctric.

2.   Resultats i discusió

2.1   Caracterització estructural

En referència al sistema Fe-Al, s'han utilitzat dos tipus de pols i per mitjà de la tècnica de projecció per Alta Velocitat s'han format els recobriments. Una de les pols, de composició Fe-40Al–0.05 Zr (at.%) + 50 ppm B + 1%pes Y_2O_3, atomitzada + molturada (nom comercial FeAl grade 3), mentre que l'altra s'ha format a través d'un aliatge mecànic a temperatures criogèniques. Diferents anàlisis experimentals però, confirmen que aquesta pols és una solució sòlida de l'Al en el Fe ja que degut a les baixes temperatures la difusió no ha estat suficient per poder arribar a formar l'intermetàl.lic $Fe_{50}Al_{50}$.

Per tant, per una banda s'han projectat aquestes dues pols obtenint recobriments amb una microestructura molt semblant, on les partícules estan majoritàriament foses (*splats*) i entre aquestes, trobem zones d'òxid juntament amb zones pobres en Al degut a la formació d'aquests òxids. A més a més, a fi d'obtenir una microestructura el més semblant possible a la d'un material sinteritzat, es va provar de projectar només el rang de partícules comprès entre 40 i 60 micres. A la secció 4.1.2 es mostren les micrografies dels tres recobriments. Els estudis de microscopia electrònica de transmissió varen indicar que en molts casos, l'estructura nanocristal.lina de la pols inicial es mantenia en el recobriment; no obstant, com que també apareixen indicis d'ordenament de l'estructura (degut a la molturació, la pols mostrava una estructura desordenada de l'aleació), també és possible que aquesta estructura nanocristal.lina provingui d'una recristal·lització durant la projecció.

La pols de $NbAl_3$ també és molturada però, a diferència de les anteriors, mostra una distribució de tamanys de partícules molt heterogènia, amb tendència a l'aglomeració de les més fines, fet que va donar molts problemes en el moment de la projecció degut a l'obturació de l'injector. Per això, es va haver d'escalfar prèviament dita pols ajudant a millorar-ne la fluïdesa. Com

que aquest intermetàl.lic té un punt de fusió més elevat que el FeAl, les condicions de projecció es van haver de modificar per optimitzar-ne els resultats. Els recobriments obtinguts mostren partícules totalment foses amb gran quantitat d'òxids entre "splats".

En referència al sistema Ni-Ti, la pols de partida és una pols atomitzada i, per tant, amb morfologia esfèrica que no ofereix problemes en quant a fluïdesa. Una mostra en secció transversal i atac d'aquestes partícules mostra la presència d'una matriu de NiTi amb precipitats d'una segona fase $NiTi_2$ / Ti_4Ni_2O. La projecció d'aquesta pols es va realitzar a través de tres tècniques diferents: VPS, APS i HVOF. La primera és la més emprada i nomenada en la bibliografia ja que degut a l'atmosfera de buit, s'evita l'oxidació del titani. L'apartat 4.3.2 mostra les microestructures dels tres recobriments, on s'aprecia les diferències entre ells. El recobriment obtingut per projecció al buit no mostra visiblement cap imperfecció, ni òxids ni porus, però quan és atacat, es distingeixen diferents fases, una més rica en Ti i l'altra més rica en Ni. A través de la tècnica d'APS, s'ha obtingut un recobriment amb presència de TiO i esquerdes transversals produïdes per l'efecte de la projecció en atmosfera de nitrogen que ha donat lloc a un refredament més ràpid de l'habitual. Finalment, el recobriment d'HVOF està format per zones on encara s'observa l'estructura inicial de la pols, mentre que l'exterior de les partícules hi ha una fina capa d'òxid.

A més de la caracterització típica a través de difracció de raigs X i microscopia d'escombrat i de transmissió, tant a la pols com els recobriments se'ls han fets unes mesures calorimètriques a fi d'identificar possibles transformacions martensita $\leftrightarrow$ autenita. S'ha observat la transformació M$\rightarrow$A durant l'escalfament mentre que no apareix cap pic durant el refredament. També s'aprecia la tendència en el desplaçament de dites temperatures de transformació: pols<HVOF$\approx$APS+Q<VPS. La primera variable a tenir en compte de cara a les temperatures de la transformació és la composició de

l'aliatge martensític. El NiTi equiatòmic té una M_S lleugerament per sobre de la temperatura ambient, valor que es manté bastant constant si l'aliatge s'enriqueix amb Ti. No obstant, l'enriquiment amb Ni provoca un ràpid descens de M_S. Els aliatges amb composicions majoritàries en níquel afavoreixen la formació de la fase R, així com la formació de precipitats rics en Ni després de tractaments tèrmics a altes temperatures. Després d'alguns processos com tractaments termomecànics, que poden ajudar a l'eliminació de defectes estructurals, la temperatura de transformació sol traslladar-se a valors més elevats.

2.2 Propietats mecàniques

La duresa dels recobriments, a més del material en si, depèn molt de la presència d'òxids i porositat. Els primers tendeixen a augmentar-ne el valor de duresa, mentre que la porositat tendeix a disminuir-la. Es va observar que els recobriments de FeAl, tot i les diferències microestructurals entre ells, eren menys durs que els de NiTi i, aquests a la vegada menys durs que els de $NbAl_3$.

En quant a la resistència al desgast, cal diferenciar entre els diferents mecanismes:

- El <u>desgast abrasiu</u> s'ha mesurat a través de l'assaig de "rubber wheel" i ve donat per la fricció entre dues superfícies, una molt més dura que l'altra (abrasió a dos cossos) o bé, per la presència de partícules dures que es deixen fluir entre les dues superfícies friccionants i que són les que produeixen el desgast (abrasió a tres cossos). Tal i com es mostren en els gràfics del capítol de discussió, hi ha una tendència clara entre la duresa dels recobriments i la resistència a aquest tipus de desgast, essent inversament proporcional, és a dir, a major duresa menys desgast.
- El <u>desgast per lliscament</u> es mesura a través de l'assaig de "Ball on disk" i mesura el coeficient de fricció d'una bola de metall dur a una càrrega

determinada sobre la superfície d'assaig en front la distància. El seu anàlisi resulta més complex que en el cas anterior ja que hi ha la possibilitat de què hi intervinguin més mecanismes. De fet, a través de l'observació dels camins de desgast, s'intueix que el mecanisme predominant en els recobriments de FeAl és per delaminació, mentre que els de NiTi i NbAl$_3$ és per abrasió a tres cossos ja que el material desgastat queda entre les dues superfícies, s'endureix i provoca un desgast més sever. Cal fer menció que els recobriments de FeAl obtinguts a partir de la projecció de la pols de 40-60 micres mostraren uns coeficients de fricció notablement més baixos que la resta de recobriments i el desgast produït en aquests és pràcticament inapreciable. També, en quant al recobriment de NiTi obtingut per APS, sembla que el mecanisme predominant és per fatiga ja que les esquerdes ja existents en el recobriment inicial es veuen agreujades pels successius cicles que la contrapoveta que llisca sobre la superfície.

2.3   Resistència a la corrosió i oxidació a altes temperatures

La resistència tant a la corrosió com a l'oxidació a alta temperatura depèn de la formació d'una capa d'òxid capaç de passivar al material impedint que aquest segueixi sent atacat pel medi agresiu.

Donat que els intermetàl.lics formats per aluminurs estan essent estudiats per possibles substitucions dels superaliatges, aquests s'han assajat a altes temperatures, especialment a 900, 1000 i 1100°C ja que és en aquest interval on es coneix que té lloc la formació de la fase α-Al$_2$O$_3$. A 900°C, els diferents recobriments de FeAl mostren certa resistència a l'oxidació: el recobriment obtingut a partir de la projecció de la pols prealeada és el que presenta millor comportament ja que, al llarg del temps la capa d'òxid es manté amb el mateix gruix sense detriment del recobriment; tot i que la formació d'alumina superficial no és completa sinó que hi ha una important quantitat d'òxids de ferro, la capa d'òxid mixte en la interficie recobriment-

òxid, juntament amb el poc decapatge d'aquest, fan que l'oxidació no avanci. El recobriment obtingut projectant-ne les partícules del rang 40-60 micres, feia pensar que donaria millor resistència en quant a què no hi ha zones empobrides en alumini ni tanta oxidació entre particules; no obstant, en base als resultats observats, sembla ser que, tot i la formació majoritària d'alúmina, les tensions internes del recobriment fan que aquest es descohesioni més fàcilment. Finalment, el recobriment format a partir de la pols cryomolturada presenta un comportament similar al del recobriment inicialment discutit però on la capa d'òxid és notablement més ample, fet que fa pensar que, amb el temps, aquesta anirà augmentant fins arribar al substrat.

Per tant, s'ha vist que a 900°C, encara es podria dir que optimitzant les condicions s'aconsegueix una millora de la resistència a l'oxidació; per contra, per sobre d'aquesta temperatura, en tots els casos, el recobriment és totalment oxidat i, fins i tot, s'oxida part de l'acer de substrat. Les raons d'aquest comportament estan en la diferència de coeficients d'expansió tèrmica, les tensions produïdes pel ràpid refredament a l'aire des de temperatures tan altes o bé, fins i tot, degut a dites tensions, el decapatge de la capa d'òxid és més important, fent que la zona immediatament inferior, pobra en alumini, s'oxidi a la vegada que es va esgotant l'alumini que queda en el recobriment. Degut a aquest procés, el recobriment en general s'empobreix en Al i per tant, l'oxidació és inevitable.

En quant al NiTi, se n'ha estudiat la corrosió en medis salins, a través d'assajos electroquímics amb una solució de NaCl, com en boira salina. S'ha observat que, el recobriment que presenta millor comportament, tant en un cas com en l'altre, és el de VPS, tot i que, sense estar polit, el potencial de corrosió és lleugerament inferior que el del HVOF. S'ha comprovat que el recobriment obtingut per plasma atmosfèric, degut a la presència d'esquerdes transversals, permet el pas de l'electròlit facilitant la corrosió de l'acer base,

mentre que el comportament catòdic dels altres dos és acceptable mentre que el recobriment es mantingui íntegre.

3. Conclusions

- En aquesta tesi s'ha aconseguit l'obtenció de recobriments de FeAl amb diferents microestructures optimitzant els paràmetres de projecció, provant diferents distribucions de partícules, etc. A partir de la tècnica d'HVOF s'han aconseguit recobriments menys porosos i amb menys oxidació. La projecció de partícules de major tamany permet retenir l'estructura nanocristal.lina inicial de la pols.

- Les diferents microestructures dels recobriments de FeAl determinen les diferents propietats on, s'observa en general, que els de major duresa mostren millor resistència al desgast abrasiu, mentre que la duresa no sembla ser una variable clau en el comportament a desgast per lliscament. El principal mecanisme que controla aquest últim tipus de desgast és el de delaminació on, degut a la fragilitat dels òxids entre partícules, es generen esquerdes que promouen la descohesió de dites partícules i la seva posterior oxidació i acumulació a ambdues bandes del camí de desgast.

- La resistència a l'oxidació a alta temperatura dels recobriment de FeAl presenta resultats acceptables a 900ºC però quan es puja a temperatures més altes, l'atac és més accelerat, donant lloc a la formació de Fe_2O_3 però no d'Al_2O_3.

- S'han obtingut per primera vegada recobriments de Nb-Al per Projecció Tèrmica, tot i que les dificultats associades a la pròpia naturalesa de la pols i la seva irregular distribució de tamanys de partícules, han fet que els recobriments estessin bastant oxidats, fet que suposa un empobriment d'alumini.

- S'han preparat recobriments de NiTi per APS modificat i HVOF i s'han comparat els resultats amb els obtinguts per VPS. Les diferents condicions a que han estat sotmeses dites partícules de pols durant el procés de projecció ha fet que els recobriments fossin formats per una varietat de zones amorfes, nanocristal.lines amb alternança de fase austenítica i martensítica.

- Per contra, sembla ser que el material desgastat en els recobriments de NiTi roman en el camí de desgast, a la vegada que s'endureix i promou un desgast més sever tant de la bola com del recobriment. En quant al desgast abrasiu, a igual que el FeAl, també hi ha una bona correlació amb la duresa del propi recobriment.

- La resistència a la corrosió dels recobriments de NiTi és major pel VPS i HVOF que no pas el d'APS ja que el mecanisme de corrosió d'aquest últim ve donat per la facilitat de penetració de la solució de clorur sòdic a través de les esquerdes del recobriment.